eman ta zabal zazu

Universidad del País Vasco Euskal Herriko Unibertsitatea

Graphene-based bionanocomposites: synthesis, physical and antimicrobial properties

Mónica Cobos Zamarreño

PhD Thesis

eman ta zabal zazu

Universidad del País Vasco   Euskal Herriko Unibertsitatea

Graphene-based bionanocomposites: synthesis, physical and antimicrobial properties

by

Mónica Cobos Zamarreño

Advisors

Prof. María Dolores Fernández Fernández

and

Prof. María Jesús Fernández Fernández

Polymers and Advanced Materials: Physics, Chemistry and Technology Department.

Faculty of Chemistry

Donostia, 2020

I

III

"All life is an experiment. The more experiments you make the better."

- Ralph Waldo Emerson

SUMMARY

The development of new materials with antimicrobial properties has attracted great interest in the healthcare industry due to the increasing use of biomedical devices in an ever-aging population. In this PhD thesis, new bionanocomposites have been developed presenting good thermal, mechanical and permeability properties, as well as antimicrobial capacity, which boosts their application in the biomedical field. To this end, different nanostructures or nanohybrids have been synthesized, and later incorporated as reinforcements in two different polymeric matrices, in both absence and presence of plasticizer. Considering their exceptional and advantageous properties, graphene and its derivatives have proved to be an interesting option for exploring and preparing new nanomaterials, while chitosan (CS) with reported antimicrobial activity and poly(vinyl alcohol) (PVA) with excellent film forming properties can be an appropriate continuous phase of the bionanocomposites.

In the first part of this research, exfoliated graphene oxide (GO) was obtained from natural graphite flakes by the modified Hummers' method and graphene sheets (GS) by chemical reduction of GO. Additionally, spherical silver nanoparticles (AgNPs) with an average size lesser than 4 nm were produced and homogeneously distributed on the surface of the partially reduced GO in the absence of any stabilizing agent (GO-AgNPs), by means of a one-step approach. According to the morphological results, the size of the AgNPs can be controlled by the concentration of the metal precursor and the reaction temperature. Additionally, the antimicrobial activity of graphene-based nanostructures against Gram-negative bacteria *Escherichia coli* and *Pseudomonas aeruginosa*, Gram-positive bacteria *Staphylococcus aureus*, and the yeast *Candida albicans* were found to be concentration- and time-dependent.

In the second part, different GO contents were added to chitosan and PVA, as well as to their blend (with 60% PVA and 40% CS) by the solution casting method, whereas the GS through *in situ* reduction of graphene oxide in presence of the polymers. SEM and TEM results revealed a good dispersion of the fillers in the polymeric matrices except in the case of direct addition of GS previously obtained in an isolated way. The exfoliated structure of GO and GS based nanocomposites resulted in increased thermal stability, mechanical properties and

water resistance. In addition, stiffness and tensile strength were accentuated by the presence of glycerol. The effect of the storage time on antimicrobial activity of CS *against Escherichia coli* was also analyzed.

Regarding GO-AgNPs nanohybrid as a reinforcing, *in situ* and *ex situ* routes were evaluated to be integrated in PVA matrix. Nanocomposites containing GO with spherical AgNPs displayed a significant antibacterial activity against *Staphylococcus aureus* and *Escherichia coli*. In contrast, PVA/GO films showed no activity against both bacteria over the GO concentration range investigated.

This work demonstrates that the tailoring of the nanocomposite properties is enabled by controlling filler type and content, as well as the use, or not, of plasticizer. The new developed materials, particularly those containing glycerol, could be employed for transdermal drug delivery and those with antibacterial properties may be potential wound dressings.

RESUMEN

El desarrollo de nuevos materiales con propiedades antimicrobianas ha suscitado un gran interés en la industria de la salud debido al constante aumento del uso de dispositivos biomédicos en una población cada vez más envejecida. En esta tesis doctoral se han desarrollado nuevos bionanocompuestos que combinan buenas propiedades térmicas, mecánicas y de permeabilidad, así como capacidad antimicrobiana, lo que permite su extensa aplicación en el ámbito sanitario. Con este fin, se han sintetizado diferentes nanoestructuras o nanohíbridos, que más tarde han sido empleados como refuerzos en dos matrices poliméricas diferentes, tanto en presencia como en ausencia de plastificante. Teniendo en cuenta sus excepcionales y ventajosas propiedades, el grafeno y sus derivados han demostrado ser una opción interesante para explorar y preparar nuevos nanomateriales, del mismo modo que el quitosano (CS), con actividad antimicrobiana documentada, y el alcohol polivinílico (PVA), con excelentes propiedades de formación de películas, pueden ser una apropiada fase continua para los bionanocompuestos.

En la primera parte de esta investigación se sintetizó óxido de grafeno exfoliado (GO) a partir de grafito natural por el método modificado de Hummers, y láminas de grafeno (GS) por reducción química del GO. Además, se obtuvieron nanopartículas de plata (AgNPs) esféricas con un tamaño medio inferior a 4 nm distribuidas homogéneamente en la superficie del GO parcialmente reducido y en ausencia de cualquier agente estabilizador (GO-AgNPs), empleando el enfoque de un solo paso. De acuerdo con los resultados morfológicos, el tamaño de las AgNPs puede ser controlado por medio de la concentración de precursor del metal y por la temperatura de reacción. También se determinó la capacidad antimicrobiana de las nanoestructuras basadas en grafeno contra las bacterias Gram-negativas *Escherichia coli* y *Pseudomonas aeruginosa*, el *Staphylococcus aureus* Gram-positivo y la levadura *Candida albicans* observándose una actividad dependiente de la concentración y el tiempo.

En la segunda parte, se añadieron diferentes contenidos de GO al quitosano y al PVA, así como a su mezcla (60% de PVA y 40% de CS), por el método de solución-evaporación, mientras que el GS fue incorporado a través de la reducción *in situ* del óxido de grafeno en presencia de los polímeros. Los resultados del SEM y el TEM revelaron una buena dispersión de los rellenos en las matrices

poliméricas, excepto en el caso de la adición directa del GS obtenido previamente de forma aislada. La estructura exfoliada de los nanocompuestos basados en GO y GS dio lugar a una mejora de la estabilidad térmica, propiedades mecánicas y resistencia al agua. Asimismo, la rigidez y la resistencia a la tracción se vieron reforzadas con la presencia de glicerol. También se analizó el efecto del almacenamiento en la actividad antimicrobiana del CS frente a *Escherichia coli*.

En cuanto al nanohíbrido de GO-AgNPs como refuerzo, se evaluaron las rutas *in situ* y *ex situ* para su integración en la matriz de PVA. Los nanocompuestos que contienen GO con AgNPs esféricas mostraron una importante actividad antibacteriana contra *Staphylococcus aureus* y *Escherichia coli*. Por el contrario, las películas de PVA/GO no mostraron actividad contra ambas bacterias en el rango de concentración de GO investigado.

Este trabajo demuestra que es posible ajustar las propiedades de los nanocompuestos mediante el control del tipo y contenido de relleno, así como del uso o no de plastificante. Los nuevos materiales desarrollados, en particular los que contienen glicerol, pueden ser empleados para la administración transdérmica de fármacos, del mismo modo que los materiales con propiedades antibacterianas podrían ser potenciales apósitos para heridas.

GENERAL INDEX

CHAPTER 1

GENERAL INTRODUCTION AND OBJECTIVES

1.1. <u>Background and Motivation</u>

The advance of science and civilization has always been closely related to the development of new materials and technologies [1]. Over the last century, polymers and composite materials have provided enormous technological support in diverse areas as automotive and aerospace industries [2], and have enabled the progress in the field of medicine [3,4] and the development of new electronic technologies [5-8]. One of the first and most common strategies for developing new polymer materials has been to mix polymers whose properties were not entirely desirable, but after combining them, they give rise to materials with improved properties that exceed their previous limitations. Nowadays, the strategies to design new materials are almost infinite, ranging from new synthesis routes and architectures to copolymerization, functionalization, grafting and even the addition of different reinforcements.

Common polymers by themselves cannot always completely satisfy the needs that a specific application may require (high mechanical or thermal properties) compared to other inorganic materials such as metals or ceramics. Therefore, inorganic additives have traditionally been incorporated into polymers as reinforcement, for example silicon oxide particles or glass fibers, resulting in composite materials with several different phases and improved properties.

In recent years, materials science has focused on reducing the size of the reinforcement phase to its nanometric structural unit, i.e. the development of nanostructures or nanomaterials, and on the search for compatibility agents between phases of different nature. Reinforcement with nano-sized fillers can overcome many drawbacks if they are well dispersed in the polymer matrix and most of the property improvements can be achieved with significantly smaller fillers than conventional micro-sized glass fillers, resulting in what is known today as nanocomposites [9]. These materials exhibit different behavior than conventional composites due to the vast increase in the surface area to volume ratio, which incorporates the possibilities of new quantum mechanical effects in such materials [1,10,11].

Nanotechnology emerges as a relatively new scientific area focused on the study of matter at the nanoscale, and which has meant a revolution in the field of materials basically for two reasons: the fact that the behavior of a material at the

nanoscale can be radically different from what is expected when extrapolating its properties to the micrometric scale, and because of its absolutely multidisciplinary nature. The revolution of nanocomposite polymeric materials lies in obtaining materials with customized properties using very low concentrations of reinforcement material and the utilization of conventional synthesis and processing methods used in microcomposite materials.

Traditionally, polymer composites are materials obtained by combining synthetic or petroleum-based polymers (matrix/continuous phase) with inorganic additives. When the polymer is of natural origin (biopolymer), or instead the filler, they can be classified as biocomposites or bioplastics. The composite differs from the nanocomposites in the size of the filler (dispersed phase) being the latter of nanometric size. However, the term nanocomposite can also be used to refer to graphene-based nanostructures to which inorganic and/or organic species have been incorporated through covalent or non-covalent bonds. Likewise, nanocomposites can be called bionanocomposites when the polymer formed is of natural origin (including polysaccharides, polypeptides and proteins, aliphatic polyesters or polynucleic acids) or even biomass and organic/inorganic filler with at least one dimension on the nanometer scale (1-100 nm). Figure 1.1 shows the place of the bionanocomposites among the other composite materials according to the above definitions.
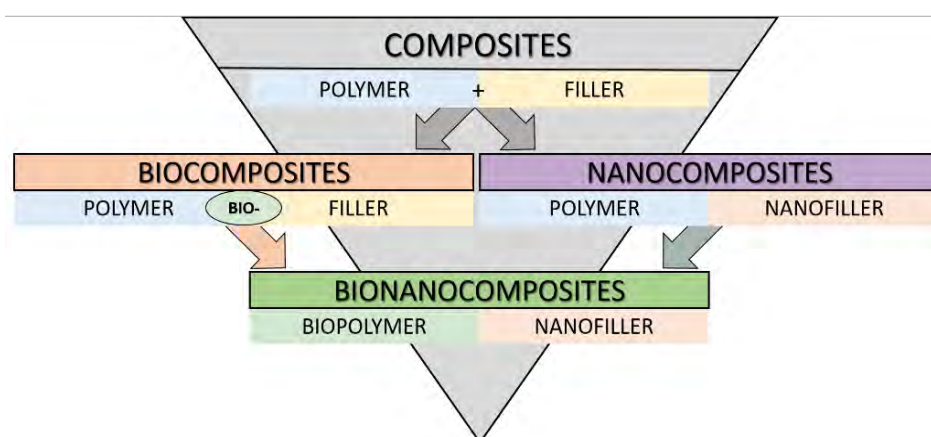

Figure 1.1. Main types of composite materials and their constituents.

Bionanocomposites, also known as 'nanobiocomposites', 'biocomposites', 'green compounds', 'biohybrids' or 'bioplastics', offer many applications in fields such as biomedical science, electronics, packaging, coating, textiles or cosmetics [12-15] proving to be an exceptional alternative to petroleum-based compound materials. These materials can be obtained from any biological source such as plants, trees or crustacean exoskeletons, and their main advantages over non-degradable petroleum-based materials are their high performance, biocompatibility and biodegradability [12,16,17]. The different properties showed by the bionanocomposites, such as thermal stability, solubility in water, biocompatibility, or biodegradability, are determined by the methods of preparation, functionalities, and the final areas of applications. Thus, composite materials with biopolymers have also become a subject of an increasing interest as an eco-friendly, cost-effective and renewable film material for food packaging and tissue engineering. As shown in Figure 1.2, in the last 20 years, there is an exponential growth in the number of annual publications dedicated not only to bionanocomposites in particular, but also to bioplastics or biocomposites.
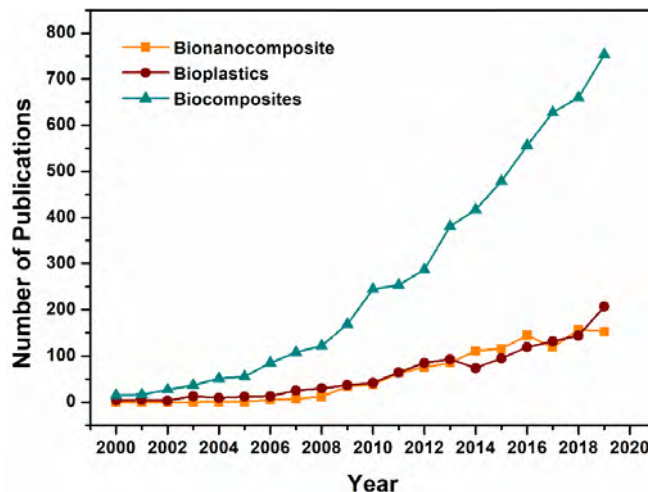

Figure 1.2. Number of publications per year according to the Web of Science (September 2020). Keywords for search: bionanocomposites, bioplastics and biocomposites.

Regarding medical materials, when talking about biopolymers, or biomaterials in general, it is dealing with materials strictly prepared to interact with biological systems, either to evaluate, treat, replace tissues, organs, or various organic functions [18]. As such, biomaterials will be in close contact with all types

of biological material, making the word biocompatibility a key factor. Avoiding any type of negative interaction with the immune system should be a priority, such as inflammatory processes, rejection, or others. In addition to biocompatibility, the maintenance of aseptic conditions of the material is of crucial importance since a minimal microbial colonization can lead to serious health problems in the host and even death. On the contrary, some functional requirements also imply the absorption/dissolution of the biomaterial in the organic environment. This process would be employed when the function of the biomaterial is required to be temporal, with an expiration date in its effects. In this case, these biomaterials are called bioabsorbable materials.

The interaction between the nanotechnology and medicine will support the next generation of nanomedicine and facilitate a personalized and efficient therapy [19,20]. Nanotechnology has demonstrated an incredible potential in improving both biomedical research and clinical applications [21]. Likewise, nanotechnology and the newest polymeric biomaterials converge in the development of new nanocomposites with complementary properties. For example, bioabsorbable polymers with hydroxyapatite are a classic example of regenerating bone structures and cells, with the polymer serving as a biodegradable support for this growth [22,23]. Nanosilver and other metallic nanoparticles have historically exhibited outstanding antimicrobial properties [24]. Also, graphene-based nanostructures have proven to be materials that promote neuronal growth in brain injuries [25], and their versatility makes them ideal for drug delivery, tissue engineering or the design of new materials with antibacterial activity [26-31].

Graphene has caused a great revolution in the field of nanoscience and technology. Since its first isolation in 2004, this material has attracted enormous scientific attention because of its marvelous chemical and physical properties [32]. The incorporation of graphene-based nanofillers offers the possibility to improve the mechanical properties of native materials, the possibility to add binding sites for further bio-functionalization with biological molecules, and get additional properties [33].

The need to develop new materials with more specific properties for medical applications, such as the manufacture of prostheses, surgical materials,

biomedical devices or wound dressings, is what has motivated the research of this thesis that deal with the development and study of graphene-based bionanocomposites with antimicrobial activity. The demand for this specific property is due to the fact that the presence of a foreign body (catheters or implants) considerably reduces the minimum number of microorganisms required to produce an infection since the biomaterial is not irrigated and the cells of the immune system would not access the area colonized by microorganisms. This results in increasing rates of infections associated with the insertion of biomaterials in health centers, which is one of the main causes of morbidity and mortality in developed countries.

There are different strategies to obtain polymeric materials with antimicrobial activity, apart from coating the surfaces of medical materials with antibiotics [34]. One approach is to use polymers matrix that possess antimicrobial properties because of the presence of certain functional groups in their chain that can damage the microbial membrane. Another way is the incorporation of inorganic antimicrobial compounds, such as clays or metallic nanoparticles or new synthesized nano-hybrids that present them avoiding the use of antibiotics, which promote the development of resistances.

1.2. <u>Objectives</u>

The main objective of this doctoral thesis is the development of new bionanocomposites with good thermal, mechanical and permeability properties, as well as antimicrobial capabilities enabling their application in the biomedical field. To this end, this research is focused on the design of different graphene-based nanoadditives that are then incorporated into biocompatible polymers with or without antimicrobial effect. Therefore, the following specific objectives are proposed:

1. To synthesize and to characterize: (a) graphite oxide, (b) graphene oxide, (c) chemically reduced graphene oxide and (d) graphene oxide decorated with silver nanoparticles.

2. To optimize and to develop synthesis methods that allow the physical and homogeneous dispersion of the nanoadditives within the polymer matrix.

3. To perform detailed morphological analysis of the composite materials according to the nanoadditive type, polymer matrix type and preparation method.

4. To study the influence of the addition of different contents of nanofillers and their dispersion degree on the thermal, mechanical, electrical (in the case of graphene), water absorption and permeability properties of the obtained nanocomposites.

5. To evaluate the antimicrobial activity of graphene-based materials and of their respective bionanocomposites.

1.3. <u>Overview of the Thesis</u>

This thesis addresses the different synthesis routes, the morphological characterization and the analysis of different properties such as mechanical, thermal and permeability, along with the antimicrobial capacity of three types of bionanocomposite films reinforced with nanostructures derived from graphene.

Chapter 2 focuses on the synthesis and characterization of graphene derivatives which in the following chapters are used as reinforcement. Graphene oxide (GO) is synthesized from natural graphite flakes by the modified Hummers method and the relevant sonication. Then, chemically reduced graphene (GS) is obtained with L-ascorbic acid as a GO reducing agent and by a one-step route. GO sheets are also decorated with silver nanoparticles (GO-AgNPs) without the need for a stabilizing agent. The physical and chemical characterization of these derivatives is done by different spectroscopies and thermogravimetric analysis (TGA). In this part, the antimicrobial properties of the synthesized nano-hybrids are evaluated against four different microorganisms.

In Chapter 3, synthesis, morphological structure and properties of chitosan/graphene nanocomposites are presented. GO is dispersed into chitosan (CS) matrix *via* solution casting method, while well-dispersed CS/GS nanocomposites are obtained *via in situ* chemical reduction of GO with L-ascorbic acid. The structural, thermal and mechanical properties of the nanocomposite films are compared, as well as the change in permeability and water absorption capacity as a function of filler type and the presence of plasticizer. Likewise, being the CS a material with antimicrobial activity, the effect of the storage in its capacity to kill the gram-negative bacteria *Escherichia coli* is also examined.

In Chapter 4, the structural, thermal, mechanical, permeability and water absorption analysis of different plasticized and unplasticized PVA/graphene based nanocomposites is discussed. Apart from the addition of GO and GS to the PVA matrix, PVA/silver nanoparticles-graphene oxide nanocomposites are also developed through *in situ* and *ex situ* method and compared between them. Moreover, antibacterial tests are performed against *Staphylococcus aureus* and *Escherichia coli* to evaluate whether the integration of graphene-silver hybrids provides a remarkable antibacterial activity in a polymer such as PVA that lacks this property by itself.

Chapter **5** presents the results of morphological, thermal and mechanical analysis of different PVA/CS blends prepared to determine which composition is the most favorable for the development of PVA/CS/graphene-based nanocomposites. Then, GO and GS are intercalated or exfoliated in the PVA/CS blend by the solution casting method and *in situ* reduction route. Structural and morphological information of dispersed fillers are obtained with different microscopies (TEM and SEM). Thermal and tensile test measurements are recorded to evaluate the effect of fillers on the thermal behavior and mechanical properties of biocomposites. Their influences on water vapor permeability, the degree of swelling and dissolution of the films are also examined.

Finally, Chapter 6 summarizes all the key results of this research focused on the development of a graphene-based bionanocomposite with antimicrobial activity. Furthermore, this chapter includes the scientific articles published in correlation with this PhD work.

In addition to the main chapters of this document, Annex A describes the scientific and technical activities, as well as the results obtained during the three-month stay at the University of Minnesota (USA).

1.4. <u>References</u>

[1] S. Stankovich, D.A. Dikin, G.H. Dommett, K.M. Kohlhaas, E.J. Zimney, E.A. Stach, et al., Graphene-based composite materials, Nature. 442 (2006) 282.

[2] P. Mangalgiri, Composite materials for aerospace applications, Bull. Mater. Sci. 22 (1999) 657-664.

[3] S. Ramakrishna, J. Mayer, E. Wintermantel, K.W. Leong, Biomedical applications of polymer-composite materials: a review, Composites Sci. Technol. 61 (2001) 1189-1224.

[4] M. Silva, N.M. Alves, M.C. Paiva, Graphene-polymer nanocomposites for biomedical applications, Polym. Adv. Technol. 29 (2018) 687-700.

[5] D. Lu, S. Luo, C. Wong, Conductive polymer composites, Encyclopedia of Polymer Science and Technology. (2002).

[6] J. Lange, Y. Wyser, Recent innovations in barrier technologies for plastic packaging—a review, Packaging Technology and Science: An International Journal. 16 (2003) 149-158.

[7] R. Duncan, H. Ringsdorf, R. Satchi-Fainaro, Polymer therapeutics—polymers as drugs, drug and protein conjugates and gene delivery systems: past, present and future opportunities, J. Drug Target. 14 (2006) 337-341.

[8] T.J. Fai, J.E. Mark, P.N. Prasad, Polymers and other advanced materials: Emerging technologies and business opportunities, Springer Science & Business Media 2013.

[9] J.R. Potts, D.R. Dreyer, C.W. Bielawski, R.S. Ruoff, Graphene-based polymer nanocomposites, Polymer. 52 (2011) 5-25.

[10] D.Y. Godovsky, Device applications of polymer-nanocomposites, Biopolymers· PVA Hydrogels, Anionic Polymerisation Nanocomposites, Springer, 2000, pp. 163-205.

[11] J. Jeevanandam, A. Barhoum, Y.S. Chan, A. Dufresne, M.K. Danquah, Review on nanoparticles and nanostructured materials: history, sources, toxicity and regulations, Beilstein journal of nanotechnology. 9 (2018) 1050-1074.

[12] M. Darder, P. Aranda, E. Ruiz-Hitzky, Bionanocomposites: a new concept of ecological, bioinspired, and functional hybrid materials, Adv Mater. 19 (2007) 1309-1319.

[13] M.M. Reddy, S. Vivekanandhan, M. Misra, S.K. Bhatia, A.K. Mohanty, Biobased plastics and bionanocomposites: Current status and future opportunities, Progress in polymer science. 38 (2013) 1653-1689.

[14] Mhd Haniffa, Mhd Abd Cader, Y.C. Ching, L.C. Abdullah, S.C. Poh, C.H. Chuah, Review of bionanocomposite coating films and their applications, Polymers. 8 (2016) 246.

[15] R. Zafar, K.M. Zia, S. Tabasum, F. Jabeen, A. Noreen, M. Zuber, Polysaccharide based bionanocomposites, properties and applications: A review, Int. J. Biol. Macromol. 92 (2016) 1012-1024.

[16] A. Mohanty, M.a. Misra, G. Hinrichsen, Biofibres, biodegradable polymers and biocomposites: An overview, Macromolecular materials and Engineering. 276 (2000) 1-24.

[17] S.S. Ray, M. Bousmina, Biodegradable polymers and their layered silicate nanocomposites: in greening the 21st century materials world, Progress in materials science. 50 (2005) 962-1079.

[18] F. Chen, X. Liu, Advancing biomaterials of human origin for tissue engineering, Progress in polymer science. 53 (2016) 86-168.

[19] C. Fornaguera, M.J. García-Celma, Personalized nanomedicine: a revolution at the nanoscale, Journal of personalized medicine. 7 (2017) 12.

[20] J.A. Barreto, W. O'Malley, M. Kubeil, B. Graham, H. Stephan, L. Spiccia, Nanomaterials: applications in cancer imaging and therapy, Adv Mater. 23 (2011) H18-H40.

[21] I.Y. Wong, S.N. Bhatia, M. Toner, Nanotechnology: emerging tools for biology and medicine, Genes Dev. 27 (2013) 2397-2408.

[22] M. Swetha, K. Sahithi, A. Moorthi, N. Srinivasan, K. Ramasamy, N. Selvamurugan, Biocomposites containing natural polymers and hydroxyapatite for bone tissue engineering, Int. J. Biol. Macromol. 47 (2010) 1-4.

[23] R. Song, M. Murphy, C. Li, K. Ting, C. Soo, Z. Zheng, Current development of biodegradable polymeric materials for biomedical applications, Drug Des. Devel. Ther. 12 (2018) 3117-3145.

[24] M. Rai, A. Yadav, A. Gade, Silver nanoparticles as a new generation of antimicrobials, Biotechnol. Adv. 27 (2009) 76-83.

[25] A. Fabbro, S. Bosi, L. Ballerini, M. Prato, Carbon nanotubes: artificial nanomaterials to engineer single neurons and neuronal networks, ACS chemical neuroscience. 3 (2012) 611-618.

[26] M. Kalbacova, A. Broz, J. Kong, M. Kalbac, Graphene substrates promote adherence of human osteoblasts and mesenchymal stromal cells, Carbon. 48 (2010) 4323-4329.

[27] S. Liu, T.H. Zeng, M. Hofmann, E. Burcombe, J. Wei, R. Jiang, et al., Antibacterial activity of graphite, graphite oxide, graphene oxide, and reduced graphene oxide: Membrane and oxidative stress. ACS Nano. 5 (2011) 6971-6980.

[28] X. Luo, C.L. Weaver, S. Tan, X.T. Cui, Pure graphene oxide doped conducting polymer nanocomposite for bio-interfacing, Journal of Materials Chemistry B. 1 (2013) 1340-1348.

[29] Z. Fan, B. Liu, J. Wang, S. Zhang, Q. Lin, P. Gong, et al., A novel wound dressing based on Ag/graphene polymer hydrogel: effectively kill bacteria and accelerate wound healing, Advanced Functional Materials. 24 (2014) 3933-3943.

[30] S. Goenka, V. Sant, S. Sant, Graphene-based nanomaterials for drug delivery and tissue engineering, J. Controlled Release. 173 (2014) 75-88.

[31] A.E. Jakus, E.B. Secor, A.L. Rutz, S.W. Jordan, M.C. Hersam, R.N. Shah, Three-dimensional printing of high-content graphene scaffolds for electronic and biomedical applications, ACS nano. 9 (2015) 4636-4648.

[32] Rao, C. E. E., Sood, A. E., Subrahmanyam, K. E., Govindaraj, A., Graphene: the new two-dimensional nanomaterial, Angewandte Chemie International Edition. 48 (2009) 7752-7777.

[33] H.H. Yoon, S.H. Bhang, T. Kim, T. Yu, T. Hyeon, B. Kim, Dual roles of graphene oxide in chondrogenic differentiation of adult stem cells: cell-adhesion substrate and growth factor-delivery carrier, Advanced Functional Materials. 24 (2014) 6455-6464.

[34] R. Greenhalgh, N.C. Dempsey-Hibbert, K.A. Whitehead, Antimicrobial strategies to reduce polymer biomaterial infections and their economic implications and considerations, Int. Biodeterior. Biodegrad. 136 (2019) 1-14.

CHAPTER 2

GRAPHENE – BASED MATERIALS

This chapter is centered on the study of different graphene derivatives. First, the graphite oxide (GrO) has been synthesized from natural graphite flakes by the modified Hummers' method, and later, the reduction of graphene oxide (GO) has been performed with L-ascorbic acid (L-AA). Fourier transform infrared (FTIR), X-ray photoelectron (XPS), Raman and UV-Vis spectroscopy, X-ray diffraction (XRD) and thermogravimetric analysis (TGA) were used to confirm graphite oxidation and the production of chemically reduced graphite (GS) sheets with different L-AA concentrations. Secondly, using a one-step approach, GO sheets decorated with silver nanoparticles (GO-AgNPs) have been synthesized. By this process, spherical AgNPs were obtained homogeneously distributed on the surface of the partially reduced GO, in the absence of any stabilizing agent, only with L-AA as reducing agent and AgNO₃ as metal precursor. The size of AgNPs was examined as a function of AgNO₃ concentration and temperature. In addition, the antimicrobial properties of the synthetized nanohybrids were evaluated against the Gram-negative bacteria Escherichia coli and Pseudomonas aeruginosa, Gram-positive bacteria Staphylococcus aureus and the yeast Candida albicans. These nanohybrids can be used as nanofillers in polymeric nanocomposites to develop materials with antimicrobial activity for applications in different areas.

The results discussed in this chapter correspond to different parts of three papers published previously in: Journal of Applied Polymer Science (2017), International journal of biological macromolecules (2018) and Nanomaterials (2020).

INDEX

2.1. <u>Introduction</u>

There was a time when diamond and graphite represented the only and abundant natural carbon allotropes. However, that changed significantly in 1985 when Kroto *et al.* [1] reported the production of synthetic carbon allotropes named fullerenes (Figure 2.1), and five years later Krätschmer and Huffman [2] described the successful preparation in macroscopic amounts.

Regarding the atomic structure of the natural allotropes, diamond is specifically formed by carbon atoms with a sp^3-hybridization, where each atom is joined to four other atoms in a tetrahedral arrangement that forms a three-dimensional network. However, graphite is made up of flat layers of carbon atom with sp^2-hybridization. Each layer is a two-dimensional network where each carbon atom is joined by strong covalent bonds to other three, forming six-carbon-atoms rings. The fourth electron of each atom contributes to the formation of extended delocalized electron clouds lying between the layers. This makes the layers to be held together by Van der Waals forces. Both of these forms show interesting traits such as high thermal conductivity and impressive hardness for the diamond, and lubrication behavior for the graphite since its layers can slide over each other or exfoliate easily.
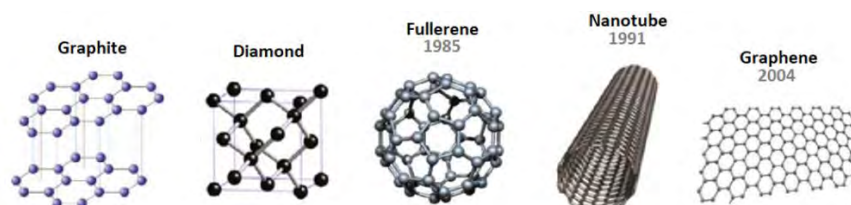

Figure 2.1. Allotropes of carbon.

The first and smallest synthetic carbon allotrope, fullerene C_{60}, consists of a network of sixty structurally equivalent sp^2-hybridized carbon atoms in the shape of a ball. Among its interesting properties, it has been found that chemically functionalized fullerenes vastly increase their solubility in any solvent and make them desirable for biomedical applications [3]. The discovery of carbon nanotubes (CNTs) in 1991 [4] and graphene in 2004 [5] was a scientific breakthrough in the carbon family. In the CNTs, the carbon atoms are arranged in hexagons, as in the graphite arrangement, but the structure consists of enrolled cylindrical graphitic

sheet (or graphene) rolled up into a seamless cylinder with a diameter of the order of one nanometer and a length of micrometric size.

2.1.1. Graphene

Graphene as a monoatomic two-dimensional structure of carbon atoms was first achieved in 2004 by Andre K. Geim and Konstantin S. Novoselov at the University of Manchester, for which they were honored with the Nobel Prize in Physics in 2010. Highly oriented pyrolytic graphite monolayer samples were isolated on solid support through mechanical exfoliation [5]. Up to that point, the studies had progressed, resulting in fewer and fewer layers of graphite [6], but it was assumed that a single layer of such a material did not exist in nature. This was due to the belief that such atomic planes would be thermodynamically unstable on that scale [7], and unsupported those planes would buckle and roll- up [8]. Therefore, this pioneering discovery of a single layer of carbon led to an explosion of interest in the scientific community.

Nonetheless, it should be noted that graphene-like structures had already been mentioned in 1840 by Schafhaeutl, a German scientist who first reported the insertion of acid or alkali metal between the carbon lamellae and exfoliation of graphite with sulfuric and nitric acids. Later, Brodie in 1855, Staudenmaier in 1898 and Hummers in 1958 also produced graphene oxide (GO) by exfoliating the graphite *via* high oxidizing reagents [9]. In 1962, Boehm and co-workers described thin and lamellar carbon structure that contained a small amount of hydrogen and oxygen after the chemical reduction of GO-dispersions in dilute alkaline media with hydrazine, hydrogen sulfide, or iron(II) salts [10]. Afterwards, the thermal reduction of GO was also published by the same group, which assumed that the achieved thinnest lamellae was a single layer of carbon. This hypothesis was attempted to be confirmed through Transmission Electron Microscopy (TEM) micrograph densitometry measurements, but the technology at that time did not allow such verification.

In any case, it should be noted that reduced graphene oxide or chemically derived graphene was first described by H. P. Boehm and co-workers, while Andre K. Geim and Konstantin S. Novoselov were the first to obtain pristine graphene, without heteroatomic defects.

2.1.1.1. <u>Structure and properties</u>

Graphene is the name given to a flat monolayer (2D system) of carbon atoms organized into hexagonal rings as honeycomb lattice with sp²-hybridization, or in other words, is a single layer of graphite. Three valence electrons of carbon atoms form σ-bonds with their next neighbors with an interatomic carbon-carbon length of 1.42 Å, arranged in a trigonal plane geometry with a separation angle of 120°. The fourth electron of each carbon atom localized in the pz (π) orbitals (perpendicular to the planar sheet) form highly delocalized π-bonds with the others (Figure 2.2). The great mobility of the delocalized electrons in the parallel directions to the plane is what determines the electrical properties of this material. Electrons can flow through graphene more easily than even through copper, being reported in literature an electrical conductivity up to 6,000 S/cm for a single layer of graphene [11].
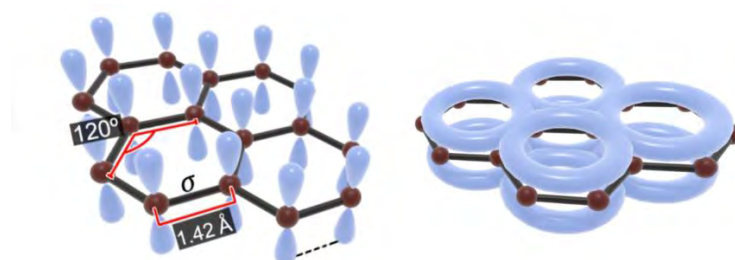

Figure 2.2. Structure of graphene: orbital representation and bonds.

Graphene can be considered as the parent material for all carbon allotropes (Figure 2.3A). It can be stacked to form bulk graphite, rolled into cylindrical CNTs or curved into spherical ball like fullerenes. It is assumed that a material categorized as 0D is one that cannot grow in any dimension of space as it is the case of fullerenes, while a 1D material is considered to be one that can grow in one dimension of space, such as CNTs. Likewise, a 2D material is one restricted to two dimensions of space, which is the case of graphene, and consequently, a 3D material will be one that can grow in all the three dimensions of space.

Individual graphene sheets (2D) in a stack (graphite) are bound together by Van der Waals forces at a distance of 0.34 nm, as shown in Figure 2.3B. These forces are weak relative to the covalent interatomic bonds within a given lattice,

and allow graphite to be stripped down to a few or even single layer sheets, by mechanical cleavage or other means [5].
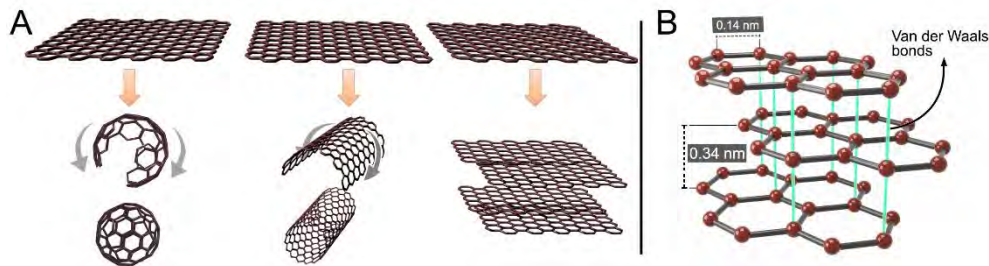

Figure 2.3. A) Graphene 2D building material for carbon materials of all other dimensionalities. B) The hexagonal structure of tri-layer graphene.

Originally it was assumed that graphene was perfectly flat, but ripples in the lattice were found to be present and caused by thermal fluctuations [12]. Since the advancement of high resolution TEM, it has been possible to get directly images of graphene honeycomb lattice structure [13]. In terms of optical properties, graphene absorbs 2.3% of the incident light per layer [14].

Regarding the electrical conductivity, materials can be classified as insulators, conductors or semiconductors. However, graphene is a special case of semi-metal, since it shares properties of conductors and semiconductors. It has a zero gap, like metals, with the peculiarity that the density of states at the Fermi level is zero, as it happens in semiconductors. The positions of the energy bands according to conductivity are shown in Figure 2.4. The plane drawn represents the Fermi energy (εf), the maximum energy level that electrons reach in a solid at zero temperature. When the Fermi level is in the conduction band (since the valence band overlaps the conduction band), it is a metal, the electrons circulate freely. In semiconductors and insulators, the Fermi level is between the valence and conduction bands and both differ in the bandwidth, called gap. Semiconductors do not exhibit too wide separation, so applying sufficient energy the electrical current can be conducted. In the case of graphene, there is no gap, but Fermi level is right at the connection between two energy bands, i.e. being the density of states at the Fermi level zero as in semiconductors, electrons can easily jump from the valence layer to the conduction layer and greatly facilitate electrical conduction. However, high carrier mobility is not always ideal for all

applications. Electronic circuits require small, but significant band gaps for "on" and "off" states. Using graphene directly would imply not controlling and stopping the electrons. With this purpose, researchers have been actively looking for ways to achieve this band [12].
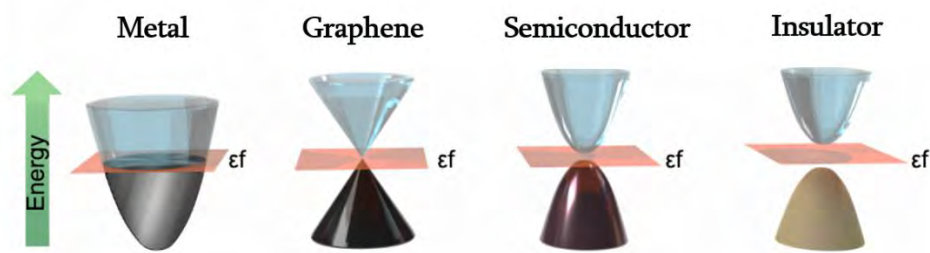

Figure 2.4. Graphene energy bands diagrams.

Graphene has become such interesting research subject because of its outstanding and unique properties, which are directly related to the two-dimensionally spread C=C resonance structure and the hybridized electrons, which give it a high conductivity and great mechanical resistance in the plane. Its carrier mobility is foretold to be 200,000 cm^2/Vs at room temperature [15], however, for actual samples this value is reduced to around 15,000 cm^2/Vs [12] due to defects and substrate effects. The adsorption of molecules on graphene surface results in the doping of the material (with electrons or voids depending on the nature of the adsorbed material) and consequently small changes in its resistivity. This variation along with its high specific surface area (2630 m^2/g) makes graphene a potential candidate for the development of highly sensitive sensors [16]. At room temperature this material presents a thermal conductivity above 5000 W/mK, higher than that of copper, diamond or silver, which allows it to dissipate heat and withstand intense electrical currents without heating up [17].

Its exceptional mechanical properties make graphene the strongest material known, with a tensile strength of 130 GPa and a high Young's modulus (≈1 TPa) [18]. It also presents a complete impermeability to any gases [18] and thermal stability up to 600 °C. All these superlative properties of graphene make it suitable for applications in a wide variety of fields which will be detailed in a later section.

2.1.1.2. <u>Nomenclature for 2D carbon materials</u>

The term graphene is often used to refer to a material composed of carbon structures in the form of sheets, but currently, there is an extensive variety of similar materials. Despite their similarities, these materials have significant differences in the number of layers, lateral dimension and chemical modification. Therefore, the correct definition of the material when presenting the results is of great importance. On this matter, the international editorial team of Carbon magazine published in 2013 a proposed nomenclature for 2D carbon materials [19]. The nomenclature used in this thesis is based on this proposal and is set out below (Figure 2.5):

- **<u>Graphene (G):</u>** A single-atom thick sheet of hexagonally arranged sp^2-bonded carbon atoms that is not an integral part of a carbon material, but is freely suspended or adhered on a foreign substrate, or in other words, one sheet of graphite. It is also called pristine graphene (PG), when it has been obtained by physical exfoliation and its electronic nature has not been altered.

- **<u>Graphite Oxide (GrO):</u>** A laminated material prepared by treating graphite with strong oxidants, whereby the surface and edges of the graphite undergo covalent chemical oxidation, resulting in an increase in the interlaminar distance from the graphite.

- **<u>Graphene Oxide (GO):</u>** Chemically modified graphene prepared by oxidation and exfoliation of graphite. Graphene oxide is a monolayer material with a high oxygen content, typically characterized by C/O atomic ratios less than 3.0 and usually closer to 2.0.

- **<u>Reduced Graphene Oxide (rGO):</u>** Graphene oxide (as above) that has been processed by chemical, thermal, microwave, photo-chemical, photo-thermal or microbial/bacterial methods to reduce its oxygen content. In the specific case of the **chemically reduced graphene**, **GS** abbreviation will be used and in **thermally reduced graphene oxide, TRGO**. It must be distinguished from pristine graphene because of the presence of heteroatoms and structural defects.

- **<u>Graphene materials</u>** (also graphene-based materials or graphene nanomaterials): Terms for the collection of 2D materials defined above that contain the word "graphene", including multilayered materials, chemically

modified forms (GO, rGO), and materials made using graphene, graphene oxide, or another graphene material as a precursor.
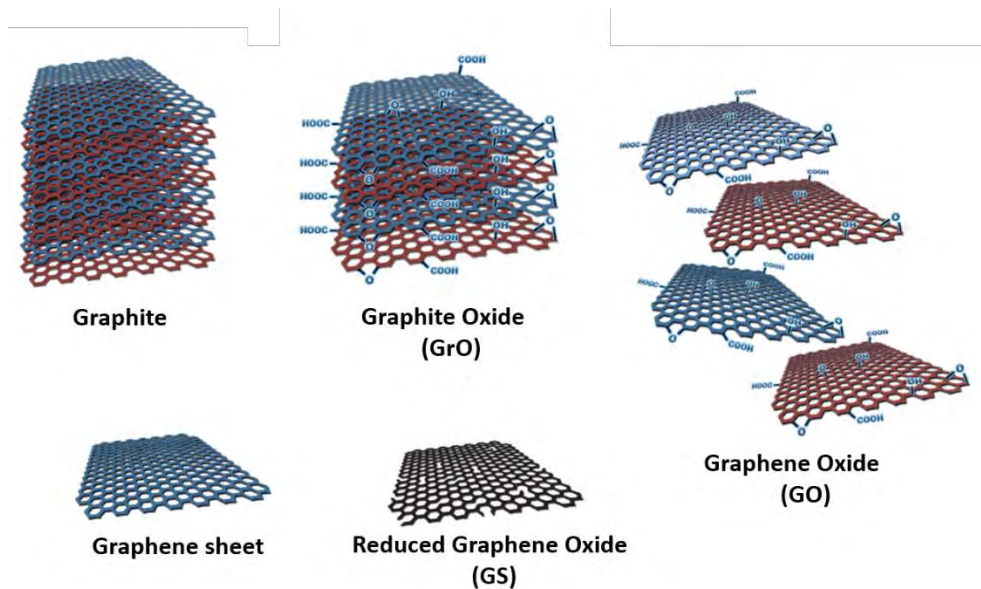

Figure 2.5. Proposed nomenclature for graphene based materials.

In view of all the terms that exist in the field of graphene, the exhaustive characterization of the same is an unavoidable step in the research of related subjects, whether it has been purchased or has been obtained in the laboratory.

2.1.1.3. Graphene synthesis

The large-scale production of graphene with high-quality sheets and defect free has become a crucial challenge. On this matter, to meet the demanding requirements, extensive research efforts have focused on developing large-scale methods of synthesis [20-23]. Graphene production can be classified in two groups (Figure 2.6): **"Top-down"**, consisting in the obtaining of graphene from a bulk material, and the **"Bottom-up"**, that involves the growth of the carbon lattice atom by atom [11,24]. Some of the methods are described below:
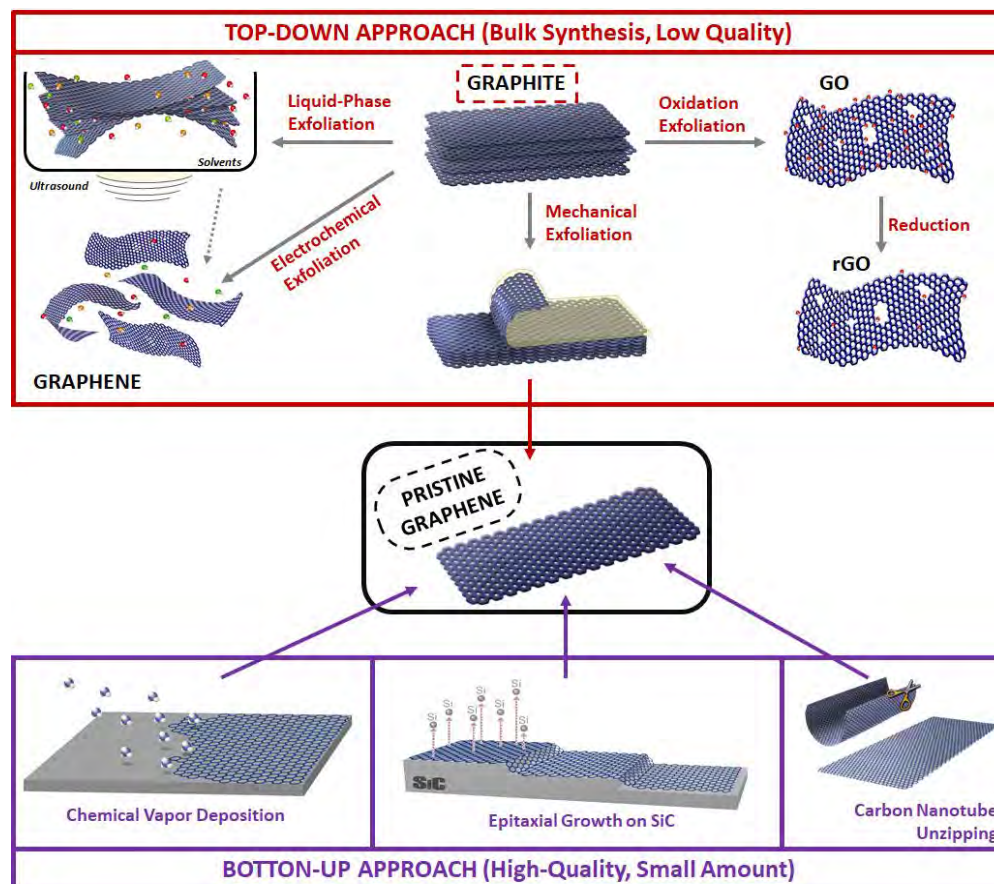
Figure 2.6. Schematic representation of the methods developed for graphene synthesis.

"Top-Down"

• **Mechanical exfoliation:** Micromechanical cleavage using adhesive tape to peel thin graphitic layers from bulk graphite and depositing them on a silicon substrate [5]. This method provides the highest quality, with no lattice damage. However, the yield obtained is not suitable for large-scale production of graphene.

• **Reduction of graphite oxide:** Obtaining of graphite oxide by the Hummers method [25] (described in section 2.1.2.2), followed by its exfoliation and reduction. The reduction process can be carried out *thermally*, *chemically*, *solvothermally* and *electrochemically*.

i. Thermal annealing reduction: The fast temperature increment makes the oxygen containing functional groups attached on carbon plane decompose into gases (CO or CO_2) generating a huge pressure between the stacked layers, and thus the spacing of them. The rapid heating process not only exfoliates graphite oxide, but also reduces the functionalized graphene sheets [26,27]. Nevertheless, the decomposition of the oxygen-containing groups also removes the carbon atoms which affects properties such as electrical conductivity [27].

ii. Chemical reduction: A cheaper and easily available way for the mass production of graphene. Hydrazine was first employed to remove oxide functional groups [28,29], but it also introduces heteroatom impurities such as nitrogen that remains covalently bound to the surface of graphene sheets. Metal hydrides, such as sodium hydride, sodium borohydride and lithium aluminium hydride, have been accepted as strong reducing reagents in organic chemistry. Hydriodic acid has also been reported as a strong reducing reagent for GO [30,31]. However, all these reduction agents are toxic, hazardous and corrosive, so that other alternatives such as ascorbic acid (vitamin C) [32-35], amino acids [36] or reducing sugar [37] have been developed. Other reductants including hydroquinone [38], pyrogallol [35], hot strong alkaline solutions (KOH, NaOH) [39], hydroxylamine [40], urea and thiourea have been also used, but these reagents tend to be inferior to strong reductants.

iii. Solvothermal reduction: This method is performed in a sealed container, so that the solvent can be brought to a temperature well above its boiling point by the increase of pressure resulting from heating [41]. In a hydrothermal process, overheated supercritical (SC) water can play the role of reducing agent because under high temperature and pressure conditions, high reactive hydrogen ions are generated [41,42]. Other studies reported reduction of GO by solvothermal reduction using *N,N*-dimethylformamide as the solvent [43] and, unlike hydrothermal reduction, a small amount of hydrazine was added as the reducing agent.

iv. Electrochemical reduction: In a standard three-electrode electrochemical system at room temperature, GO sheets are directly reduced from an aqueous colloidal suspension in the presence of buffer electrolyte to produce graphene sheets on an electrode surface. The electrochemical reduction is believed to take place when the GO sheets next to an electrode accept electrons,

yielding the insoluble graphene that attach directly onto the electrode surface [44,45]. This method can be also performed in two steps in which GO is firstly deposited onto the surface of an electrode (by drop-casting, dip-coating, layer-by-layer or spray-coating), and it is dried out to form a GO-coated electrode. This prepared electrode is then subjected to electrochemical reduction using a standard three-electrode electrochemical system in the presence of a supporting electrolyte to produce graphene sheets films on the electrode substrate [46].

• **Liquid-phase exfoliation of graphite:** The process can be divided into three steps: dispersion, exfoliation and purification. Ideal solvents are those that minimize the interfacial tension between the liquid and the graphene flakes. Water has been used by itself [47] and with the assistance of surfactants in order to stabilize the exfoliated graphene sheets against re-aggregation. Solvents with a surface tension of $\approx$40 mJ/m^2 such as N-methyl-pyrrolidone (NMP) and N,N-dimethylformamide (DMF) have been confirmed as the best media for graphite exfoliation [48,49], but it should be noted that they are toxic, expensive and not so volatile. The exfoliation in ionic liquids have also been investigated [50,51]. The limitation of the phase exfoliation of graphite is the platelet size, since the exfoliation procedure by means of ultrasonication induces in-plane fractures.

• **Electrochemical exfoliation of graphite:** A platinum wire is used as a counter electrode, graphite as a working electrode (where the voltage is applied), and aqueous sulfuric acid (H_2SO_4) as electrolyte solution. The mechanism consists of the electrolysis of water at the electrode, producing hydroxyl radicals and oxygen. These radicals, initially oxidize the edge and/or grain boundaries of the graphite. Those defects at the edge and grain boundaries leads to depolarization and expansion of the graphite layers which enables the interleaving of SO_4^{2-} anions within the graphite layers along with the water. Moreover, the reduction of intercalated SO_4^{2-} anions and self-oxidation of water produce gaseous species, such as SO_2 and O_2, which exert a high force on the graphite layers, and thus separate weakly bonded graphite layers from one another [52,53]. Generally, the electrochemical method offers some advantages over the other methods, such as the simple one-step operation and control of the synthesis, functionalization and exfoliation process [54]. However, the graphene produced by this method presents a number of defects, which modify its electronic properties [11].

"Bottom-up"

- **Chemical vapor deposition (CVD):** Is one of the most promising techniques for large-scale production of graphene [55]. Generally, CVD of graphene is performed in a gas phase where a precursor (usually a small hydrocarbon) reacts with a catalyst in a reaction chamber at high temperature (temperature up to the melting point of the catalyst metal). Consequently, the graphene is formed on the catalyst surface. In this process, different metal substrates can be employed as catalysts, but for large-scale production, Cu and Ni are the most commonly used [23,56].

- **Epitaxial growth on SiC:** Based on the epitaxial growth of graphene film on the surface of a silicon carbide (SiC) crystal by thermal decomposition [57]. The SiC is heated to temperatures exceeding 1100 °C in a low pressure environment to be reduced to graphene. The size and properties of the SiC wafer govern the properties of the formed graphene, such as its mobility and carrier density. This method is very promising due to the production of large size graphene sheets, elevated purity without defects, and uniform properties [58]. The high cost of the substrates and the requirement of highly specialized equipment still remain as the most remarkable limitations.

- **Carbon nanotube unzipping**: Based on opening longitudinally and unrolling carbon nanotubes by different methods such as the intercalation of lithium and ammonia followed by exfoliation [59].

2.1.1.4. Graphene dispersions

Graphene is generally recognized as a hydrophobic material that is not soluble in solvents, i.e. exfoliated sheets or multi-layer aggregates are phase separated from any solvent. Graphene sheets tend to form irreversible agglomerates or even restack to form graphite unless they are well separated from each other, due to the important π-π interactions between the different layers. As a result of this behavior, the excellent graphene properties worsen rapidly as more layers are stacked. This can be avoided by solvent selection [60,61], or by the modification of graphene either covalently or non-covalently [22].

Commonly, the exfoliation of graphene in the absence of any surface modifying agent, surfactant or polymer is performed using a suitable solvent and applying some form of sonication, either in the bath or at the tip, in order to provide high energy by shear stress and cavitation in the solvent, and thus overcome interlayer adhesion. Both effects help to break the binding energy between graphene surfaces. Some solvents have been identified as remarkably good at dispersing graphene, such as N-mehtyl pyrrolidone (NMP), dimethyl sulfoxide (DMSO) and dimethylformamide (DMF) [60]. Ionic liquids (ILs) have shown some promising results, however, they are not widely used in industry [62]. Mainly, it is known that the concentration of graphene is related to both sonication time and power. Nonetheless, long sonication times are generally undesirable, as they can reduce the size of the sheet and introduce defects that undermine the properties of graphene.

The chemical functionalization of the graphene surface is another strategy that allows the solvation and exfoliation of the sheets. Concretely, this method has offered many possibilities to overcome graphene's restrictions. As far as dispersion is concerned, covalent modifications, non-covalent modifications and atom substitutions have been studied [63]. The addition of certain functional groups can enable the right incorporation of hydrophobic graphene monolayer to multiple media. The most common way is the oxidation of graphene to GO. The variety of functional groups containing oxygen makes an easier solvation in some solvents. In the case of reduced graphene oxide, it should be noted that in the process of reduction the structure of the graphene is restored, but some of the functional groups are retained and they can facilitate dispersion [64].

The choice of solvent opens up a range of possibilities for achieving dispersed graphene sheets. However, dispersions also have their own drawbacks due to the instability of suspended graphene. Sheets tend to agglomerate with the time (faster depending on the solvent chosen) when sonication-induced energy ceases, leading to noticeable differences in graphene concentration for aliquots taken from the same dispersion. Moreover, for many applications, exfoliation of graphene in solvents is undesirable due to solvent high boiling point, toxicity, incompatibility with other aspects of processing, etc. To address these issues, the possibility of exfoliating graphene in water in the presence of a surfactant stabilizer was studied. Surfactants can enclose the graphene surface and provide

steric or electrostatic repulsions to avoid the close contact between different layers. Most surfactants consist of a hydrophobic tail group and a hydrophilic head group. The mentioned repulsions will depend on the nature of the head group [65]. A great variety of studies have been carried out for the surfactant-stabilized graphene exfoliation [64]. The first detailed study of surfactant-stabilized graphene was described by the Coleman group [66] who used sodium dodecylbenzenesulphate (SDBS) as a surfactant. In other works, sodium chlorate and sodium deoxycholate have been widely used, being the last one five times more effective [67]. Poly(vinylpyrrolidone) (PVP), an example of a non-ionic surfactant, is also used to assist in the exfoliation of graphene and for the dispersion of rGOs under aqueous conditions [68,69] or with organic solvents. Other polymers have also been shown to stabilize graphene dispersions in water and organic solvents [70,71].

Fundamentally, to get a useful graphene dispersion, sheets must be dispersed at a suitable concentration, in an appropriate solvent for the selected application and must remain dispersed for a reasonable period of time.

2.1.1.5. Chemistry and functionalization

Graphene is aromatic in nature and, as described in previous sections (2.1.1.1), it has a dense electron cloud above and below the plane. With this structure, the frontier molecular orbitals of organic molecules can easily interact with the π-electrons of graphene making its electrophilic substitution much easier than nucleophilic one.

The cycloadditions, the click reactions and carbide insertion reactions are some of the types of reactions in which graphene can take part [72,73]. However, reactions on the surfaces of graphene hamper its planar structure. The destruction of the sp^2 structure leads to the formation of defects and thus to the loss of electrical conductivity, thermal conductivity, etc. According to Loh *et al.* [74], the chemical reactivity of geometrically strained regions of graphene lattices is much higher in comparison with other regions due to the easier displacement of electron density from the upper plane of the ring.

The properties and applications of graphene can be adjusted by parameters, such as number of layers, dimensions, and in particular, with surface functionalization [75]. Surface modification is one of the foremost methods used to reduce the cohesive force between the graphene sheets and also to manipulate the physical and chemical properties [76,77]. It provides numerous additional functions to the graphene sheets which play a crucial role in their commercial applications. Generally speaking, functionalization of the carbonaceous structure of graphene is a path with a wide variety of possibilities. For this reason, there has been a huge increase in the number of research projects aimed at functionalization of graphene. Multiple attempts from different perspectives have been reported and can be summarize in the following groups:

i. Covalent bonding: The main objectives pursued with this type of functionalization are the improvement of graphene sheets dispersion and the addition of new properties related to the added groups. In most cases when organic molecules are covalently attached on the graphene surface, its extended aromatic character is perturbed, enabling changes or control of its electronic properties. The covalent functionalization includes the formation of covalent bonds between free radicals and C=C bonds of pristine graphene, as well as the formation of covalent bonds between organic functional groups and the oxygen groups of GO. The most attractive organic species for the reaction with sp^2-carbons of graphene are organic free radicals and dienophiles. This type of reaction allows a variety of organic derivatives, which show interesting applications in polymer compounds, biotechnology, nanoelectronic devices, drug delivery and solar cells [78-80].

ii. Non-covalent bonding: This functionalization offers the possibility of attaching functional groups to graphene by π-interactions without disturbing its electronic network. It is defined as non-destructive method, since the electronic, chemical, physical, and mechanical properties of the pristine graphene are preserved after the modification [81].

iii. Substitutional doping of graphene: This strategy involves the substitution of some of the carbon atoms from the honeycomb lattice by other atoms, frequently boron or nitrogen. Depending on the electrophilic character of the atoms that substitute the carbon atoms, the doped graphene sheets show N-

type (electron donor) or P-type (electron acceptor) behavior. Furthermore, the control in the degree of the doping modification can be used to regulate the electrical properties of graphene, thereby expanding extraordinarily the application of graphene in nanoelectronics. The most studied one is nitrogen doped graphene [82-84]. In this process, nitrogen atoms use their three sp^3 orbitals to incorporate into the sheet, what makes their lone pair electrons to conjugate with the graphitic π-system. The N-doped graphene sheets are electron-rich so that N-type semiconducting behavior is expected [85].

iv. Functionalization of graphene with nanoparticles: It is based on the immobilization of metallic or metal-oxide nanoparticles over the graphene sheet surface. A pristine graphene sheet can be considered as an ideal substrate for the dispersion of nanoparticles due to its large active surface area per mass unit, in comparison with carbon nanotubes or graphite, which have a lower active surface area because only the external surface is active. Frequently, the precursors for nanoparticles (NPs) are metal salts, which are reduced in a solvent that contains dispersed GO, rGO, or pristine graphene sheets. This strategy presents great variety of applications in catalysis, optoelectronics and energy storage devices such as fuel cells, batteries and supercapacitors as well as in medical or biological fields [86]. Taking into account the aims established for this thesis, different researches in relation to the metallic nanoparticles deposited on the surface of graphene will be described in more detail in a later section (2.1.3.1).

2.1.1.6. Potential applications of graphene

The excellent properties of graphene as the lightest and strongest material, and its ability to conduct heat and electricity make it an outstanding candidate for a wide variety of applications in fields such as bioengineering, composite materials, energy technology and nanotechnology. A review of 2014 shows the increase in patent applications on graphene for a very diverse range of applications, including characterization, polymer compounds, transparent screens, transistors, capacitors, solar cells, biosensors, conductive inks or photo detectors (Figure 2.7) [87].

A recent interesting graphene application is on DNA sequencing [88]. The main concept is to create a membrane of graphene with nanopores, immerse it in a conductive fluid and apply a voltage to one end in order to extract the DNA through the miniscule pores of graphene. The base pairs C, G, A, T cross the pore affecting the electronic structure of the graphene and the electric field in different degrees, distinguishing and sequencing them. In the field of biotechnology, the large surface area, chemical purity and the possibility of easy functionalization of graphene offer opportunities for drug delivery [89]. Likewise, its unique mechanical properties suggest the use of graphene in tissue engineering and regenerative medicine [90], and its thinness and conductivity impart it as an ideal support for imaging biomolecules in transmission electron microscopy [91].

Chemically functionalized graphene may lead to fast and ultrasensitive measurement devices, capable of detecting a range of biological molecules [85]. Graphene is used to develop enzyme biosensors [92], electrochemical immunosensor electrodes [93], as well as gas sensors [16]. The simplest and common configuration for graphene-based sensors is the field-effect transistor (FET) [94]. Likewise, graphene is a good candidate to function as a part of the optical fiber [95], which is used in a variety of advanced sensors as refractive index sensor, pressure sensor, acoustic sensor, current sensor and so on.

Regarding environmental issues, membrane separation has turned into a technology of great importance where the graphene offers the advantage of achieving size-selective separation membrane. Selective permeability can be obtained by adjusting the structure or chemical properties of graphene, generating nanopores. These membranes are useful as ion separation membranes for desalination [96] and water disinfection [97].

One field in which graphene is becoming increasingly essential is optoelectronics [98]. In particular, it is present in touch screens, liquid crystal displays (LCD) and organic light-emitting diodes (OLED) [99]. In these devices, graphene functions as a transparent conductor because of its low resistance and high transparency. Up to now, indium tin oxide (ITO) has been used for this function, however, graphene has emerged as a promising material. The optical transmittance of monolayer or few-layer graphene grown by chemical vapor deposition (CVD) is superior to that of ITO. In addition, high quality graphene

has high tensile strength and is flexible meanwhile ITO tends to crack when bent or stretched, causing deterioration of its electrical properties.

Figure 2.7. Graphene potential applications.

It is undeniable that in the last few decades the area of electronics has advanced rapidly and will continue to do so, however, batteries and capacitors have progressed more slowly due to energy storage problems. Currently, Li-ion battery technology offers the best source of energy, and therefore governs the global mobile electronics market being graphite used as the anode material for these batteries. However, fulfill the growing demand for high energy density and durable systems, new electrode materials need to be developed. Graphene-based nanomaterials have been reviewed as a potential alternative to Li-ion batteries due to their greater chemical stability, greater surface area and higher

conductivity compared to graphite [100], causing a reduction in the amount of material and improving the mechanical integrity of the electrode, which could achieve good performance, high capacity and flexibility during the charge and discharge process [101]. Lithium-ion batteries enhanced with graphene could be used in energy-intensive applications such as electric vehicles. In electronic field, graphene transistors on the basis of graphene grown on Cu films has been proposed as a method to achieve large-scale transistor arrays with uniform electrical properties [102].

Photovoltaic cells, or solar cells, are another potential application of graphene. At present, silicon is mainly used in the production of these devices, thus increasing their price. Since graphene offers high electron mobility and very low levels of light absorption, it can be a cheap alternative to silicon. When materials such as silicon convert light into electricity, it produces one electron for each photon received, which means that a lot of potential energy is lost in the form of heat. In contrast, a different research has proved that when graphene absorbs a photon, it actually generates multiple electrons [103]. In addition, graphene is capable of generating electricity from all wavelengths unlike silicon which is efficient with certain wavelength of light.

From the perspective of materials science, graphene plays an important role in the development of different and new nanocomposites due to its excellent properties. Besides, its large surface area compared with other nano-structural materials makes it ideal as nano multifunctional reinforcement for many polymer composites [104,105]. In this way, graphene sheets can provide, for instance, percolated pathways for electron transfer, making the composites electrically conductive. Moreover, this reinforcement can significantly improve the mechanical properties of the polymeric matrix at extremely small loading, as well as thermal stability and gas barrier properties [11].

2.1.2. <u>Graphene Oxide</u>

Graphene oxide (GO) is not a natural compound. Its development dates back more than 150 years, when in an attempt to determine the "atomic weight" of graphite, Brodie first reported the preparation of graphite oxide through chemical treatments using potassium chlorate ($KClO_3$) and nitric acid (HNO_3) [9]. Later, Sraudenmaier modified this method adding one more acid, H_2SO_4, as the oxidizing agent [9]. However, these two methods were time consuming and hazardous. In 1958, Hummers and Offeman [25] developed a more rapid and safer method to prepare graphite oxide from graphite, in which an essentially anhydrous mixture of $NaNO_3$, H_2SO_4 and $KMnO_4$ was used as the oxidizing agent. This method provided a substantial C/O ratio in the final product. Graphite oxide preparation has been revived and Hummers' method has been modified to become more effective by adding pre-oxidation steps [106,107].

The chemical reduction of GO to graphene is one of the most important topic in GO research. GO is an electrical insulator, and after reduction, it becomes electrically conductive. Usually some orders of magnitude of the electrical conductivity increase during the reduction process. However, graphene materials derived from GO have much lower crystallinity and much lower carrier mobility [5,108,109]. The harsh environment of chemical oxidation in GO synthesis processes creates many defects and vacancies within the sp^2 carbon network, which are almost impossible to recover by subsequent chemical treatments [109]. Despite defects, GOs, rGOs and their derivatives have shown some promising applications in catalysis, compounds, energy storage, detection, water purification, electronics, etc.

2.1.2.1. <u>Structure and properties</u>

In terms of chemistry, GO is a new kind of nonstoichiometric macromolecule that is chemically labile and hygroscopic in ambient conditions. As mentioned above, synthesis of GO has been adapted several times with different chemicals such as potassium permanganate, concentrated sulfuric acid, and even phosphoric acid. The resulted compounds differ slightly in their chemical composition depending on the reaction used.

Graphene oxide is a single layer of graphite consisting of aromatic regions (carbon atoms sp^2) and oxygenated aliphatic regions (carbon atoms sp^3) containing epoxy, hydroxyl, carbonyl and carboxyl functional groups in random order along the basal plane. Generally, the functional epoxy and hydroxyl groups extend above the graphene while the carboxylic functional groups tend to lie at the edges of the graphene oxide layers (Figure 2.8). However, it should be highlighted that throughout many decades the exact chemical structure of GO has been the subject of considerable debate. The detailed structure of GO and its oxidation mechanism are still not completely understood due to its complex structure (with irregular packing of the layers, strong disorder, nonstoichiometric atomic composition and lack of consistent and reproducible samples) [63]. What is clear is that the structure and properties of GO mainly depend on the preparation method, the degree of oxidation achieved and the source of graphite used.

During the oxidation, polar oxygen functional groups are induced to the surface and render it hydrophilic. These groups are chemically active and ready to be functionalized making GO a suitable material for biomedical applications. For instance, covalent attachment of GO to chitosan [110], folic acid [111] or PEG [112] provides a platform for the delivery of anti-inflammatory and water-insoluble anticancer drugs [113]. Moreover, the abundant surface functional groups are also used as nucleation site to grow nanoparticles [97]. In short, thanks to the rich chemistry of the oxygenated groups, GO can be functionalized through covalent and non-covalent bonds.
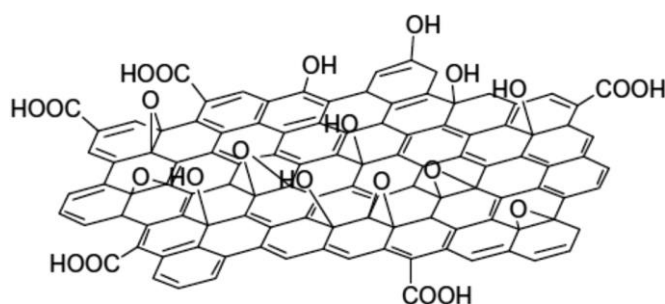

Figure 2.8. Scheme of GO sheet and oxygen-containing groups.

On the other hand, unlike graphene, the functional groups present on the surface of the GO enables it to disperse easier in a wide variety of solvents. Some authors have detailed that homogeneous colloidal suspensions of graphene oxide

in aqueous and organic solvents can be achieved by simple sonication of graphite oxide [28,29,114]. In particular, complete exfoliation of graphite oxide into individual GO sheets can be achieved in water, giving brown/dark-brown suspension. Organic solvents such as ethylene glycol, DMF, NMP and THF have proven to be ideal for preparing GO dispersions. However, as with graphene, as time goes by exfoliated GO sheets tend to aggregate through π–π stacking, although in the case of GO in a less pronounced way. Therefore, some protective agents such as large aromatic molecules or octadecylamine have been presented for the stabilization of GO sheets in the solution [115,116].

Regarding the electrical conductivity, as mentioned above, graphene oxide works as an electrical insulator, due to the disturbance of its sp^2-bonding network. It is essential to reduce the graphene oxide to recover the hexagonal graphite network (rGO) in order to restore electrical conductivity. The reduction process, as described in the section on graphene synthesis (2.1.1.3), can be done by thermal, chemical, solvothermal and electrochemical methods, although it has not yet been possible to reduce the material fully back to graphene. The C/O ratio of the resulting rGO must be greater than 6 to restore conductivity.

2.1.2.2. Synthesis methods

• <u>Brodie and Staudermaier method:</u> The first batch of graphite oxide (GrO) was prepared in 1859 by the British chemist Benjamin Collins Brodie when he was studying graphite chemistry. A new product consisting of carbon, oxygen and hydrogen was obtained by adding potassium chlorate ($KClO_3$) to a graphite/nitric acid (HNO_3) mixture. After repeatedly washing, drying and re-oxidation, the graphite oxide was light yellow and stable. Based on their research and analysis, the empirical formula for the final product obtained was $C_{11}H_4O_5$. His observations and conclusions were limited by the theories and characterization technology available at the time [117-119].

The improvement of Brodie's work occurred in 1898 by L. Staudenmaier who introduced two important changes: the addition of concentrated sulfuric acid (H_2SO_4) to increase the acidity of the mixture and the addition of multiple aliquots of potassium chlorate ($KClO_3$) solution to the reaction mixture during the reaction

process. With these modifications, the synthesis process was simplified and the GO product obtained was highly oxidized in a single reaction vessel. However, in terms of security, this method was time consuming as the addition of $KClO_3$ typically took more than a week and the evolved chlorine dioxide (ClO_2) needed to be removed by an inert gas, while the explosion was a constant danger. Therefore, an improvement was needed to develop this oxidation process [118].

- **Hummers' method and its modifications:** Almost 60 years after Staudenmaier's strategy, Hummer and his colleagues developed the oxidation process for the preparation of GO known nowadays as Hummers' Method. The proposed graphite oxide preparation consisted of a water-free combination of sodium nitrate ($NaNO_3$), concentrated sulfuric acid (H_2SO_4) and potassium permanganate ($KMnO_4$) that was kept under 45 °C for 2 hours. The final product was found to have a higher degree of oxidation than the Staudenmaier product. However, it was noted that the product obtained by the Hummers' method had an incompletely oxidized graphite core. As a result, a pre-expansion process was necessary for excellent oxidation with this method. Kovtyukhova [120] developed the pre-treatment by adding graphite to the mixture of concentrated sulfuric acid (H_2SO_4), potassium persulfate ($K_2S_2O_8$) and phosphorus pentoxide (P_2O_5) and leaving it at 80 °C for several hours. The pre-treated mixture was diluted, filtered, washed and dried before the real Hummers' oxidation took place. It was later learned that pre-treatment may be omitted if the graphite samples have a smaller flake size or have thermally expanded.

Currently, the most commonly used method for the preparation of GO is known as the modified Hummers' method. It is based on the same reagents as the conventional method, but with different conditions and quantities. Additionally, it implies using hydrogen peroxide (H_2O_2) to reduce residual ions from permanganate ($KMnO_4$) and manganese dioxide (MnO_2). A series of washes is required for the removal of impurities, including sulfate ions with the use of hydrochloric acid (HCl). The chloride ions are dissolved in the distilled water during washing. The solution is centrifuged with a high-speed centrifuge and washed to a pH of 5 to 7 in the supernatant. The final product is dispersed in deionized water.

However, it is noteworthy that different reaction conditions or different versions of the modified Hummers' method are also reported in the literature, in which the amounts of reagents, reaction time or even the addition of phosphoric acid (H_3PO_4) to increase the acidity of the medium, vary significantly from study to study. In other synthesis processes the removal of $NaNO_3$ (which together with $KMnO_4$ acts as oxidant agent) is also proposed, since it can form toxic gases like NO_2 and N_2O_4, as well as residual Na^+ and NO_3^- ions [106,121].

In view of all the possible variants of the Hummers' method, there is no doubt that an exhaustive characterization of the final product is necessary, since depending on the chosen synthesis conditions, both the degree of oxidation and the size of GO sheets can significantly differ.

2.1.3. <u>Graphene nanocomposites</u>

Considering the exceptional and advantageous properties of graphene and its derivatives (GO and rGO), in the last decades many efforts have been made in the implementation of these materials alone or in combination with other materials to obtain new composites for particular applications. Generally, graphene-based nanomaterials are composed of two components, but multi-component composites have also been prepared for specific applications. The incorporation of inorganic species and/or cross-linking of organic species through covalent and/or non-covalent interactions in graphene are known as hybrid materials. Based on the architecture of nanocomposites (Figure 2.9), graphene-based nanocomposites can be classified into four groups [122]:

1. Graphene-supported nanocomposites: Where graphene sheets form a continuous phase and act as a substrate to support the second component, which adheres to the sheets. Frequently, the second components are inorganic nanoparticles such as metals, metal oxides or carbon building blocks, as CNT, fullerene, etc. Therefore, this group can also be named as **graphene-based inorganic nanocomposites**. It should be highlighted that this thesis will mainly focus on **graphene-metal nanocomposites**, where the secondary component is a noble metal, concretely for this work **silver nanoparticles (AgNPs)**. This subgroup will be detailed in the following section (2.1.3.1).

2. Graphene-encapsulated nanocomposites: In this type of nanocomposite graphene sheets are enwrapping a second component and working as a protective layer which could prevent the aggregation of the other component. These structures are used as high performance lithium storage electrode materials.

3. Graphene-incorporated nanocomposites: Graphene sheets or graphene composites work as fillers in a continuous polymeric matrix in order to improve the properties of the material. Likewise, they are known as **graphene-based polymer nanocomposites** (more detailed in section 2.1.3.2). The polymeric compounds prepared and studied in this thesis work are classified within this group since graphene and synthesized graphene hybrids have been used as additives.

4. Graphene-based multilayered nanocomposites: Obtained by stacking graphene sheets with a second component alternatively. These structures are frequently employed for charge generation, transfer and separation.
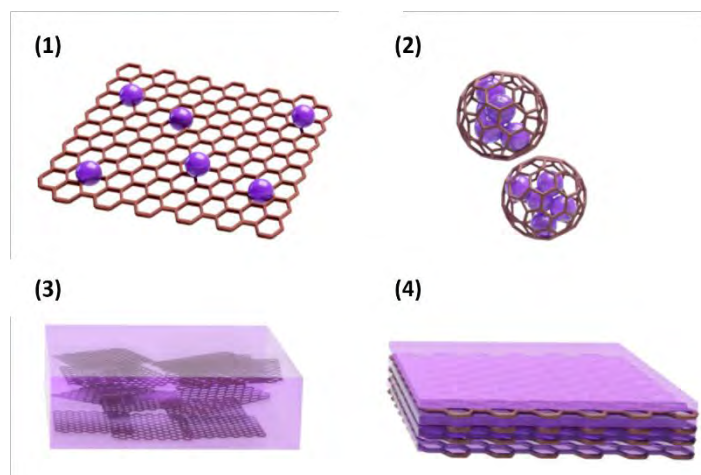
Figure 2.9. Scheme of graphene-based nanocomposite architectures.

2.1.3.1. Graphene – metal nanocomposites

The integration of metallic nanostructures onto graphene have attracted great interest in the scientific community due to numerous potential applications, including energy storage and energy conversion devices, biosensors, catalysts, photocatalysts, surface enhanced Raman scattering (SERS), diagnostics, imaging, drug delivery or antibacterial agents. For instance, in the case of biosensor

applications, graphene/metal nanocomposites not only overcome the limitations of using a single component, but also provide greater effective surface area, increased the surface/volume ratio, etc. [123,124]. Therefore, nanoparticles (NPs) of Au, Ag, Ni, Cu, Ru, Pt etc., and graphene have become essential components in the formation of new hybrids [125].

Nanoparticles are defined as agglomerations of atoms in the range of 1-100 nm. Their outstanding properties make them suitable for application in different fields, such as optoelectronics, catalysis, environment and biomedicine [126]. NPs of noble metals are attracting a great deal of attention because of their antimicrobial activity against many pathogens, making them attractive potential alternatives to antibiotics. Particularly, silver nanoparticles (AgNPs) have emerged as the most exploited nano-antimicrobials for different commercial applications [127,128]. Currently, they are commonly used in healthcare products, cosmetics, women's hygiene products, medical devices, sunscreen, in food industry, colloidal coating, biosensors, filtration membranes of water and electronics [129,130]. Compared to silver bulk form, AgNPs have novel biological, chemical and physical characteristics. Several physical, chemical, and biological methods have been reported to synthesize AgNPs [131-135]. Among chemical processes, the chemical reduction, based on the reduction of a silver salt solution by a reducing agent, is the simplest, cost-effective and frequently applied method. Borohydride, sodium citrate, ascorbic acid, alcohol, and hydrazine compounds have been used as reducing agents. The reduction of silver ions (Ag^+) results in silver atoms (Ag^0), which agglomerates into oligomeric clusters leading to the formation of colloidal AgNPs. However, they have low colloidal stability when used in liquid systems and aggregations to form clusters occurs owing to the high surface area of nanoparticles. The stabilization of nanoparticles in a dispersant medium can be achieved by creating sufficient repulsive forces to counteract the Van der Waals interactions, which are acting on the nanoparticle surface. This can be accomplished by an electrostatic and/or a steric mechanism. In the first case, a surface charge on the nanoparticle is developed, while in the second case nonionic surfactants or polymer layers can be chemically anchored or physically adsorbed on the surface of nanoparticle.

The experimental conditions (temperature, pH), the kinetics of the interaction of metal ions with reducing agents and the stabilizing agents play a

crucial role in the synthesis of AgNPs with controlled size, a well-defined shape and stability, and therefore the final physicochemical properties of nanoparticles [136-139]. In general, the use of different synthesis methods results in nanoparticles of different sizes and shapes, such as spherical, triangular, square, cubic, rectangular, rod, oval, and floral. The characterization of these morphological parameters is of great importance since they determine the antimicrobial activity of the AgNPs. Different researches have proved that small size AgNPs against bacteria, exhibit higher antibacterial activity compared to higher size nanoparticles due to the high specific surface area and easy cell penetration [126,140-143]. On the other hand, the effect of shape has been less reported and the results show that silver nanoparticles undergo shape-dependent interaction with the bacteria [136,144]. Consequently, the development of AgNPs with well-controlled morphological features is essential for biomedical applications.

Among the graphitic structures, GO is known to be an appropriate substrate to disperse and stabilize metal nanoparticles due to the oxygen-containing groups present on the surface, in addition to a large surface area, and ability to yield stable dispersions in water due to its hydrophilic nature. These properties enable GO to act as a suitable platform for growing metal nanoparticles (nucleation center) and their stabilization [145-147]. In general, the use of graphene as a substrate for NPs dispersion provides the following advantages:

i. The limited growth of nanoparticles, and their better stability and dispersion on the surface.

ii. The attached nanoparticles are also useful for extending the interplanar spacing of GO or rGO in solid state, and for avoiding the aggregation of GO or rGO sheets.

iii. A highly-specific surface which could prevent the aggregation of NPs.

iv. The excellent properties of individual GO or rGO sheets, such as thermal conductivity, high mobility of charge carriers, optical transmission, etc. are added.

Graphene oxide-nanoparticle composites can be obtained by means of two types of synthesis: *ex situ* and *in situ* (Figure 2.10). Moreover, within these two groups, other synthesis methods can be found as described below:
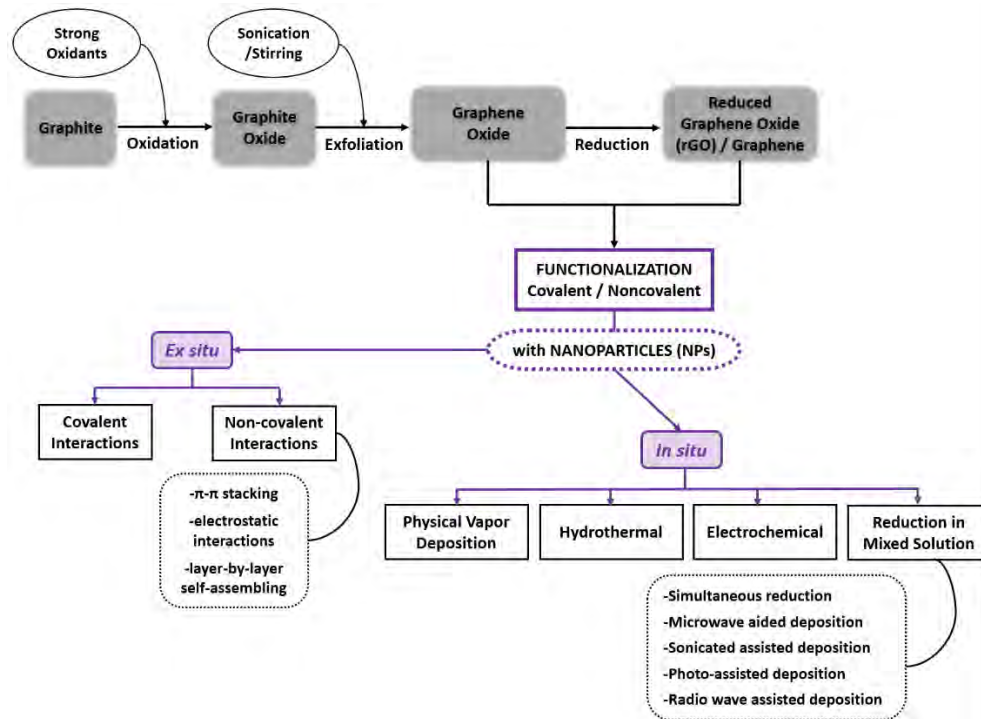
Figure 2.10. Schematic diagram of graphene/metal-NPs synthesis procedures.

- ***Ex situ* approach:** Solutions of pre-synthetized nanoparticles and graphene material nanosheets are mixed. The success of the synthesis of NPs is established by the ability to get a uniform size distribution, as well as a long stability, given their tendency to agglomerate in an aqueous solution. Consequently, prior to mixing, NPs and/or graphene sheets are usually functionalized to increase solubility and thus facilitate handling during the process. The anchoring of the nanoparticles takes place by either covalent or non-covalent interactions. A large number of functional groups are required for covalent bonding, so GO is preferred to rGO. Non-covalent attachment can occur by π-π stacking, where aromatic compounds are usually adhered to the nanoparticle surface [148], and by electrostatic interactions based on the inherent negative charge of the GO and rGO surface (a result of the ionization of oxygen functional groups) which is utilized to assemble positively charged NPs. Likewise, it can be, though, layer-by-layer self-assembling where two layers are generated by altering the graphene sheets and nanoparticles with opposite charges. The *ex situ* method has the disadvantage of low density and non-uniform coverage of the nanostructures over

the graphene sheets. This is attributed to the non-uniformity of the surface of the sheets (defects, sheets with low lateral dimension depending on the production method). In contrast, this method allows a precise control of the size and shape of NPs.

• ***In situ* approach:** A one-step method, where the chemical reduction of an aqueous solution of both metal precursor and GO sheets with reductants is carried out simultaneously to generate metal nanoparticles on the graphene material surface. The groups and defects on the GO or rGO can not only improve the solubility of the nanosheets, but also offer the nucleation sites of nanoparticles. More concretely, the negative charges in the GO sheets due to oxygen rich functional groups, allow strong electrostatic interactions with free metal ions. Once the attachment of the metal ions to the graphene oxide surface has taken place, these ions can be reduced by the reducing agents, enabling the growth of metal nanoparticles on the graphene surface. The presence of the oxygen functionalities at the graphene oxide surface plays an important role on the nucleation, growth and stabilization of the metal nanoparticles. In this sense, as in the previous strategy GO and rGO sheets act as stabilizers of NPs.

Among the possibilities offered by *in situ* strategy, the reduction in mixed solution has been the most popular way for growing metal particles on graphene. Precursors for noble metals, such as $AgNO_3$, K_2PtCl_4 and so on can be easily reduced by chemical reducers [149-151]. The free metal ions obtained are adhered through electrostatic interactions. As an alternative, microwave irradiation can also be used to unleash a uniform and rapid heating that allows the fast reduction of metal ions and GO [152,153] in presence or absence of the reducing agent. Other supports for this reduction could be the use of high-frequency ultrasound, UV radiation known as photo-assisted deposition [154] and radiofrequency. Compared to *ex situ* approach, this process gives uniform surface coverage by controlling the nucleation sites on GO through surface modification, but the size and morphology control is hard to achieve.

The deposition of graphene sheets on an electrode, followed by immersion of that electrode in an electrolytic solution with the metallic precursor, and then the application of an electrochemical potential to reduce and assemble both components is another *in situ* route, identified as electrochemical method [155].

The hydrothermal reduction [156] and the physical vapor deposition methods [157] are other different alternatives to get graphene-metal nanocomposites.

Regarding the synthesis of GO-AgNPs hybrids, different strategies have been reported as well as the use of different reducing and stabilizing agents. Bao *et al.* used hydroquinone as the reductant and citrate as the stabilizer [97]. Das *et al.* employed NaBH4 in the absence and presence of trisodium citrate as a stabilizing agent [158,159]. Shen *et al.* used a mixed reducing agent, ethylene glycol and NaBH4 [150]. In the study of Chook *et al.* a microwave approach with glucose as a reducing agent was used [153]. Ma *et al.* also reported the preparation of Ag–GO composites under ultrasonication using glucose as a reducing agent [160]. Tang *et al.* [161], Fonseca de Faria *et al.* [162], and Yuan *et al.* [163] used sodium citrate as a reducing and stabilizing agent at boiling temperature, 130 °C and 95 °C, respectively. Hydrazine monohydrate was used as a reductant by Cai *et al.* to prepare polyethyleneimine-modified reduced graphene oxide-AgNP hybrids [164]. KOH was used as a reducing agent at boiling temperature in the work reported by Pasricha *et al.* [151]. In the study by Hui *et al.* AgNP–GO composites were fabricated under ultrasonication with ascorbic acid as the reductant [146]. Shen *et al.* synthesized Ag-GO composites at 160 °C with ascorbic acid as the reductant and an ionic liquid as a dispersing agent [165]. Several of the mentioned methods have the disadvantage of using toxic reducing agents in the synthesis process.

It has been demonstrated that in these nanostructures GO and AgNPs work synergistically to enhance their properties, such as higher antimicrobial and catalytic activities and thermal conductivity. Therefore, these hybrids have proven to be useful in a variety of applications (electronics, catalysis, electrochemical biosensing, drug delivery, and antimicrobial agents) [166-171].

2.1.3.2. Graphene/polymer nanocomposites

Nanocomposites are mainly composed of a polymer matrix, organic/inorganic fillers, and plasticizers. The good dispersion and distribution of nanofillers in the matrix is one of the essential conditions for obtaining nanocomposite materials with enhanced properties. Commonly, the

improvement is attributed to the high interfacial area between nanofillers and polymer matrices. For all these reasons, the literature includes different preparation processes to achieve a homogeneous and well-dispersed graphene polymer nanocomposite [172]:

• **Solution casting:** Mainly due to its simplicity, the solution casting is one of the most widely used methods to manufacture uniformly dispersed nanocomposites. Graphene is dispersed in a solvent by sonication before being added to the polymer solution. Then, the solvent is removed by evaporation at high or room temperature. The chosen solvent must be capable of dissolving the host polymer and be volatile to promote rapid evaporation [173]. The challenge of this procedure comes from the need for a correct initial dispersion of the graphene, where the choice of solvent is a key factor (section 2.1.1.4).

• _In situ_ **polymerization:** The monomer and graphene are initially dissolved in a common solvent and subjected to ultrasound to achieve a uniform dispersion. Then, the polymerization reaction proceeds by adding initiator and adjusting parameters such as temperature and time [105].

• **Melt processing:** This process is more commercially attractive than the other two methods, considering that both solvent processing and _in situ_ polymerization process are less environmentally friendly and versatile. This strategy involves the direct inclusion of the graphene sheets into the melted polymer using a twin-screw extruder and adjusting parameters such as screw speed, temperature and time [174]. The main shortcomings of this procedure are the low bulk density of exfoliated graphene that makes extruder feeding a troublesome task and the lower degree of dispersion compared to solvent blending.

In addition to providing a support for the above-mentioned metal-graphene nanocomposites (2.1.3.1), GO has been successfully used as a filler material for polymers owing to its remarkable thermal, mechanical, and electrical properties. GO has proven to be an ideal precursor for the cost-effective and mass production of **polymer/graphene nanocomposites**. The different strategies for obtaining this type of compounds are shown in Figure 2.11.

The ***ex situ*** processes involve first the reduction of graphite oxide through the techniques described in section 2.1.1.3, and then the mixing with the polymer, both in solution and in melting. However, this strategy has the disadvantage of the possible phenomenon of flocculation (irreversible precipitation and agglomeration) during reduction, since graphene sheets naturally tend to rearrange as in the parent graphite structure, which makes it difficult to disperse within a polymer matrix at the individual sheet level. Consequently, GO reduction in the presence of the polymer matrix seems to be the best alternative to achieve polymer/graphene nanocomposites with well-dispersed graphene. The presence of the polymer prevents the agglomeration of the graphene sheets. Within the ***in situ*** strategy, four processes can be distinguished.

i. *In situ* polymerization: With polar or hydrophilic monomers that can interact and intercalate between the GO sheets. For this process, the GO is initially dispersed in a polar solvent using ultrasonication. The dispersed sheets are then mixed with the monomer and the polymerization reaction is carried out at high temperature and under inert atmosphere [175]. High temperatures help to achieve correct dispersion and ensure the reduction of GO. This method generally provides a homogeneous dispersion of graphene into polymer matrix and consequently, the electrical and thermal conductivity of the composite is significantly increased.

ii. GO reduction during the compositing process: This strategy involves the dispersion of GO in the polymer followed by thermal reduction resulting in a monolayer rGO compound. In this process the polymer/GO compound is first prepared by solution mixing and then dried overnight in order to immobilize the graphene oxide sheets in the rigid polymer matrix. The reduction process is then carried out by hot pressing or compression molding of polymer/GO film at temperatures exceeding 200 °C, yielding nanocomposites with isolated single layers of TRGO [176,177].

iii. *In situ* GO-reduction in quiescent melt and under shear: A recent research work has shown that composite materials that are sheared in the melt have a greater degree of reduction compared to the resting condition [178].
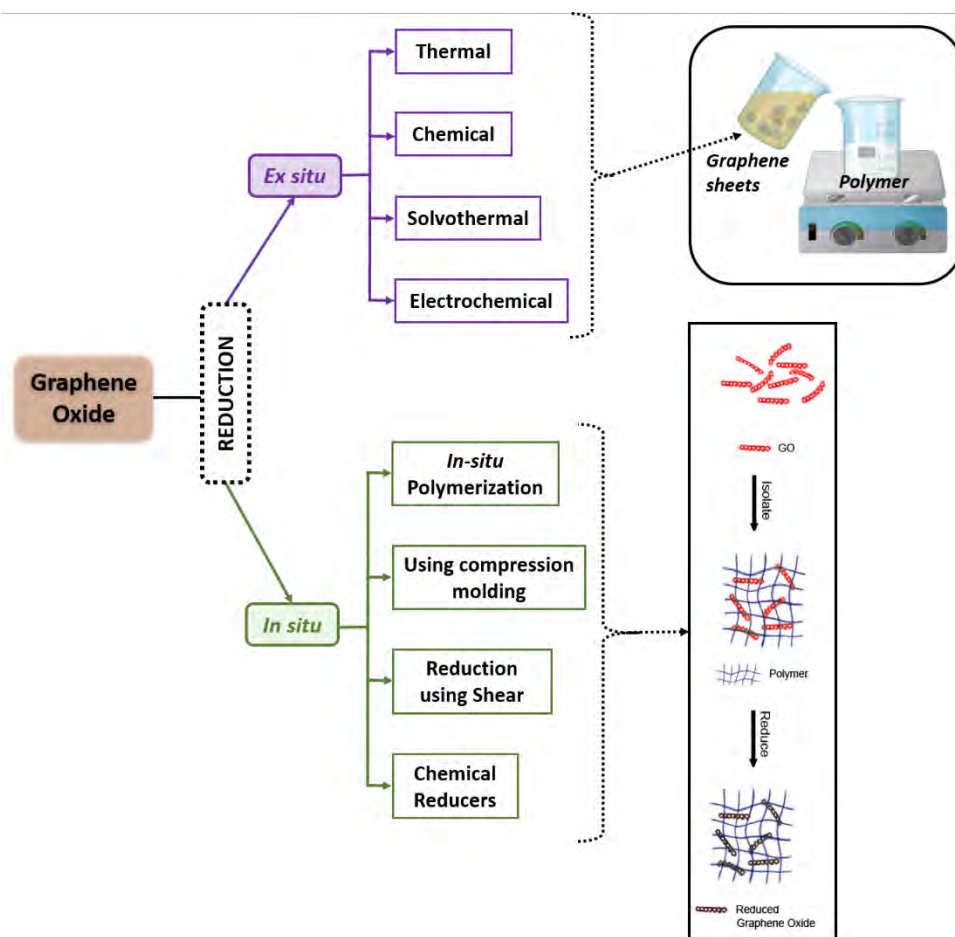
Figure 2.11. Outline of strategies to obtain graphene polymer nanocomposites through GO.

iv. In situ GO-reduction using reducing agents: This method is the one carried out and studied in this thesis (in the following chapters). The process consists of preparing a stable dispersion of GO in a previously dissolved polymer, followed by the addition of the reducing agent when the solution mixture is at high temperature.

2.1.4. <u>Antimicrobial properties of graphene based materials</u>

The antimicrobial properties of graphene based materials have been proven to be influenced by its intrinsic physicochemical properties (size, surface area, functional groups, oxygen content, surface roughness, layer number, purity and arrangement mode), as well as the interacting conditions between graphene materials and bacterial or fungi cells, such as concentration, incubation time, medium and the characteristics of microorganisms used. Both the graphite source and the level of oxidation/exfoliation (governed by the preparation method) determine most of these features. These numerous variations are the reason why the reported results in literature show discrepancies [179-182].

Different studies have demonstrated that the antibacterial activity of GO is lateral dimension dependent and, furthermore, the effect of GO in suspension is different from that of GO film. Large sheets displayed stronger activity against *Escherichia coli* and *Staphylococcus aureus* than smaller ones when GO was in suspension [183], whereas the antibacterial activity of GO-coated surface produced with smaller GO sheets was higher [184]. In addition, it has been reported that highly purified GO did not show antibacterial properties against *E. coli* and *S. aureus* over a broad concentration, and that the size of GO did not impact the bacterial growth [185]. The study of Ruiz *et al.* [179] demonstrated that pure graphene oxide did not have intrinsic antibacterial properties, and indeed an increase in bacterial growth was observed. This was explained by the stimulation of bacterial proliferation *via* GO, which acts as a surface for cellular attachment and growth. The number of layers, the density of functional groups and dispersion state of the graphene material are factors that have been shown to influence the antibacterial activity of graphene materials [181,186]. Additionally, GO has shown concentration- and time-dependent antimicrobial activity [181,182,187-189].

Several mechanisms of microbial inactivation by graphene-based materials have been proposed, which can be classified into two groups: physical and chemical interactions (Figure 2.12). These mechanisms can act separately or together to either bactericidally or bacteriostatically inhibit bacterial growth. Physical mechanisms are based on the physical interaction of graphene with microorganisms. When bacterial cells come into direct contact with the sharp

edges or basal planes of GO, membrane stress of bacteria can be induced, resulting in disruption and physical damage to cell membranes. The sharp edges of graphene sheets act as nanoknives, cutting the bacterial cell membrane, which leads to the leakage of intracellular components followed by cell death [190]. Wrapping and trapping of bacterial membranes by the flexible thin sheets of GO after their direct contact has also been proposed as another antimicrobial mechanism of the graphene materials [183,184,190,191]. In this situation, bacterial cells die by being isolated from the growth medium. However, cell inhibition by GO embedding can be reversible and all the originally viable cells may possibly be recovered by their separation from GO nanosheets *via* several techniques, e.g. sonication. Regarding chemical mechanisms, the high oxidation capacity of graphene material plays a key role, with oxidative stress being the main mechanism of bacterial inactivation [190,192]. Oxidative stress can occur through either a reactive oxygen species (ROS)-dependent or a ROS-independent pathway. In the first case oxidative stress is mediated by production of reactive oxygen species (ROS), which can damage cellular components. In the second one, however, the production of ROS is not involved, being the charge transfer from the cellular membrane to graphene surface which induces cell death.
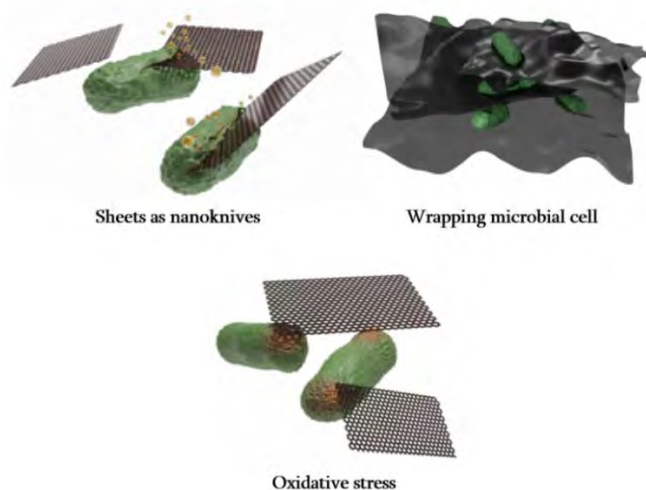
Figure 2.12. Scheme for physical and chemical mechanisms for antimicrobial activity of graphene-based materials.

2.2. Experimental section

2.2.1. Materials

Graphite flakes were purchased from Alfa Aesar (99.8%, 325 mesh) and sodium nitrate ($NaNO_3$) was obtained from Merck. Sulfuric acid (H_2SO_4, 98%), potassium permanganate ($KMnO_4$), hydrogen peroxide (H_2O_2, 30 wt% aq.), hydrochloric acid (HCl, 37% aq.) and ammonium hydroxide (NH_4OH) were acquired from Panreac (Spain). L-Ascorbic acid (L-AA), silver nitrate ($AgNO_3$), phosphate-buffered saline (PBS), and RPMI were supplied by Sigma-Aldrich. All chemicals were used as received without further purification. Gram-negative bacteria *Escherichia coli* ATCC 25922 and *Pseudomonas aeruginosa* ATCC 27853, and Gram-positive bacteria *Staphylococcus aureus* ATCC 25923 were obtained from CECT (Spanish Type Culture Collection, Valencia, Spain). Yeast *Candida albicans* SC5314 was obtained from the American Type Culture Collection (ATCC, Manassas, Virginia, WV, USA), and brain heart infusion (BHI) broth and Mueller–Hinton broth were supplied by Condalab.

2.2.2. Synthesis of Graphene oxide (GO)

To obtain graphene oxide, first, graphite oxide (GrO) was prepared from the oxidation of graphite, which was then exfoliated to obtain graphene oxide. GrO was synthesized from natural graphite flakes by the modified Hummers method. 1 g $NaNO_3$, 2 g graphite, and 50 mL H_2SO_4 were mixed in an ice bath. $KMnO_4$ (6 g) was slowly added while stirring for 1 h at 0 °C. The mixture was stirred with a magnetic stirring bar for another 2 hours and kept at 0 °C. The mixture was then transferred to a water bath at 35 °C and stirred for approximately 1 hour. Subsequently, 100 mL of deionized water was added gradually (3 h of addition) into the mixture at 0 °C, and right after, 5 mL of H_2O_2 (30% by weight in water) slowly. The solution was washed with warm water under centrifugation and then with HCl solution (3 M) to remove the sulphate ions. Finally, the graphite oxide was washed with deionized water under centrifugation until the absence of chloride ions was confirmed ($AgNO_3$ test and neutral pH). Finally, the solid was separated by centrifugation and re-dispersed in water to obtain GrO by freeze-drying. The exfoliation of GrO by ultrasonication led to GO.

2.2.3. Chemical reduction of graphite oxide (GS)

GS was obtained by chemical reduction of the exfoliated graphene oxide sheets. In a typical procedure, GO was dispersed in deionized water at a concentration of 0.1 mg/mL, and the mixture was sonicated with a tip sonicator for 15 min. The dispersion mixture was then placed into an oil bath at 60 °C and different appropriate amounts of the reducing agent (L-AA) were added under magnetic stirring. The mixture was left for 6 h with constant agitation and in the absence of light. After the completion of the reaction time, the reaction medium was cooled to room temperature. Next, 4 mL of H_2O_2 (30% by weight in water) were added to the black suspension and stirred for 30 min at 60 °C in order to oxide the remaining L-ascorbic acid. The product was isolated by filtration, washed with deionized water four times and then vacuum dried overnight at room temperature to yield chemically reduced graphene powders. The reduction reaction was accomplished at different molar concentrations of reducing agent in the dispersions to assess its effect on the reduction level of graphene oxide and to establish the optimal amount of L-AA required.

2.2.4. Graphene oxide – Silver nanoparticles (GO-AgNPs)

GO-AgNP nanohybrids were synthetized *via* the *in situ* method, through the simultaneous reduction of the metal precursor and GO using L-ascorbic acid as green reducing agent (Figure 2.13). Graphite oxide powder was dispersed in deionized water (190 mL) by sonication in a water bath for 1 h achieving a yellow-brown suspension of graphene oxide sheets (0.5 mg/mL). Next, ammonium hydroxide was added until the pH value reach approximately 10. The dispersion became dark-brown and was placed in an oil bath which was heated at 60 °C. The desired amount of aqueous silver nitrate solution was slowly added to the dispersion under vigorous stirring and in the absence of light. Then, aqueous solution of L-AA was added at a concentration that maintained the weight ratio between L-AA and $AgNO_3$ fixed at 2.07. The reaction mixture was held at 60 °C for 1 hour with constant stirring and in the absence of light. During this period of time, small aliquots were extracted and diluted to record UV-Vis spectra. The dark-brown color of the solution immediately turned dark-blue, suggesting that Tollen's reagent formation, $[Ag(NH_3)_2]^+$, had occurred. The mixture of the

aqueous solution of GO and ammonia with the aqueous silver nitrate solution led to metallic silver NPs in the presence of L-AA. Subsequently, the reaction mixture was cooled and dialyzed for one week to remove the residual salts. The suspension was then washed with deionized water and centrifuged at high speed repeatedly. Finally, GO-AgNPs powder was obtained by freezing the solution and lyophilizing.
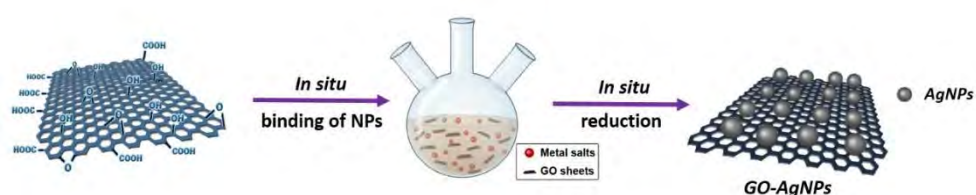

Figure 2.13. Illustration of *in situ* binding mechanism of NPs onto GO sheets.

AgNPs were prepared at two different concentrations of $AgNO_3$, 1.50 and 2.00 mM, while keeping the GO amount and the weight ratios of L-AA constant. The reaction was also carried out at 80 ℃ in order to analyze the effect of temperature on the process. Likewise, one experiment was carried out where no reducing agent was used to confirm that the synthesis does not take place. The nomenclature used to name GO-AgNPs hybrids is shown in Table 2.1 where the reaction temperature and silver nitrate concentration are specified.

Table 2.1. Nomenclature and reaction conditions for GO-AgNPs.

Sample	Temperature (℃)	$AgNO_3$ (mM)
GO-AgNPs-**A**	60	1.50
GO-AgNPs-**B**	60	2.00
GO-AgNPs-**C**	80	1.50
GO-AgNPs-**D**	80	2.00

2.2.5. Characterization

The structural and morphological characterization of graphite, GO, GS and GO-AgNPs hybrids was performed by UV-Vis spectroscopy, Fourier-transform infrared (FTIR) spectroscopy, X-ray photoelectron spectroscopy (XPS), Raman spectroscopy, X-ray diffraction (XRD), atomic force microscopy (AFM), scanning electron microscopy (SEM) and transmission electron microscopy (TEM). In addition, a thermogravimetric analysis (TGA) was carried out to study the stability of the different graphene-based nanocomposites.

A complete description of the different procedures for structural, morphological and thermal characterization is given in Appendix I and the section of each technique or method is detailed in Table 2.2.

Table 2.2. Characterization methods used for the analysis of graphene-based nanocomposites.

Analysis	Technique or Method	Appendix Section
Formation of AgNPs	UV-Vis	I.1.2
Chemical structure	FTIR	I.1.3
Surface Chemistry	XPS	I.1.4
Chemical structure	Raman	I.1.5
Interlayer separation	XRD	I.1.6
Nanostructure and morphology	AFM	I.1.7
	SEM	I.1.8
	TEM	I.1.9
Thermal behavior	TGA	I.2.1

2.2.6. Antimicrobial activity assays

2.2.6.1. Microbial strains and culture

Three well-described bacterial species and one clinically relevant yeast were evaluated: Gram-negative bacteria *E. coli* ATCC 25922 and *P. aeruginosa* ATCC 27853, the Gram-positive bacterium *S. aureus* ATCC 25923, and *C. albicans* SC5314. Briefly, microorganisms were harvested on plate count agar (PCA) for 24 h at 37 °C from frozen stock, and inoculum was prepared from single colonies grown to stationary phase in BHI broth at 37 °C overnight in an orbital incubator under 100 rpm. Cultures were centrifuged (3000 × g, 10 min) and washed twice in PBS. A cell suspension adjusted to a cell density equivalent to 0.5 McFarland (representing approximately $1–5 \times 10^8$ cells/mL) was prepared using sterile saline for bacteria, and *C. albicans* was adjusted at 1×10^6 cells/mL upon counting cells in a hemocytometer. Viable counts were enumerated using PCA after overnight incubation at 37 °C.

2.2.6.2. Determination of the minimum inhibitory concentrations (MICs)

The minimum inhibitory concentration (MIC) is defined as the lowest concentration, recorded in mg/L or μg/mL, of an agent that inhibits the growth of a microorganism. In the present study, the MIC of GO, GS and GO-AgNPs was determined for four different microorganisms: *C. albicans* SC5314, *S. aureus* ATCC 25923, *E. coli* ATCC 25922, and *P. aeruginosa* ATCC 27853. The EUCAST broth microdilution method (EUCAST EDef 7.3.1) was used to stablish these MICs, since it is a reference method for antimicrobial susceptibility testing, and one of its main purposes is to establish the activity of new antimicrobial agents.

Firstly, to maintain the same concentration of culture medium in each well of the 96-well polystyrene microdilution plates, stock solutions of graphene derivatives, 200 times more concentrated than the concentrations to be analyzed, were prepared. Next, these solutions were diluted 100 times (in tubes, dilution vol. 10 mL) in the corresponding culture medium which was previously prepared at double concentration. The culture medium was RPMI with 2% of glucose (RPMI 2% G) and Muller-Hinton broth (recommended by EUCAST) for *Candida* and bacteria, respectively. Subsequently, 100 μL of each dilution was added to

each well of columns 1 to 10 of the plate (Figure 2.14). The final test concentration for each compound ranged from 0.25 µg/mL to 128 µg/mL. The columns 11 and 12, which contained the growth control (GC) and a sterility control (SC), respectively, were filled with 100 µL of the medium. Then, the microbial suspensions were diluted 1:10 for *C. albicans* and 1:100 for bacteria in sterile distilled water, and 100 µL was pipetted into each well (except in column 12 where 100 µL of sterile distilled water where added) obtaining the final inoculum concentration of 5×10^4 CFU/mL and 5×10^5 CFU/mL, respectively. Finally, the microdilution plates were read using a microdilution plate reader (iMark Microplate Reader) at a wavelength of 450 nm at 0 h and 24 h at 37 °C. The MIC corresponds to the concentration of the compound that resulted in an absorbance reduction of 50% or greater with respect to the absorbance found in the wells of the growth control. This test was conducted in triplicate.
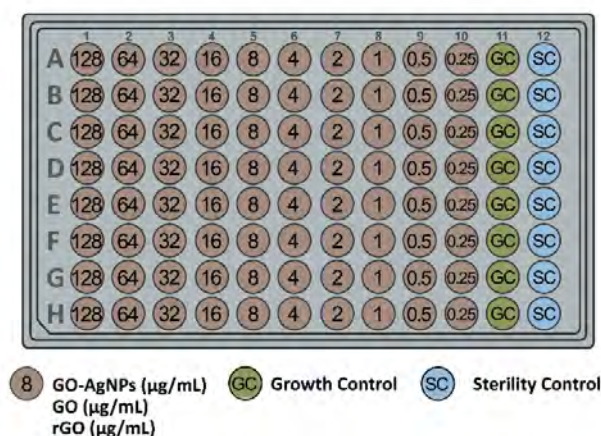
Figure 2.14. Diagram of the microdilution plate for each microorganism.

2.2.6.3. Microbial growth kinetics in the presence of GO-AgNPs.

This assay was focused on the assessment of the microbial growth in the presence of GO-AgNPs and GO. Since GS had the same behavior as GO in the determination of MIC, it was not considered in this test.

The four previously mentioned microorganisms were analyzed at a final inoculum density of 5×10^4 CFU/mL and 5×10^5 CFU/mL for yeast and bacteria, respectively. The highest GO concentration in the MIC determination assay (128

µg/mL) was tested along with three concentrations of GO–AgNPs, selected on the basis of its MIC value for each microorganism: 64 µg/mL, 32 µg/mL, and 16 µg/mL for *C. albicans* and *S. aureus*, and 128 µg/mL, 64 µg/mL, and 32 µg/mL for *E. coli,* and *P. aeruginosa*. Briefly, a microplate was loaded with culture medium, the GO–AgNP hybrid, and the microorganism as mentioned above. The microorganism in the culture medium was considered the growth control (GC), and the different concentrations of the compounds without microorganisms but with the culture medium, the blank. The microplates (100-well honeycomb polystyrene plates, Labsystems) were placed in a microplate reader (BioScreen C) configured to read the absorbance at 430–580 nm every hour for 72 hours at 37 °C. Five wells for each compound concentration were used, and the assay was performed in duplicate (Figure 2.15).
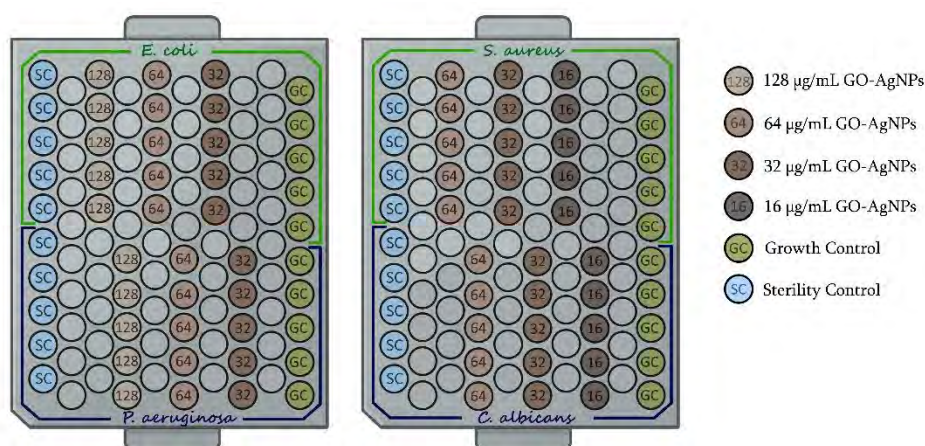
Figure 2.15. Diagram of the 100-well microplates for BioScreen C.

2.3. Results and discussion

In this thesis, GO production was performed three times. In this section the characterization results for one of the three GO samples are shown, since all exhibited similar results.

2.3.1. Structural and morphological characterization

UV–vis spectroscopy

The UV–vis spectroscopy was used to confirm the formation of GS and GO-AgNPs from GO. The UV–vis spectra of GO and the reduced GO by 2.00 mM L-AA are shown in Figure 2.16A. The spectrum obtained for the GO sheets dispersion exhibits a maximum at 233 nm attributed to the $\pi \rightarrow \pi^*$ transitions of the aromatic C=C bonds and a shoulder at ≈300 nm, ascribed to n $\rightarrow \pi^*$ transitions of C=O bonds. The maximum absorption peak of GS is located at 270 nm, and the absorption in the whole spectral region increases, indicating that the electronic conjugation inside the reduced graphene sheets has been restored. The absorption spectrum of GO-AgNPs-A (60 °C, 1.50 mM L-AA) hybrid exhibits the red shift of the maximum peak of GO, from 230 to 265 nm, suggesting the simultaneous partial reduction of GO during the preparation of the GO-AgNPs nanohybrids, and therefore the recovery of the electronic conjugation of the graphene sheets.
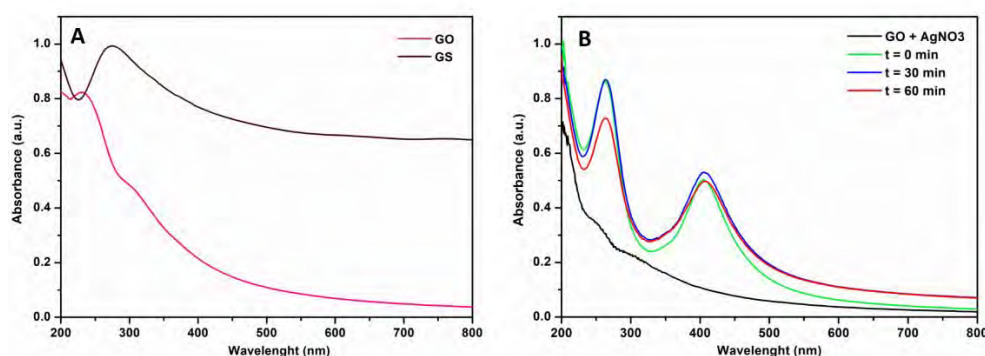
Figure 2.16. UV-Vis absorption spectra. (A) GO and GS aqueous suspensions. (B) GO-AgNPs-A aqueous suspension at different time intervals.

In addition, the presence of the characteristic Surface Plasmon Resonance (SPR) band at 404 nm indicates the reduction of silver nitrate to AgNPs [193]. As

it can be seen in Figure 2.16B, the Plasmon resonance did not change during the reaction time. The intensity, wavelength and shape of the SPR absorption band depend on particle size, shape, aggregation state and the dielectric constant of the surrounding medium [194]. The peak position found for the different prepared GO-AgNPs is characteristic of small roughly spherical AgNPs. The intense SPR band is responsible for bluish color of the $[Ag(NH_3)_2]^+$ and GO solution after adding L-AA.

UV-Vis spectroscopy was also employed to analyze the effect of reaction temperature and the AgNPs precursor concentration on the synthesis of AgNPs hybrids. As can be seen from Figure 2.17, the intensity, wavelength and shape of the SPR absorption band remain similar at both temperatures when 1.50 mM $AgNO_3$ was used. However, the absorbance peak becomes more intense as temperature increases in the case of 2.00 mM $AgNO_3$. The increase in intensity can be due to an increase of the number of the nanoparticles formed. The position of the SPR band remains practically unchanged as the temperature and silver precursor concentration increase.
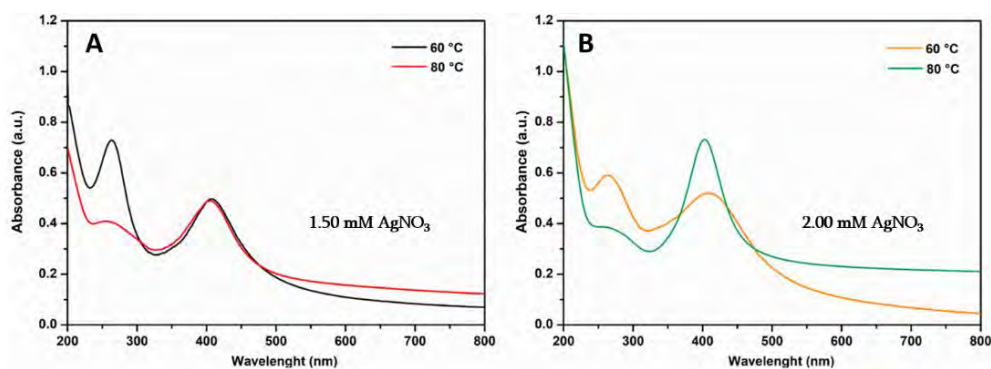
Figure 2.17. UV–vis spectra of GO-AgNPs suspensions synthetized with different $AgNO_3$ concentrations at 60 °C and 80 °C.

Aliquots were extracted during the reaction and diluted in order to record the UV-spectrum as shown in Figure 2.18A. Considering the stability of the dispersions, agglomeration and precipitation are visible for the suspension of GO-AgNPs-D, while for GO-AgNPs-A this phenomenon has not occurred (Figure 2.18B).
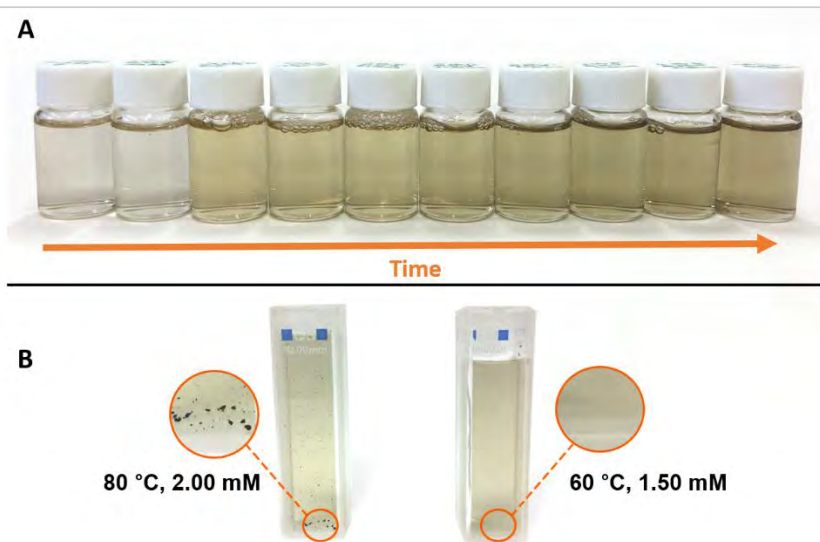
Figure 2.18. (A) Photographs of the dilutions of the aliquots extracted of GO-AgNPs-A at different times during synthesis. (B) Dilutions of the GO-AgNPs-D and GO-AgNPs-A.

Fourier-transform infrared (FTIR) spectroscopy

The Fourier transform infrared (FTIR) spectroscopy has been used to identify the oxygenated functional groups attached to the basal plane of graphene derivatives. Figure 2.19A shows the FTIR spectra of graphite, GO, different GS and GO-AgNPs samples.

Natural graphite shows two peaks at 3433 cm^{-1} for O–H stretching and at 1630 cm^{-1} assigned to the vibrations of the adsorbed water molecules, and a shoulder at 1577 cm^{-1} due to the C=C bond stretching vibration. In the case of GO, the overlapping bands in the 3800–3000 cm^{-1} range correspond to the stretching vibrations of structural OH groups and physisorbed water molecules. The strong band at 1734 cm^{-1} is related to the C=O carbonyl stretching of COOH groups situated at the edges of the oxidized graphenes, and the peak located at 1621 cm^{-1} is attributed to the deformation vibration of water molecules. The absence of the peak at 1577 cm^{-1} reflects the absence of unoxidized aromatic regions in GO. The absorption peak at 1362 cm^{-1} is assigned to the bending of tertiary C-OH groups, while the peak at 1052 cm^{-1} arises from the vibration of C–O of epoxide groups (C–O–C). Finally, the peak at 980 cm^{-1} is attributed to epoxide

or peroxide group. Thus, the FTIR data verify the existence of epoxy groups in GO and demonstrate that –C=O and –OH groups are present.
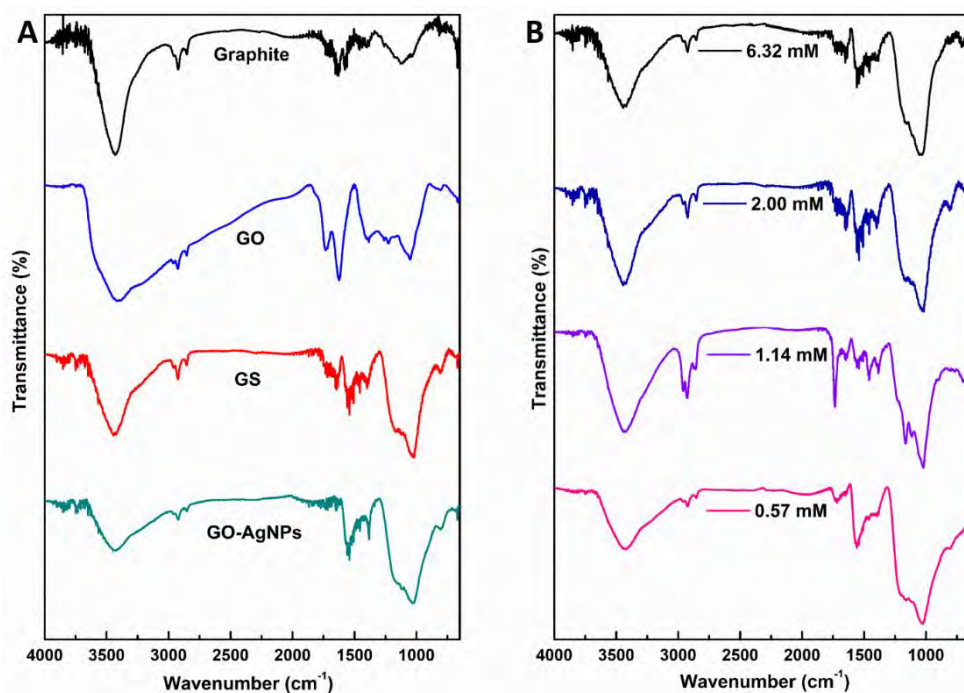
Figure 2.19. Infrared spectra of (A) graphite, GO, GS (2.00 mM) and GO-AgNPs-A. (B) GS obtained at different concentrations of L-AA: 0.57 mM, 1.14 mM, 2.00 mM and 6.32 mM.

In the spectrum for GS samples (Figure 2.19B) there is a signal at 3417 cm^{-1} due to the intercalated water. In the case of GO this signal is wider due to the contribution of two peaks at about 3584 cm^{-1} and 3194 cm^{-1} associated to hydroxyl and –COOH groups. The intensities of the bands assigned to carbonyl stretching, epoxides and hydroxyls weakened substantially, and the band at 1621 cm^{-1} disappears upon reduction. Two new bands appear in the GS samples, one at 1558 cm^{-1} and another one at 1117 cm^{-1} associated to the aromatic C=C stretching and the in plane bending vibrations, respectively, evidencing the restoration of the sp^2 structure. The spectra of GS samples when reduction was carried out with 2.00 mM and 6.32 mM L-AA are similar, and show a higher decrease in the intensities of the bands associated to oxygen functional groups compared to the other reduced materials.

For GO-AgNPs nanohybrids, the signals obtained are very closed to those of the GS. Specifically, as in the case of the chemical reduction of GO, the intensities of the bands assigned to carbonyl, epoxides and hydroxyl are considerably weakened, and the band at 1621 cm^{-1} disappears. These results indicate the simultaneous partial reduction of GO. The interaction of AgNPs with graphene cannot be clearly distinguished with this technique.

X-ray photoelectron spectroscopy (XPS)

The chemical change of natural graphite during the reactions was followed by the analysis of X-ray photoelectron spectroscopy (XPS), a technique that allows the determination of the relative amount of carbon, oxygen and other functional groups present in graphene-based materials [195]. Figure 2.20A shows the XPS survey spectra of graphite, GO, GS and GO-AgNPs, and Figures 2.20B-E present high resolution C1s XPS spectra for GO, GS and GO-AgNPs, and Ag3d for GO-AgNPs. In the XPS spectrum of graphite, it can be seen an intense peak corresponding to C–C stretching (284.6 eV), and the peak corresponding to O1s (532.3 eV) which intensity is very small, associated with atmospheric oxidation. Both O1s and C1s signals are used to calculate the peak intensity ratio, e.i. the atomic C/O ratio. Thus, the intensity of the peaks (O1s/C1s) of GS decreases significantly in comparison with that of GO. The presence of silver nanoparticles in GO-AgNPs is observed in the doublet associated with Ag3d (368.4 - 374.4 eV).

In order to carry out the quantitative analysis, C1s and O1s peaks are separated into their individual components. This is performed by fitting the total spectrum into a linear superposition for all elements. Gaussian–Lorentzian peak method is used to fit the C1s and O1s curves after performing the Shirley background correction [196]. This separation helps to calculate the fractions of every single element present in the sheet. The C1s XPS spectrum of GO clearly indicates a considerable degree of oxidation (Figure 2.20B). The binding energy of 284.6 eV is attributed to the C-C/C-H bonds, and the ones of 286.6 and 288.9 eV are typically assigned to the C–O (including epoxy and hydroxyl groups) and –O–C=O functional groups, respectively. This result suggests that GO is heavily oxidized, which is in good agreement with previous reports [197].
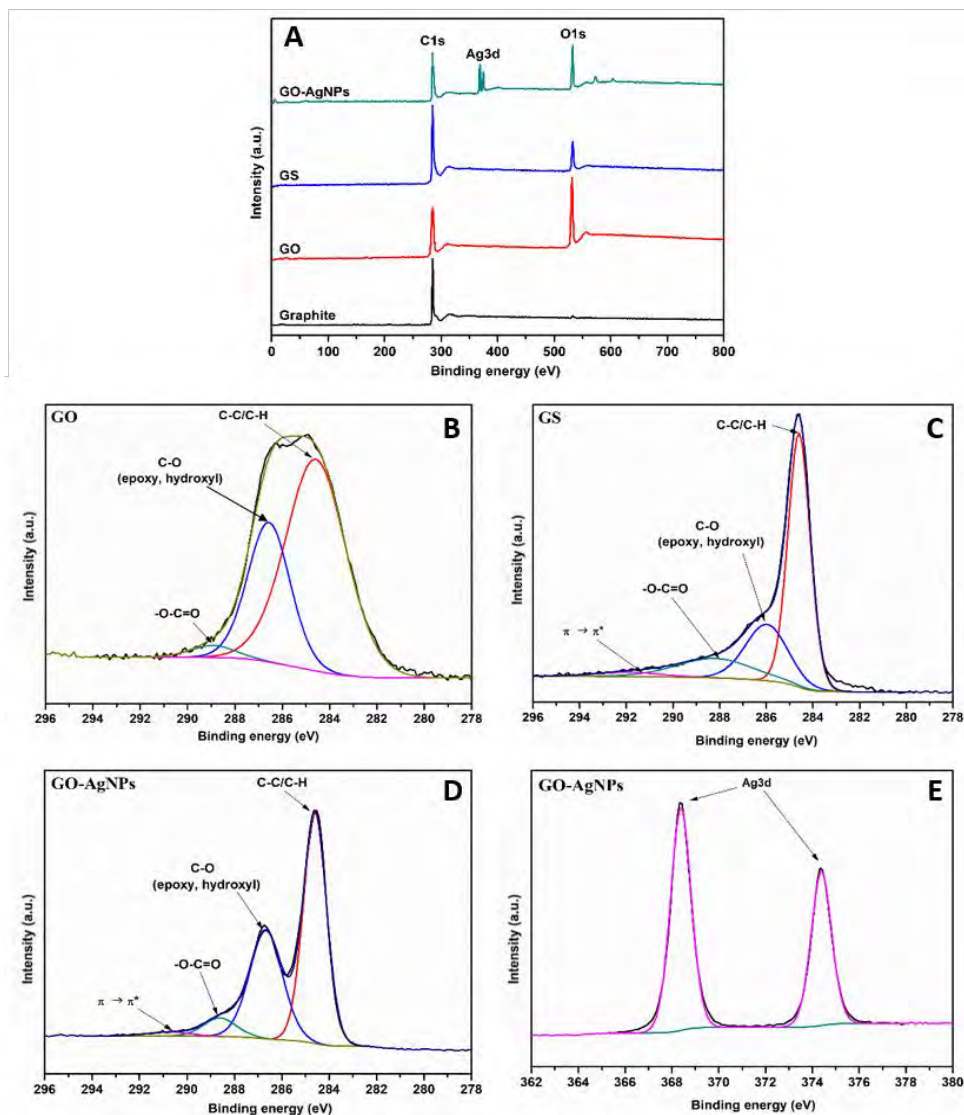
Figure 2.20. (A) XPS survey spectra of natural graphite, GO, GS and GO-AgNPs. High-resolution C1s XPS for (B) GO, (C) GS and (D) GO-AgNPs. High-resolution Ag3d XPS of (E) GO-AgNPs.

After the reduction of GO with L-AA (2.00 mM) for 6 h, the C1s spectrum of GS (Figure 2.20C) reveals that the graphitic C–C signal (284.6 eV) is narrower than in GO, FWHM (full width at half maximum) value of 1.117 eV compared to 2.976 eV, which indicates the development of a more homogeneous chemical environment and/or ordered graphitic structure. Moreover, XPS spectrum of GS

exhibits the same oxygen functionalities that have been assigned for GO, while the intensities of all C1s peaks of the carbons binding to oxygen, especially the peak of C–O (epoxy and alkoxy), decrease dramatically, revealing that most oxygen-containing functional groups were removed after the reduction. In addition, the peak at the binding energy 291.1 eV, assigned to the $\pi \to \pi^*$ transition of the aromatic C–C bonds, appears after the chemical reduction. The relative C/O atomic ratio increases from 2.05 for GO to 5.61 for GS. XPS results suggest significant removal of oxygen functional groups in the chemical reduction.

The C1s XPS spectrum of the GO-AgNPs-A (60 °C, 1.50 mM L-AA) shows signals very similar to those of GS (Figure 2.20D) revealing that functional groups containing oxygen were removed during the reaction, although to a lesser extent than in the case of GS. The relative C/O atomic ratio for GO-AgNPs-A is 3.09. High-resolution Ag3d spectra shows two separate peaks at 368.4 and 374.4 eV that are correlated to Ag3d$_{5/2}$ and Ag3d$_{3/2}$ (Figure 2.20E). These peak positions are typical of Ag^0, confirming the formation of silver nanoparticles on the graphene surface. XPS analysis have demonstrated the presence of silver for all the different GO-AgNPs hybrids prepared in this work.

Raman spectroscopy

The structural changes underwent by graphene sheets during the different reactions was also monitored through Raman spectroscopy. This is a non-destructive technique based on the inelastic scattering of monochromatic light. There are two kinds of inelastic scattering: stokes (output energy is smaller than input energy) and anti-stokes scattering (output energy larger than input energy). The difference between the output and input light provides the data of vibrational modes, which are materials fingerprints.

In order to investigate the spectral reproducibility, spectra were collected from different positions on each sample. Raman spectra of graphite, GO, GS (2.00 mM L-AA) and GO-AgNPs-A (60 °C, 1.50 mM L-AA) are shown in Figure 2.21. From this figure, two characteristic bands can be seen in the first-order region, the D band at around 1353 cm^{-1}, and the G band at around 1598 cm^{-1}. The D band,

typical for sp^3-hybridized carbon atoms (graphitic domains), is associated with the presence of defects in the graphite material derived from vacancies, bond-angle disorder, bond-length disorder, edge defects, etc., [198] and the G band is due to the first order scattering of the E_{2g} phonon of sp^2 carbon atoms [199,200].
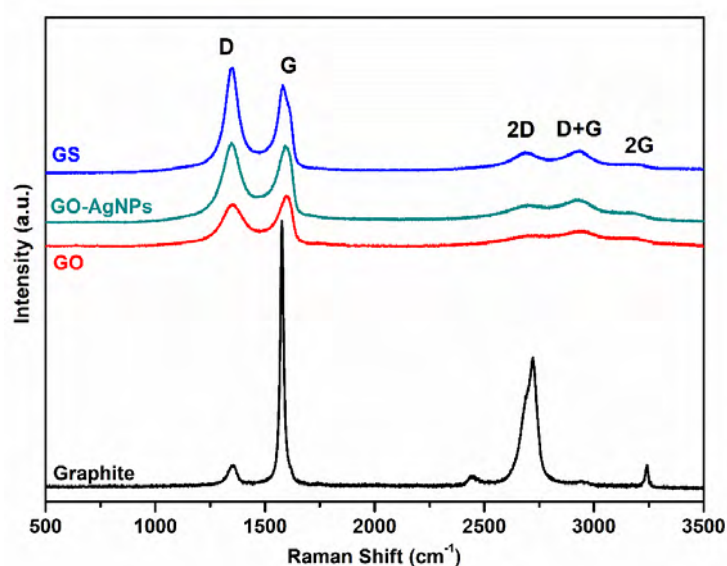

Figure 2.21. Raman spectra of graphite, GO, GS and GO-AgNPs.

Table 2.3 lists the Raman data for the mentioned samples. The D band for GO becomes broader and more prominent and shifts to lower wavenumber compared to that of graphite. This can be attributed to the introduction of oxygen groups and other structural defects in the graphitic structure. The intensity of the D band is related to the size of the in-plane sp^2 domains. The increase in the D peak intensity indicates the reduction in size of sp^2 domains, or what is the same, the formation of more sp^2 domains. On the other hand, the G band for GO is broadened and shifted towards a higher wavenumber compared to that of graphite, due to the high oxidation level of graphite. This shift in G band is associated with the presence of isolated double bonds, which shows higher resonance frequencies than that of G band in graphite [199,200].

Comparison of Raman spectra of GS and GO shows significant changes. The G band of GS shifts to lower wavenumber due to the recovery of the hexagonal network of carbon atoms with defects [29,31,201], and the D band becomes

narrow and the intensity is significantly increased, indicating the presence of lattice distortions of graphene basal planes [202], structural defects are introduced. The intensity ratio of D and G peaks (I_D/I_G) is a measure of disorder degree and is inversely proportional to the average size of the sp^2 clusters [29,203]. The I_D/I_G ratio for GS (1.23 ± 0.03) is larger than that for GO (0.83 ± 0.02). This suggests that the areas formed by sp^2 hybridized carbon atoms are smaller in size, but higher in quantity than what is shown in GO before reduction. The conjugated graphene network (sp^2 carbon) is re-established, but the size of the restored network is smaller than the original one.

Table 2.3. Raman peak positions and intensity of I_D/I_G.

Material	D (cm⁻¹)	G (cm⁻¹)	2D (cm⁻¹)	D+G (cm⁻¹)	2G (cm⁻¹)	I_D/I_G	I_{2D}/I_{D+G}
Graphite	1355	1579	2723	-	3244	0.03±0.02	-
GO	1353	1598	2741	2944	3181	0.83±0.02	0.74±0.03
GS	1350	1585	2691	2939	3187	1.23±0.03	0.90±0.07
GO-AgNPs-A	1345	1594	2712	2934	3176	1.03±0.01	0.70±0.03

The D and G bands of GO-AgNPs shift to lower wavenumbers, 1345 and 1594 cm⁻¹, respectively, when compared to GO. This is due to the partial reduction of GO during the AgNPs binding process, in which structural defects are added in addition to NPs. However, the position of G band is not as low as that of GS, since the reduction is not complete and some oxygenated groups of the initial GO remain. In addition, the I_D/I_G ratio for GO-AgNPs is higher (1.03 ± 0.01) than that for GO. The insertion of AgNPs on graphene sheets contributes to an increase in the degree of disorder of the GO matrix, in part due to the interactions between the carbon matrix and the NPs, which causes a decrease in the average size of the sp^2 domains in the plane [97]. Additionally, it should be highlighted that D and G peak intensities of GO-AgNPs increased considerably due to the surface-enhanced Raman scattering effect of AgNPs [204,205].

The second-order region of the Raman spectra includes several bands at ≈2400 cm⁻¹, at ≈2700 cm⁻¹ (2D band, typical for sp^2-hybridized carbon atoms, overtone of the D band), at ≈2900 cm⁻¹ (D + G band) and at ≈3200 cm⁻¹ (2G band),

depending on the graphenic material. In a defect-free graphitic structure, D band is not present, while a large 2D band is seen. This band is highly sensitive to the number of graphene layers [9,206]. The 2D band (2723 cm^{-1}) broadens and reduces its intensity after oxidation, and suggests a significant reduction of sp^2 domains, while after the reduction process the band is more intense and defined. It has been reported in the literature [207] that the I_{2D}/I_{D+G} ratio is another indicator for the aromatic C-structural order of the graphitic materials, since the 2D mode is sensitive to the electronic structure in the graphene, whereas the D+G combination mode is induced by disorder. The data displayed in Table 2.3 show an increase in the I_{2D}/I_{D+G} ratio from GO to GS (about 1.2 times), indicating the restoration of graphitic electronic conjugation upon reduction of GO by L-AA [200,208,209]. The I_{2D}/I_{D+G} ratio for GO and GO-AgNPs is practically similar confirming the low reduction of GO during the reaction to obtain graphene-silver hybrids.

X-ray diffraction (XRD)

This is a non-destructive method of characterization that deals with the space between the layers and the crystalline structure of graphene. Bragg's law described in Appendix I (Eqn. I.1.6) was used to calculate the distance between the sheets. Figure 2.22 shows the obtained X-ray diffraction patterns. For natural graphite, the sharp strong peak at 26.7° of 2θ corresponds to the (002) diffraction line with the interlayer spacing along the c-axis of 0.33 nm [38,210]. In contrast to the XRD spectrum of graphite, GO displays a broad peak at 2θ = 11.1°, and lower in intensity which clearly indicates the damage of the regular crystalline of natural graphite during the oxidation. The exact position of this peak (between 9- 11°) depends on the oxidation method used, as it increases directly with the increase in the degree of oxidation. From this result, it can be said that the inter layer spacing of graphene material is proportional to the degree of oxidation.

According to Bragg diffraction formula, the *d* spacing of GO was 0.79 nm. The intercalation of epoxide and hydroxyl groups between the GO layers during oxidation process and a conversion of hybridization of the oxidized carbon atoms from sp^2 to sp^3 leads to the increase of the *d* spacing [26]. Compared with natural graphite and the parent GO, the XRD pattern of GS shows a broad peak (2θ =

24.3°; d spacing ≈0.37 nm) with the disappearance of the characteristic peaks. This indicates that chemically reduced graphene has been exfoliated into a few layers.
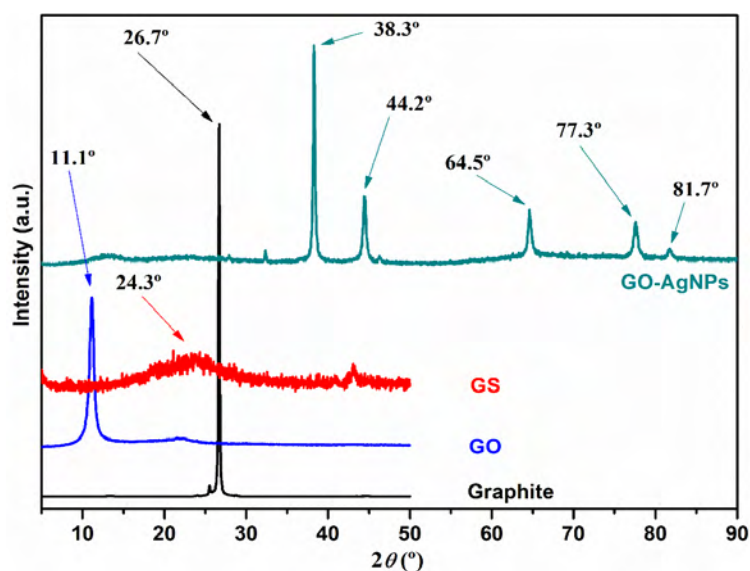

Figure 2.22. XRD of graphite, GO, GS and GO-AgNPs.

Regarding GO-AgNPs, the XRD pattern shows strong Bragg reflections at 38.3°, 44.2°, 64.5°, 77.3° and 81.7° of 2θ, which correspond to the (111), (200), (220), (311) and (222) crystal planes of face centred cubic crystal structure of AgNPs. These results corroborate the formation of AgNPs on GO surface. In addition, the non-appearance of the GO diffraction peak after the attachment of AgNPs onto its surface, suggest the exfoliation of GO-AgNPs sheets [211].

Nanostructure and Morphology

In order to investigate the morphology of synthesized graphene-based fillers Atomic Force Microscopy (AFM), Transmission Electros Microscopy (TEM) and Scanning Electron Microscopy (SEM) measurements were performed.

AFM allows to analyze morphology and texture of the graphene materials at a nanometric scale. It also helps to measure the height, lateral size and number of layers in the specimen. The AFM image provides topographic contrast, making it difficult to distinguish between graphene oxide and graphite layers in normal operation mode. Phase imaging is one of the attractive features of tapping-mode AFM. This facilitates to distinguish between a defect free pristine graphene and its functionalized version due to the difference in the interaction forces between the AFM tip and the attached functional group [212]. The different AFM modes allow the study of mechanical, frictional, electrical, magnetic and even elastic properties of graphene sheets. However, in our case the AFM was used to measure the size of GO sheets (Figure 2.23A). For this purpose, the lyophilized graphene oxide was exfoliated in aqueous medium *via* bath-sonication. The analysis of the AFM images revealed GO sheets with lateral dimensions of 0.2 to 1.4 μm, and thickness in the range from 0.8 to 1.4 nm. Considering the size distribution, Figure 2.23B, more than 65% of the GO sheets have a lateral dimension of <0.5 μm, and a mean lateral dimension of ≈0.48 μm is observed. A mean thickness of 1.11 nm is measured for the obtained graphene oxide sheets (Figure 2.23C), which is typical for a one-atom-thick GO nanolayer [29,213-215]. It can be seen that about 83% of GO sheets have thickness lesser than 1.2 nm.
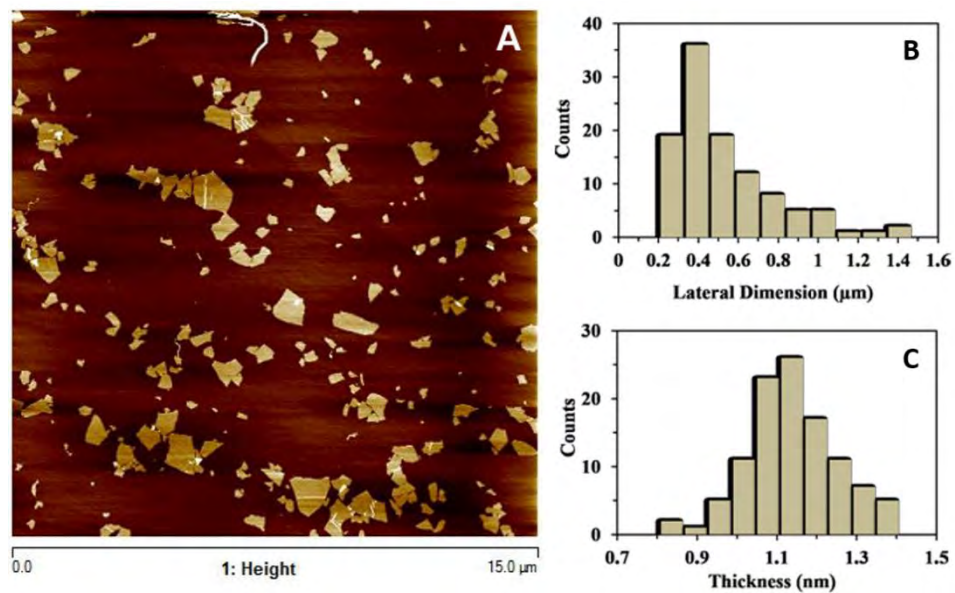
Figure 2.23. (A) AFM image of GO sheets. (B) Histogram distribution of sheet lateral sizes. (C) Histogram distribution of sheet thickness.
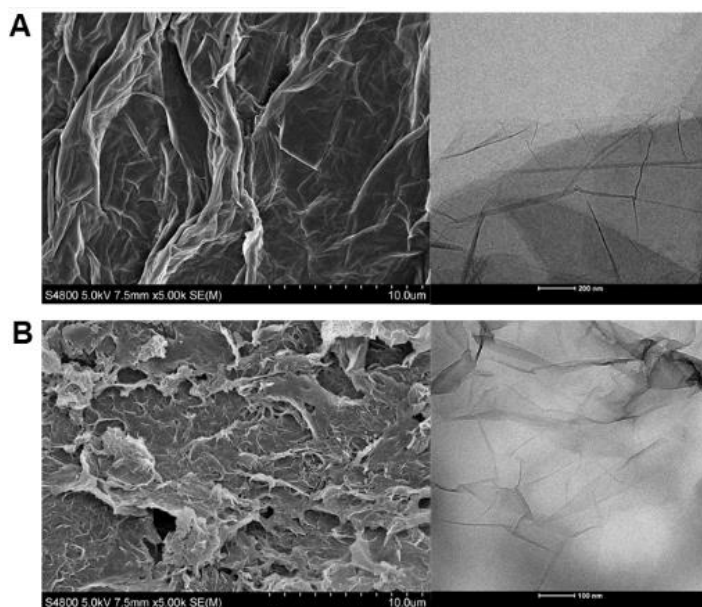
Figure 2.24. Microscopy images of GO and GS. (A) SEM (left) and TEM (right) images of GO. (B) SEM (left) and TEM (right) images of GS.

TEM is often used to image nano-sized materials at atomic scale resolution. This technique is based on the diffraction patterns emitted by the samples after a high-energy electron beam is transmitted through the sheets. The scattered electrons are captured and processed by an electromagnetic lens to display an image. The low magnification TEM image is pretty useful in sheet visualization, but they are unable to provide complete information about the internal atomic structure of the sheets. Particularly, high resolution transmission electron microscopy (HR-TEM) is able to exhibition the number of layers. Likewise, SEM microscopy is also frequently used to study the surface morphology of graphene, GO and graphite. Figure 2.24 shows SEM and TEM images of exfoliated GO and GS aqueous suspension prepared by ultrasonic bath sonication. GO sheets appeared as thin flexible sheets randomly aggregated, with wrinkled surfaces, and folding. In the case of GS, SEM image reveals that sheets are crumpled, aggregated, entangled with each other and forming a solid with big pores. TEM image shows a general view of GS nanosheets, clearly illustrating a large wrinkled and folded sheet of graphene.

Regarding the GO-AgNPs nanohybrids, the morphology of the synthesized nanostructures was investigated by TEM. Figure 2.25 shows TEM images, selected area electron diffraction (SAED) patterns of GO-AgNPs nanohybrids and particle size distributions of AgNPs on GO sheets. The micrographs confirm the decoration of GO with AgNPs. For all samples, spherical AgNPs well dispersed throughout the GO surface are observed. For each sample 1200 nanoparticles in several GO-AgNPs micrographs were analyzed to determine the AgNPs sizes. Table 2.4 summarizes the characterization of AgNPs by TEM analysis and the position of SRP absorption band obtained by UV-Vis. The results indicate that the size of the AgNPs is dependent on the $AgNO_3$ concentration and temperature. The smallest AgNPs are formed at the lowest silver precursor concentration and temperature. Under these conditions (1.50 mM $AgNO_3$ and 60 °C), the reaction leads to silver nanoparticles whose size ranges from 0.9 nm to 5.8 nm, with an average size of 3.1 ± 0.8 nm (Figure 2.25A, Table 2.4), where about 90% of the AgNPs counted are under 4 nm in diameter. An increase in the silver precursor concentration results in an increase of the particle size and a broader size distribution when the reaction temperature is 60 °C (Figure 2.25B). Thus, for GO-AgNPs-B nanohybrid the particle size ranges from 0.7 nm to 10.8 nm, with an

average size of 4.1 ± 1.5 nm, where only 51% of nanoparticles exhibit diameters lesser than 4 nm. These findings are in accordance with previous studies reported by other authors [146,158,216-218]. On the other hand, in Figures 2.25C,D it can be seen that both the size and size distribution are unaffected by the $AgNO_3$ concentration when the reaction temperature is maintained at 80 °C. Consequently, the effect of $AgNO_3$ concentration on AgNPs size and size distribution is significant when the synthesis is performed at lower temperature.

The effect of temperature on silver nanoparticles size can be seen comparing particle size distribution shown in Figure 2.25. It may be noted that as the temperature increases to 80 °C, the nanoparticles size increases and the size distribution becomes broader. For the samples GO-AgNPs-C and GO-AgNPs-D, $\approx$89% of nanoparticles have diameters lesser than 9 nm. Similar effect have been reported in the literature [219,220]. The nucleation of AgNPs on graphene oxide surface has been explained through the interaction of silver cations with the oxygen functional groups. The negatively charged GO sheets allow the attachment of positively charged metal ions via electrostatic interactions. The addition of L-AA reduces both the Ag^+ species to AgNPs and GO to rGO. At higher temperature, the reduction rate of silver precursor increases, and the nanoparticle growth reaction rate is faster. From the above results, it can be inferred that both silver precursor concentration and temperature are the key parameters for controlling the size of AgNPs. The sizes of the nanoparticles synthesized in this work are smaller than those reported in the literature using the solution phase chemical reduction method, either with or without the stabilizing agent. In the present part of the thesis, only the silver precursor and the reducing agent have been used to prepare the nanohybrids, whereas in most of the reported studies a stabilizing agent, ultrasonication or a dispersing agent have also been employed.

The insets in the TEM images of Figure 2.25 present the SAED patterns of the AgNPs synthesized in the GO sheets. They show diffraction rings and bright spots attributed to the cubic metallic silver centered on the face (fcc). The rings correspond to the crystallographic planes (111), (200), (220) and (311) of the AgNPs. These results are consistent with those of XRD and indicate the polycrystalline nature of silver.
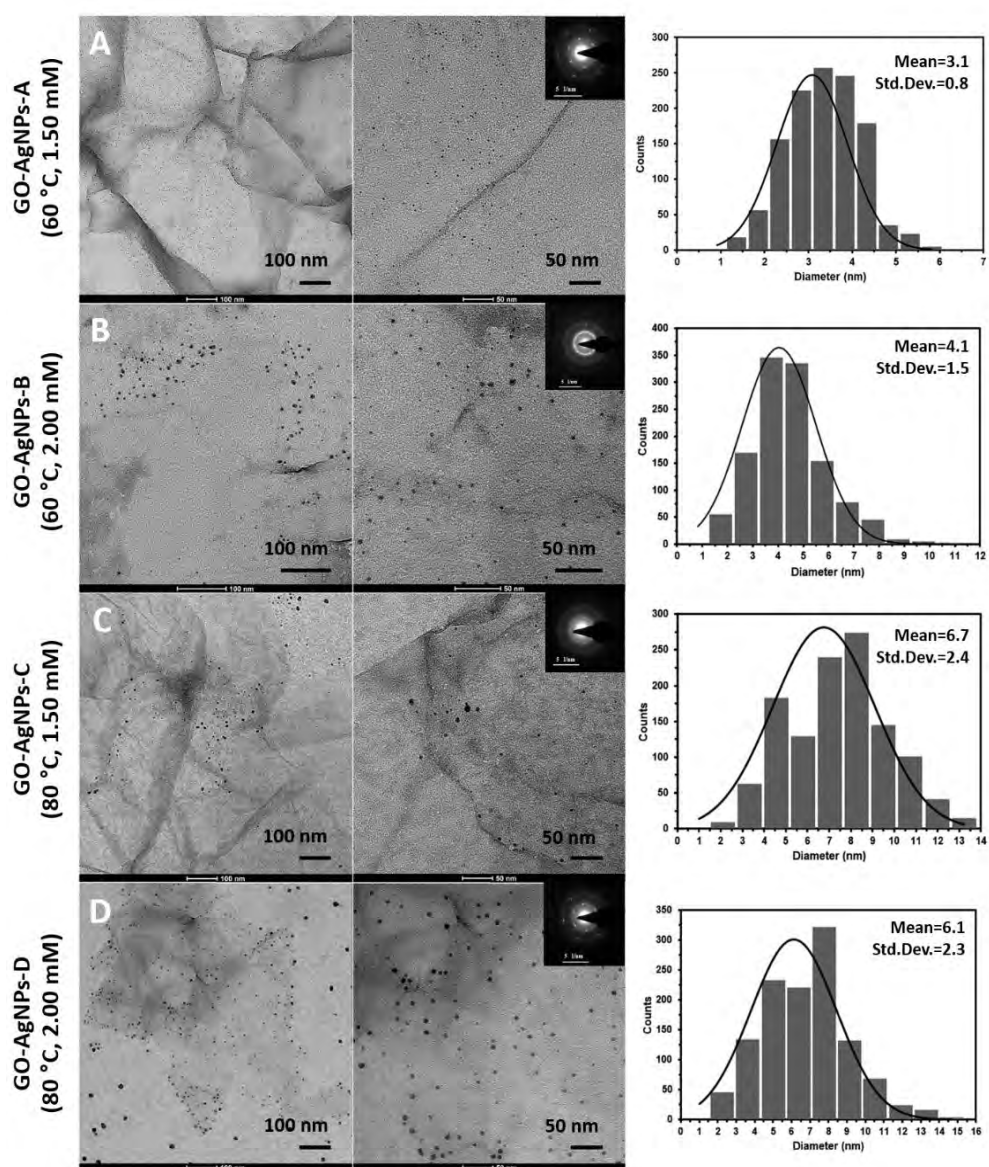
Figure 2.25. TEM images of the GO-AgNPs nanohybrids, where the insets present the SAED of the nanoparticles (rings and spots). (A) GO-AgNPs-A; (B) GO-AgNPs-B; (C) GO-AgNPs-C; (D) GO-AgNPs-D; and particle size distributions of nanoparticles.

Table 2.4. Characterization of AgNPs using TEM analysis.

Sample	UV-Vis Absorption	Particle size (µm)	
	λ_{max}	Mean ± SD	Size Range
GO-AgNPs-**A**	407	3.1 ± 0.8	0.9 to 5.8
GO-AgNPs-**B**	405	4.1 ± 1.5	0.7 to 10.8
GO-AgNPs-**C**	408	6.7 ± 2.4	0.9 to 13.2
GO-AgNPs-**D**	403	6.1 ± 2.3	0.9 to 14.7

Several research has reported the synthesis of AgNPs supported on graphene oxide by using the solution phase chemical reduction method. Shen *et al.* synthesized Ag-chemically converted graphene (CCG) by an *in situ* solution based chemical approach with mixed reducing agents at 110 °C [150]. The AgNPs on CCG sheets had a size in the range of 5-10 nm. Pasricha *et al.* reported the synthesis of Ag-GO nanocomposites by chemical reduction of silver sulfate precursor by GO in the presence of aqueous KOH at boiling temperature [151]. The results revealed the formation of silver nanoparticles with sizes in the range of 3-12 nm. Das *et al.* reported the preparation of AgNPs using $AgNO_3$ with sodium borohydride in the presence of GO [158]. The size of the AgNPs obtained by this method was in the range of 5-25 nm. Later, Das *et al.* informed about the synthesis of AgNPs on GO sheets by chemical reduction of silver metal ions by sodium borohydride in the presence of trisodium citrate as stabilizing agent, which showed the formation of silver nanoparticles with particle size of 2-25 [159]. Tang *et al.* prepared GO-Ag nanocomposites with different Ag/GO ratios by chemical reduction of $AgNO_3$ precursor with sodium citrate, at boiling temperature [161]. The AgNPs attached onto the GO sheet surface were found to have an average diameter of about 46 nm and 68 nm depending on the Ag/GO ratio. The results reported by Fonseca de Faria *et al.* showed GO sheets decorated with 7.5 nm sized Ag nanoparticles [162]. In their study the GO-Ag nanocomposite was prepared in the presence of silver nitrate and sodium citrate at 130 °C. Hui *et al.* reported the formation of AgNPs with an average size ranging from 15 to 55 nm, depending on the ultrasonication time of the mixture of $AgNO_3$, GO and vitamin C [146].

2.3.2. Thermal characterization of GO, GS and GO-AgNPs

Thermogravimetric analysis (TGA)

TGA measurement was performed under nitrogen atmosphere to study the thermal stability of natural graphite, GO, GS and GO-AgNPs (Figure 2.26). This characterization provided information about the ability of the reducing agent to restore the structure of graphene, as well as the accuracy of the C/O ratio of GO and GS obtained by XPS spectroscopy.

Graphite is highly stable up to 600 °C and exhibits a very small weight loss step, it is almost flat. The GO decomposes in two steps, the first weight loss at 50–120 °C is associated with the elimination of loosely bound or adsorbed water and gas molecules. The major mass loss for GO (32%) takes place between 125 °C and 300 °C due to the decomposition of the most labile oxygen functionalities present in the material, which is very close to the value obtained by XPS (32.6% of O). Besides, a steady mass loss is observed in the whole temperature range above 300 °C, which can be ascribed to the removal of more stable oxygen functionalities and the decomposition of the carbon structure [221,222]. The GS samples show similar thermograms but with lower amount of weight loss, compared to that of GO (Figure 2.26A). This could be explained by a smaller amount of oxygen functional groups in the structure as a result of the removal of those groups from the surface of GO sheets during the reduction process. The mass loss for GS, from 125 °C to 300 °C, attributed to unreduced GO functional groups is between 19% and 7% depending on the amount of reducing agent used in the reduction process. GS samples obtained after reduction with 2.00 mM and 6.32 mM L-AA exhibit similar mass loss. The thermograms of chemically reduced graphenes obtained with high levels of L-AA, show a continuous weight loss with a relatively constant rate, revealing a higher stability compared to those obtained with the low levels of L-AA (0.57 mM and 1.14 mM). At 700 °C, the chemically reduced graphenes obtained with the highest levels of L-AA exhibit a much smaller weight loss ($\approx$18%) than GO ($\approx$50%) but still higher than graphite ($\approx$3%). These results suggest that a certain fraction of oxygen functionalities remain even after reduction of GO with the highest levels of L-AA. These findings are in accordance with results in the literature [35].
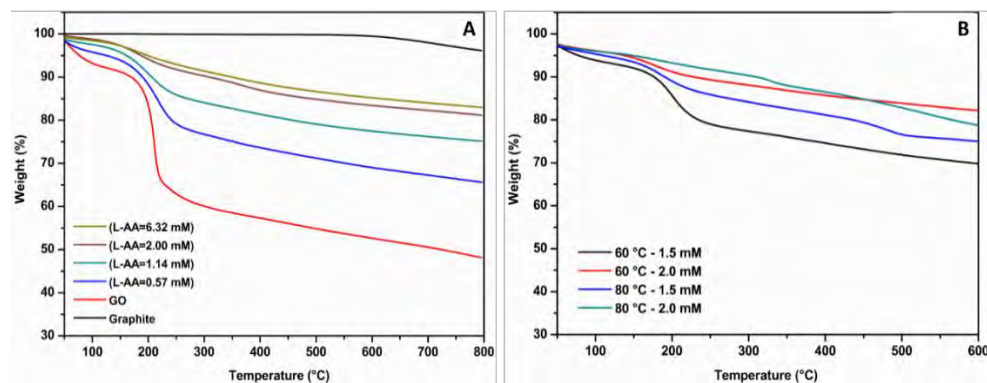
Figure 2.26. TG curves: (A) Graphite, GO, and chemically reduced graphenes by 0.57 mM, 1.14 mM, 2.00 mM and 6.32 mM L-AA, and (B) different GO-AgNPs.

The decomposition pattern of all synthesized GO-AgNPs nanohybrids is shown in Figure 2.26B. The first mass loss, attributed to the elimination of interlaminar water, is found at 50-120 °C, and the second, where the decomposition of the oxygen groups occurs, at 140-300 °C. The mass loss for GO-AgNPs-A and GO-AgNPs-B is 16.1% and 7.7% respectively, which decreases with the increase in the amount of silver nitrate used, and consequently, also with a higher amount of reducing agent (the weight ratio between L-AA and AgNO₃ is always 2.07). Regarding GO-AgNPs-C and GO-AgNPs-D, the weight loss is 12.2% and 5.4% respectively. From these results, it can be concluded that the most stable hybrid is the one obtained at the highest silver precursor concentration and the highest temperature (GO-AgNPs-D). The improvement in the thermal stability is attributed to the deoxygenation and better graphitization of the hybrids, because of the partial reduction of GO. Therefore, GO-AgNPs-D would be the most stable product, but also the most difficult to re-disperse in an aqueous medium since many functional groups have been removed.

2.3.3. Antimicrobial activity assessment

The study of materials in the healthcare area is a topic of increasing interest since biomedical devices are responsible for a high percentage of healthcare-associated infections. These infections place an enormous economic burden on both patients and healthcare services and are related to increased patient morbidity and mortality. The main problem lies in the fact that biomedical devices are inert materials where the immune system's defenses cannot reach, so the number of microorganisms needed to generate an infection is greatly reduced. In addition, these microorganisms usually produce biofilms that protect them from antimicrobial drugs, which ends up causing an increase in multi-drug resistant microorganisms.

The microorganisms chosen in this doctoral thesis are some of the most frequent etiological agents of healthcare-associated infections: Gram-negative (*E. coli* and *P. aeruginosa*) and Gram-positive bacteria (*S. aureus*), and yeasts (*C. albicans*) [223,224]. They were selected in order to understand the behavior of synthesized graphene nanocomposites on different microbial structures. These infectious agents are transmitted mainly by contact with people who carry or are infected by them, as well as through objects (fomites), food, water and animals. These four microorganisms can become part of the human microbiota and subsequently cause opportunistic infections. Epidemic strains of these species have also been described to cause moderate and severe infections in people without any underlying disease or immunodeficiency [225].

Gram-positive *S. aureus* is a major human pathogen that causes a wide range of clinical infections. It is a leading cause of bacteremia and one of the most important causes of death associated with bloodstream infection [226]. Antibiotic resistance is common, with the most problematic strains being those called MRSA (methicillin-resistant *S. aureus*). Gram-negative *E. coli* is a major cause of bloodstream infection, as well as the most common pathogen causing urinary tract infection and catheter-associated urinary tract infections, and a critical antimicrobial resistance issue [227]. Gram-negative *P. aeruginosa* is the main cause of ventilated-associated pneumonia in the intensive care unit and a common cause of other nosocomial infections exhibiting innate antibiotic multi-drug resistance [228]. *C. albicans* was also included because it is the most important

cause of healthcare-associated fungal diseases, ranked as the fourth or fifth most common nosocomial bloodstream pathogen in USA and some European countries with mortality rates as high as 45% [223,229].

In this context, the antimicrobial properties of GO, GS and GO-AgNPs were studied on *E. coli* ATCC 25922, *P. aeruginosa* ATCC 27853, *S. aureus* ATCC 25923 and *C. albicans* SC5314. The antimicrobial activity was analyzed by means of the Minimal Inhibitory Concentration (MIC), defined as the lowest concentration of antimicrobial drug capable of inhibiting the microbial growth by at least 50%, and by the microbial growth kinetics assay. In line with other studies [126,141,142] which reveal that the antibacterial activity of AgNPs decreases with increasing particle size, only GO-AgNPs-A was selected to characterize its antimicrobial activity. MIC values are shown in Table 2.5

Table 2.5. Minimum inhibition concentrations of GO, GS and GO-AgNPs-A.

Microorganism	MIC$_{50}$ (µg/mL)		
	GO	GS	GO-AgNPs-A
Escherichia coli	>128	>128	**64**
Pseudomonas aeruginosa	>128	>128	**64**
Staphylococcus aureus	>128	>128	**32**
Candida albicans	>128	>128	**32**

For GO and GS samples with concentrations within the range of 0.25 µg/mL to 128 µg/mL, the MIC was not determined as there was not a 50% reduction in absorbance in comparison to the growth control for any of the four microorganisms studied. Hence, they were not considered to exert antimicrobial activity at these concentrations. However, in the case of GO-AgNPs-A, the MIC value varied depending on the microorganism. Gram-positive bacteria *S. aureus* and yeast *C. albicans* were more susceptible to the effect of GO-AgNPs-A (MIC = 32 µg/mL) than Gram-negative bacteria (MIC = 64 µg/mL), after 24 h to exposure. The variation in MIC found may be due to the different cell wall structure of the four microorganisms, as indicated by Tang *et al.* [161] (further explanation of the differences cell wall in Chapter 4).

The microbial growth kinetics test offers an interesting approach to study the antimicrobial activity, since it takes into consideration the influence of two important variables: the amount of nanomaterial and the exposure time (longer than in the MIC test) of microbial cells to the nanomaterial. The absorbance of the microplate wells was monitored every hour, which allowed us to create the growth curve for each microorganism. Owing the lack of antimicrobial activity found for GO in the previous assay, it was used as a negative inhibition control in this test. The growth kinetics of the microorganisms were obtained in the presence of the highest GO concentration previously tested (128 µg/mL) for 72 h (Figure 2.27). Confirming once again the lack of antimicrobial activity in the concentration range studied, not only did GO not prevent the growth of any of this microorganisms, but also it seemed that GO acted as a growth stimulator. This is in accordance with the results reported in the literature [179,180], since the growth curve of microorganisms in contact with the nanomaterial exceeded the absorbance of those which had not been in contact.

However, controversial results regarding the antimicrobial properties of GO are reported in the literature [179,181-184]. Both the physicochemical properties of GO, (sheet size, functional groups, oxygen content, surface roughness, number of layers, purity, etc.) and the interaction graphene-microorganism (concentration, incubation time and culture medium) have been shown to affect its antimicrobial properties. Liu *et al.* [181] [181][181][181][181](181)reported that various dispersions of graphene material had a concentration- and time-dependent antibacterial effect. In their study, GO dispersions (at concentrations from 10 to 80 µg/mL) showed the highest antibacterial activity in *E. coli* among all the different graphene-base materials studied, and an almost complete loss of cell viability at a concentration of 80 µg/mL. Moreover, most of the bacterial inactivation was observed in the first hour of incubation. Hu *et al.* showed that the growth inhibition of *E. coli* by GO was almost completely suppressed when treated with 85 µg/mL GO for 2 h [186]. Other studies, however, have concluded otherwise. In the study by Nguyen *et al.*, the ineffectiveness of GO (up to 400 µg/mL) against *E. coli* was demonstrated [191]. The lack of antifungal activity against *C. albicans* by GO was demonstrated in the studies carried out by Li *et al.* [192], and Al-Thani *et al.* [193]. Ruiz *et al.* reported a rapid and irreversible attachment of bacterial cells to GO [183].
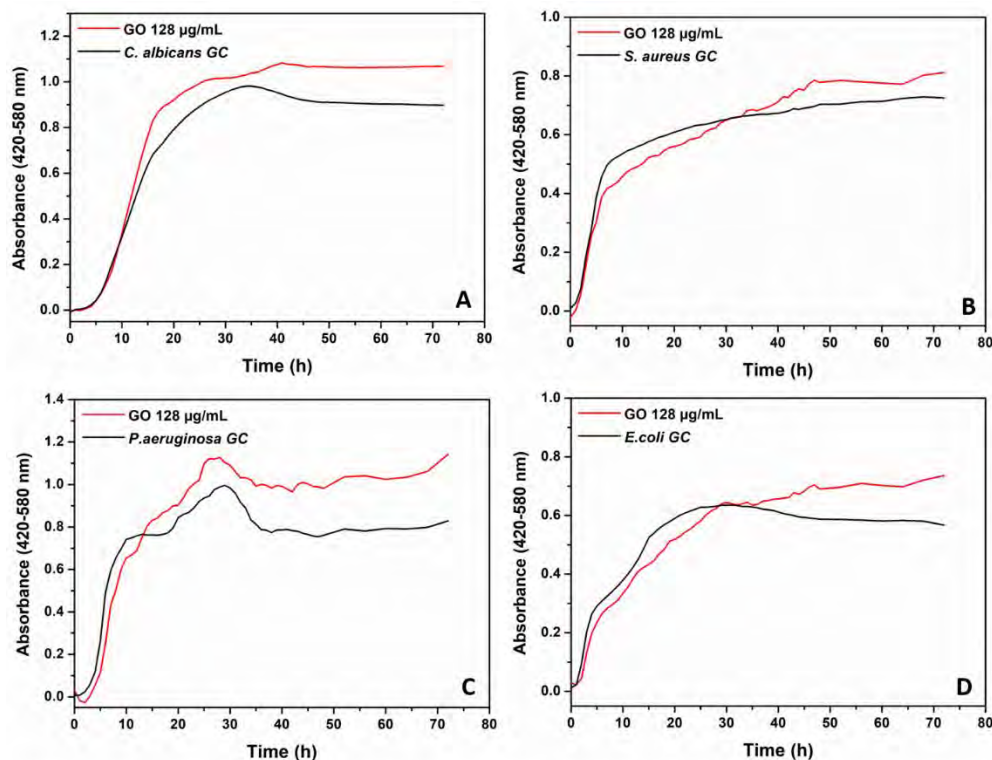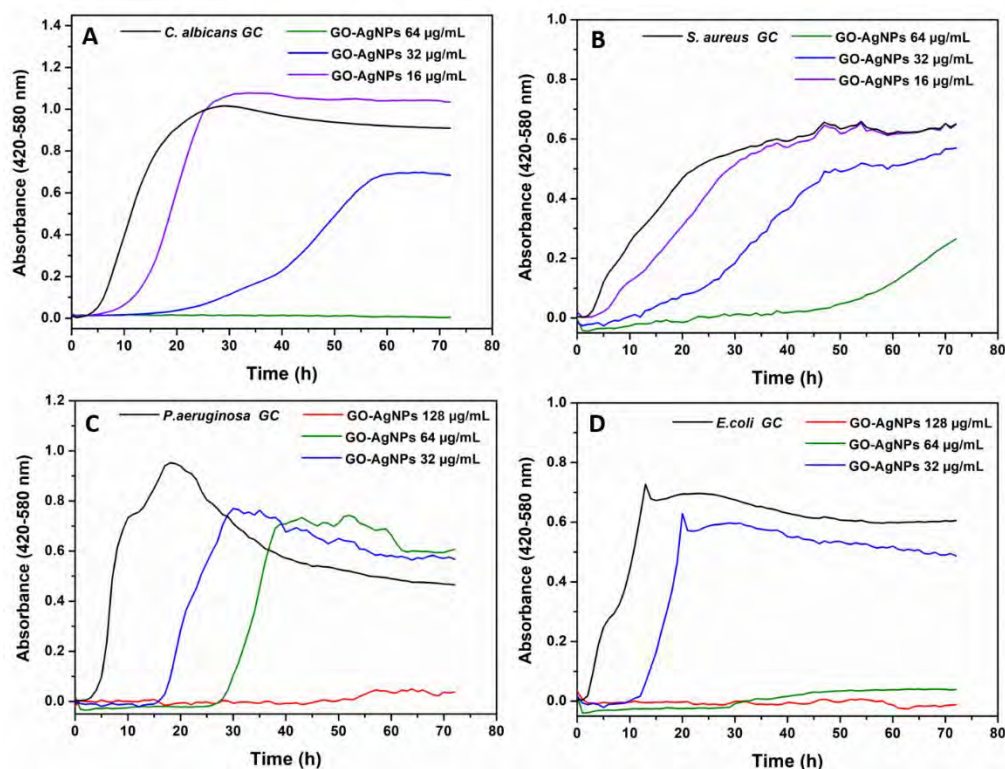
Figure 2.27. Microbial growth kinetics in contact with GO. (A) *C. albicans*, (B) *S. aureus*, (C) *P. aeruginosa* and (D) *E. Coli*.

It has also been suggested that the culture medium can play a key role in the toxicity of GO against bacteria. Hui *et al.* [230] studied the antimicrobial properties of GO in saline and Luria-Bertani (LB) broth. They concluded that LB broth rendered GO inactive observing an increased bacterial growth. The loss of antibacterial activity was attributed to non-covalent adsorption of the LB components in GO basal planes. Likewise, Ruiz *et al.* [183] investigated the effect of colloidal GO on *E. coli* growth in LB nutrient broth, observing a significant increase in microbial cell proliferation and GO precipitation. Scanning electron microscopy (SEM) analysis revealed that the precipitated GO observed was covered by a thick bacterial biofilm containing a large mass of aggregate cells and extracellular polymeric material. The authors suggested that the GO precipitates acted as scaffolds for cell surface attachment, proliferation, and biofilm formation. Chen *et al.* [184] also found that GO acted as scaffold promoting proliferation of gut bacteria such as *Bifidobacterium adolescentis*. More recently, Gusev *et al.*

[231] in their study of the interaction of *E. coli* with reduced graphene oxide (rGO) also have demonstrated the important role of the culture medium in the antimicrobial properties of rGO.

Regarding the GO-AgNPs-A sample, MIC, half of the MIC concentration (MIC/2) and twice the MIC concentration (MICx2) were the nanomaterial concentrations analyzed for each microorganism. The results obtained are presented in Figure 2.28, where it can be observed that microbial growth is completely prevented at one of the concentrations for all the microorganisms. The curves show four distinct growth phases: latent period (lag), exponential (log), stationary, and death phases. Lag phase corresponds to the delay before exponential growth begins. In the log or exponential phase, cell division proceeds at a constant rate, whereas in the stationary phase, the conditions become unfavorable for growth and microbes stop replicating, and reach an equilibrium level. Finally, in the death phase cells lose viability. The length of the lag phase is the time it takes for the inoculum to increase its cell number when introduced into a fresh medium. When microorganisms have to face environmental changes, they enter the lag phase during which cell growth is stopped since the have to adapt to the new situation and to synthesize the cellular components necessary for growth such as RNA, enzymes and other molecules. Depending on the cell structure, the type of antimicrobial agent and its concentration the growth profile differs. Our results are in line with Theophel et al. [232] showing longer lag phases as the concentration of antimicrobial agent increases.

According to Table 2.5, the MIC value for *C. albicans* is 32 μg/mL, and this concurs with the degree of inhibition shown in its growth curve at 24 h for this concentration (Figure 2.28A). However, 64 μg/mL (MICx2) of GO-AgNPs-A was required to fully inhibit the growth of *C. albicans* after 72 h of incubation with the nanomaterial. For *S. aureus*, the concentration that inhibited its growth by at least 50% at 24 h (MIC) was 32 μg/mL. Nonetheless, from its growth curve (Figure 2.28B) it can also be seen that the growth during 72 h of expose to the nanomaterial was similar to the growth at lower GO-AgNPs-A concentration (16 μg/mL). Thus, the concentration of 32 μg/mL of GO-AgNPs-A led to a longer lag phase due to the adaptation of the microorganism to this concentration and the killing effect in the inoculum. This effect was enhanced by increasing concentrations of the nanomaterial.

Figure 2.28. Microbial growth kinetics in contact with GO-AgNPS-A. (A) *C. albicans*, (B*) S. aureus*, (C) *P. aeruginosa* and (D) *E. Coli*.

Considering, the two Gram-negative bacteria, both displayed a MIC value of 64 µg/mL. However, the antibacterial effect of this concentration on *P. aeruginosa* caused a prolonged lag phase, whereas the growth of *E. coli* was fully inhibited (Figures 2.28C and D). These results also suggested an increased susceptibility to GO-AgNPs-A nanohybrid by *C. albicans* and *S. aureus* at 32 µg/mL confirming our MIC assay.

Taking together, these findings lead to the conclusion that GO-AgNPs-A nanohybrid exhibits a dose- and exposure time-dependent antimicrobial activity. The concentration of GO-AgNPs-A that would hinder at least the 50% growth of any of these microorganisms for 72 hours, should be higher than 64 µg/mL. Several authors have studied the antimicrobial behavior of GO-AgNPs, recording low exposure time ranges compared to our 72-hour-assay. Fonseca de Faria *et al.* reported that GO dispersion lacks antibacterial activity against *P. aeruginosa* at

the evaluated concentrations in the study (from 0.1 μg/mL to 5.0 μg/mL) after 0-6 hours range, whereas 100% of *P. aeruginosa* cells were fully inhibited after contact with GO/Ag concentrations of 2.5 and 5.0 μg/mL for 30-60 min [166]. Cui *et al.* investigated the inhibitory effect against *C. albicans* of both GO and the GO-Ag composite [233]. They concluded that GO did not show growth inhibition in fungal cells, but the antifungal effect of GO-Ag was confirmed and was even improved when compared to the activity of bare AgNPs. Jaworski *et al.* studied the antimicrobial activity of GO-, AgNPs- and GO-AgNPs-coated polyurethane foils against *E. coli*, *S. aureus*, *S. epidermidis*, and *C. albicans* at 37 °C for 24 h [234]. The foil coated with GO-Ag showed the strongest antibacterial effect against all tested microorganisms, being the growth of bacterial cells greatly inhibited, while the GO and AgNPs coated films only slightly reduced it. The yeast *C. albicans* was the most resistant to the effect of GO-Ag, followed by Gram-positive and Gram-negative bacteria. The study carried out by Tang *et al.* revealed that both pure GO and AgNPs and the simple mixture of both had no effect on *E. coli* and *S. aureus* at the concentrations studied, whereas the nanocomposite GO-Ag showed dose- and Ag:GO ratio-dependent antibacterial activity [165]. In addition, the results showed that the antibacterial effect of GO-AgNPs was species dependent. The enhanced antimicrobial activity of GO-AgNPs compared to GO and AgNPs is attributed to a synergistic effect of GO an AgNPs and not to an additive effect of both components. Shao *et al.* investigated the antibacterial activity of GO-Ag nanocomposite against *E. coli* and *S. aureus* [235]. The synthesized GO-Ag showed a dose-dependent antimicrobial effect, and stronger towards *E. coli* than towards *S. aureus*. Das *et al.* investigated the antibacterial activity of Ag-GO against *E. coli* and *P. aeruginosa* [162]. They found that *P. aeruginosa* was more sensitive than *E. coli* to Ag-GO. The investigation on the antibacterial activity of GO-Ag hybrid by Mohammadnejad *et al.* showed a higher toxicity against *E. coli* than against *S. aureus* [236].

The results of the present study indicate that AgNPs play an essential role in the antimicrobial activity of GO-AgNPs hybrids. The activity of AgNPs is dependent on several parameters, including those inherent to them such as size and shape. The size dependency has been investigated in different works studies [140,144-147,237] and it has been concluded that the smaller the size, the greater the toxicity. This was the reason why GO-AgNPs-A was selected for the

antimicrobial assay. Small sized AgNPs can cover a larger surface area, resulting in more efficient cell-particle contact. Bare-silver nanoparticles tend to aggregate not being stable in aqueous suspensions, which limit their applications. GO plays an active role in the enhancement of the stability of the AgNPs, acting as a platform to prevent their agglomeration. The formation mechanism of the GO-AgNP hybrids seems to be through electrostatic interactions between the negatively charged oxygen-containing functional groups on the GO surface and the free silver ions, which are then reduced by the reducing agent, leading to the formation of AgNPs attached to the GO surface [97,150,155,166,235].

The antimicrobial mechanism of action of AgNPs has been described in several studies, but it is not completely elucidated [144,238-242]. It is assumed that the attachment of AgNPs to the microbial surface could be mediated by the electrostatic interaction between the negative charged cell membrane of many microbes and the positive surface charged nanoparticles. Silver nanoparticles are able to enter the cell interior after adhering to the cell surface. This results in irreparable damage to different internal components. In addition, the cellular internalization of AgNPs can also generate reactive oxygen species (ROS) and induce oxidative stress in bacterial cells due to the release of Ag^+ ions. In the presence of dissolved oxygen (in aqueous solutions) the surface of silver nanoparticles is oxidized, and the AgNPs oxidative dissolution leads to Ag^+ ions. Both AgNPs and Ag^+ ions damage microbial cells by interacting with sulfur-containing proteins present in both microbial membranes or cytosol as well as with phosphorous-containing compounds such as DNA. All these processes will lead finally to the death of microorganisms. Consequently, the antimicrobial effect of GO-AgNPs nanohybrid could be explained by the combine action of direct contact between the AgNPs and the microbial cells, and the dissolution of Ag^+ ions from AgNPs.

The antimicrobial properties make GO-AgNPs potential candidates as materials for biomedicine as well as for the preparation of antimicrobial polymer nanocomposites. A particularly important aspect to consider about nanomaterials is their cytotoxicity, which is governed by physicochemical properties such as size, shape, surface load, coating and concentration [243]. AgNPs have been found to be toxic to several human cell lines, and their cytotoxicity occurs in a dose–, size– and time–response manner (especially for those with sizes ≤10 nm) by

creating ROS, oxidative stress, and DNA damage [244,245]. The smaller silver nanoparticles showed higher biological activity in comparison with the larger ones. Similarly, toxicity threshold for the same cell line was higher for small particles than for large ones [246]. However, no cytotoxicity has been observed when AgNPs are coated with appropriate polymers at certain concentrations [247]. Several research suggest that reasonable doses of AgNPs present many beneficial effects in different applications without any adverse effects on human cells [248]. As for cytotoxicity of GO-AgNPs, it has been reported that also occurs in a dose-dependent manner and that is affected by the mass ratio of GO:Ag. It has been found that GO-AgNPs is more toxic than its pristine counterparts. The reported studies revealed that the cytotoxicity of GO-AgNPs towards human cell is related to the synergistic effect between GO and AgNPs [244]. As with any other compounds, the concentration of GO-AgNPs present in the materials and the final applications should be considered to avoid adverse effects. Moreover, it has been reported the anticancer activity of GO, AgNPs and GO-AgNPs nanohybrids [249], especially, nanohybrids of GO-AgNPs seem to show increased anticancer activity compared to GO [250] making these nano-hybrids potential candidates in cancer therapy.

2.4. <u>Conclusions</u>

In this work, GO was successfully produced from natural graphite flakes by the modified Hummers method. In addition, GS was obtained effectively through chemical reduction of the exfoliated graphene oxide sheets by adding different amounts of reducing agent (L-AA) in order to determine the optimum concentration to obtain the highest level of reduction of GO. The characterization results of FTIR and TGA suggested that 2.00 mM L-AA was the appropriate concentration. On the other hand, GO-AgNPs nanohybrids were successfully synthesized by an environmentally friendly one step approach in the absence of any stabilizer. The simultaneous reduction of $AgNO_3$ and GO in the presence of ascorbic acid resulted in the decoration of partially reduced graphene oxide with uniformly distributed AgNPs of an average size lesser than 4 nm. The size of the silver nanoparticles was altered by the concentration of silver precursor and temperature. The lower the concentration of silver precursor and the lower the temperature, the smaller the size of the silver nanoparticles anchored on GO surface. GO and GS dispersions showed lack of antimicrobial activity against four common pathogens, *E. coli*, *P. aeruginosa*, *S. aureus* and *C. albicans* over the concentration range investigated, while the nanohybrids exhibited species-specific antimicrobial activity. GO-AgNPs displayed the highest activity against *C. albicans* and *S. aureus*. GO-AgNPs nanohybrids induce a dose- and exposure time-dependent toxicity to the four microorganisms. This class of nanohybrids can be used as antimicrobial fillers for the preparation of polymer nanocomposites with antimicrobial properties, which can find applications in different fields.

2.5. <u>References</u>

[1] H.W. Kroto, J.R. Heath, S.C. O'Brien, R.F. Curl, R.E. Smalley, C60: buckminsterfullerene. Nature (London). 318 (1985) 162-163.

[2] W. Kraetschmer, L.D. Lamb, K. Fostiropoulos, D.R. Huffman, Solid C60: a new form of carbon. Nature (London). 347 (1990) 354-358.

[3] A. Hirsch, The era of carbon allotropes. Nat. Mater. 9 (2010) 868-871.

[4] S. Iijima, Helical microtubules of graphitic carbon, Nature. 354 (1991) 56.

[5] K.S. Novoselov, A.K. Geim, S.V. Morozov, D. Jiang, Y. Zhang, S.V. Dubonos, *et al.*, Electric Field Effect in Atomically Thin Carbon Films. Science (Washington, DC, U. S.). 306 (2004) 666-669.

[6] X. Lu, M. Yu, H. Huang, R.S. Ruoff, Tailoring graphite with the goal of achieving single sheets. Nanotechnology. 10 (1999) 269-272.

[7] O.A. Shenderova, V.V. Zhirnov, D.W. Brenner, Carbon nanostructures. Crit. Rev. Solid State Mater. Sci. 27 (2002) 227-356.

[8] J. Sakamoto, J. van Heijst, O. Lukin, A.D. Schluter, Two-dimensional polymers: just a dream of synthetic chemists?. Angew. Chem. , Int. Ed. 48 (2009) 1030-1069.

[9] S. Eigler, A. Hirsch, Chemistry with graphene and graphene oxide - challenges for synthetic chemists, Angewandte Chemie International Edition. 53 (2014) 7720-7738.

[10] J.R. Potts, D.R. Dreyer, C.W. Bielawski, R.S. Ruoff, Graphene-based polymer nanocomposites, Polymer. 52 (2011) 5-25.

[11] H. Kim, A.A. Abdala, C.W. Macosko, Graphene/polymer nanocomposites, Macromolecules. 43 (2010) 6515-6530.

[12] A.K. Geim, K.S. Novoselov, The rise of graphene, Nature materials. 6 (2007) 183.

[13] J.C. Meyer, A.K. Geim, M.I. Katsnelson, K.S. Novoselov, T.J. Booth, S. Roth, The structure of suspended graphene sheets, Nature. 446 (2007) 60.

[14] R.R. Nair, P. Blake, A.N. Grigorenko, K.S. Novoselov, T.J. Booth, T. Stauber, *et al.*, Fine structure constant defines visual transparency of graphene, Science. 320 (2008) 1308.

[15] K.I. Bolotin, K. Sikes, Z. Jiang, M. Klima, G. Fudenberg, J. Hone, *et al.*, Ultrahigh electron mobility in suspended graphene, Solid State Commun. 146 (2008) 351-355.

[16] F. Schedin, A. Geim, S. Morozov, E. Hill, P. Blake, M. Katsnelson, *et al.*, Detection of individual gas molecules adsorbed on graphene, Nature materials. 6 (2007) 652.

[17] A.A. Balandin, S. Ghosh, W. Bao, I. Calizo, D. Teweldebrhan, F. Miao, *et al.*, Superior thermal conductivity of single-layer graphene, Nano letters. 8 (2008) 902-907.

[18] C. Lee, X. Wei, J.W. Kysar, J. Hone, Measurement of the elastic properties and intrinsic strength of monolayer graphene, Science. 321 (2008) 385-388.

[19] A. Bianco, H. Cheng, T. Enoki, Y. Gogotsi, R.H. Hurt, N. Koratkar, *et al.*, All in the graphene family – A recommended nomenclature for two-dimensional carbon materials, Carbon. 65 (2013) 1-6.

[20] A.A. Green, M.C. Hersam, Solution phase production of graphene with controlled thickness via density differentiation, Nano letters. 9 (2009) 4031-4036.

[21] B. Jayasena, S.N. Melkote, An investigation of PDMS stamp assisted mechanical exfoliation of large area graphene, Procedia Manufacturing. 1 (2015) 840-853.

[22] T. Kuila, S. Bose, A.K. Mishra, P. Khanra, N.H. Kim, J.H. Lee, Chemical functionalization of graphene and its applications, Progress in Materials Science. 57 (2012) 1061-1105.

[23] G. Mittal, V. Dhand, K.Y. Rhee, S. Park, W.R. Lee, A review on carbon nanotubes and graphene as fillers in reinforced polymer nanocomposites, Journal of Industrial and Engineering Chemistry. 21 (2015) 11-25.

[24] K.S. Novoselov, V. Fal, L. Colombo, P. Gellert, M. Schwab, K. Kim, A roadmap for graphene, Nature. 490 (2012) 192.

[25] W.S. Hummers Jr, R.E. Offeman, Preparation of graphitic oxide, J. Am. Chem. Soc. 80 (1958) 1339-1339.

[26] M.J. McAllister, J. Li, D.H. Adamson, H.C. Schniepp, A.A. Abdala, J. Liu, *et al.*, Single sheet functionalized graphene by oxidation and thermal expansion of graphite, Chemistry of materials. 19 (2007) 4396-4404.

[27] Z. Wu, W. Ren, L. Gao, J. Zhao, Z. Chen, B. Liu, *et al.*, Synthesis of graphene sheets with high electrical conductivity and good thermal stability by hydrogen arc discharge exfoliation, ACS nano. 3 (2009) 411-417.

[28] S. Stankovich, R.D. Piner, X. Chen, N. Wu, S.T. Nguyen, R.S. Ruoff, Stable aqueous dispersions of graphitic nanoplatelets via the reduction of exfoliated graphite oxide in the presence of poly(sodium 4-styrenesulfonate), Journal of Materials Chemistry. 16 (2006) 155-158.

[29] S. Stankovich, D.A. Dikin, R.D. Piner, K.A. Kohlhaas, A. Kleinhammes, Y. Jia, *et al.*, Synthesis of graphene-based nanosheets via chemical reduction of exfoliated graphite oxide, carbon. 45 (2007) 1558-1565.

[30] S. Pei, J. Zhao, J. Du, W. Ren, H. Cheng, Direct reduction of graphene oxide films into highly conductive and flexible graphene films by hydrohalic acids, Carbon. 48 (2010) 4466-4474.

[31] I.K. Moon, J. Lee, R.S. Ruoff, H. Lee, Reduced graphene oxide by chemical graphitization, Nature communications. 1 (2010) 73.

[32] J. Zhang, H. Yang, G. Shen, P. Cheng, J. Zhang, S. Guo, Reduction of graphene oxide via L-ascorbic acid, Chemical Communications. 46 (2010) 1112-1114.

[33] D. He, L. Shen, X. Zhang, Y. Wang, N. Bao, H.H. Kung, An efficient and eco-friendly solution-chemical route for preparation of ultrastable reduced graphene oxide suspensions, AIChE J. 60 (2014) 2757-2764.

[34] C. Xu, X. Shi, A. Ji, L. Shi, C. Zhou, Y. Cui, Fabrication and characteristics of reduced graphene oxide produced with different green reductants, PLoS One. 10 (2015) e0144842.

[35] M.J. Fernández-Merino, L. Guardia, J. Paredes, S. Villar-Rodil, P. Solís-Fernández, A. Martínez-Alonso, *et al.*, Vitamin C is an ideal substitute for hydrazine in the reduction of graphene oxide suspensions, The Journal of Physical Chemistry C. 114 (2010) 6426-6432.

[36] D. Chen, L. Li, L. Guo, An environment-friendly preparation of reduced graphene oxide nanosheets via amino acid, Nanotechnology. 22 (2011) 325601.

[37] C. Zhu, S. Guo, Y. Fang, S. Dong, Reducing sugar: new functional molecules for the green synthesis of graphene nanosheets, ACS nano. 4 (2010) 2429-2437.

[38] G. Wang, J. Yang, J. Park, X. Gou, B. Wang, H. Liu, *et al.*, Facile synthesis and characterization of graphene nanosheets, The Journal of Physical Chemistry C. 112 (2008) 8192-8195.

[39] X. Fan, W. Peng, Y. Li, X. Li, S. Wang, G. Zhang, *et al.*, Deoxygenation of exfoliated graphite oxide under alkaline conditions: a green route to graphene preparation, Adv Mater. 20 (2008) 4490-4493.

[40] X. Zhou, J. Zhang, H. Wu, H. Yang, J. Zhang, S. Guo, Reducing graphene oxide via hydroxylamine: a simple and efficient route to graphene, The Journal of Physical Chemistry C. 115 (2011) 11957-11961.

[41] G. Demazeau, Solvothermal processes: a route to the stabilization of new materials, Journal of Materials Chemistry. 9 (1999) 15-18.

[42] Y. Zhou, Q. Bao, L.A.L. Tang, Y. Zhong, K.P. Loh, Hydrothermal dehydration for the "green" reduction of exfoliated graphene oxide to graphene and demonstration of tunable optical limiting properties, Chemistry of Materials. 21 (2009) 2950-2956.

[43] H. Wang, J.T. Robinson, X. Li, H. Dai, Solvothermal reduction of chemically exfoliated graphene sheets, J. Am. Chem. Soc. 131 (2009) 9910-9911.

[44] C. Liu, K. Wang, S. Luo, Y. Tang, L. Chen, Direct Electrodeposition of Graphene Enabling the One-Step Synthesis of Graphene–Metal Nanocomposite Films, small. 7 (2011) 1203-1206.

[45] L. Chen, Y. Tang, K. Wang, C. Liu, S. Luo, Direct electrodeposition of reduced graphene oxide on glassy carbon electrode and its electrochemical application, Electrochemistry communications. 13 (2011) 133-137.

[46] S. Liu, J. Ou, J. Wang, X. Liu, S. Yang, A simple two-step electrochemical synthesis of graphene sheets film on the ITO electrode as supercapacitors, J. Appl. Electrochem. 41 (2011) 881.

[47] J. Kim, S. Kwon, D. Cho, B. Kang, H. Kwon, Y. Kim, *et al.*, Direct exfoliation and dispersion of two-dimensional materials in pure water via temperature control, Nature communications. 6 (2015) 8294.

[48] R. Narayan, S.O. Kim, Surfactant mediated liquid phase exfoliation of graphene, Nano Convergence. 2 (2015) 20.

[49] Y. Hernandez, V. Nicolosi, M. Lotya, F.M. Blighe, Z. Sun, S. De, *et al.*, High-yield production of graphene by liquid-phase exfoliation of graphite, Nature nanotechnology. 3 (2008) 563.

[50] D. Nuvoli, L. Valentini, V. Alzari, S. Scognamillo, S.B. Bon, M. Piccinini, *et al.*, High concentration few-layer graphene sheets obtained by liquid phase exfoliation of graphite in ionic liquid, Journal of Materials Chemistry. 21 (2011) 3428-3431.

[51] X. Wang, P.F. Fulvio, G.A. Baker, G.M. Veith, R.R. Unocic, S.M. Mahurin, *et al.*, Direct exfoliation of natural graphite into micrometre size few layers graphene sheets using ionic liquids, Chemical Communications. 46 (2010) 4487-4489.

[52] Z.Y. Xia, S. Pezzini, E. Treossi, G. Giambastiani, F. Corticelli, V. Morandi, *et al.*, The exfoliation of graphene in liquids by electrochemical, chemical, and sonication-assisted techniques: A nanoscale study, Advanced Functional Materials. 23 (2013) 4684-4693.

[53] K. Parvez, R. Li, S.R. Puniredd, Y. Hernandez, F. Hinkel, S. Wang, *et al.*, Electrochemically exfoliated graphene as solution-processable, highly conductive electrodes for organic electronics, ACS nano. 7 (2013) 3598-3606.

[54] K. Parvez, S. Yang, X. Feng, K. Müllen, Exfoliation of graphene via wet chemical routes, Synth. Met. 210 (2015) 123-132.

[55] V. Singh, D. Joung, L. Zhai, S. Das, S.I. Khondaker, S. Seal, Graphene based materials: past, present and future, Progress in materials science. 56 (2011) 1178-1271.

[56] O. Frank, M. Kalbac, Chemical vapor deposition (CVD) growth of graphene films, Graphene, Elsevier, 2014, pp. 27-49.

[57] R. Zhang, H. Li, Z. Zhang, Z. Wang, S. Zhou, Z. Wang, *et al.*, Graphene synthesis on SiC: Reduced graphitization temperature by C-cluster and Ar-ion implantation, Nuclear Instruments and Methods in Physics Research Section B: Beam Interactions with Materials and Atoms. 356 (2015) 99-102.

[58] B. Kumar, M. Baraket, M. Paillet, J. Huntzinger, A. Tiberj, A. Jansen, *et al.*, Growth protocols and characterization of epitaxial graphene on SiC elaborated in a graphite enclosure, Physica E: Low-dimensional Systems and Nanostructures. 75 (2016) 7-14.

[59] A.G. Cano-Marquez, F.J. Rodríguez-Macías, J. Campos-Delgado, C.G. Espinosa-González, F. Tristán-López, D. Ramírez-González, *et al.*, Ex-MWNTs: graphene sheets and ribbons produced by lithium intercalation and exfoliation of carbon nanotubes, Nano letters. 9 (2009) 1527-1533.

[60] Y. Hernandez, M. Lotya, D. Rickard, S.D. Bergin, J.N. Coleman, Measurement of multicomponent solubility parameters for graphene facilitates solvent discovery, Langmuir. 26 (2009) 3208-3213.

[61] U. Khan, H. Porwal, A. O'Neill, K. Nawaz, P. May, J.N. Coleman, Solvent-exfoliated graphene at extremely high concentration, Langmuir. 27 (2011) 9077-9082.

[62] S. Ravula, S.N. Baker, G. Kamath, G.A. Baker, Ionic liquid-assisted exfoliation and dispersion: stripping graphene and its two-dimensional layered inorganic counterparts of their inhibitions, Nanoscale. 7 (2015) 4338-4353.

[63] V. Georgakilas, M. Otyepka, A.B. Bourlinos, V. Chandra, N. Kim, K.C. Kemp, *et al.*, Functionalization of graphene: covalent and non-covalent approaches, derivatives and applications, Chem. Rev. 112 (2012) 6156-6214.

[64] J. Texter, Graphene dispersions, Current Opinion in Colloid & Interface Science. 19 (2014) 163-174.

[65] R.J. Smith, M. Lotya, J.N. Coleman, The importance of repulsive potential barriers for the dispersion of graphene using surfactants, New Journal of Physics. 12 (2010) 125008.

[66] M. Lotya, Y. Hernandez, P.J. King, R.J. Smith, V. Nicolosi, L.S. Karlsson, *et al.*, Liquid phase production of graphene by exfoliation of graphite in surfactant/water solutions, J. Am. Chem. Soc. 131 (2009) 3611-3620.

[67] P. Ramalingam, S.T. Pusuluri, S. Periasamy, R. Veerabahu, J. Kulandaivel, Role of deoxy group on the high concentration of graphene in surfactant/water media, RSC Advances. 3 (2013) 2369-2378.

[68] A.B. Bourlinos, V. Georgakilas, R. Zboril, T.A. Steriotis, A.K. Stubos, C. Trapalis, Aqueous-phase exfoliation of graphite in the presence of polyvinylpyrrolidone for the production of water-soluble graphenes, Solid State Commun. 149 (2009) 2172-2176.

[69] S. Yoon, I. In, Role of poly(N-vinyl-2-pyrrolidone) as stabilizer for dispersion of graphene via hydrophobic interaction, J. Mater. Sci. 46 (2011) 1316-1321.

[70] E. Ou, Y. Xie, C. Peng, Y. Song, H. Peng, Y. Xiong, *et al.*, High concentration and stable few-layer graphene dispersions prepared by the exfoliation of graphite in different organic solvents, Rsc Advances. 3 (2013) 9490-9499.

[71] A.M. Pinto, J. Martins, J.A. Moreira, A.M. Mendes, F.D. Magalhães, Dispersion of graphene nanoplatelets in poly(vinyl acetate) latex and effect on adhesive bond strength, Polym. Int. 62 (2013) 928-935.

[72] J. Choi, K. Kim, B. Kim, H. Lee, S. Kim, Covalent functionalization of epitaxial graphene by azidotrimethylsilane, The Journal of Physical Chemistry C. 113 (2009) 9433-9435.

[73] M. Fang, K. Wang, H. Lu, Y. Yang, S. Nutt, Single-layer graphene nanosheets with controlled grafting of polymer chains, Journal of Materials Chemistry. 20 (2010) 1982-1992.

[74] K.P. Loh, Q. Bao, P.K. Ang, J. Yang, The chemistry of graphene, Journal of Materials Chemistry. 20 (2010) 2277-2289.

[75] J. Liu, Z. Liu, C.J. Barrow, W. Yang, Molecularly engineered graphene surfaces for sensing applications: A review, Anal. Chim. Acta. 859 (2015) 1-19.

[76] D. Boukhvalov, M. Katsnelson, Chemical functionalization of graphene, Journal of Physics: Condensed Matter. 21 (2009) 344205.

[77] R.K. Layek, A.K. Nandi, A review on synthesis and properties of polymer functionalized graphene, Polymer. 54 (2013) 5087-5103.

[78] C. Cioffi, S. Campidelli, F.G. Brunetti, M. Meneghetti, M. Prato, Functionalisation of carbon nanohorns, Chemical Communications. (2006) 2129-2131.

[79] R. Singh, D. Pantarotto, L. Lacerda, G. Pastorin, C. Klumpp, M. Prato, *et al.*, Tissue biodistribution and blood clearance rates of intravenously administered carbon nanotube radiotracers, Proc. Natl. Acad. Sci. U. S. A. 103 (2006) 3357-3362.

[80] K. Kostarelos, L. Lacerda, G. Pastorin, W. Wu, S. Wieckowski, J. Luangsivilay, *et al.*, Cellular uptake of functionalized carbon nanotubes is independent of functional group and cell type, Nature nanotechnology. 2 (2007) 108.

[81] D. Chen, H. Feng, J. Li, Graphene oxide: preparation, functionalization, and electrochemical applications, Chem. Rev. 112 (2012) 6027-6053.

[82] X. Li, H. Wang, J.T. Robinson, H. Sanchez, G. Diankov, H. Dai, Simultaneous nitrogen doping and reduction of graphene oxide, J. Am. Chem. Soc. 131 (2009) 15939-15944.

[83] D. Wei, Y. Liu, Y. Wang, H. Zhang, L. Huang, G. Yu, Synthesis of N-doped graphene by chemical vapor deposition and its electrical properties, Nano letters. 9 (2009) 1752-1758.

[84] L. Panchakarla, K. Subrahmanyam, S. Saha, A. Govindaraj, H. Krishnamurthy, U. Waghmare, *et al.*, Synthesis, Structure, and Properties of Boron-and Nitrogen-Doped Graphene, Adv Mater. 21 (2009) 4726-4730.

[85] T. Kuila, S. Bose, P. Khanra, A.K. Mishra, N.H. Kim, J.H. Lee, Recent advances in graphene-based biosensors, Biosensors and Bioelectronics. 26 (2011) 4637-4648.

[86] T.A. Pham, N.A. Kumar, Y.T. Jeong, Covalent functionalization of graphene oxide with polyglycerol and their use as templates for anchoring magnetic nanoparticles, Synth. Met. 160 (2010) 2028-2036.

[87] A.C. Ferrari, F. Bonaccorso, V. Fal'Ko, K.S. Novoselov, S. Roche, P. Bøggild, *et al.*, Science and technology roadmap for graphene, related two-dimensional crystals, and hybrid systems, Nanoscale. 7 (2015) 4598-4810.

[88] S. Agah, M. Zheng, M. Pasquali, A.B. Kolomeisky, DNA sequencing by nanopores: advances and challenges, J. Phys. D. 49 (2016) 413001.

[89] J. Liu, L. Cui, D. Losic, Graphene and graphene oxide as new nanocarriers for drug delivery applications, Acta biomaterialia. 9 (2013) 9243-9257.

[90] T.R. Nayak, H. Andersen, V.S. Makam, C. Khaw, S. Bae, X. Xu, *et al.*, Graphene for controlled and accelerated osteogenic differentiation of human mesenchymal stem cells, ACS nano. 5 (2011) 4670-4678.

[91] R. Nair, P. Blake, J. Blake, R. Zan, S. Anissimova, U. Bangert, *et al.*, Graphene as a transparent conductive support for studying biological molecules by transmission electron microscopy, Appl. Phys. Lett. 97 (2010) 153102.

[92] Y. Yu, Z. Chen, S. He, B. Zhang, X. Li, M. Yao, Direct electron transfer of glucose oxidase and biosensing for glucose based on PDDA-capped gold nanoparticle modified graphene/multi-walled carbon nanotubes electrode, Biosensors and Bioelectronics. 52 (2014) 147-152.

[93] J. Yukird, T. Wongtangprasert, R. Rangkupan, O. Chailapakul, T. Pisitkun, N. Rodthongkum, Label-free immunosensor based on graphene/polyaniline nanocomposite for neutrophil gelatinase-associated lipocalin detection, Biosensors and Bioelectronics. 87 (2017) 249-255.

[94] Y. He, H. Dong, T. Li, C. Wang, W. Shao, Y. Zhang, *et al.*, Graphene and graphene oxide nanogap electrodes fabricated by atomic force microscopy nanolithography, Appl. Phys. Lett. 97 (2010) 210.

[95] M. Hernaez, C.R. Zamarreño, S. Melendi-Espina, L.R. Bird, A.G. Mayes, F.J. Arregui, Optical fibre sensors using graphene-based materials: A review, Sensors. 17 (2017) 155.

[96] D. Cohen-Tanugi, J.C. Grossman, Mechanical strength of nanoporous graphene as a desalination membrane, Nano letters. 14 (2014) 6171-6178.

[97] Q. Bao, D. Zhang, P. Qi, Synthesis and characterization of silver nanoparticle and graphene oxide nanosheet composites as a bactericidal agent for water disinfection. J. Colloid Interface Sci. 360 (2011) 463-470.

[98] F. Bonaccorso, Z. Sun, T. Hasan, A. Ferrari, Graphene photonics and optoelectronics, Nature photonics. 4 (2010) 611.

[99] S. Bae, H. Kim, Y. Lee, X. Xu, J. Park, Y. Zheng, *et al.*, Roll-to-roll production of 30-inch graphene films for transparent electrodes, Nature nanotechnology. 5 (2010) 574.

[100] M.D. Bhatt, C. O'Dwyer, Recent progress in theoretical and computational investigations of Li-ion battery materials and electrolytes, Physical Chemistry Chemical Physics. 17 (2015) 4799-4844.

[101] M.M. Atabaki, R. Kovacevic, Graphene composites as anode materials in lithium-ion batteries, Electronic Materials Letters. 9 (2013) 133-153.

[102] M.P. Levendorf, C.S. Ruiz-Vargas, S. Garg, J. Park, Transfer-free batch fabrication of single layer graphene transistors, Nano letters. 9 (2009) 4479-4483.

[103] K. Tielrooij, J. Song, S.A. Jensen, A. Centeno, A. Pesquera, A.Z. Elorza, *et al.*, Photoexcitation cascade and multiple hot-carrier generation in graphene, Nature Physics. 9 (2013) 248.

[104] M. Hirata, T. Gotou, S. Horiuchi, M. Fujiwara, M. Ohba, Thin-film particles of graphite oxide 1:: High-yield synthesis and flexibility of the particles, Carbon. 42 (2004) 2929-2937.

[105] H. Kim, Y. Miura, C.W. Macosko, Graphene/polyurethane nanocomposites for improved gas barrier and electrical conductivity, Chemistry of Materials. 22 (2010) 3441-3450.

[106] D.C. Marcano, D.V. Kosynkin, J.M. Berlin, A. Sinitskii, Z. Sun, A. Slesarev, *et al.*, Improved synthesis of graphene oxide, ACS nano. 4 (2010) 4806-4814.

[107] N. Zaaba, K. Foo, U. Hashim, S. Tan, W. Liu, C. Voon, Synthesis of graphene oxide using modified hummers method: solvent influence, Procedia engineering. 184 (2017) 469-477.

[108] K.S. Novoselov, A.K. Geim, S. Morozov, D. Jiang, M. Katsnelson, I. Grigorieva, *et al.*, Two-dimensional gas of massless Dirac fermions in graphene, Nature. 438 (2005) 197.

[109] C. Mattevi, G. Eda, S. Agnoli, S. Miller, K.A. Mkhoyan, O. Celik, *et al.*, Evolution of electrical, chemical, and structural properties of transparent and conducting chemically derived graphene thin films, Advanced Functional Materials. 19 (2009) 2577-2583.

[110] V.K. Rana, M. Choi, J. Kong, G.Y. Kim, M.J. Kim, S. Kim, *et al.*, Synthesis and drug-delivery behavior of chitosan-functionalized graphene oxide hybrid nanosheets, Macromolecular Materials and Engineering. 296 (2011) 131-140.

[111] D. Depan, J. Shah, R.D.K. Misra, Controlled release of drug from folate-decorated and graphene mediated drug delivery system: Synthesis, loading efficiency, and drug release response, Materials Science and Engineering: C. 31 (2011) 1305-1312.

[112] Z. Liu, J.T. Robinson, X. Sun, H. Dai, PEGylated nanographene oxide for delivery of water-insoluble cancer drugs, J. Am. Chem. Soc. 130 (2008) 10876-10877.

[113] X. Sun, Z. Liu, K. Welsher, J.T. Robinson, A. Goodwin, S. Zaric, *et al.*, Nano-graphene oxide for cellular imaging and drug delivery, Nano research. 1 (2008) 203-212.

[114] J. Paredes, S. Villar-Rodil, A. Martínez-Alonso, J. Tascon, Graphene oxide dispersions in organic solvents, Langmuir. 24 (2008) 10560-10564.

[115] S. Niyogi, E. Bekyarova, M.E. Itkis, J.L. McWilliams, M.A. Hamon, R.C. Haddon, Solution properties of graphite and graphene, J. Am. Chem. Soc. 128 (2006) 7720-7721.

[116] Q. Su, S. Pang, V. Alijani, C. Li, X. Feng, K. Müllen, Composites of graphene with large aromatic molecules, Adv Mater. 21 (2009) 3191-3195.

[117] T. Nakajima, Y. Matsuo, Formation process and structure of graphite oxide, Carbon. 32 (1994) 469-475.

[118] H.L. Poh, F. Šaněk, A. Ambrosi, G. Zhao, Z. Sofer, M. Pumera, Graphenes prepared by Staudenmaier, Hofmann and Hummers methods with consequent thermal exfoliation exhibit very different electrochemical properties, Nanoscale. 4 (2012) 3515-3522.

[119] C. Botas, P. Álvarez, P. Blanco, M. Granda, C. Blanco, R. Santamaría, *et al.*, Graphene materials with different structures prepared from the same graphite by the Hummers and Brodie methods, Carbon. 65 (2013) 156-164.

[120] N.I. Kovtyukhova, P.J. Ollivier, B.R. Martin, T.E. Mallouk, S.A. Chizhik, E.V. Buzaneva, *et al.*, Layer-by-layer assembly of ultrathin composite films from micron-sized graphite oxide sheets and polycations, Chemistry of materials. 11 (1999) 771-778.

[121] G. Santamaría-Juárez, E. Gómez-Barojas, E. Quiroga-González, E. Sánchez-Mora, M. Quintana-Ruiz, J.D. Santamaría-Juárez, Safer modified Hummers' method for the synthesis of graphene oxide with high quality and high yield, Materials Research Express. 6 (2020) 125631.

[122] O.C. Compton, B. Jain, D.A. Dikin, A. Abouimrane, K. Amine, S.T. Nguyen, Chemically active reduced graphene oxide with tunable C/O ratios, ACS nano. 5 (2011) 4380-4391.

[123] D. Yang, A. Velamakanni, G. Bozoklu, S. Park, M. Stoller, R.D. Piner, *et al.*, Chemical analysis of graphene oxide films after heat and chemical treatments by X-ray photoelectron and Micro-Raman spectroscopy, Carbon. 47 (2009) 145-152.

[124] A.C. Ferrari, J. Meyer, V. Scardaci, C. Casiraghi, M. Lazzeri, F. Mauri, *et al.*, Raman spectrum of graphene and graphene layers, Phys. Rev. Lett. 97 (2006) 187401.

[125] J. Paredes, S. Villar-Rodil, P. Solís-Fernández, A. Martínez-Alonso, J. Tascon, Atomic force and scanning tunneling microscopy imaging of graphene nanosheets derived from graphite oxide, Langmuir. 25 (2009) 5957-5968.

[126] S. Bai, X. Shen, Graphene–inorganic nanocomposites, Rsc Advances. 2 (2012) 64-98.

[127] I. Khalil, S. Rahmati, N. Muhd Julkapli, W.A. Yehye, Graphene metal nanocomposites — Recent progress in electrochemical biosensing applications, Journal of Industrial and Engineering Chemistry. 59 (2018) 425-439.

[128] M.Y. Wang, T. Shen, M. Wang, D. Zhang, J. Chen, One-pot green synthesis of Ag nanoparticles-decorated reduced graphene oxide for efficient nonenzymatic H2O2 biosensor, Mater Lett. 107 (2013) 311-314.

[129] X. Zhou, X. Huang, X. Qi, S. Wu, C. Xue, F.Y. Boey, *et al.*, In situ synthesis of metal nanoparticles on single-layer graphene oxide and reduced graphene oxide surfaces, The Journal of Physical Chemistry C. 113 (2009) 10842-10846.

[130] M. De, P.S. Ghosh, V.M. Rotello, Applications of nanoparticles in biology, Adv Mater. 20 (2008) 4225-4241.

[131] V.K. Sharma, R.A. Yngard, Y. Lin, Silver nanoparticles: green synthesis and their antimicrobial activities, Adv. Colloid Interface Sci. 145 (2009) 83-96.

[132] M. Rai, A. Yadav, A. Gade, Silver nanoparticles as a new generation of antimicrobials, Biotechnol. Adv. 27 (2009) 76-83.

[133] V. Edwards-Jones, The benefits of silver in hygiene, personal care and healthcare, Lett. Appl. Microbiol. 49 (2009) 147-152.

[134] M. Ahamed, M.S. AlSalhi, M. Siddiqui, Silver nanoparticle applications and human health, Clinica chimica acta. 411 (2010) 1841-1848.

[135] M.A. Faramarzi, A. Sadighi, Insights into biogenic and chemical production of inorganic nanomaterials and nanostructures, Adv. Colloid Interface Sci. 189 (2013) 1-20.

[136] M. Shah, D. Fawcett, S. Sharma, S.K. Tripathy, G.E.J. Poinern, Green synthesis of metallic nanoparticles via biological entities, Materials. 8 (2015) 7278-7308.

[137] S. Iravani, H. Korbekandi, S.V. Mirmohammadi, B. Zolfaghari, Synthesis of silver nanoparticles: chemical, physical and biological methods, Res. Pharm. Sci. 9 (2014) 385-406.

[138] O.V. Kharissova, H.R. Dias, B.I. Kharisov, B.O. Pérez, V.M.J. Pérez, The greener synthesis of nanoparticles, Trends Biotechnol. 31 (2013) 240-248.

[139] A. Scala, A. Piperno, A. Hada, S. Astilean, A. Vulpoi, G. Ginestra, et al., Marine Bacterial Exopolymers-Mediated Green Synthesis of Noble Metal Nanoparticles with Antimicrobial Properties, Polymers. 11 (2019) 1157.

[140] S. Pal, Y.K. Tak, J.M. Song, Does the antibacterial activity of silver nanoparticles depend on the shape of the nanoparticle? A study of the gram-negative bacterium Escherichia coli, Appl. Environ. Microbiol. 73 (2007) 1712-1720.

[141] H.R. Ghorbani, A.A. Safekordi, H. Attar, S. Sorkhabadi, Biological and non-biological methods for silver nanoparticles synthesis, Chemical and Biochemical Engineering Quarterly. 25 (2011) 317-326.

[142] A. Albanese, P.S. Tang, W.C. Chan, The effect of nanoparticle size, shape, and surface chemistry on biological systems, Annu. Rev. Biomed. Eng. 14 (2012) 1-16.

[143] Y.A. Rodríguez Nuñez, R.I. Castro, F.A. Arenas, Z.E. López-Cabaña, G. Carreño, V. Carrasco-Sánchez, et al., Preparation of Hydrogel/Silver Nanohybrids Mediated by Tunable-Size Silver Nanoparticles for Potential Antibacterial Applications, Polymers. 11 (2019) 716.

[144] J.R. Morones, J.L. Elechiguerra, A. Camacho, K. Holt, J.B. Kouri, J.T. Ramírez, et al., The bactericidal effect of silver nanoparticles, Nanotechnology. 16 (2005) 2346.

[145] G. Martinez-Castanon, N. Nino-Martinez, F. Martinez-Gutierrez, J. Martinez-Mendoza, F. Ruiz, Synthesis and antibacterial activity of silver nanoparticles with different sizes, Journal of Nanoparticle Research. 10 (2008) 1343-1348.

[146] Z. Lu, K. Rong, J. Li, H. Yang, R. Chen, Size-dependent antibacterial activities of silver nanoparticles against oral anaerobic pathogenic bacteria, J. Mater. Sci. Mater. Med. 24 (2013) 1465-1471.

[147] M.A. Raza, Z. Kanwal, A. Rauf, A.N. Sabri, S. Riaz, S. Naseem, Size-and shape-dependent antibacterial studies of silver nanoparticles synthesized by wet chemical routes, Nanomaterials. 6 (2016) 74.

[148] A. Alshareef, K. Laird, R. Cross, Shape-dependent antibacterial activity of silver nanoparticles on Escherichia coli and Enterococcus faecium bacterium, Appl. Surf. Sci. 424 (2017) 310-315.

[149] C. Xu, X. Wang, J. Zhu, Graphene– metal particle nanocomposites, The Journal of Physical Chemistry C. 112 (2008) 19841-19845.

[150] K. Hui, K. Hui, D. Dinh, C. Tsang, Y. Cho, W. Zhou, *et al.*, Green synthesis of dimension-controlled silver nanoparticle–graphene oxide with in situ ultrasonication, Acta Materialia. 64 (2014) 326-332.

[151] R. Muszynski, B. Seger, P.V. Kamat, Decorating graphene sheets with gold nanoparticles, The Journal of Physical Chemistry C. 112 (2008) 5263-5266.

[152] Y. Wang, S.J. Zhen, Y. Zhang, Y.F. Li, C.Z. Huang, Facile fabrication of metal nanoparticle/graphene oxide hybrids: a new strategy to directly illuminate graphene for optical imaging, The Journal of Physical Chemistry C. 115 (2011) 12815-12821.

[153] Y. Kim, Z.A. Akbar, D.Y. Kim, S.M. Jo, S. Jang, Aqueous dispersible graphene/Pt nanohybrids by green chemistry: application as cathodes for dye-sensitized solar cells, ACS applied materials & interfaces. 5 (2013) 2053-2061.

[154] J. Shen, M. Shi, N. Li, B. Yan, H. Ma, Y. Hu, *et al.*, Facile synthesis and application of Ag-chemically converted graphene nanocomposite, Nano research. 3 (2010) 339-349.

[155] R. Pasricha, S. Gupta, A.K. Srivastava, A facile and novel synthesis of Ag–graphene-based nanocomposites, Small. 5 (2009) 2253-2259.

[156] Y. Lin, D.W. Baggett, J. Kim, E.J. Siochi, J.W. Connell, Instantaneous formation of metal and metal oxide nanoparticles on carbon nanotubes and graphene via solvent-free microwave heating, ACS applied materials & interfaces. 3 (2011) 1652-1664.

[157] S.W. Chook, C.H. Chia, S. Zakaria, M.K. Ayob, K.L. Chee, N.M. Huang, *et al.*, Antibacterial performance of Ag nanoparticles and AgGO nanocomposites prepared via rapid microwave-assisted synthesis method, Nanoscale research letters. 7 (2012) 541.

[158] A. Caires, D. Alves, C. Fantini, A. Ferlauto, L. Ladeira, One-pot in situ photochemical synthesis of graphene oxide/gold nanorod nanocomposites for surface-enhanced Raman spectroscopy, RSC Advances. 5 (2015) 46552-46557.

[159] S. Wu, Z. Yin, Q. He, G. Lu, Q. Yan, H. Zhang, Nucleation mechanism of electrochemical deposition of Cu on reduced graphene oxide electrodes, The Journal of Physical Chemistry C. 115 (2011) 15973-15979.

[160] Y. Qin, J. Li, Y. Kong, X. Li, Y. Tao, S. Li, *et al.*, In situ growth of Au nanocrystals on graphene oxide sheets, Nanoscale. 6 (2014) 1281-1285.

[161] P.A. Pandey, G.R. Bell, J.P. Rourke, A.M. Sanchez, M.D. Elkin, B.J. Hickey, *et al.*, Physical vapor deposition of metal nanoparticles on chemically modified graphene: observations on metal–graphene interactions, Small. 7 (2011) 3202-3210.

[162] M.R. Das, R.K. Sarma, R. Saikia, V.S. Kale, M.V. Shelke, P. Sengupta, Synthesis of silver nanoparticles in an aqueous suspension of graphene oxide sheets and its antimicrobial activity, Colloids and Surfaces B: Biointerfaces. 83 (2011) 16-22.

[163] M.R. Das, R.K. Sarma, S.C. Borah, R. Kumari, R. Saikia, A.B. Deshmukh, *et al.*, The synthesis of citrate-modified silver nanoparticles in an aqueous suspension of graphene oxide nanosheets and their antibacterial activity, Colloids and Surfaces B: Biointerfaces. 105 (2013) 128-136.

[164] J. Ma, J. Zhang, Z. Xiong, Y. Yong, X. Zhao, Preparation, characterization and antibacterial properties of silver-modified graphene oxide, Journal of Materials Chemistry. 21 (2011) 3350-3352.

[165] J. Tang, Q. Chen, L. Xu, S. Zhang, L. Feng, L. Cheng, *et al.*, Graphene oxide–silver nanocomposite as a highly effective antibacterial agent with species-specific mechanisms, ACS applied materials & interfaces. 5 (2013) 3867-3874.

[166] A. Fonseca de Faria, D.S.T. Martinez, S.M.M. Meira, A.C. Mazarin de Moraes, A. Brandelli, A.G. Souza Filho, *et al.*, Anti-adhesion and antibacterial activity of silver nanoparticles supported on graphene oxide sheets. Colloids Surf. , B. 113 (2014) 115-124.

[167] W. Yuan, Y. Gu, L. Li, Green synthesis of graphene/Ag nanocomposites, Appl. Surf. Sci. 261 (2012) 753-758.

[168] X. Cai, M. Lin, S. Tan, W. Mai, Y. Zhang, Z. Liang, *et al.*, The use of polyethyleneimine-modified reduced graphene oxide as a substrate for silver nanoparticles to produce a material with lower cytotoxicity and long-term antibacterial activity, Carbon. 50 (2012) 3407-3415.

[169] J. Shen, M. Shi, B. Yan, H. Ma, N. Li, M. Ye, One-pot hydrothermal synthesis of Ag-reduced graphene oxide composite with ionic liquid, Journal of Materials Chemistry. 21 (2011) 7795-7801.

[170] Y. Li, Y. Chen, N. Tai, Fast process to decorate silver nanoparticles on carbon nanomaterials for preparing high-Performance flexible transparent conductive films, Langmuir. 29 (2013) 8433-8439.

[171] M. Ayán-Varela, M.J. Fernández-Merino, J. Paredes, S. Villar-Rodil, C. Fernández-Sánchez, L. Guardia, *et al.*, Highly efficient silver-assisted reduction of graphene oxide dispersions at room temperature: mechanism, and catalytic and electrochemical performance of the resulting hybrids, Journal of Materials Chemistry A. 2 (2014) 7295-7305.

[172] S. Navalon, A. Dhakshinamoorthy, M. Alvaro, H. Garcia, Metal nanoparticles supported on two-dimensional graphenes as heterogeneous catalysts, Coord. Chem. Rev. 312 (2016) 99-148.

[173] J. Li, D. Kuang, Y. Feng, F. Zhang, Z. Xu, M. Liu, *et al.*, Green synthesis of silver nanoparticles–graphene oxide nanocomposite and its application in electrochemical sensing oftryptophan, Biosensors and Bioelectronics. 42 (2013) 198-206.

[174] F. Zeng, D. Xu, C. Zhan, C. Liang, W. Zhao, J. Zhang, *et al.*, Surfactant-free synthesis of graphene oxide coated silver nanoparticles for sers biosensing and intracellular drug delivery, ACS Applied Nano Materials. 1 (2018) 2748-2753.

[175] T.T. Vi Truong, K.S. Rajesh, S.J. Lue, B. Rout, C. Liu, C. Wong, *et al.*, The Preparation of Graphene Oxide-Silver Nanocomposites: the Effect of Silver Loads on Gram-Positive and Gram-Negative Antibacterial Activities, Nanomaterials (Basel). 8 (2018).

[176] X. Huang, Z. Yin, S. Wu, X. Qi, Q. He, Q. Zhang, *et al.*, Graphene-based materials: synthesis, characterization, properties, and applications, small. 7 (2011) 1876-1902.

[177] X. Li, Y. Xiao, A. Bergeret, M. Longerey, J. Che, Preparation of polylactide/graphene composites from liquid-phase exfoliated graphite sheets, Polymer Composites. 35 (2014) 396-403.

[178] R. Verdejo, M.M. Bernal, L.J. Romasanta, M.A. Lopez-Manchado, Graphene filled polymer nanocomposites, Journal of Materials Chemistry. 21 (2011) 3301-3310.

[179] K. Liu, L. Chen, Y. Chen, J. Wu, W. Zhang, F. Chen, *et al.*, Preparation of polyester/reduced graphene oxide composites via in situ melt polycondensation and simultaneous thermo-reduction of graphene oxide, Journal of materials chemistry. 21 (2011) 8612-8617.

[180] H. Tang, G.J. Ehlert, Y. Lin, H.A. Sodano, Highly efficient synthesis of graphene nanocomposites, Nano letters. 12 (2011) 84-90.

[181] D. Yan, H. Pang, L. Xu, Y. Bao, P. Ren, J. Lei, *et al.*, Electromagnetic interference shielding of segregated polymer composite with an ultralow loading of in situ thermally reduced graphene oxide, Nanotechnology. 25 (2014) 145705.

[182] S. Ye, D. Hu, Q. Zhang, J. Fan, B. Chen, J. Feng, Flow-Induced Enhancement of in Situ Thermal Reduction of Graphene Oxide during the Melt-Processing of Polymer Nanocomposites, The Journal of Physical Chemistry C. 118 (2014) 25718-25724.

[183] O.N. Ruiz, K.S. Fernando, B. Wang, N.A. Brown, P.G. Luo, N.D. McNamara, *et al.*, Graphene oxide: a nonspecific enhancer of cellular growth, ACS nano. 5 (2011) 8100-8107.

[184] H. Chen, D. Gao, B. Wang, R. Zhao, M. Guan, L. Zheng, *et al.*, Graphene oxide as an anaerobic membrane scaffold for the enhancement of B. adolescentis proliferation and antagonistic effects against pathogens E. coli and S. aureus, Nanotechnology. 25 (2014) 165101.

[185] S. Liu, T.H. Zeng, M. Hofmann, E. Burcombe, J. Wei, R. Jiang, *et al.*, Antibacterial activity of graphite, graphite oxide, graphene oxide, and reduced graphene oxide: Membrane and oxidative stress. ACS Nano. 5 (2011) 6971-6980.

[186] W. Hu, C. Peng, W. Luo, M. Lv, X. Li, D. Li, *et al.*, Graphene-Based Antibacterial Paper. ACS Nano. 4 (2010) 4317-4323.

[187] S. Liu, M. Hu, T.H. Zeng, R. Wu, R. Jiang, J. Wei, *et al.*, Lateral Dimension-Dependent Antibacterial Activity of Graphene Oxide Sheets. Langmuir. 28 (2012) 12364-12372.

[188] F. Perreault, A. Fonseca de Faria, S. Nejati, M. Elimelech, Antimicrobial Properties of Graphene Oxide Nanosheets: Why Size Matters. ACS Nano. 9 (2015) 7226-7236.

[189] I. Barbolina, C. Woods, N. Lozano, K. Kostarelos, K. Novoselov, I. Roberts, Purity of graphene oxide determines its antibacterial activity, 2D Materials. 3 (2016) 025025.

[190] A. áde Leon, On the antibacterial mechanism of graphene oxide (GO) Langmuir–Blodgett films, Chemical communications. 51 (2015) 2886-2889.

[191] T.H. Nguyen, M. Lin, A. Mustapha, Toxicity of graphene oxide on intestinal bacteria and Caco-2 cells, J. Food Prot. 78 (2015) 996-1002.

[192] C. Li, X. Wang, F. Chen, C. Zhang, X. Zhi, K. Wang, et al., The antifungal activity of graphene oxide–silver nanocomposites, Biomaterials. 34 (2013) 3882-3890.

[193] R.F. Al-Thani, N.K. Patan, M.A. Al-Maadeed, Graphene oxide as antimicrobial against two gram-positive and two gram-negative bacteria in addition to one fungus, (2014).

[194] X. Zou, L. Zhang, Z. Wang, Y. Luo, Mechanisms of the Antimicrobial Activities of Graphene Materials. J. Am. Chem. Soc. 138 (2016) 2064-2077.

[195] O. Akhavan, E. Ghaderi, A. Esfandiar, Wrapping bacteria by graphene nanosheets for isolation from environment, reactivation by sonication, and inactivation by near-infrared irradiation, The Journal of Physical Chemistry B. 115 (2011) 6279-6288.

[196] D.D. Evanoff Jr, G. Chumanov, Synthesis and optical properties of silver nanoparticles and arrays, ChemPhysChem. 6 (2005) 1221-1231.

[197] A. Gautam, S. Ram, Preparation and thermomechanical properties of Ag-PVA nanocomposite films, Mater. Chem. Phys. 119 (2010) 266-271.

[198] K. Krishnamoorthy, M. Veerapandian, K. Yun, S. Kim, The chemical and structural analysis of graphene oxide with different degrees of oxidation, Carbon. 53 (2013) 38-49.

[199] M. Pimenta, G. Dresselhaus, M.S. Dresselhaus, L. Cancado, A. Jorio, R. Saito, Studying disorder in graphite-based systems by Raman spectroscopy, Physical chemistry chemical physics. 9 (2007) 1276-1290.

[200] A.C. Ferrari, J. Robertson, Interpretation of Raman spectra of disordered and amorphous carbon, Physical review B. 61 (2000) 14095.

[201] F. Tuinstra, J.L. Koenig, Raman spectrum of graphite, J. Chem. Phys. 53 (1970) 1126-1130.

[202] I. Childres, L.A. Jauregui, W. Park, H. Cao, Y.P. Chen, Raman spectroscopy of graphene and related materials, New developments in photon and materials research. 1 (2013).

[203] J. Chen, B. Yao, C. Li, G. Shi, An improved Hummers method for eco-friendly synthesis of graphene oxide, Carbon. 64 (2013) 225-229.

[204] J. Zhao, L. Liu, F. Li, Graphene oxide: physics and applications, Springer 2015.

[205] K. Hsu, D. Chen, Green synthesis and synergistic catalytic effect ofAg/reduced graphene oxide nanocomposite, Nanoscale research letters. 9 (2014) 484.

[206] K. Hsu, D. Chen, Microwave-assisted green synthesis of Ag/reduced graphene oxide nanocomposite as a surface-enhanced Raman scattering substrate with high uniformity, Nanoscale research letters. 9 (2014) 193.

[207] D. Zhan, Z. Ni, W. Chen, L. Sun, Z. Luo, L. Lai, *et al.*, Electronic structure of graphite oxide and thermally reduced graphite oxide, Carbon. 49 (2011) 1362-1366.

[208] A. Kaniyoor, S. Ramaprabhu, A Raman spectroscopic investigation of graphite oxide derived graphene, Aip Advances. 2 (2012) 032183.

[209] A. Ganguly, S. Sharma, P. Papakonstantinou, J. Hamilton, Probing the thermal deoxygenation of graphene oxide using high-resolution in situ X-ray-based spectroscopies, The Journal of Physical Chemistry C. 115 (2011) 17009-17019.

[210] S. Park, J. An, J.R. Potts, A. Velamakanni, S. Murali, R.S. Ruoff, Hydrazine-reduction of graphite-and graphene oxide, Carbon. 49 (2011) 3019-3023.

[211] T.T. Baby, S. Ramaprabhu, Synthesis and nanofluid application of silver nanoparticles decorated graphene, Journal of Materials Chemistry. 21 (2011) 9702-9709.

[212] H.C. Schniepp, J. Li, M.J. McAllister, H. Sai, M. Herrera-Alonso, D.H. Adamson, *et al.*, Functionalized single graphene sheets derived from splitting graphite oxide, The Journal of Physical Chemistry B. 110 (2006) 8535-8539.

[213] S. Stankovich, D.A. Dikin, G.H. Dommett, K.M. Kohlhaas, E.J. Zimney, E.A. Stach, *et al.*, Graphene-based composite materials, Nature. 442 (2006) 282.

[214] S. Zu, B. Han, Aqueous dispersion of graphene sheets stabilized by pluronic copolymers: formation of supramolecular hydrogel, The Journal of Physical Chemistry C. 113 (2009) 13651-13657.

[215] S.P. Dubey, M. Lahtinen, H. Särkkä, M. Sillanpää, Bioprospective of Sorbus aucuparia leaf extract in development of silver and gold nanocolloids, Colloids and Surfaces B: Biointerfaces. 80 (2010) 26-33.

[216] L. Huang, H. Yang, Y. Zhang, W. Xiao, Study on synthesis and antibacterial properties of Ag NPs/GO nanocomposites. J. Nanomater. (2016) 5685967/1-5685967/9.

[217] J. Tian, S. Liu, Y. Zhang, H. Li, L. Wang, Y. Luo, *et al.*, Environmentally friendly, one-pot synthesis of Ag nanoparticle-decorated reduced graphene oxide composites and their application to photocurrent generation, Inorg. Chem. 51 (2012) 4742-4746.

[218] X. Jiang, W. Chen, C. Chen, S. Xiong, A. Yu, Role of temperature in the growth of silver nanoparticles through a synergetic reduction approach, Nanoscale Res Lett. 6 (2011) 32.

[219] H. Liu, H. Zhang, J. Wang, J. Wei, Effect of temperature on the size of biosynthesized silver nanoparticle: deep insight into microscopic kinetics analysis, Arabian Journal of Chemistry. (2017).

[220] X. Tang, W. Li, Z. Yu, M.A. Rafiee, J. Rafiee, F. Yavari, *et al.*, Enhanced thermal stability in graphene oxide covalently functionalized with 2-amino-4,6-didodecylamino-1,3,5-triazine, Carbon. 49 (2011) 1258-1265.

[221] H. Yang, F. Li, C. Shan, D. Han, Q. Zhang, L. Niu, *et al.*, Covalent functionalization of chemically converted graphene sheets via silane and its reinforcement, Journal of Materials Chemistry. 19 (2009) 4632-4638.

[222] M. Haque, M. Sartelli, J. McKimm, M. Abu Bakar, Health care-associated infections - an overview, Infect. Drug Resist. 11 (2018) 2321-2333.

[223] G. Quindós, C. Marcos-Arias, R. San-Millán, E. Mateo, E. Eraso, The continuous changes in the aetiology and epidemiology of invasive candidiasis: from familiar Candida albicans to multiresistant Candida auris, International Microbiology. 21 (2018) 107-119.

[224] A. Kramer, I. Schwebke, G. Kampf, How long do nosocomial pathogens persist on inanimate surfaces? A systematic review, BMC infectious diseases. 6 (2006) 130.

[225] K.B. Laupland, O. Lyytikäinen, M. Sgaard, K. Kennedy, J.D. Knudsen, C. Ostergaard, *et al.*, The changing epidemiology of Staphylococcus aureus bloodstream infection: a multinational population-based surveillance study, Clinical microbiology and infection. 19 (2013) 465-471.

[226] J.T. Spadafino, B. Cohen, J. Liu, E. Larson, Temporal trends and risk factors for extended-spectrum beta-lactamase-producing Escherichia coli in adults with catheter-associated urinary tract infections, Antimicrobial resistance and infection control. 3 (2014) 39.

[227] H. Fazeli, R. Akbari, S. Moghim, T. Narimani, M.R. Arabestani, A.R. Ghoddousi, Pseudomonas aeruginosa infections in patients, hospital means, and personnel's specimens, J. Res. Med. Sci. 17 (2012) 332-337.

[228] H. Wisplinghoff, T. Bischoff, S.M. Tallent, H. Seifert, R.P. Wenzel, M.B. Edmond, Nosocomial bloodstream infections in US hospitals: analysis of 24,179 cases from a prospective nationwide surveillance study, Clinical infectious diseases. 39 (2004) 309-317.

[229] S. Gurunathan, J.W. Han, A.A. Dayem, V. Eppakayala, J.H. Kim, Oxidative stress-mediated antibacterial activity of graphene oxide and reduced graphene oxide in Pseudomonas aeruginosa, Int. J. Nanomedicine. 7 (2012) 5901-5914.

[230] L. Hui, J. Piao, J. Auletta, K. Hu, Y. Zhu, T. Meyer, *et al.*, Availability of the basal planes of graphene oxide determines whether it is antibacterial, ACS applied materials & interfaces. 6 (2014) 13183-13190.

[231] A. Gusev, O. Zakharova, D.S. Muratov, N.S. Vorobeva, M. Sarker, I. Rybkin, *et al.*, Medium-Dependent Antibacterial Properties and Bacterial Filtration Ability of Reduced Graphene Oxide, Nanomaterials. 9 (2019) 1454.

[232] K. Theophel, V.J. Schacht, M. Schlüter, S. Schnell, C. Stingu, R. Schaumann, *et al.*, The importance of growth kinetic analysis in determining bacterial susceptibility against antibiotics and silver nanoparticles, Frontiers in microbiology. 5 (2014) 544.

[233] J. Cui, Y. Yang, M. Zheng, Y. Liu, Y. Xiao, B. Lei, *et al.*, Facile fabrication of graphene oxide loaded with silver nanoparticles as antifungal materials, Materials Research Express. 1 (2014) 045007.

[234] S. Jaworski, M. Wierzbicki, E. Sawosz, A. Jung, G. Gielerak, J. Biernat, *et al.*, Graphene oxide-based nanocomposites decorated with silver nanoparticles as an antibacterial agent, Nanoscale research letters. 13 (2018) 116.

[235] W. Shao, X. Liu, H. Min, G. Dong, Q. Feng, S. Zuo, Preparation, characterization, and antibacterial activity of silver nanoparticle-decorated graphene oxide nanocomposite, ACS applied materials & interfaces. 7 (2015) 6966-6973.

[236] J. Mohammadnejad, F. Yazdian, M. Omidi, A.D. Rostami, B. Rasekh, A. Fathinia, Graphene oxide/silver nanohybrid: Optimization, antibacterial activity and its impregnation on bacterial cellulose as a potential wound dressing based on GO-Ag nanocomposite-coated BC, Engineering in Life Sciences. 18 (2018) 298-307.

[237] S. Liao, Y. Zhang, X. Pan, F. Zhu, C. Jiang, Q. Liu, *et al.*, Antibacterial activity and mechanism of silver nanoparticles against multidrug-resistant Pseudomonas aeruginosa, International journal of nanomedicine. 14 (2019) 1469.

[238] A. Panáček, L. Kvitek, R. Prucek, M. Kolář, R. Večeřová, N. Pizúrová, *et al.*, Silver colloid nanoparticles: synthesis, characterization, and their antibacterial activity, The Journal of Physical Chemistry B. 110 (2006) 16248-16253.

[239] M.J. Fernández-Merino, L. Guardia, J.I. Paredes, S. Villar-Rodil, A. Martínez-Alonso, J.M. Tascón, Developing green photochemical approaches towards the synthesis of carbon nanofiber-and graphene-supported silver nanoparticles and their use in the catalytic reduction of 4-nitrophenol, RSC advances. 3 (2013) 18323-18331.

[240] S. Agnihotri, S. Mukherji, S. Mukherji, Size-controlled silver nanoparticles synthesized over the range 5–100 nm using the same protocol and their antibacterial efficacy, Rsc Advances. 4 (2014) 3974-3983.

[241] C. Baker, A. Pradhan, L. Pakstis, D.J. Pochan, S.I. Shah, Synthesis and antibacterial properties of silver nanoparticles, Journal of nanoscience and nanotechnology. 5 (2005) 244-249.

[242] G.A. Sotiriou, S.E. Pratsinis, Antibacterial activity of nanosilver ions and particles, Environ. Sci. Technol. 44 (2010) 5649-5654.

[243] A. Burduşel, O. Gherasim, A.M. Grumezescu, L. Mogoantă, A. Ficai, E. Andronescu, Biomedical applications of silver nanoparticles: An up-to-date overview, Nanomaterials. 8 (2018) 681.

[244] de Luna, Luis Augusto Visani, de Moraes, Ana Carolina Mazarin, S.R. Consonni, C.D. Pereira, S. Cadore, S. Giorgio, *et al.*, Comparative in vitro toxicity of a graphene oxide-silver nanocomposite and the pristine counterparts toward macrophages, Journal of nanobiotechnology. 14 (2016) 12.

[245] J.W. Han, S. Gurunathan, J. Jeong, Y. Choi, D. Kwon, J. Park, *et al.*, Oxidative stress mediated cytotoxicity of biologically synthesized silver nanoparticles in human lung epithelial adenocarcinoma cell line, Nanoscale research letters. 9 (2014) 459.

[246] T. Kim, M. Kim, H. Park, U.S. Shin, M. Gong, H. Kim, Size-dependent cellular toxicity of silver nanoparticles, Journal of biomedical materials research Part A. 100 (2012) 1033-1043.

[247] K.C. Nguyen, V.L. Seligy, A. Massarsky, T.W. Moon, P. Rippstein, J. Tan, *et al.*, Comparison of toxicity of uncoated and coated silver nanoparticles, 429 (2013) 012025.

[248] S.J. Cameron, F. Hosseinian, W.G. Willmore, A current overview of the biological and cellular effects of nanosilver, International journal of molecular sciences. 19 (2018) 2030.

[249] V. De Matteis, M. Cascione, C.C. Toma, S. Leporatti, Silver nanoparticles: synthetic routes, in vitro toxicity and theranostic applications for cancer disease, Nanomaterials. 8 (2018) 319.

[250] T. Kavinkumar, K. Varunkumar, V. Ravikumar, S. Manivannan, Anticancer activity of graphene oxide-reduced graphene oxide-silver nanoparticle composites, J. Colloid Interface Sci. 505 (2017) 1125-1133.

CHAPTER 3

CHITOSAN/GRAPHENE NANOCOMPOSITES

The previous chapter is based on the synthesis and characterization of different graphene-based materials. The optimal ratio of reagents and the ideal reaction conditions were studied in order to achieve high stability and antimicrobial properties in the filler. In this connection, this chapter is focused on the intercalation or exfoliation of GO and GS fillers in chitosan polymer matrix in order to prepare different nanocomposites. Unplasticized and glycerol plasticized chitosan/graphene oxide (CS/GO) nanocomposites with different GO loadings have been prepared by solution casting. Likewise, unplasticized and glycerol plasticized chitosan/graphene (CS/GS) nanocomposites have been synthesized via in situ chemical reduction of GO with L-ascorbic acid as reductant. The combined effect of the fillers and glycerol on structural, thermal and mechanical properties of nanocomposite films was studied, as well as the change in permeability and water absorption capacity. Electrical properties of CS/GS nanocomposites were evaluated. Furthermore, the storage effect on antimicrobial activity of CS against Escherichia Coli was also analyzed. This study reveals how chitosan and graphene-based nanocomposites properties can be tailored by controlling filler and plasticizer content.

Most of the results presented in this chapter have been previously published in two different publications: Journal of Applied Polymer Science (2017) and International journal of biological (2018). Additionally, part of the work discussed in this chapter has also been presented at 3rd International Conference on Bio-based Polymers and Composites in Szeged (Hungary), at 5th International Symposium "Frontiers in Polymer Science" in Seville (Spain) and at 10th ECNP International Conference on Nanostructured Polymers and Nanocomposites in San Sebastian (Spain).

INDEX

3.1. Introduction

The increased use of petroleum-based polymers has led to ecological problems due to their non-biodegradability. This has initiated the need for biodegradable polymers that are compatible with the ecosystem. Among these polymers, chitin (CT) and chitosan (CS) have attracted the attention of both scientists and industries, not only because of their biodegradability, but also because of their wide availability in nature, biocompatibility, bioactivity, non-toxicity and antimicrobial activity. Both polymers have potential applications in biomedicine, agriculture, paper manufacturing and the food and the textile industries [1-5].

Historically, chitin was the first polysaccharide isolated from the cell walls of mushrooms in 1811 by Henry Braconnot, who named it as "fungine". Afterwards, in 1823, Odier isolated an insoluble compound from beetles in alkaline solutions that was called chitin, almost three decades before the isolation of cellulose. In 1859, Prof. C. Rouget subjected chitin to alkali treatment, which resulted in a substance that could, unlike chitin itself, be dissolved in acids [6]. Later, in 1894 Hoppe-Seiler gave the term "chitosan" to deacetylated chitin [7]. While chitin remained an unusual natural resource for a long time, the interest in this polymer and its derivatives, such as chitosan and chitooligosaccharides (COS), has increased in recent years because of its versatile biological, chemical and physical properties [8,9].

Chitin is a linear polysaccharide composed of N-acetyl-D-glucosamine units linked by β-(1$\rightarrow$4), in the same way as glucose units compose cellulose (Figure 3.1). This biopolymer is synthesized by an enormous number of living organisms and, in terms of abundance, it is estimated that around 100 billion tons are produced in nature each year, being therefore, one of the most abundant polymers in the world [10]. Chitin is white-yellowish, rigid, linear polymer and it occurs in nature as ordered crystalline microfibrils forming structural components in the exoskeleton of arthropods or in the cell wall of fungi and yeasts. There are two allomorphic forms of chitin, known as α-chitin and β-chitin, which differ in packing and polarities of adjacent chains in successive sheets.
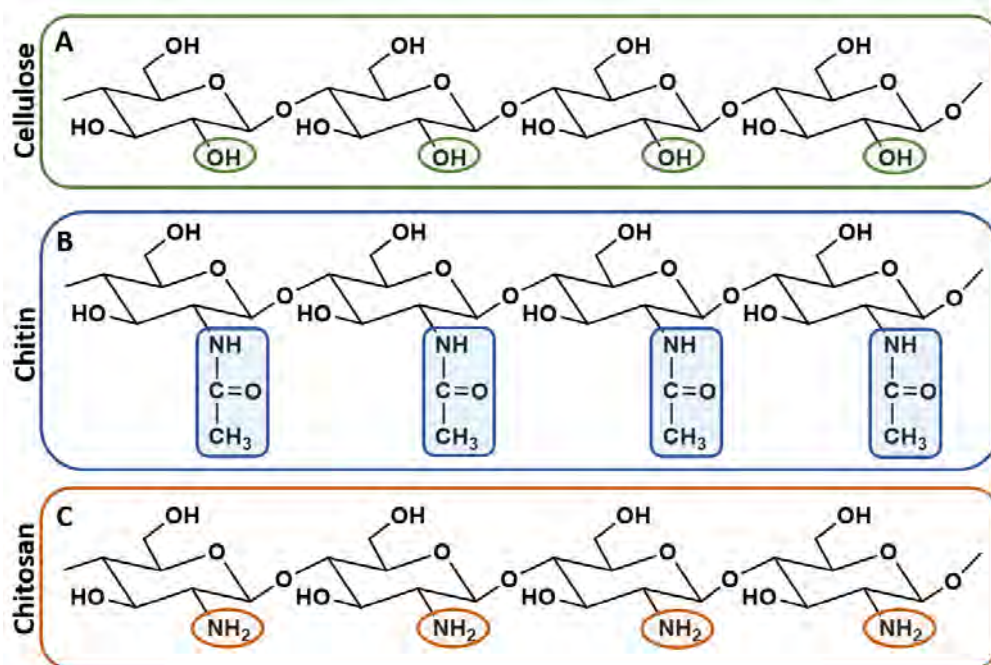
Figure 3.1. Molecular structure of (A) cellulose, (B) chitin and (C) chitosan.

The most important derivative of chitin is chitosan (Figure 3.1C). Although it has been found in some types of fungi, chitosan is mostly obtained by (partial) deacetylation of chitin under alkaline conditions or by enzymatic hydrolysis in the presence of chitin deacetylase. The deacetylation process can be performed at room temperature (homogeneous deacetylation) or at high temperature (heterogeneous deacetylation) depending on the desired properties for the final product, being the latter process the preferred one for industrial purposes. Chitosan is one of the few natural cationic polysaccharides, which is a peculiar feature, since in an acidic environment most polysaccharides are usually neutral or negatively charged. It is a biodegradable, non-toxic and biocompatible polymer with good film-forming, adhesive and antimicrobial properties, making it a versatile material with great potential for food packaging [11]. CS is insoluble in either organic solvents or water, but almost all aqueous acids dissolve it readily. The primary $-NH_2$ groups in chitosan (Figure 3.1) are very useful in pharmaceutical applications in comparison to other natural polymers.

3.1.1. Sources of chitin and chitosan

The production of chitin *via* chemical synthesis is not technically possible, although small quantities of chitooligomers can be reached by appropriate procedures. Likewise, the biotechnological production of chitin is currently not economically attractive. Therefore, the primary sources of chitin and chitosan are aquatic and terrestrial organisms and some microorganisms.

Chitin is the main structural polysaccharide found in many invertebrate animals. Insects, mushrooms and crustaceans are probably the best-known sources [12]. Despite the wide distribution of chitin in nature, from a practical viewpoint, the shells of marine crustaceans such as crabs and shrimps are appropriate since they are available as waste from the seafood processing industry. The main components of crustacean shells are chitin (15–40%), protein (20–40%), calcium and magnesium carbonate (20–50%), together with other minor constituents, such as astaxanthin, lipids and other minerals. This polysaccharide, in smaller quantities, exists in numerous other species. It is an important component of the spikes of marine diatoms, of the skeletal tissue of squid), and it is also found in many lower marine plants and animals and in terrestrial plants.

Chitosan exists naturally in some fungi, but in a lower proportion than chitin, so it is necessary to undergo a deacetylation process to obtain it. The most common production process is the thermochemical transformation of chitin extracted from exoskeletons of discarded crustaceans. However, chitosan can be found naturally in the cell walls of *Zygomycetes* fungi, also in *Basidiomycetes* and in some *Ascomycetes*, in algae, cuticles of insects and in some arachnids [13].

Chitin and chitosan extraction techniques found in the literature are very varied as they depend largely on the characteristics of the source, in particular the composition of the starting material which varies considerably from one species to another. Most of the techniques developed are based on chemical processes of hydrolysis and the removal of inorganic matter. Some include a discoloration step of the extracted chitin by solvent extraction or oxidation of the remaining pigments. The procedure for the extraction of chitin and chitosan from the raw materials is illustrated in Figure 3.2.

In general, the protocol includes demineralization, deproteinization, discoloration and deacetylation steps which can be carried out by chemical or biological methods [14-19]. The conversion of chitin to chitosan can be achieved either by enzymatic or chemical deacetylation [20-22]. Due to economic issues and the feasibility of mass production, chemical deacetylation is generally used in commercial preparation. This process consists of the hydrolysis of acetamide groups in a strongly alkaline medium, at high temperatures. Regularly, the reaction is carried out in a heterogeneous phase using concentrated solutions of NaOH or KOH (30-50%) at 100 °C, preferably in an inert atmosphere or in the presence of reducing agents such as $NaBH_4$ or Na_2SO_3 to avoid depolymerization. Prolonged treatments usually cause degradation of the polymer without resulting in a significant increase in the degree of deacetylation.
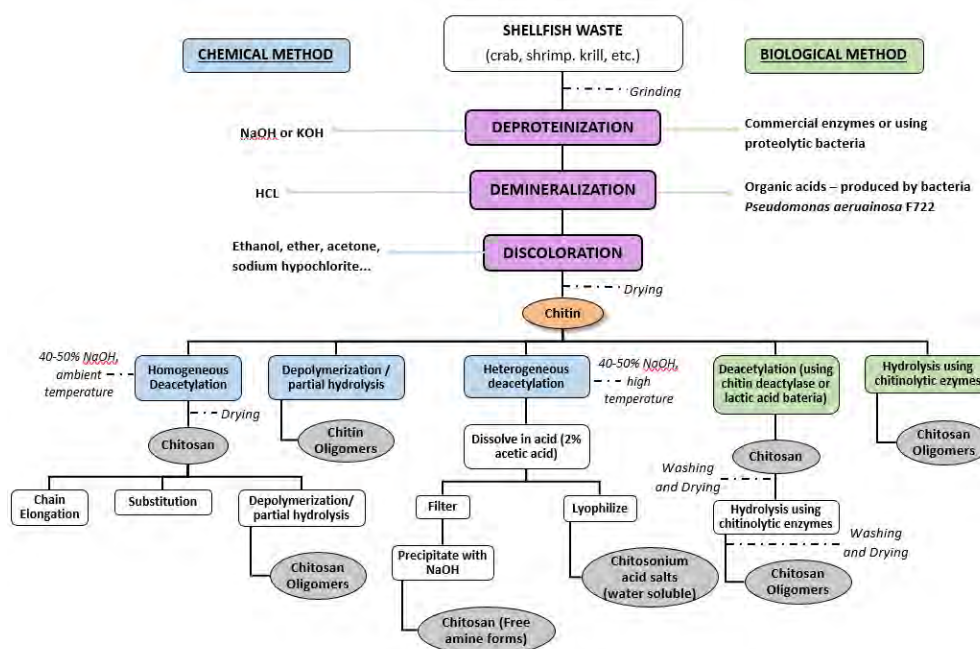
Figure 3.2. Chemical and biological extraction of chitin and chitosan from marine sources.

3.1.2. Physical, chemical and biological properties

Native chitin (β-(1→4)-poly-N-acetyl-D-glucosamine) samples may contain different amounts of N-acetyl groups, depending on their origin and isolation procedure [23]. In general, the degree of N-acetylation of native chitin is in the range of 0.9-0.95. Similar to cellulose, chitin is characterized by an ordered fibrillar structure, a developed system of intra- and intermolecular hydrogen bonds, a high degree of crystallinity, and polymorphism [24,25].

Chitosan (CS) is a heteropolysaccharide composed of two repeating units, D-glucosamine (deacetylated unit) and N-acetyl-D-glucosamine (acetylated unit) randomly distributed along the polymer chain and linked by β-(1→4)-bonds. Although, a sharp nomenclature border does not exist between chitin and chitosan, the term "chitosan" can also be found as copolymer of 2-amino-2-deoxy-D-glucopyranose and 2-acetamido-2-deoxy-D-glucopyranose, where the degree of deacetylation is usually more than 60% (Figure 3.3). It should be noted that chitin deacetylation is rarely complete, so it still contains acetamide groups to some extent. Heterogeneous conditions during deacetylation provide a block-wise distribution [26], whereas under homogeneous conditions, random distribution of acetyl groups appears in CS [27]. In the solid state, chitosan is a semicrystalline polymer which exhibits polymorphism [3].
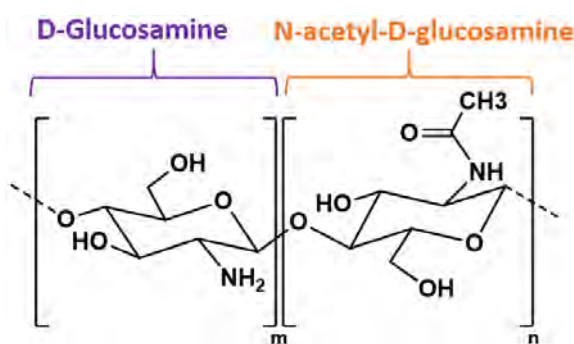
Figure 3.3. Chemical structure of chitosan composed of β-(1 → 4)-linked 2-amino-2-deoxy-D-glucopyranose (m) and 2-acetamido-2-deoxy-D-glucopyranose (n).

At molecular level, chitin and chitosan appear similar as both possess reactive hydroxyl and amino groups. However, chitosan, being less crystalline, is more accessible to reagents. These two biopolymers after heating, decompose

before melting, so these polymers do not have melting points. Probably the most striking difference between chitin and chitosan lies in their solubility. While there are few solvents for chitin, almost all aqueous acids easily dissolve chitosan, being formic acid and acetic acid the most commonly used [10]. CS forms salts with organic and inorganic acids, such as chitosan acetate or chitosan lactate [28].

Chitosan is a basic polysaccharide, while most of the natural polysaccharides such as pectin, dextrin, agar, agarose, carragenas and cellulose are of an acidic nature. Owing to the presence of one -NH$_2$ and two -OH reactive groups, chitosan exhibits marvelous chemical as well as biological properties. The active primary amino group provides a specific platform for the fixation of side groups under mild reaction conditions. Therefore, chitosan is an ideal candidate for bio-fabrication [29]. This polymer is inert in the intestinal tract of mammals and biodegradable due to the presence of chitinases widely distributed in nature, in bacteria, fungi and plants, as well as in the digestive system of various animals. The products of the degradation are non-toxic.

The physicochemical and biological properties of CS differ significantly depending on the production process, conditions and the natural source. Concretely, the important chemical characteristics that influence the properties, and hence the applications of chitosan are molecular weight, solubility, degree of deacetylation (DD), charge and viscosity. The techniques for studying some of the above mentioned properties are summarized in Table 3.1.

Commercially, the average molecular weight (M_w) of chitosan may range from 3.8 to 2000 kDa depending on the source and the method of preparation [30,31]. In some chitosan derivatives such as chitosan oligosaccharides, the M_w can be as low as 1.5 kDa. Due to this extensive range of molecular weight, chitosan can be categorized into low molecular weight chitosan of 3.8-20 kDa, medium molecular weight chitosan of ≈100 kDa and high molecular weight chitosan of higher than 300 kDa. The average molecular weight can be obtained by steric exclusion chromatography equipped with a viscometer and light scattering detector [32] or by matrix-assisted laser desorption/ionization-mass spectrometer.

Table 3.1. Physicochemical characteristics of chitosan and their methods of determination.

Physicochemical Properties	Determination Methods
Molecular weight	- Viscometry - Gel permeation chromatography - Light scattering - High performance liquid chromatography - Matrix-assisted laser desorption/ionization – mass spectrometer.
Degree of deacetylation	- Infrared spectroscopy - Ultra violet spectrophotometry - Nuclear magnetic resonance spectroscopy (^{1}H-NMR and ^{13}C-NMR) - Conductometric titration - Potentiometric titration - Enzymatic degradation - Differential scanning calorimetry
Crystallinity	- X-ray diffraction

The pH considerably alters the state of charge and properties of the chitosan. At low pH, the amino groups present in the chemical structure are protonated and positively charged, causing this polymer to become a water-soluble cationic polyelectrolyte. However, at high pH, the amino groups are deprotonated and the polymer loses its charge and becomes insoluble (Figure 3.4). It is important to mention that chitosan pKa is almost neutral, and the soluble-insoluble transition occurs at pHs between 6 and 6.5, which is a particularly suitable range for biological applications. At a high pH, the electrostatic repulsions of the chitosan are reduced, which allows the formation of polymer associations (e.g. liquid crystal domains or net bonds) that can give rise to fibers, films or hydrogels, depending on the conditions used to initiate the soluble-insoluble transition. CS solubility is also dependent on the distribution pattern of acetyl group along the main chain and molecular weight of polymer. Formic acid is considered to be the best solvent for chitosan and solutions are acquired in

aqueous systems with 0.2–100% of formic acid [29]. The most widespread solvent is 1% acetic acid (as a reference) at a pH near 4. In addition, chitosan is soluble in 1% hydrochloric acid and dilute nitric acid, but it is insoluble in sulfuric and phosphoric acids. Sulfuric acid would react with chitosan to form chitosan sulfate, which is a white crystalline solid.
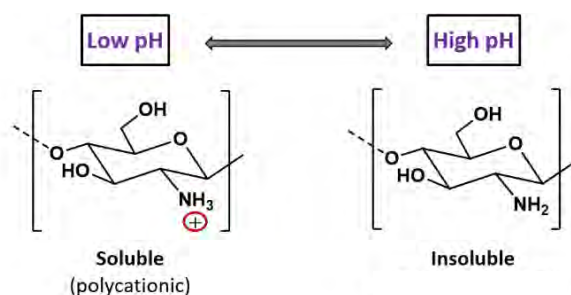
Figure 3.4. Chitosan protonated and deprotonated molecular structure.

The degree of deacetylation (DD) is one of the most important parameters that affects the physical and chemical properties of chitin and chitosan. Samples of these polymers commonly require the determination of the ratio of 2-acetamido-2-deoxy-D-glucopyranose to 2-amino-2-deoxy-D-glucopyranose structural units. Different methods of analysis have been suggested to measure this feature, such as elemental analysis, hydrolysis of acetamide groups, free amino group titration [33], infrared spectroscopy (IR) [34,35], UV spectroscopy [36], circular dichroism measurements, ^{1}H-NMR spectroscopy [37], ^{13}C solid state NMR [38,39], enzymatic degradation [40] and pyrolysis. Currently, ^{1}H-NMR seems to be the most suitable technique for obtaining the correct acetylation degree (DA) for soluble samples and ^{13}C-NMR to establish the distribution of acetyl groups along the chitosan chains [41,42]. The degree of deacetylation of commercial chitosan generally ranges from 66 to 95%.

The viscosity of chitosan is largely affected by chitosan M_w, ionic strength, pH and temperature of solution. Low molecular weight chitosan oligomers provide a low solution viscosity. Under a similar pH environment, the viscosity of the solution of chitosan varied with the use of different organic acids [43]. Chitosan solutions exhibit pseudo-plastic behavior since their viscosity decreases by increasing shear rate.

3.1.2.1. Antimicrobial activity of chitosan

Chitin and chitosan have excellent and beneficial properties such as biocompatibility, biodegradability and non-toxicity, as well as interesting biological activity, qualities that are very beneficial for their application in the biomedical, biotechnological, pharmaceutical and food fields [44-46]. The biological activities include antimicrobial, antioxidant and anti-tumor activities, which are relevant for applications in the field of packaging, food preservation and health. The good film-forming properties and antimicrobial activity make chitosan a good substitute for the use of chemical preservatives.

The antimicrobial activity of chitin, chitosan and their derivatives have been widely analyzed since 1980s, either in solution, film or composite form against different microorganisms (bacteria, yeast and fungi). Many studies have demonstrated the antimicrobial activity of chitosan, but the mechanism by which it acts as an antimicrobial compound is not fully clarified. Three main hypotheses have been proposed in the literature [47-53].

The first, and most accepted mechanism, states that the polycationic nature of chitosan and the charge of the microbial cell surface are the reason for the antimicrobial activity. The electrostatic interaction between the protonated groups of CS ($-NH_3^+$) and the negative charge of the bacterial membranes interferes with bacterial metabolism [50]. Specifically, this interaction involves changes in membrane wall permeability causing internal osmotic imbalances that inhibit the growth of microorganisms. Additionally, peptidoglycans of the bacterial cell wall can be hydrolyzed resulting in leakage of intracellular material (potassium ions, proteins, nucleic acids, etc.). Both alterations cause the death of the microorganism. This hypothesis assumes that the greater the number of cationic aminos, the greater the antimicrobial activity [54]. However, it should be noted that the amount of cationic CS available to bind to a charged bacterial surface seems to be reduced as the concentration of chitosan increases [55]. This is because in the presence of a greater number of charged sites, the chains tend to form clusters by aggregation of molecules while they are still in solution [56].

The second mechanism states that chitosan inhibits the action of several enzymes, as it interferes with protein synthesis. It is supposed that low molecular

weight chitosan is able to enter the cell nucleus and interact with DNA, interfere with messenger RNA (mRNA) synthesis, and thus affect protein synthesis [51].

The third mechanism suggests that chitosan acts as a chelating agent, forming complexes with traces of metals essential for cell metabolism, since it has been shown that chitosan attracts certain metals [52] that inhibit microbial growth. Generally, this hypothesis would be more consistent at high pH because CS positive ions are restricted, since the amino groups are unprotonated and the electron pair on the amino nitrogen would be available for donation to metal ions.

These three mechanisms have been proposed for chitosan in solution and in direct contact with the microorganism. However, the antimicrobial mechanism of action of chitosan film has not been completely elucidated. Among the physical properties mentioned above, molecular weight (M_w) [57,58] and degree of deacetylation (DD) [59] are the characteristics that significantly influence the antimicrobial activity of chitosan.

3.1.3. Chitin and chitosan applications

Due to its multifunctional properties mentioned throughout this chapter, chitin and chitosan find applications in many fields, such as food preservation [60,61], drug delivery and antimicrobial agents in biomedical field [62,63], in the cosmetics industry [3,8], in wastewater treatment [64,65], chemical industries [66], in tissue engineering [67-69] and biotechnology [70].

Biomedical and pharmaceutical applications

Chitosan and its derivatives are widely used in the field of biomedicine and pharmacology. In particular, their biodegradability and non-toxicity make them ideal for applications such as surgical sutures, biodegradable bandages and sponges, matrices (in microspheres, microcapsules, membranes and compressed tablets) for drug delivery systems [71]. CS improves drug absorption, stabilizes the ingredients and prolongs the duration of activity, in addition to improving therapeutic efficiency [72,73]. These natural polymers have also been used in various medical devices and as orthopaedic and dental materials.

Chitosan simultaneously with chitin has been employed in the treatment of wounds, ulcers and burns, because of its haemostatic characteristics and its accelerating effect on wound healing. Chitosan activates the formation of clots in contact with the blood, due to the interaction of the amino groups with the acid groups of the blood cells. In addition, it has been reported that CS is highly thrombogenic [74] because it has the ability to activate both complement [75] and blood coagulation systems [76].

Both natural polymers are promising materials to support tissue regeneration and restoration, including their use as scaffolds in tissue engineering [67-69] due to their cell affinity, low immunogenic activity, and controlled biodegradability [63]. Chitosan serves as a potential material for nerve regeneration, cancer treatment, artificial kidney membrane, bioartificial liver (BAL), artificial skin, artificial tendon, articular cartilage, blood anticoagulation, bone damage and antimicrobial applications.

Agricultural applications and Packaging material

In recent years, increasing attention has been given to the development of films with improve food safety and shelf life. In the field of food preservation, chitosan and its derivatives have proven to play an important role in view of their antimicrobial activity and biodegradability. In agriculture, these biopolymers provide: a) plant protection against plagues and diseases, (b) enhancing antagonist microorganism action and biological control, (c) support of beneficial plant-microorganism symbiotic relationships and (d) plant growth regulation and development. Chitin and chitosan have fungicidal activity against many phytopathogenic (an organism parasitic on a plant host) fungi. This property and its outstanding film-creating aptitude have been exploited in the post-harvest preservation of fruits and vegetables to enhance shelf life [77,78]. Chitosan causes desirable changes in the metabolism of plants and fruits. The incorporation of chitosan biomass into soil stimulates natural microbes that provide protection to certain crops. This brings about improved germination and higher crop yields.

There are many studies in this field and all agree that chitosan can be defined as a versatile and promising biodegradable and antimicrobial food packaging material. Chitosan films show resistance to fat diffusion and selective permeability to gases [79], but low resistance to the transmission of water and

water vapor due to its hydrophilic character [80]. That is why chitosan tends to be used in polymer blends, biocomposites or multilayer systems. In these situations, this polymer does not migrate out of the protective film [81].

Cosmetics

A natural amino-polysaccharide such as chitosan can be included in the class of hydrocolloids. However, unlike most other hydrocolloids which are polyanions, chitosan is the only natural cationic that becomes viscous once neutralized with acid. This behavior enables its interaction with common skin covers and hair. Chitosan is compatible with many biologically active components incorporated into cosmetic product compositions [82]. Chitosan and its derivatives have two advantages that make it a good candidate for skin care: its positive charge and the fact that it does not penetrate the skin. Most chitosan products have such high molecular weights that prevent the product from penetrating the skin, and therefore remain on the surface as a moisturizer or skin protector. Because of its lower costs, it might compete with hyaluronic acid in this application. Both chitin and chitosan can be used in toothpaste, mouthwashes and chewing gum. They freshen the breath, prevent the formation of plaque, and tooth decay.

Wastewater treatment

Due to its inert, safe, non-toxic, biocompatible, biodegradable, low cost, eco-friendly and abundant nature, CS is regarded as one of the most efficient materials for adsorption of pollutants in water treatment systems. The presence of amino and hydroxyl groups allows adsorption interactions with pollutants such as dyes [83], metals [84] and organic compounds [85]. Moreover, these functional groups are subjected to modifications, which enhance the absorption efficiency and specificity [86]. The United State Environmental Protection has approved the use of commercially available chitosan for potable water purification. Chitosan, carboxymethyl chitosan, and cross-linked chitosan have been shown to be effective in the removal of Pb^{2+}, Cu^{2+}, and Cd^{2+} from drinking water [87,88].

3.1.4. Chitosan films and plasticizers

Chitosan has a good ability to form films that are generally clear, transparent and non-porous. The films show moderate values of water and oxygen permeability. Commonly, both the mechanical properties and the permeability vary according to the molecular weight, the degree of deacetylation and the selected solvent system [89]. For example, an increase in the molecular weight of chitosan would increase the tensile strength and elongation as well as the moisture absorption capacity of the resulting films [90]. In general, the mechanical properties of commercial polymers with medium strength, such as cellulose, are comparable to those of chitosan films [91]. The most popular method of producing CS films is solution casting, and films produced by this technique are rigid and brittle. Consequently, the addition of plasticizers is necessary to overcome the brittleness of chitosan films [92].

Plasticizers are substances widely used as polymeric additives to improve their flexibility and processability. Typically, plasticizers reduce the intermolecular forces among polymer chains and the energy required for molecular motion and the formation of hydrogen bonds between chains, thus increasing free volume and, hence, the molecular mobility. Plasticizers modify the physical properties of the polymers, such as thermal and mechanical, as well as affect the antimicrobial properties. In biopolymer-based films and coatings production, plasticizers are also essential additives since they can improve flexibility, thereby allowing deformation without rupture, and handling of films, decrease brittleness, maintain integrity and avoid pores and cracks in the polymer matrix. Water is the most powerful plasticizer for hydrophilic polymers. In addition to water, the most commonly used plasticizers are monosachcharides, oligosaccharides, polyols, lipids and derivatives [93]. Polyols have been found to be particularly effective to plasticize hydrophilic polymers such as CS, producing flexible, easy-to-handle films [49,94-96]. Concretely it is known that a glycerol (GLY) concentration of 20% (w/w) is enough to obtain flexible chitosan films with stable properties during 5 months of storage [96]. Ideal plasticizers are miscible and compatible in all proportions with plastic components. The efficiency of these plasticizers is related to their molecular size, shape, number of oxygen atoms, spacing of oxygen atoms and water holding capacity [97].

3.1.5. <u>Chitosan nanocomposites</u>

Chitosan has low to moderate mechanical properties that currently limit its wide range of applications. Several efforts to improve physical and mechanical properties of chitosan films by incorporating several fillers such as nanoclays [98-101], cellulose whiskers [102,103], and carbon nanotubes [104-106] have been reported. Graphene and graphene derivatives have also been successfully incorporated into biopolymers such as chitosan.

Various studies have confirmed that GO incorporated into CS *via* simple solution mixing, is a novel reinforcing filler [107-112]. These studies reported the preparation of CS/GO composite films containing varying GO contents uniformly distributed and finely dispersed in CS matrix, with greatly improved physical and mechanical properties. The authors concluded that these nanocomposites could have promising new applications as biomaterials. Several reports have been published on biological and medical applications of the CS/GO hybrid systems. Justin and Chen [112] studied the effects of GO on the drug release profiles of chitosan and the results proved high potential applications of CS/GO nanocomposites as microneedle array materials for transdermal drug delivery. Bao *et al.* [113] and Rana *et al.* [114] reported the covalent functionalization of GO with CS and the application of the CS-grafted GO for drug and gene delivery.

As for graphene, different strategies have been reported for its incorporation into the matrix, such as *in situ* chemical reduction of GO by CS [115], by hydrazine [116] or by L-ascorbic acid in the presence of CS [117], as well as the addition of graphene sheets prepared through *ex situ* processes such as cryogenic graphene powder [118], GS [108,119], thermally expanded graphite [120,121], sulfonated rGO [122], silane-functionalized graphene [123], chitosan-grafted rGO sheets [124], chemically reduced GO (by NaOH [111], hydrazine [125-127], tea polyphenol [128]), non-covalently functionalized of graphene by chitosan-ionic liquid conjugation [129], reduced GO with hydrazine in the presence of stabilizers [130,131] and dispersion of thermally reduced GO in DMF by ultra-sonication [132]. In the studies focused on the effect of graphene on the physical and mechanical properties of CS films, improvements have been observed. However, Justin and Chen [115] claim that CS/rGO nanocomposites with rGO concentrations higher than 5 wt% were too brittle to form into tensile-

test specimens. The enhanced mechanical properties, electrical conductivity and antibacterial activity observed in CS/graphene nanocomposites make these materials suitable for biomedical applications such as antibacterial materials in biomedical devices, drug delivery systems [115], electrochemical sensors and biosensors [122,125-127,132-136].

3.2. Experimental Section

3.2.1. Materials

Glycerol and chitosan powder (M_w=190,000–310,000 Da) were supplied by Sigma-Aldrich. We have applied a method based on the NMR spectrum of a chitosan sample to estimate the chitosan degree of deacetylation (DD) [137] and confirmed a DD of 82%. All chemicals were used as received without further purification.

3.2.2. Preparation of CS films

Two grams of chitosan powder were dissolved in 120 mL 2% (v/v) acetic acid aqueous solution upon stirring overnight. After that, the chitosan solution was poured into a leveled plastic plate that was left at room temperature to evaporate water and acetic acid. The as-prepared film was dried under vacuum at 40 °C for 2 days. CS film containing glycerol (20% weight) as plasticizer was prepared in the same manner. In addition, CS and CS/GLY films in an oil bath at 60 °C for 6 h with constant stirring were prepared to compare with CS/GS nanocomposites prepared through *in situ* method.

3.2.3. Preparation of CS/GO nanocomposite films

GO suspension was prepared by dispersing the desired amount of graphite oxide in 120 mL 2% (v/v) aqueous acetic acid solution and treated with a tip sonicator for 15 min. Then 2 g of chitosan powder was added into the GO suspension while stirring. The mixture was left stirring overnight until CS was completely dissolved, and then was sonicated for 2 h at room temperature in a bath-type ultrasound sonicator. The homogeneous solution was then cast onto a

leveled plastic plate, left to dry at room temperature and subsequently peeled off as a free-standing film. The film was dried under vacuum at 40 °C for 2 days. CS/GO films containing glycerol (20% weight) as plasticizer were prepared in the same manner. Glycerol was added to the mixture CS/GO after the complete dissolution of polysaccharide. The nanocomposites were named **CS/GO-x**, where x denotes the weight percentage of GO.

3.2.4. Synthesis of CS/GS nanocomposite films by *in situ* reduction

Following the above procedure, GO homogeneous suspension was prepared by dissolving the desired amount of graphite oxide in 120 mL 2% (v/v) aqueous acetic acid solution and treated with a tip sonicator for 15 min. Then 2 g of chitosan powder was added into the GO suspension while stirring. The mixture was left stirring overnight until CS was completely dissolved, and then was sonicated for 2 h at room temperature in a bath-type ultrasound sonicator. After that, the mixture was heated in an oil bath at 60 °C. In order to maintain the weight relationship between the L-AA and the GO fixed at 3.5, the desired amount of a water solution of L-AA was subsequently added to the CS/graphene oxide sheets mixture under vigorous stirring. The mixture was then held at 60 °C for 6 h with constant stirring and in the absence of light, to reduce the graphene oxide sheets into graphene sheets (GS). The homogeneous solution was then cast onto a levelled plastic plate, left to dry at room temperature and subsequently peeled off as a free-standing film. The film was dried under vacuum at 40 °C for two days. Chitosan/graphene (CS/GS) films containing glycerol (20% weight) as plasticizer were prepared in the same manner. Glycerol was added to CS/graphene mixture after the complete dissolution of CS. In this case, the nanocomposites were named CS/GS-x, where x denotes the weight percentage of GS.

3.2.5. Characterization

The structural and morphological characterization of unplasticized and plasticized CS, CS/GO and CS/GS nanocomposites was performed by Fourier-transform infrared (FTIR) spectroscopy, X-ray diffraction (XRD), scanning

electron microscopy (SEM) and transmission electron microscopy (TEM). Solid state ^{13}C -NMR was used to evaluate the degree of acetylation (DA) of chitosan.

Thermal characterization of the chitosan-based nanocomposites films was carried out by thermogravimetric analysis (TGA) and the mechanical properties were measured by means of tensile tests (MTS). Water vapor permeability (WVP) of the nanocomposites was determined according to the ASTM E96 standard, using the upright cup method (UCM), and water absorption capacity (WAC) was calculated by applying a specific equation (Appendix I, Eqn. I6) with the weights of the samples before and after being immersed in deionized water at room temperature for 24 h. Finally, the electrical conductivity was measured using a four-point resistivity meter (FPR).

The complete description of the structural, morphological, thermal, mechanical and electrical characterization methods is provided in Appendix I and the section of each technique or method is detailed in the Table 3.2.

Table 3.2. Characterization methods used for the analysis of chitosan-based nanocomposites.

Analysis	Technique or Method	Appendix Section
CS acetylation degree (DA)	^{13}C-NMR	I.1.1
Chemical structure	FTIR	I.1.3
Crystalline structure	XRD	I.1.6
Nanostructure and morphology	SEM	I.1.8
	TEM	I.1.9
Thermal behavior	TGA	I.2.1
Mechanical Properties	MTS	I.3
Permeability	UCM	I.5
Water Absorption	WAC	I.6
Electrical conductivity	FPR	I.4

3.2.6. <u>Antimicrobial activity assay</u>

The antimicrobial activity of CS was evaluated using broth diffusion method. For this procedure, 20 mm diameter discs of CS film were cut out and introduced into a tube containing 4,950 μL of Mueller-Hinton broth. Then 50 μL of a 0.5 McFarland inoculum (approx. $1\text{-}5 \times 10^8$ cell/mL) of *Escherichia coli* ATCC 25922 was pipetted. The tubes were incubated for 48 h in an orbital shaker incubator at 100 rpm and 37 °C. Finally, the inhibition of the growth was determined by colony count method in plate count agar (PCA). These assay was performed with four replicates and repeated three times at different days using either CS films stored for a year at room temperature and CS films stored for 7 days at room temperature in order to analyze the effect of storage period on the antimicrobial activity.

Bacterial growth was presented as the mean of the logarithms of colony-forming units (CFU) per milliliter. Data were analyzed using analysis of variance (ANOVA) with Tukey's post hoc test, and significant differences between CS and stored-CS were determined (p value < 0.05). Calculations were performed with statistical software SPSS 24 (IBM SPSS statistic, USA).

3.3. Results and discussion

3.3.1. Structural and morphological characterization

13C CP/MAS-RMN spectroscopy analysis

The acetylation degree (DA) of chitosan was determined by ^{13}C CP/MAS-NMR. As shown in Figure 3.5, the ^{13}C CP/MAS-NMR spectrum of the chitosan contains six signals. The C1-C6 carbons of N-acetylglucosamine monomeric unit are observed between 50 and 110 ppm, the methyl group of the acetyl group produces a peak at around 23 ppm, while the carbonyl group is not detected. The less the peaks of carbonyl and acetyl groups, the less the degree of acetylation. CPMAS ^{13}C NMR has been shown to give reliable results when the acetyl CH3 signal is used to estimate the acetyl content in solid samples [38-40]. Corresponding chemical shifts appear in Table 3.3. The chemical shift assignments have been done according to the literature [38,138,139]. The degree of acetylation determined using equation I.1.1 (NMR spectroscopy section of Appendix I) was 18%, which is equal to a degree of deacetylation, DD, (DD=100 – DA), of 82%.
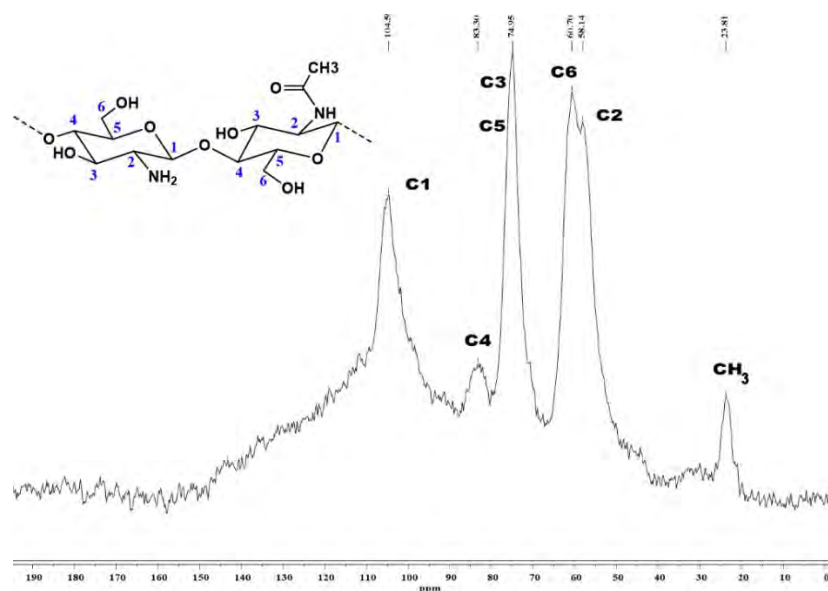
Figure 3.5. ^{13}C CP-MAS NMR spectrum and chemical structure of chitosan.

Table 3.3. Chemical shifts of chitosan obtained by ^{13}C CP-MAS.

	C=O	C1	C4	C3-5	C6	C2	CH$_3$
Shift (ppm)	ND	104.6	83.3	75	60.7	58.1	23.8

Fourier-transform infrared (FTIR) spectroscopy

The spectrum of commercial chitosan powder, Figures 3.6A-B(a), displays a strong and broad band in the range of 3800 to 3000 cm^{-1} which is attributed to O-H, N-H, hydrogen-bonded OH, and hydrogen-bonded NH stretching vibrations. The C-H stretching vibrations appear at 2926 and 2873 cm^{-1}. The band registered at 1644 cm^{-1} is attributed to the carbonyl (C=O) asymmetrical stretching of the secondary amide (Amide I band), while that at 1567 cm^{-1} is assigned to the N-H bending vibration from amine (N-H$_2$) overlapping the amide vibration (Amide II band). The peaks at 1420 and 1375 cm^{-1} belong to the asymmetrical C-H bending vibration of the CH$_2$OH group and CH$_3$ symmetrical deformation in acetamide group (NHCOCH$_3$), respectively. The band at 1316 cm^{-1} belongs to the stretching vibrations of C-N in secondary amide group HNCO (Amide III band). The weak band at 1261 cm^{-1} results from interaction between the N-H bending and C-N stretching. The bands at 1150, 1062, and 1026 cm^{-1} are assigned to C-O-C antisymmetric, N-H stretching vibrations, and to C-O stretching vibrations in secondary and primary OH groups, respectively. Finally, the bands situated in the range of 1000 to 900 cm^{-1} (990, 946, and 894 cm^{-1}) are characteristic of the vibrations from the carbohydrate ring of saccharide.

The spectrum of the chitosan film cast from acetic acid solution, after being peeled off from the Petri dish and before storage and further drying, is shown in Figures 3.6A-B(b). The FTIR spectra of the film and the powder show similar patterns, however, the film displays a higher intensity of the absorption bands in the 3700 to 2700 cm^{-1} and in the 1800 to 1200 cm^{-1} regions. Furthermore, a new peak appears in the spectrum of chitosan film at 1538 cm^{-1} due to the symmetric deformation vibration of cationic group (NH$_3^+$) obtained by protonation of the amino group of chitosan in acidic conditions, while the peak which corresponds to the N-H$_2$ band at 1567 cm^{-1} present in the FTIR spectrum of chitosan powder

disappears in the spectrum of the film, and the carbonyl band shifts from 1644 to 1632 cm^{-1} due to the antisymmetric deformation of protonated amino. This band observed at 1632 cm^{-1} can be assigned to the amide I and to the antisymmetric deformation of NH$_3^+$, while the band at 1538 cm^{-1} is due to the amide II, N-H bending vibration and the symmetric NH$_3^+$ deformation [140]. Also, a new band around 1404 cm^{-1} arises from the symmetric carboxylate ion stretching mode.
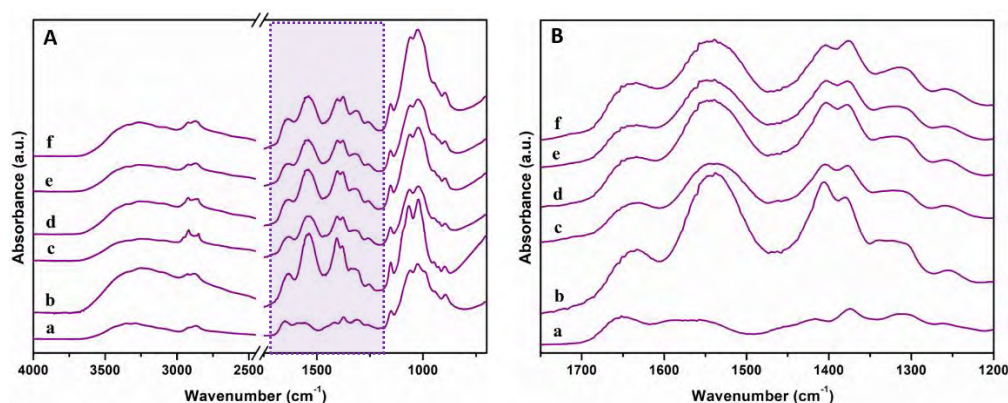
Figure 3.6. FTIR spectra (A) and (B) enlarged FTIR spectra in the 1750 to 1200 cm^{-1} region of: (a) CS powder, (b) CS freshly cast film, (c) CS dried film 27 °C 48 h, (d) CS dried film 40 °C 24 h, (e) CS dried film 60 °C 24 h, and (f) CS dried film 60 °C 7 days.

Figures 3.6A-B(c–f) display the infrared spectra of chitosan after ageing at different temperatures (27, 40, and 60 °C) and specific exposure times. The main changes observed between those spectra and the spectrum obtained before ageing are a decrease in relative intensity of the NH$_3^+$ and carboxylate bands at 1538 and 1404 cm^{-1}, respectively. In the case of the CS film before ageing, the intensity of the peak at 1404 cm^{-1} is higher than the intensity of the band around 1377 cm^{-1}, while the relative intensity of the carboxylate peak decreases with ageing temperature and time (Figure 3.6B). In the case of ageing at 60 °C for 7 days, the intensity of the peak at around 1377 cm^{-1} is higher than the intensity of the band at 1404 cm^{-1}. This result indicates that the NH$_3^+$ groups decrease when the CS films are stored.

The FTIR spectra of plasticized and unplasticized CS/GO nanocomposite films cast from acetic acid solution are shown Figure 3.7A. All the samples exhibit the characteristic absorption peaks of the neat CS, but subtle differences in the

position of some individual bands are observed. The presence of glycerol affects the position of the carbonyl group (Amide I) and the NH_3^+ group bands of unplasticized chitosan film. These bands move at a higher frequency, 1643 and 1556 cm^{-1}, respectively. Likewise, for the CS/GO-1 nanocomposite, the amide I and NH_3^+ bands shift from 1632 to 1644 cm^{-1} and from 1538 cm^{-1} to 1557 cm^{-1}, respectively. For the plasticized CS/GO nanocomposite, the FTIR spectrum is similar to that of the glycerol-plasticized CS, but the amide I and NH_3^+ bands shift slightly to a higher wavelength.
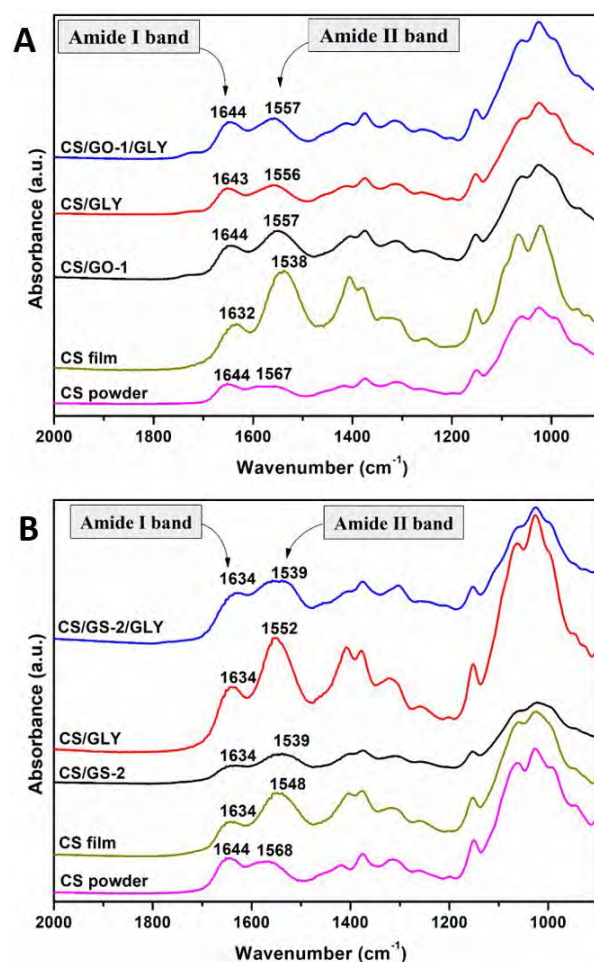
Figure 3.7. FTIR spectra in the 2000 to 900 cm^{-1} region of (A): CS powder, CS, CS/GO-1, CS/GLY, and CS/GLY/GO-1. (B) CS powder, CS, CS/GS-1, CS/GLY, and CS/GS-1/GLY.

The typical bands of CS shift back to the positions of CS powder (i.e., CS without acetic acid) with addition of GO and glycerol. This shift indicates a change from symmetric deformation vibration of NH_3^+ to N-H bending vibration from NH_2 in the CS molecules. These results confirm that GO and glycerol displace bound acetic acid from CS (amino nitrogen in CS interacts with the protons in the acetic acid). Due to the interaction of GO and glycerol with CS throughout hydrogen bonding with amino groups, a lower amount of NH_2 groups would be available to interact with acetic acid. Thus, the amide II band would be less shifted than in CS film. However, in CS/GO/GLY nanocomposite, the addition of GO to the plasticized CS does not exhibits this effect due to the low amount of GO relative to that of glycerol. In the CS/GO nanocomposites there can be two types of interactions: (i) interactions through hydrogen bonding of NH_2 groups and primary OH groups of the CS to the functional groups on the graphene oxide surface, and (ii) electrostatic interaction between the protonated NH_3^+ groups of CS and negative surface charge of graphene oxide due to its acidic groups. Thus, part of protonated amino groups disappears due to the interaction through hydrogen bonding between chitosan and GO, and another part of the amino groups remains in the protonated form bound, through electrostatic interactions, to the surfaces of GO.

Regarding CS/GS nanocomposites (Figure 3.7B), the FTIR spectrum of CS/GS-2 nanocomposite shows the characteristic absorption peaks of neat CS film. However, the absorption band due to the NH_3^+ shifts from 1548 cm^{-1} to 1539 cm^{-1}. In the FTIR spectrum of plasticized CS/GS-2 the NH_3^+ band shifts from 1552 cm^{-1} to 1539 cm^{-1} in comparison with the pure plasticized chitosan. The shift of the NH_3^+ band towards a lower frequency which takes place in the case of the glycerol plasticized and unplasticized CS/GS is due to the electrostatic interaction of negatively charged surface of GS and positively charged chitosan.

X-ray diffraction (XRD)

The XRD patterns of pure chitosan powder, neat unplasticized and glycerol-plasticized CS films are presented in Figure 3.8. Chitosan powder exhibits two main peaks at 9.7° and 20.1°. The peaks correspond to a hydrated crystalline structure ("tendon form") and regular crystal lattice, respectively [104,141]. The XRD pattern of unplasticized chitosan film shows peaks at 8.8°, 11.8°, 16.3°, 18.6°,

and 23.5°. Such a pattern characterizes a chitosan polymorph ("tendon" hydrated polymorph) [142]. The first two peaks are assigned to the hydrated crystals due to the integration of water molecules in the crystal lattice, the peak located at 18.6° is attributed to the regular crystal lattice of chitosan, while the peak at 23.5° indicates the existence of an amorphous structure. The very weak diffraction peak at $2\theta = 16.3°$ indicates the existence of a very small amount of anhydrous crystals. The addition of glycerol produces an effect on the XRD pattern of CS film manifested by an increase in the reflections at 11.3°, 16.2°, 18.1°, and 22.7°. Glycerol molecules interact with CS macromolecules, which favors the chains mobility and thus the chitosan crystallization process.
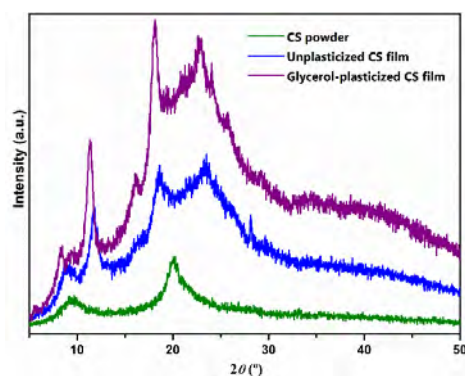
Figure 3.8. XDR patterns of CS powder, unplasticized CS film and glycerol-plasticized CS film.
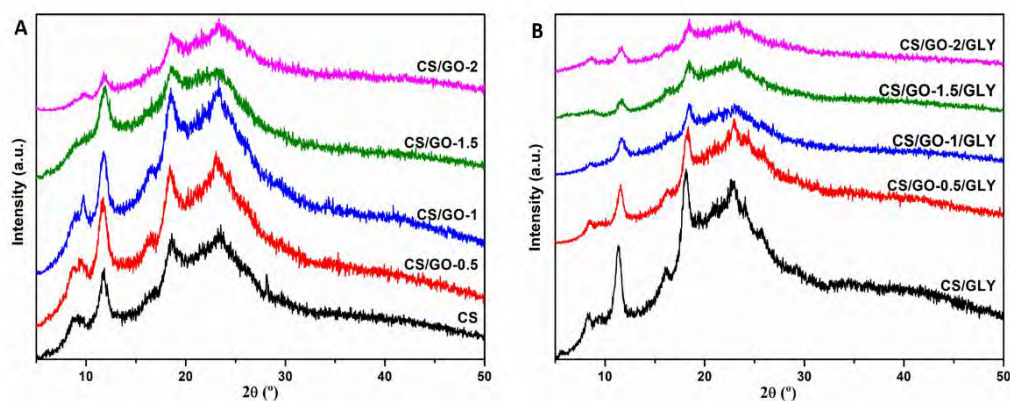
Figure 3.9. XDR patterns of neat CS and CS/GO nanocomposite films: (A) unplasticized and (B) glycerol-plasticized.

XRD results of neat CS film and its unplasticized nanocomposite films with the addition of 0.5, 1, 1.5, and 2 wt% of GO are shown in Figure 3.9A. XRD pattern of the unplasticized chitosan nanocomposite films with GO content keeps the characteristic peaks of neat chitosan. By increasing the GO content beyond 1 wt%, the intensity of the crystalline peaks diminishes. The XRD analysis indicates that the incorporation of the GO within the chitosan matrix leads to a decrease of the chitosan crystallinity at the highest GO contents used in the present work. Similarly, Figure 3.9B presents X-ray diffraction patterns of neat plasticized CS film and CS/GO nanocomposite films plasticized with 20 wt% of glycerol. The combined addition of glycerol and GO results in a weakening of reflection at $2\theta = 8.8°$, $2\theta = 11.3°$, $2\theta = 18.1°$, and $2\theta = 22.7°$, indicating a decrease of the chitosan crystallinity with the incorporation of GO within the polysaccharide matrix.
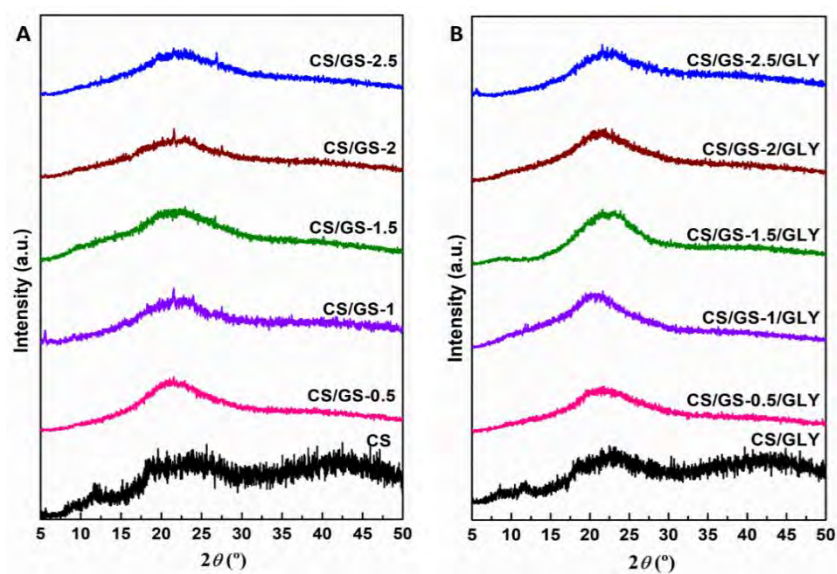
Figure 3.10. XDR patterns of neat CS and CS/GS nanocomposite films: (A) unplasticized and (B) glycerol-plasticized.

Regarding GS nanocomposites, Figures 3.10A,B show the XRD patterns of the CS film and the unplasticized and plasticized nanocomposites with 0.5, 1, 1.5, 2 and 2.5 wt% of GS. Compared with the original CS, the unplasticized and glycerol plasticized chitosan nanocomposite samples show only the peak at $2\theta = 23°$. The XRD analysis shows that the incorporation of the GS within the chitosan matrix leads to a decrease of the chitosan crystallinity.

Nanostructure and morphology

TEM images of unplasticized and plasticized CS, CS/GO and CS/GS nanocomposites are shown in Figure 3.11. It can be appreciated that the GO and GS nanosheets are well dispersed throughout the polymeric matrix.

Figure 3.12 displays SEM images of fractured surfaces of the unplasticized and glycerol plasticized CS, CS/GO-1 and CS/GS-1 nanocomposites at different magnifications. CS shows a very clean and smooth fractured surface. The cross-sectional image of glycerol-free CS with 1 wt% GO content shows a rough fractured surface without any aggregates of GO, and has a wave-like morphology, confirming that GO nanosheets are dispersed homogeneously in CS matrix. The plasticized nanocomposite exhibits a stratified surface, and the direction of the layers is parallel to the film surface. The cross-sectional image of CS with 1 wt% GS content shows a rough fractured surface without any aggregates of GS, and has a wave-like morphology. It confirms that graphene sheets are dispersed homogeneously in CS matrix.
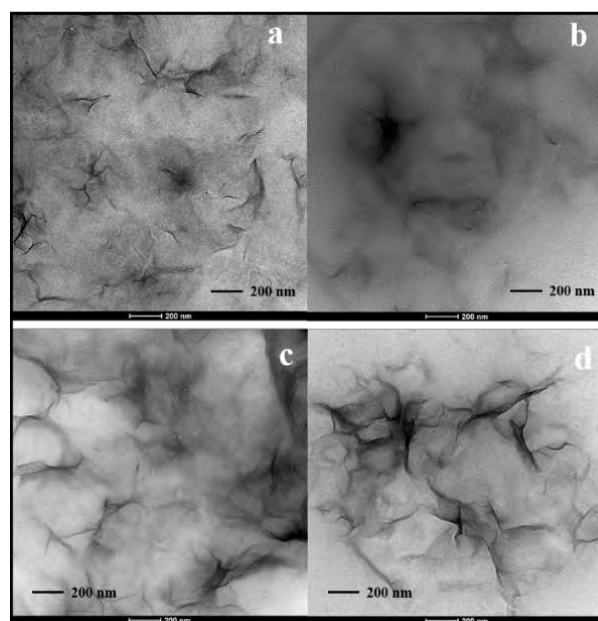
Figure 3.11. TEM images of: (a) CS/GO-1, (b) CS/GO-1/GLY, (c) CS/GS-1 and (d) CS/GS-1/GLY.
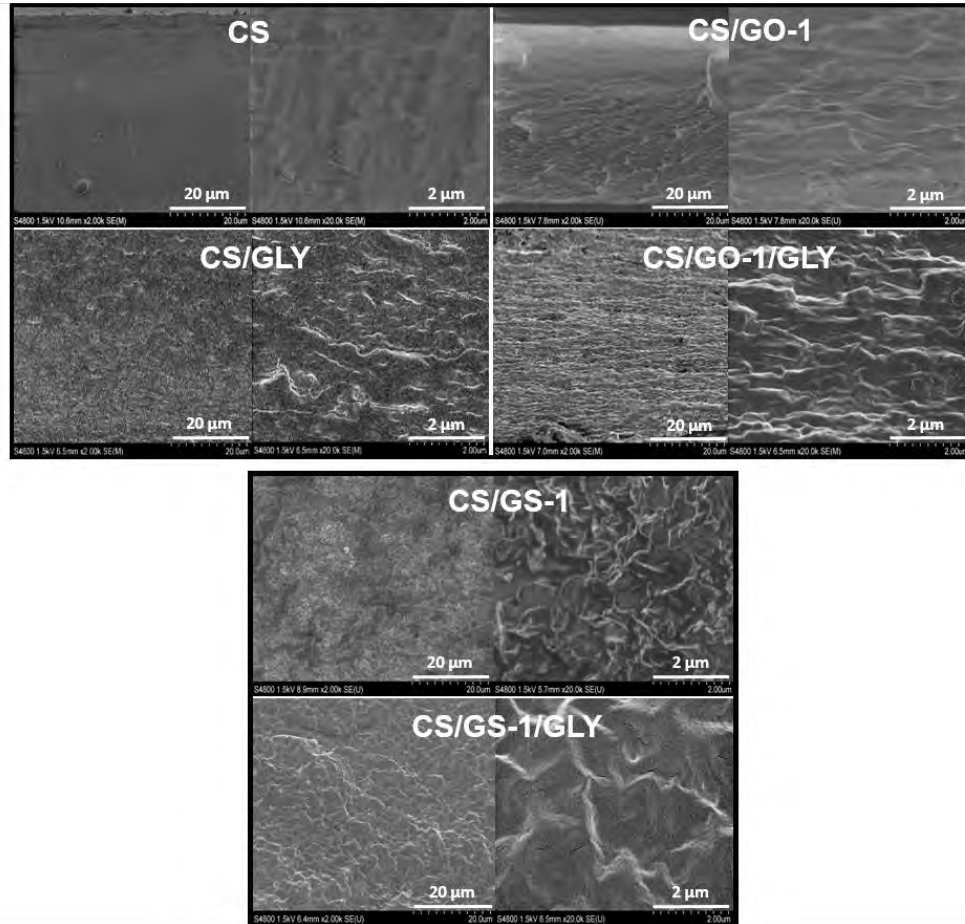
Figure 3.12. SEM images of the fracture surfaces of unplasticized and glycerol-plasticized CS, CS/GO-1 and CS/GS-1 nanocomposite at different magnifications.

3.3.2. Thermal characterization of chitosan nanocomposites

Thermogravimetric analysis

TGA has been used to evaluate the effect of addition of GO and GS on the thermal stability of chitosan. Figure 3.13 shows thermogravimetric (TG) and derivative thermogravimetric (DTG) curves of unplasticized and plasticized CS and CS/GO-1 nanocomposites. Chitosan, in inert atmosphere is degraded in a three stage process as can be seen from Figure 3.13A. The first stage observed below 145 °C with a weight loss of about 5% is ascribed to the evaporation of physically adsorbed water and/or chemisorbed water through hydrogen bonds.

The second stage, that takes place between 150 °C and 215 °C with a weight loss of 5%, represents the weight loss of methane and a weight loss of NH_3 from an elimination reaction between -NH_2 and –H groups [143]. The third stage between 215 and 460 °C, with its maximum at 294 °C, and a weight loss of 47%, represents the decomposition of the main chain, decomposition of pyranose rings through dehydration and deamination and finally ring-opening reaction with the production of H_2O, CO, and CO_2 and some other fragments from the glucosaminic ring [144-147]. Finally, a carbonaceous residue from the remaining degraded structures of about 36% is found at 600 °C that is constant at least up to 800 °C. The chitosan film is degraded in nitrogen maintaining its original shape and leaving a residue of about 34% at 800 °C.
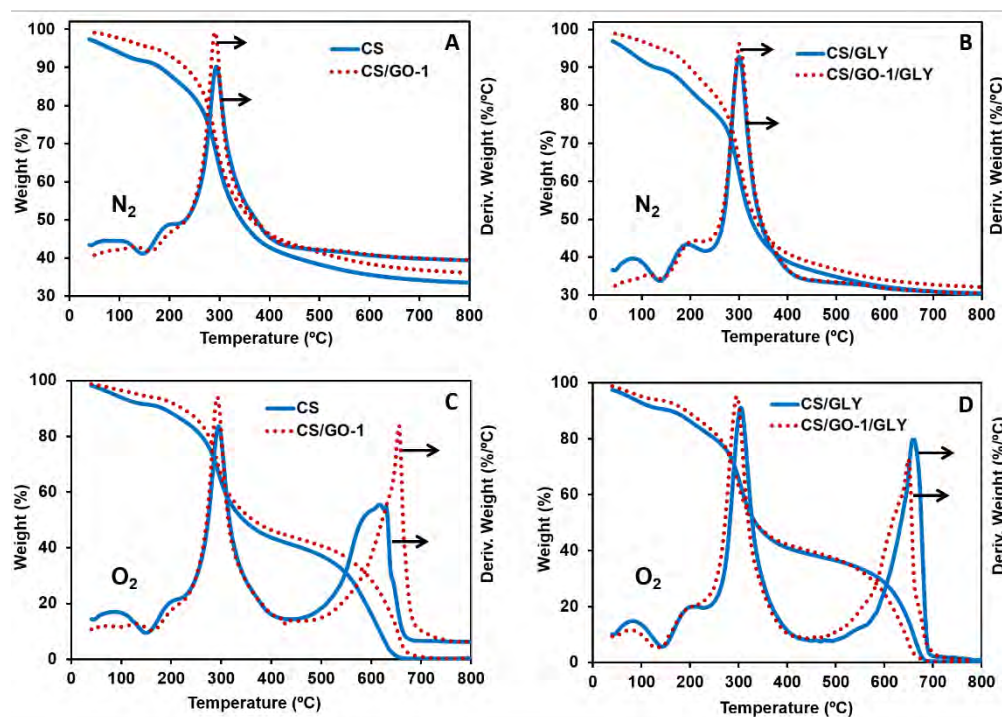
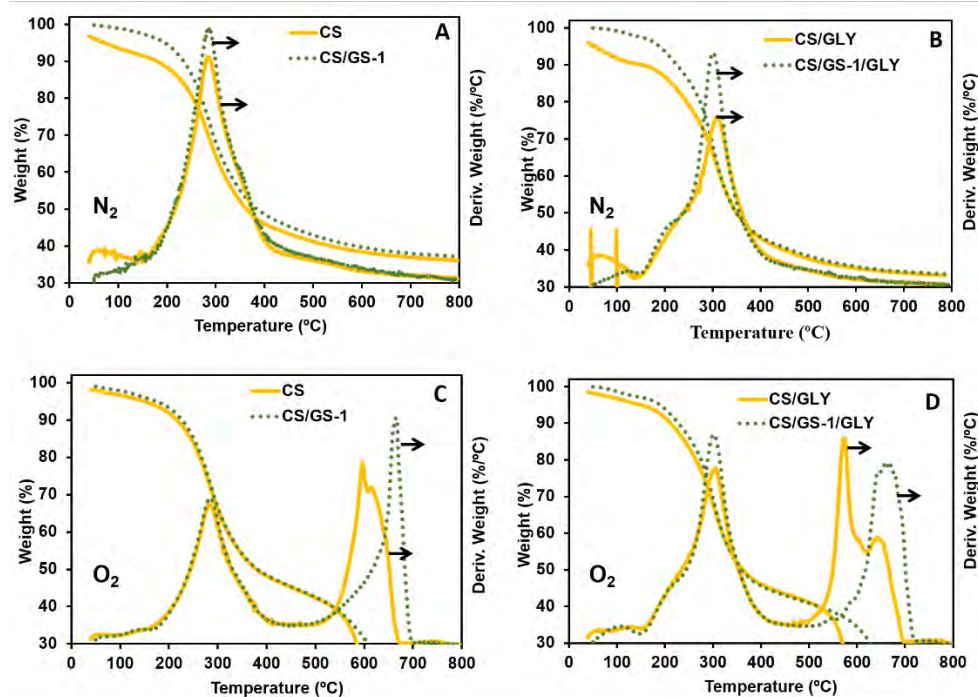**Figure 3.13.** TG and DTG curves: (A) unplasticized and (B) glycerol-plasticized in nitrogen, (C) unplasticized and (D) glycerol-plasticized in air of CS and CS/GO-1.

The presence of GO does not significantly alter the degradation mechanism of CS matrix, since its degradation profile is similar to that of neat CS. The thermal decomposition temperatures for 5 and 50% weight loss ($T_{5\%}$ and $T_{50\%}$), the

temperature of the maximum loss rate (T_{max}) and the fraction of solid residue at 800 °C of the thermograms obtained in nitrogen are reported in Table 3.4. The $T_{5\%}$ and $T_{50\%}$ increase with the addition of GO, the $T_{5\%}$ value of the nanocomposite with 1% GO is 16 °C higher than that of neat CS and the $T_{50\%}$ value is 20 °C higher than that of neat CS. However, the T_{max} value is almost unaffected by the incorporation of GO. The nanocomposite containing 1 wt% GO exhibits the highest thermal stability. In addition, the water loss that takes place in the first stage of decomposition process decreases as the GO loading increases, from 5 wt% in the case of CS to less than 3 wt% in the case of CS/GO nanocomposite containing 2 wt% GO. The CS/GO nanocomposites leave higher char residue at 800 °C as compared with neat CS.

Table 3.4. TGA data for unplasticized and glycerol plasticized CS and CS/GO nanocomposites.

Sample	$T_{5\%}$ (°C)		$T_{50\%}$ (°C)		T_{max} (°C)		
	in N_2	in O_2	in N_2	in O_2	in N_2	in O_2	
					(a)	(a)	(b)
CS	213	218	344	345	294	295	617
CS/GO-0.5	221	225	353	350	290	294	605
CS/GO-1	229	231	364	364	291	292	656
CS/GO-1.5	218	226	359	348	287	290	659
CS/GO-2	216	213	358	364	289	287	661
CS/GLY	195	206	325	335	301	305	660
CS/GO-0.5/GLY	201	210	335	346	302	306	671
CS/GO-1/GLY	199	210	334	345	302	306	659
CS/GO-1.5/GLY	198	206	337	347	303	307	658
CS/GO-2/GLY	193	208	335	346	303	306	661

[a] 3rd stage; [b] 4th stage

TGA curves of plasticized CS and its nanocomposite containing 1 wt % GO, under inert atmosphere, are displayed in Figure 3.13B. The thermograms of plasticized CS and unplasticized CS exhibit a similar shape, although there are certain differences in $T_{5\%}$ and $T_{50\%}$ values. Plasticized CS exhibits lower $T_{5\%}$ and $T_{50\%}$, about 19 °C lower than that of unplasticized CS, whereas the T_{max} value is

slightly higher for plasticized CS (7 °C). As far as the thermal decomposition of plasticized CS and its nanocomposites is concerned, the $T_{5\%}$ and T_{max} are almost unaffected with the addition of GO, whereas the $T_{50\%}$ value of the nanocomposites is 10 °C higher than that of neat CS (Table 3.4). However, the T_{max} value of the third stage is almost unaffected by the incorporation of GO. In addition, as with unplasticized CS/GO, the water loss decreases as the GO loading increases. As in the case of the unplasticized nanocomposites, the glycerol plasticized CS/GO nanocomposites leave higher char residue at 800 °C as compared with neat CS.

Consequently, it leads to the conclusion that the addition of GO in the chitosan matrix leads to an improvement of thermal stability of CS under inert conditions, especially in the case of unplasticized samples. The improved thermal stability of chitosan may rise from the formation of the carbonaceous layer that would protect the underlying polymer from the flux of degradation product and heat. Furthermore, strong interaction between CS and GO enhances the dispersion as well as the interfacial adhesion and could also restrict the polymer motion during heating.

The weight loss thermograms of CS and CS/GO-1 obtained under oxygen are shown in Figure 3.13C. The thermal oxidation of CS takes place in four stages. In the first stage below 150 °C takes place the evaporation of water (6%). The second stage, between 150 and 215 °C with a weight loss of 5%, is not as well separated as in nitrogen analysis. The third decomposition stage, the main decomposition step, occurs almost over the same temperature range (215–430 °C) as in nitrogen atmosphere; also the weight loss of this step (45%) is similar as in nitrogen (Table 3.4). The fourth decomposition step in the range of 430 to 690 °C is the main difference in thermal degradation in both atmospheres, which can be associated to the oxidative degradation of the carbonaceous residue formed during the second step. Total degradation of chitosan ring is close to 650 °C. The degradation profile of the CS/GO nanocomposites is similar to that of neat CS, indicating that the presence of GO does not significantly alter the oxidative degradation mechanism of CS matrix. $T_{5\%}$ and $T_{50\%}$ increase with the addition of GO, the $T_{5\%}$ value of the nanocomposite with 1% GO is 13 °C higher than that of neat CS and the $T_{50\%}$ value is 19 °C higher than that of neat CS (Table 3.4). The nanocomposite containing 1 wt% GO exhibits the highest thermal stability.

The weight loss thermograms of plasticized CS and its nanocomposite with 1 wt% GO, under oxygen, are displayed in Figure 3.13D. The thermograms of plasticized CS and unplasticized CS exhibit a similar shape, although there are certain differences in $T_{5\%}$ and $T_{50\%}$ values. Plasticized CS exhibits lower $T_{5\%}$ and $T_{50\%}$, about 10 °C lower than that of unplasticized CS, whereas the T_{max} values for the third and fourth stages are higher for plasticized CS (10 °C and 40 °C). As far as the thermal decomposition of plasticized CS and its nanocomposites is concerned, the $T_{5\%}$ and T_{max} (third and fourth stages) are almost unaffected with the addition of GO, whereas the $T_{50\%}$ value of the nanocomposites is 10 °C higher than that of CS/GLY (Table 3.4). In addition, as with unplasticized CS/GO, the water loss decreases as the GO loading increases. This part of thermogravimetric analysis permits to conclude that unplasticized chitosan and chitosan/GO nanocomposites are more thermo-oxidative stable than the glycerol-plasticized samples. The effect of carbon nanotubes (CNT) on the thermal stability of CS composites has been reported in the literature [148-150]. Azeez *et al.* [148] and He *et al.* [149] found that the addition of CNT to CS slightly improved the thermal stability of the nanocomposites, while Tang *et al.* [150] observed that $T_{50\%}$ value of CS was improved by 12 °C after adding 3 wt% CNTs. As it is shown in the present study, $T_{50\%}$ value, in nitrogen and air atmosphere, of plasticized and unplasticized CS is improved by 10-20 °C after adding 1 wt% of GO.

Figure 3.14 shows the TG and DTG curves of unplasticized and plasticized CS and CS/GS nanocomposites in inert and oxidative atmosphere. Chitosan prepared at 60 °C for 6 h, presents a degradation profile similar to that of the film prepared from CS unheated solution. The presence of GS does not significantly alter the degradation mechanism of CS matrix, since its degradation profile is similar to that of neat CS (Figure 3.14A). The thermal decomposition temperatures obtained in nitrogen are reported in Table 3.5. The $T_{5\%}$ increases with increase in GS content up to 1% and then decreases. $T_{50\%}$ increases with increase in GS content and $T_{50\%}$ value of the nanocomposite with 2% of GS is 35 °C higher than that of neat CS. In addition, the water loss that takes place in the first stage of decomposition process decreases with increase in GS content, from 4 wt% in the case of CS to less than 0.5 wt% in the case of CS/GS nanocomposite containing 2.5 wt% of GS.

Figure 3.14. TG and DTG curves: (A) unplasticized and (B) glycerol-plasticized in nitrogen, (C) unplasticized and (D) glycerol-plasticized in air of CS and CS/GS-1.

TG and DTG curves of plasticized CS and its nanocomposite containing 1 wt% GS, under inert atmosphere, are displayed in Figure 3.14B. The thermograms of plasticized CS and unplasticized CS exhibit a similar shape. The $T_{5\%}$, $T_{50\%}$ and T_{max} values are almost unaffected by the GS loading in the plasticized CS (Table 3.5). As with unplasticized CS/GS, the presence of GS resulted in a decrease of the water weight loss, from 5.5 wt% in the case of CS to less than 1 wt% in the case of CS/GS nanocomposite containing 2.5 wt% GS. Consequently, thermal stability of CS under inert conditions is unaffected by the presence of GS.

Figure 3.14C presents the TG and DTG curves of the CS and CS/GS nanocomposite with 1 wt% of GS obtained under oxygen. The thermal oxidation of CS (6 h at 60 °C) takes place in two stages. The first stage takes place between 100-450 °C with a weight loss of 56%. The second decomposition stage that occurs over the temperature range of 470–700 °C with a weight loss of about 45%. Total degradation of chitosan ring is close to the 700 °C. The degradation profile of the CS/GS nanocomposites is similar to that of neat CS, however, the presence of GS

shifts significantly the temperature of the second degradation step to higher values. The addition of GS results in a slight increase in $T_{5\%}$ and $T_{50\%}$ values, and in a significant increase in the T_{max} value of the second step of decomposition, about 60 °C (Table 3.5). Neither in the case of CS nor in the case of CS/GS nanocomposites detectable water loss is observed.

Table 3.5. TGA data for unplasticized and glycerol plasticized CS and CS/GS nanocomposites.

Sample	$T_{5\%}$ (°C)		$T_{50\%}$ (°C)		T_{max} (°C)			
	in N_2	in O_2	in N_2	in O_2	in N_2 (a)	in O_2 (a)	(b)	
CS	215	186	362	370	286	281	597	
CS/GS-0.5	211	195	362	390	305	304	662	
CS/GS-1	222	193	384	385	286	286	669	
CS/GS-1.5	204	197	387	390	281	281	655	
CS/GS-2	200	190	396	396	282	279	650	
CS/GS-2.5	205	190	398	395	270	279	670	
CS/GLY	213	179	350	362	308	306	574	643(c)
CS/GS-0.5/GLY	212	215	361	369	303	303	657	
CS/GS-1/GLY	207	218	350	359	301	301	660	
CS/GS-1.5/GLY	212	214	353	350	305	306	665	
CS/GS-2/GLY	214	218	360	371	303	302	669	
CS/GS-2.5/GLY	216	219	361	372	304	303	669	

(a) 1st stage; (b) 2nd stage; (c) 3rd stage

The weight loss thermograms of plasticized CS and its nanocomposite with 1 wt% GS, under oxygen, are displayed in Figure 3.14D. The thermogram of plasticized CS (6 h at 60 °C) takes place in three steps: the first one in the temperature range of 150–450 °C, the second and third ones are overlapped in the region 460–700 °C. The addition of glycerol results in slight differences in the T_{max} values of the degradation steps. As far as the thermal decomposition of plasticized nanocomposites is concerned, the degradation takes place in two steps. The $T_{5\%}$ of

the nanocomposites are 36 °C higher than that of CS/GLY, while $T_{50\%}$ values are only slightly higher. The T_{max} value of the second step of the degradation of CS/GS nanocomposites is higher than that of the third step of CS decomposition. These results suggest that glycerol plasticized CS/GS nanocomposites are more thermo-oxidative stable than the neat plasticized CS.

Comparing the results in inert atmosphere for both types of unplasticized and plasticized nanocomposites, it can be highlighted that the improvement in thermal stability is higher for unplasticized CS/GO nanocomposite, while in oxidative atmosphere the higher enhancement is found for plasticized CS/GS nanocomposites.

3.3.3. Mechanical characterization

Mechanical properties were studied by means of tensile tests performed at an extension rate of 5 mm/min under room temperature. The typical stress-strain curves of unplasticized and plasticized CS, CS/GO and CS/GS nanocomposites are displayed in Figure 3.15. The plotted specimens undergo elastic deformation and plastic behavior with the exception of unplasticized CS/GS nanocomposite, which breaks before performance. The obtained results for CS/GO nanocomposites are presented in Table 3.6 and Figure 3.16, while the values for CS/GS nanocomposites are shown in Table 3.7 and Figure 3.18. In addition, Figure 3.17 shows the rate of change of properties, calculated from equation I.3 described in the mechanical characterization section of Appendix I.

The presence of glycerol in films exerts a great influence over Young's modulus, yield stress, break stress, and elongation at break. The presence of glycerol in chitosan films results in a decrease of Young's modulus around 62%, a decrease of yield stress around 65%, a decrease of break stress of 38%, and an increase in elongation at break around 111%. Plasticizer reduces drastically the intermolecular forces in the chitosan, increasing the mobility of the polymer chains, thus decreasing the elastic modulus, tensile strength at yield and at break, and increasing elongation at break of the films. The presence of glycerol leads to a decrease in the material stiffness and brittleness.
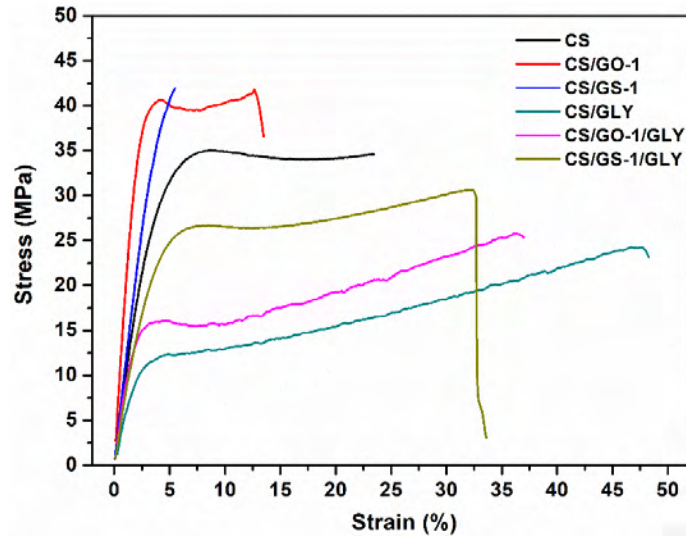
Figure 3.15. Stress-strain plots of unplasticized and plasticized CS, CS/GO-1 and CS/GS nanocomposites.

Table 3.6. Mechanical properties of unplasticized and glycerol-plasticized CS and CS/GO nanocomposites.

Sample	Young's modulus (MPa)	Yield stress (MPa)	Break Stress (MPa)	Elongation at break (%)
CS	1511±67	33.7±3.0	31.8±4.0	19.5±3.6
CS/GO-0.5	2069±190	34.7±0.9	34.4±1.5	16.9±1.5
CS/GO-1	2164±123	35.9±5.7	36.4±6.1	14.0±3.5
CS/GO-1.5	2486±174	39.5±5.2	42.5±7.6	11.3±3.6
CS/GO-2	2715±230	44.4±0.5	48.9±2.1	12.9±2.9
CS/GLY	571±78	11.8±1.7	19.7±4.3	41.1±6.0
CS/GO-0.5/GLY	927±107	18.4±3.0	25.8±2.6	28.1±4.8
CS/GO-1/GLY	948±60	18.5±2.9	26.4±4.6	33.4±6.9
CS/GO-1.5/GLY	1108±102	19.6±1.7	26.1±2.2	30.6±2.4
CS/GO-2/GLY	1428±123	23.5±3.3	29.6±4.0	28.4±4.9

The elastic modulus of all CS/GO nanocomposites is higher than that of CS, and the GO content affects the elasticity of the nanocomposites. It is found that the Young's modulus of CS/GO nanocomposites increases gradually with the increase of GO content for unplasticized and glycerol plasticized films (Figure 3.16A). The addition of GO results in an increase of the stiffness of the chitosan and chitosan/glycerol. It can be seen that for glycerol-free films with 2 wt% of GO, the tensile modulus increases by about 80% compared with neat CS (Figure 3.17A). For CS/GO films with glycerol, the maximum increment of Young's modulus is reached for the nanocomposite containing 2 wt% of GO about 150% in comparison with neat chitosan (Figure 3.17A). The results obtained suggest that the GO effect is emphasized by the glycerol influence. Thus, the presence of GO leads to a higher increase in the material stiffness when glycerol is present.
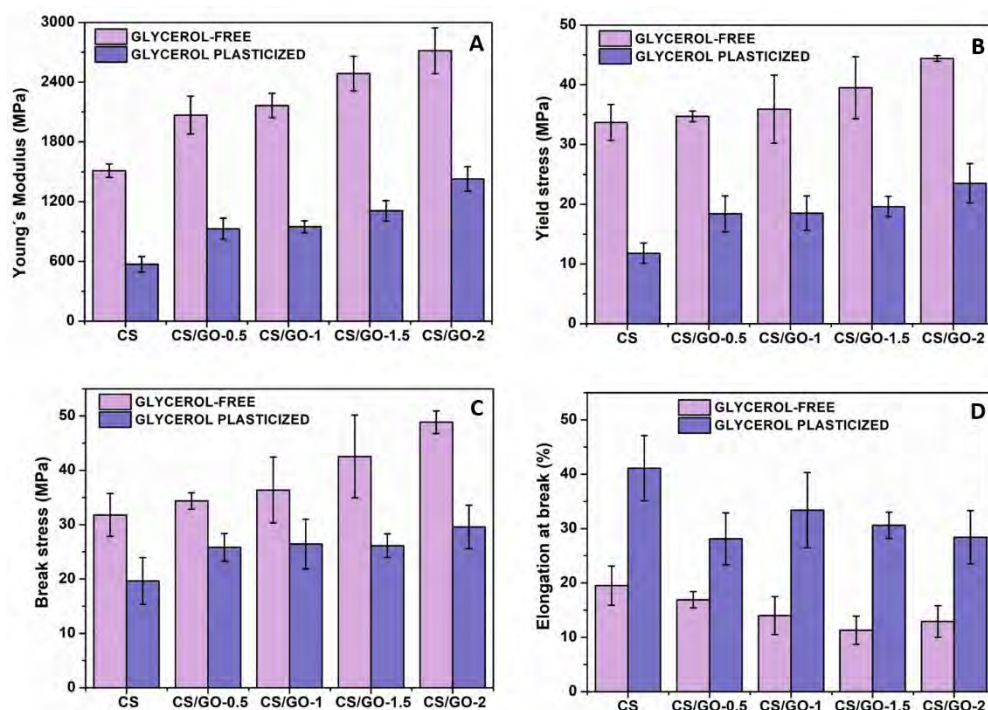
Figure 3.16. Mechanical properties of CS/GO nanocomposites: (A) Young's modulus, (B) Yield stress, (C) Break stress and (D) Elongation at break.

Yield stress and break stress of the composite films increase gradually with the increasing loading of GO (Table 3.6). With incorporation of 2 wt% of GO,

yield stress increases by 32% and 100% for unplasticized and glycerol plasticized films, respectively. These results reveal that the presence of glycerol accentuates the GO effect on yield stress (Figure 3.17B). In the case of unplasticized films, break stress also increased gradually as GO content increases (Figure 3.16C), but this pattern is somewhat different for plasticizers. CS/GO plasticized films with 0.5 wt% of GO show an increase in tensile strength at break, remaining the value constant up to 1.5 wt% and, at a higher content (2 wt%), a further increase is observed. The incorporation of 2 wt% of GO to unplasticized and plasticized CS leads to an increase of break stress values of about 51%, when compared with neat CS (Figure 3.17C). However, at low contents of GO (less than 1.5 wt%) break stress enhancement is significantly higher in the presence of plasticizer. Glycerol reduces the hydrogen bonding interactions along the CS chains and favors the formation of intermolecular hydrogen bonds between GO and CS matrix.

The elongation at break of unplasticized and plasticized CS decreases with the addition of GO (Figure 3.16D). The lowest elongation at break is obtained for unplasticized films with 1.5 wt% of GO (Table 3.6), the reduction is about 42% in comparison with neat chitosan. These results indicate that the addition of GO results in more brittle materials when compared with the pure chitosan film. These results are in agreement with other graphene oxide reinforced polymer composites [151-153]. Hussein *et al.* [151] observed that functionalized graphene oxide as reinforced filler for epoxy resin showed significant improvements in mechanical properties. Morimune *et al.* [152] and Yang *et al.* [153] observed a significant increase in both the elastic modulus and tensile strength in poly(vinyl alcohol) by the incorporation of GO.

Overall, it can be concluded that the improvement of mechanical properties for CS/GO nanocomposites is probably owing to the reinforcing effect of graphene oxide nanosheets dispersed homogeneously throughout the chitosan matrix and, the good adhesion between graphene oxide sheets and the chitosan, which efficiently transfer the load between the filler and the matrix. Graphene oxide contains hydroxyl and carboxylic groups, and chitosan in a glucosamine unit contains amino, primary and secondary hydroxyl groups. Therefore, a strong hydrogen-bond between the chitosan and the surface of graphene oxide may be formed, as it has been discussed previously from the FTIR results. Consequently, the mechanical properties of the matrix are enhanced by the addition of GO.
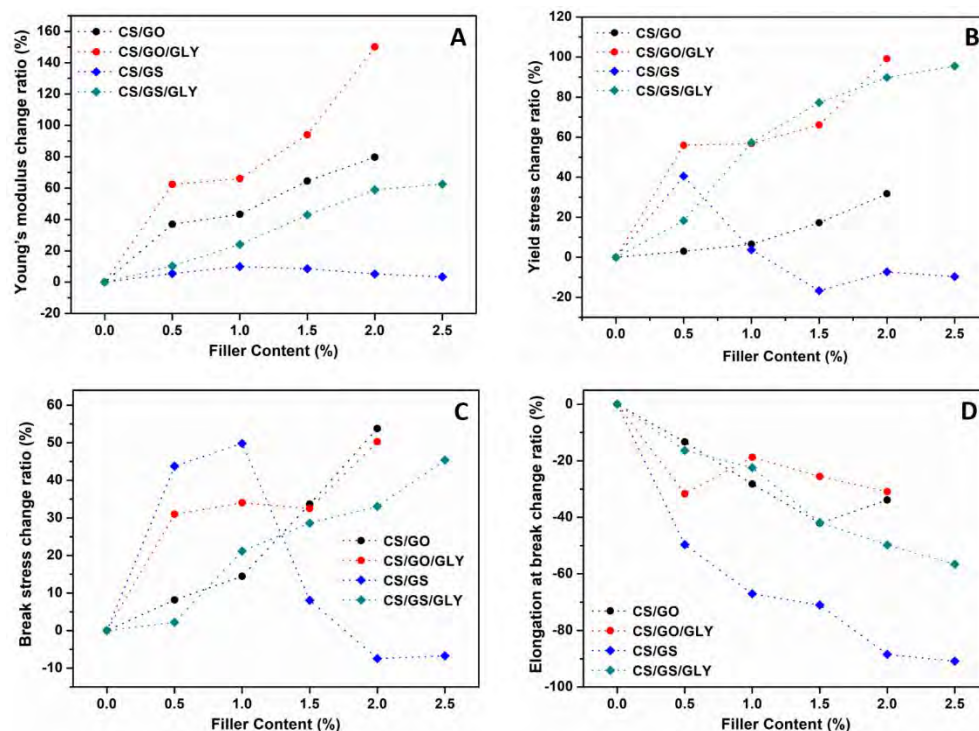
Figure 3.17. Change ratio of: (A) Young's modulus, (B) Yield stress, (C) Break stress and (D) Elongation at break for unplasticized and plasticized CS/GO and CS/GS nanocomposites.

As far as CS/GS nanocomposites are concerned, the difference in the values of tensile properties of CS and CS/GLY given in Table 3.6 and Table 3.7 can be attributed to the changes in crystallinity as a result of heat treatment of the samples in Table 3.7. The elastic modulus of all non-plasticized nanocomposites is slightly higher than that of CS and increases with increasing GS content (Figure 3.18A). The nanocomposite films with 1 wt% GS exhibits 10% increase in elastic modulus compared with neat chitosan. The Young's modulus then remains practically constant with further increase in the GS content (Figure 3.17A). The yield stress of unplasticized CS/GS nanocomposites increases by 41% with the addition of 0.5 wt% of GS, but at higher contents a reduction is observed (Figure 3.18B). The incorporation of contents higher than 1 wt% GS makes CS less elastic. The break stress of unplasticized CS nanocomposites is enhanced by increasing the GS content (Figure 3.18C). The addition of 1 wt% of GS into unplasticized CS leads to a 50% increase in the tensile strength at break (Figure 3.17C), with respect to CS, whereas it decreases as GS content increases up to 2 wt%, and it tends to

levelled off at higher GS content. Regarding the elongation at break of unplasticized CS/GS composite films (Figure 3.18D), it can be observed that the increase of GS content is accompanied by a very rapid decrease in elongation at break values, 91% of reduction with the addition of 2.5 wt% of GS as compared with neat chitosan (Figure 3.17D, Table 3.7). Reports in the literature have shown an enhancement in mechanical properties of chitosan nanocomposites with graphene loading similar to that found in the present work [115,154].
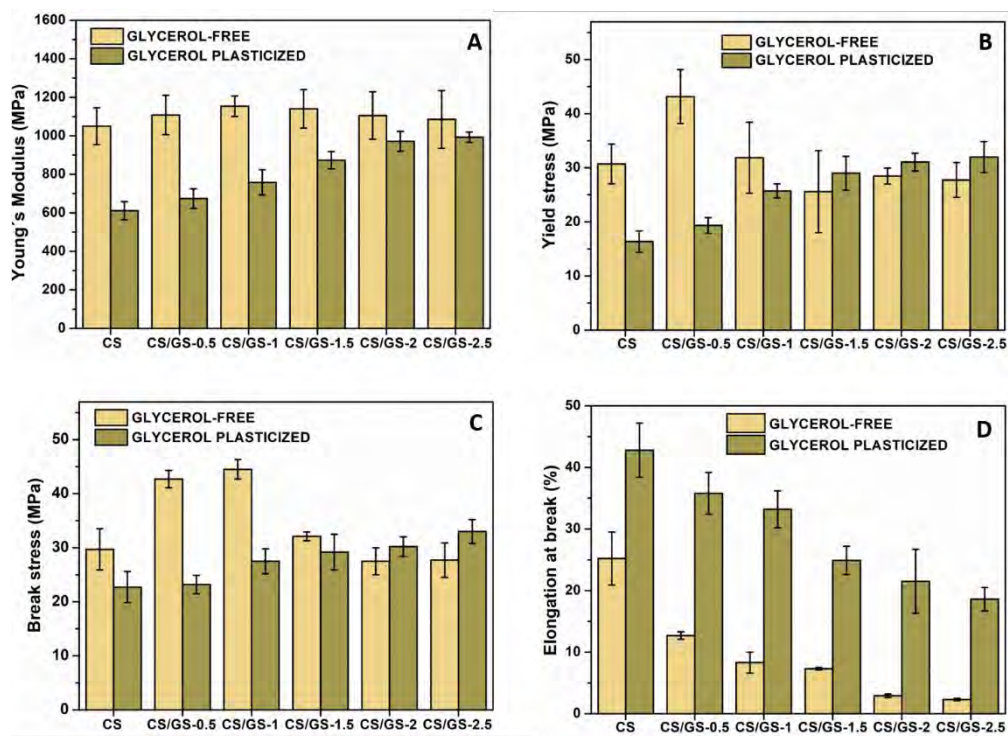
Figure 3.18. Mechanical properties of CS/GS nanocomposites: (A) Young's modulus, (B) Yield stress, (C) Break stress and (D) Elongation at break.

As can be appreciated in Figure 3.17, for CS/GS nanocomposites the mechanical properties are also substantially enhanced with plasticizer incorporation. The Young's modulus is greatly improved (63%), as well as break (45%) and yield stress (99%), while the elongation at break is reduced (56%). Thus, the presence of GS leads to an increase in the material stiffness when glycerol is present, while if the plasticizer is not present the materials become less stiff. It is worth noting that the yield and break stress values of plasticized CS/GS

nanocomposites with 2 and 2.5 wt% GS are somewhat higher than unplasticized counterparts (Table 3.7). Furthermore, the elongation at break values of the plasticized nanocomposites with those GS contents are 87% higher than the values obtained for the unplasticized nanocomposite films. The presence of glycerol favors the incorporation of high GS contents without losing properties.

Table 3.7. Mechanical properties of unplasticized and glycerol-plasticized CS and CS/GS nanocomposites.

Sample	Young's modulus (MPa)	Yield stress (MPa)	Break Stress (MPa)	Elongation at break (%)
CS	1050±96	30.7±3.7	29.7±3.8	25.2±4.3
CS/GS-0.5	1108±102	43.2±5.0	42.7±1.6	12.7±0.6
CS/GS-1	1154±53	31.9±6.6	44.5±1.8	8.3±1.7
CS/GS-1.5	1140±100	25.6±7.6	32.1±0.8	7.3±0.2
CS/GS-2	1105±123	28.5±1.5	27.5±2.5	2.9±0.0
CS/GS-2.5	1085±150	27.7±3.2	27.7±3.2	2.3±0.3
CS/GLY	611±47	16.4±2.0	22.7±2.9	42.8±4.4
CS/GS-0.5/GLY	674±51	19.4±1.4	23.2±1.7	35.8±3.4
CS/GS-1/GLY	758±66	25.7±1.3	27.5±2.4	33.2±3.0
CS/GS-1.5/GLY	873±45	29.0±3.1	29.2±3.3	24.9±2.3
CS/GS-2/GLY	971±52	31.1±1.7	30.3±1.8	21.5±5.2
CS/GS-2.5/GLY	993±27	32.0±2.9	33.0±2.2	18.6±1.9

Overall, from this mechanical properties analysis it can be inferred that good dispersion of graphene sheets throughout the plasticized biopolymer matrix and strong interfacial adhesion with the plasticized matrix enhance the mechanical properties of plasticized CS with the addition of GS. On the other hand, the less improvement achieved in mechanical properties of CS in the absence of the plasticizer, may be attributed to the lower degree of interaction between GS and CS matrix. These results show that it could be obtained CS/GS nanocomposites with different mechanical properties by adjusting the GS content and incorporating a plasticizer.

The tensile properties of CS improve with the addition of GO and GS, achieving the highest increase for GO nanocomposites. The improved mechanical strength of unplasticized and glycerol plasticized CS/GO and CS/GS nanocomposite films is very important for their potential application as biomaterials in bone tissue engineering. The range of values of the Young's modulus for both the unplasticized and glycerol plasticized CS/nanocomposites are lower than literature values of cortical bone (12–20 GPa), but comparable to trabecular bone (0.3–10 GPa) [155]. The biomaterial to be implanted should have mechanical properties comparable to those of the tissue to be regenerated. Glycerol plasticized CS/GO and CS/GS nanocomposite films could be suitable for wound dressing applications due to their higher elasticity [156]. For these biomedical applications, one of the major concerns is the cytotoxicity of graphene. The studies of the *in vitro* and *in vivo* cyto- and bio- compatibility of graphene-based nanomaterials have shown that toxicity of graphene is dependent on several physiochemical properties such as shape, size, composition, dispersion state, synthesis methods, route and dose of administration, and exposure times [157-159]. When graphene is incorporated in chitosan matrix, the studies on the toxic effects of graphene have revealed that its cytotoxicity effects are attenuated [108,157]. With respect to glycerol, Guitian *et al.* [160] examined the toxicity of glycerol plasticized chitosan. They concluded that glycerol is an effective and biocompatible plasticizer for chitosan without any impact on cytotoxicity. On the basis of the above observations, CS/GO and CS/GS nanocomposites with 0.5–1 wt% GO and GS could be considered as the most suitable materials for the above mentioned applications.

3.3.4. Water vapor permeability

Water vapor permeability (WVP) of unplasticized and plasticized CS/GO and plasticized CS/GS nanocomposites with different filler contents was measured at a vapor pressure difference of 100/58% RH (i.e. at a RH gradient of 100/58) across the film. WVP data are shown in Figure 3.19. CS films show significant differences ($p < 0.05$) with respect to CS/GLY. The WVP of CS increases by about 97% with the addition of glycerol. This can be ascribed to the hydrophilic nature of glycerol, its hydroxyl functions interact with the hydroxyl groups of CS, decreasing the intermolecular attractions along the CS chains and, consequently,

the chain mobility increases thus facilitating the water vapor diffusivity through the CS film and accelerating the water vapor transmission [161].

The addition of 1 and 2 wt% of GO into unplasticized CS leads to statistically significant changes ($p < 0.05$) in permeability, compared to the pure polymer, giving an increase of 9.2% and 9.9%, respectively, whereas for 0.5 wt% of GO no significant modifications are registered. This small increase in permeability can be due to the reduction in the crystallinity of CS with the addition of the filler. The results shown in the XRD spectra (Figure 3.9) where the increase in GO content decreases the crystallinity of the polymer, support this behavior in permeability. As for the plasticized CS/GO films, there are no statistically significant differences compared to CS/GLY.
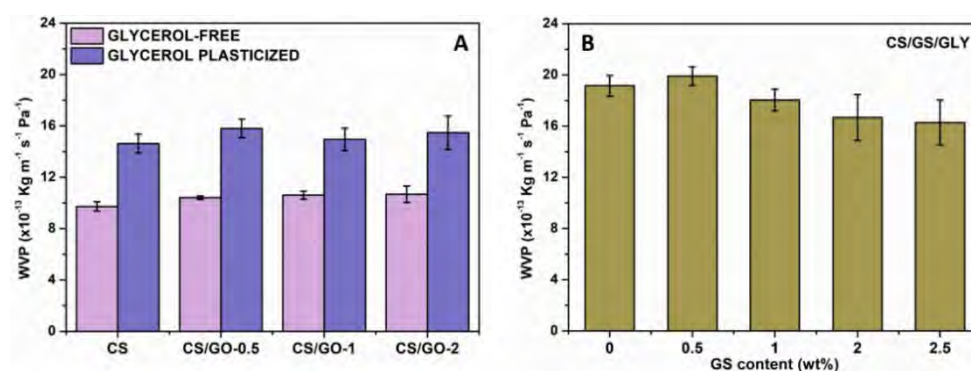
Figure 3.19. Water vapor permeability (WVP) for: (A) unplasticized and glycerol plasticized CS and CS/GO nanocomposites and (B) plasticized CS/GS nanocomposites.

It is important to note that the permeability of unplasticized CS/GS films could not be measured. The brittleness of these nanocomposites prevents the films from being cut into small discs without cracking. However, the addition of glycerol allowed permeability measurements. The WVP values for plasticized CS/GS nanocomposites do not present statistically significant variations with respect to the CS/GLY subjected to a heating of 60 °C during 6 h.

Comparing water vapor permeability values for GO and GS chitosan nanocomposites, it can be highlighted that the WVP is higher for heat-treated nanocomposites. This difference can be attributed to the fact that heating causes a decrease in the crystallinity of CS, making it more amorphous and, consequently, increasing permeability.

3.3.5. Water absorption

The total water absorbed by CS and its nanocomposites as a function of type and content of filler is showed in Figure 3.20. Neat unplasticized CS film exhibits the highest water absorption value, whilst in the presence of glycerol a significantly reduction in the water uptake ($\approx$80%) is observed (Figure 3.20A). This reduction can be attributed to the interaction between glycerol and CS. Hydroxyl and amino groups of CS form hydrogen bonds with hydroxyl groups of plasticizer and they are unable to fix water molecules, and therefore the insertion of water molecules is hindered. Heated-CS film (60 °C, 6 h) shown lower absorption value ($\approx$17%) than neat-CS film and in presence of glycerol water absorption decreases in 68% (Figure 3.20B). This difference can be attributed to the fact that heating causes a decrease in the crystallinity of CS, and therefore makes it difficult to keep the water molecules.
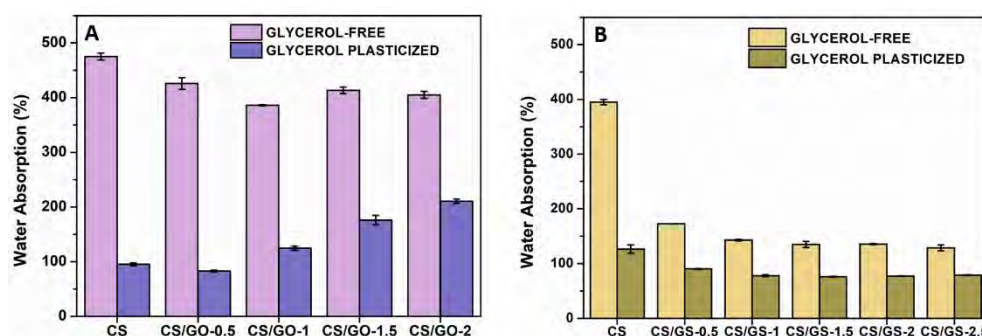
Figure 3.20. Water Absorption of plasticized and unplasticized (A) CS/GO and (B) CS/GS nanocomposites.

The incorporation of GO into unplasticized CS nanocomposites leads to a reduction in the amount of water uptake. With the addition of 1 wt% GO the lowest decrease is obtained, exactly the water absorption of the nanocomposite decreases by 19% when compared with CS film. The water absorption remains practically constant with the incorporation of higher GO contents. On the contrary, the water absorption of plasticized CS nanocomposites increases by $\approx$31%, $\approx$84% and $\approx$121% after the incorporation of 1 wt%, 1.5 wt%, and 2 wt% of GO respectively, when compared with CS/GLY. This behavior can be explained through the polar functional groups that the graphene oxide contains in random

order along the basal plane (hydrophilic surface) that serves as anchor to fix water molecules. Therefore, increasing the GO content increases the number of functional groups that can hold water molecules. However, in the absence of plasticizer this behavior is not appreciated because the functional groups of GO interact with the hydroxyl and amino groups of CS. When the plasticizer is added, the polymer-filler interaction competes with the polymer-plasticizer interaction, and significantly more plasticizer (20 wt%) is added than filler (higher content 2.5 wt%). The presence of the plasticizer allows the GO to be available to interact with the water.

The incorporation of GS into unplasticized and glycerol plasticized CS by *in situ* method leads to a reduction in the amount of water uptake (Figure 3.20B). The water absorption of CS/GS nanocomposites decreases by ≈56%, ≈64% and ≈66% after incorporation of 0.5 wt%, 1 wt% and 1.5 wt% of GS, respectively, when compared with CS/GLY. Incorporating a GS content of over 1.5 wt%, the water absorption remains almost constant. Similarly, the incorporation of these quantities of GS into the glycerol-plasticized CS reduces water absorption by up to 40%, with 1.5 wt% of GS and with higher contents remaining constant.

The water resistance increase found for the CS nanocomposites can be attributed to different factors. First, the strong interfacial adhesion between the polymer matrix and fillers through hydrogen bonding leads to less free hydrophilic groups and therefore less absorption sites for lodging of water. Secondly, due to the reduction of polar functional groups in GS, being material more hydrophobic. Finally, because of the interactions between the polymer and the filler, a constrained polymer region is formed in which a restriction of polymer motion occurs, which inhibits the absorption of water [162,163].

3.3.6. Electrical conductivity

For unplasticized and glycerol plasticized CS and CS/GS nanocomposites containing 0.5 wt% GS, the conductivity was measured to be below 10^{-8} S/cm, which is lower measurable limit by our four-point-probe set-up. The conductivity of the composites containing a GS content higher than 0.5 wt% satisfied the antistatic criterion (10^{-8} S/cm) for thin films. The maximum electrical

conductivity of $\approx 7.7 \times 10^{-4}$ S/cm was achieved for the composite containing 2.5 wt% GS (Figure 3.21). The conductivity of CS composites with GS is low. However, the reported conductivity of pure unplasticized CS was approximately 1.19×10^{-10} S/cm [164]. The results presented in this work are similar to those reported by Justin and Chen [115] for chitosan and rGO nanocomposites at higher concentrations of reduced GO, and higher than the values obtained by Zhou *et al.* [165] for CS-rGO films with similar rGO contents. The low values of electrical conductivity can be attributed to the oxygen content in GS, due to the presence of oxygenated functional groups, since with chemical reduction it is difficult to achieve a complete reduction of GO. Furthermore, chitosan may coat the surfaces of well-dispersed GS and prevent direct interparticle contact, since as inferred by SEM and TEM analysis, a good dispersion of GS in CS matrix has been obtained in the CS/GS nanocomposites prepared by the *in situ* reduction of graphite oxide. It has been reported that the best dispersions not necessarily lead to the highest conductivities [166], since the conductive network formation requires direct contact between conductive filler particles, that is their slight aggregation [167,168].
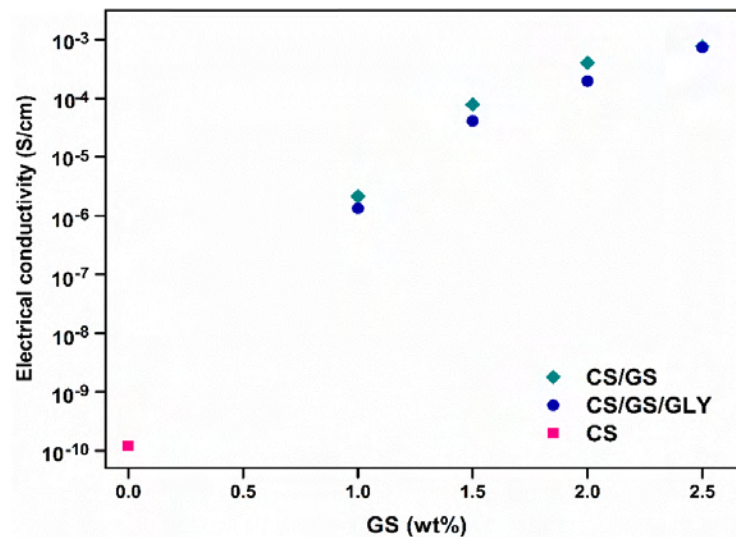
Figure 3.21. Electrical conductivity of CS/GS nanocomposites.

3.3.7. Antimicrobial activity assessment

The effect of the storage period of CS films on the antibacterial activity was studied using the broth diffusion method. The results obtained are shown in Figure 3.22A, where both CS films stored in different time periods show a significant reduction in *Escherichia coli* growth ($p < 0.05$). However, chitosan films stored for one year were statistically less active than CS films stored for 7 days ($p < 0.001$), indicating the low long-term stability of chitosan. This change can be explained by the reduction of cationic amino group (NH_3^+) in the chitosan as previously reported [50].
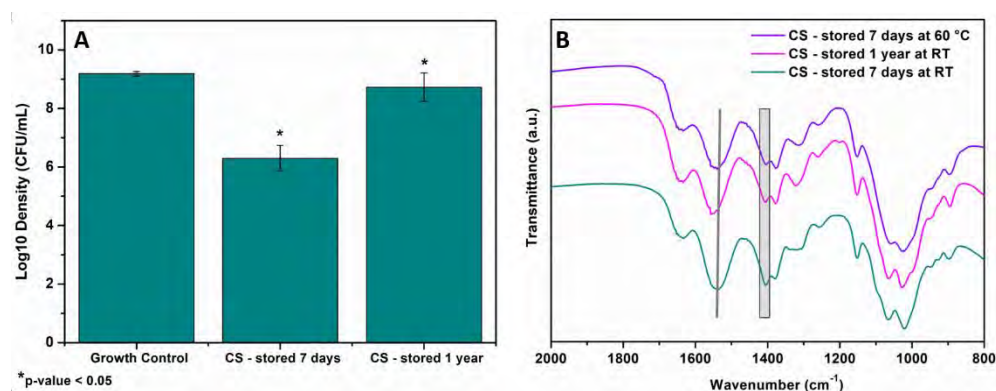
Figure 3.22. (A) Inhibition of *E.coli* growth by CS films stored for two different time periods. (B) FTIR spectra of CS stored at 60 °C and at RT for 7 days and 1 year.

FTIR spectroscopy was used to support this result (Figure 3.22B). The FTIR spectrum of the CS film stored for one year and that of stored at 60 °C for one week were similar. However, CS film spectrum stored for a year (at RT) shows a decrease in relative intensity of the NH_3^+ and carboxylate bands at 1538 and 1404 cm^{-1}, respectively. These results are in agreement with those obtained in the previous section of structural and morphological characterization suggesting that NH_3^+ groups decrease with the storage time of CS films [169,170].

Therefore, the higher amount of positive charges on the CS film stored for 7 days allows it to interfere more actively with the negatively charged residues of the macromolecules on the cell surface. It mainly competes with Ca^{2+} for electronegative sites, preventing the entry of this cation into the cell which triggers a loss in the integrity of the cell membrane [50].

3.4. Conclusions

GO was successfully incorporated to CS and glycerol plasticized CS, obtaining new nanocomposites *via* solution casting method. Non-plasticized and glycerol plasticized CS/GS nanocomposite films were effectively prepared *via in situ* reduction of graphene oxide sheets using an environmentally friendly method that employs L-ascorbic acid as the reducing agent. FTIR analysis demonstrated the existence of interactions between the amino and hydroxyl groups in the units of CS and the oxygenated groups on the surface of GO, as well as the interactions between CS and the residual oxygen groups present in GS *via* hydrogen bonds and electrostatic attractions. GO and GS were well dispersed and oriented along the surface of the nanocomposite films as revealed by SEM and TEM.

The addition of glycerol, GO and GS altered the crystallinity, thermal and mechanical properties of CS, as well as the electrical conductivity with GS. Unplasticized CS/GO nanocomposites showed a significant improvement in thermal stability, while thermo-oxidative stability was improved in plasticized CS/GS nanocomposites. The homogenous dispersion of GO and GS, and the strong interfacial adhesion with the matrix enhanced their mechanical properties being this improvement significantly higher in the presence of plasticizer. Glycerol has a remarkable impact on Young's modulus and break stress due to the reduction of hydrogen interactions between chitosan chains, which leads to improved interfacial interactions between CS and GO, or between CS and GS. An increase in electrical conductivity was observed with increasing GS content. The water vapor permeability of nanocomposites increased with the presence of glycerol, being higher for nanocomposites undergoing thermal treatment due to the decrease in the crystallinity of the matrix. However, the permeability of CS was not affected by the increase in GO or GS content. The strong interfacial adhesion between the CS and fillers through hydrogen bonding led to less water absorption. The antibacterial activity of CS against *Escherichia coli* decreased with the storage period. Consequently, due to their characteristics, these plasticized bionanocomposites can be potentially used for biomedical applications, such as tissue engineering, in which good physicochemical properties are essential for an efficient performance.

3.5. <u>References</u>

[1] S. Hirano, Chitin and chitosan as novel biotechnological materials, Polym. Int. 48 (1999) 732-734.

[2] P.K. Dutta, J. Dutta, V. Tripathi, Chitin and chitosan: Chemistry, properties and applications, (2004).

[3] M. Rinaudo, Chitin and chitosan: properties and applications. Prog. Polym. Sci. 31 (2006) 603-632.

[4] K. Kurita, Chitin and Chitosan: Functional Biopolymers from Marine Crustaceans. Mar. Biotechnol. 8 (2006) 203-226.

[5] R. Akila, Fermentative production of fungal Chitosan, a versatile biopolymer (perspectives and its applications), Adv Appl Sci Res. 5 (2014) 157-170.

[6] K. Novak, M.J. Cupp, T.S. Tracy, Chitosan, Dietary Supplements, Springer, 2003, pp. 33-39.

[7] G. McKay, Editor, Use of Adsorbents for the Removal of Pollutants from Wastewaters. (1996) 186.

[8] M.N.V.R. Kumar, A review of chitin and chitosan applications. React. Funct. Polym. 46 (2000) 1-27.

[9] P.K. Dutta, M.N.V. Ravikumar, J. Dutta, Chitin and chitosan for versatile applications. J. Macromol. Sci. , Polym. Rev. C42 (2002) 307-354.

[10] R.N. Tharanathan, F.S. Kittur, Chitin - the undisputed biomolecule of great potential. Crit. Rev. Food Sci. Nutr. 43 (2003) 61-87.

[11] P.C. Srinivasa, R.N. Tharanathan, Chitin/chitosan - safe, ecofriendly packaging materials with multiple potential uses. Food Rev. Int. 23 (2007) 53-72.

[12] S. Tokura, H. Tamura, Chitin and chitosan, in: H. Kamerling, G. Boons, Y. C. Lee, A. Suzuki, N. Taniguchi, A. G. J. Voragen (Eds.), Comprehensive Glycoscience, Elsevier Ltd, Amsterdam, the Netherlands, 2007, pp. 449-475.

[13] R. Sentandreu, M. Elorza, E. Valentín, J. Ruiz-Herrera, The Structure and Composition of the Fungal Cell Wall, in: G. San-Blas (Ed.), Pathogenic Fungi: Structural Biology and Taxonomy, Academic Press Washington DC, 2004, pp. 7-37.

[14] M. Zhang, A. Haga, H. Sekiguchi, S. Hirano, Structure of insect chitin isolated from beetle larva cuticle and silkworm (Bombyx mori) pupa exuvia. Int. J. Biol. Macromol. 27 (2000) 99-105.

[15] A.T. Paulino, J.I. Simionato, J.C. Garcia, J. Nozaki, Characterization of chitosan and chitin produced from silkworm crysalides. Carbohydr. Polym. 64 (2006) 98-103.

[16] A. Khanafari, R. Marandi, S. Sanatei, Recovery of chitin and chitosan from shrimp waste by chemical and microbial methods, Iranian Journal of Environmental Health, Science and Engineering. 5 (2008) 19-24.

[17] N. Pacheco, M. Garnica-Gonzalez, M. Gimeno, E. Bárzana, S. Trombotto, L. David, et al., Structural characterization of chitin and chitosan obtained by biological and chemical methods, Biomacromolecules. 12 (2011) 3285-3290.

[18] W. Arbia, L. Arbia, L. Adour, A. Amrane, Chitin extraction from crustacean shells using biological methods–a review, Food Technology and Biotechnology. 51 (2013) 12-25.

[19] S. Kumari, P. Rath, A. Sri Hari Kumar, T.N. Tiwari, Extraction and characterization of chitin and chitosan from fishery waste by chemical method, Environmental Technology & Innovation. 3 (2015) 77-85.

[20] D. Kafetzopoulos, A. Martinou, V. Bouriotis, Bioconversion of chitin to chitosan: purification and characterization of chitin deacetylase from Mucor rouxii, Proc. Natl. Acad. Sci. U. S. A. 90 (1993) 2564-2568.

[21] H.K. No, S.P. Meyers, Preparation and characterization of chitin and chitosan—a review, J. Aquat. Food Prod. Technol. 4 (1995) 27-52.

[22] I. Younes, M. Rinaudo, Chitin and chitosan preparation from marine sources. Structure, properties and applications, Marine drugs. 13 (2015) 1133-1174.

[23] G. Galed, B. Miralles, I. Paños, A. Santiago, Á Heras, N-Deacetylation and depolymerization reactions of chitin/chitosan: Influence of the source of chitin, Carbohydr. Polym. 62 (2005) 316-320.

[24] P. Tasch, Chitin, in: Fairbridge R., Jablonski D. (Eds.), Paleontology, encyclopedia of earth science ed., Springer, Berlin, 1979, pp. 186-189.

[25] M. Jang, B. Kong, Y. Jeong, C.H. Lee, J. Nah, Physicochemical characterization of Î±-chitin, Î²-chitin, and Î³-chitin separated from natural resources. J. Polym. Sci. , Part A: Polym. Chem. 42 (2004) 3423-3432.

[26] K.L.B. Chang, G. Tsai, J. Lee, W. Fu, Heterogeneous N-deacetylation of chitin in alkaline solution, Carbohydr. Res. 303 (1997) 327-332.

[27] T. Sannan, K. Kurita, Y. Iwakura, Studies on chitin, 2. Effect of deacetylation on solubility, Die Makromolekulare Chemie: Macromolecular Chemistry and Physics. 177 (1976) 3589-3600.

[28] R. Hejazi, M. Amiji, Chitosan-based gastrointestinal delivery systems, J. Controlled Release. 89 (2003) 151-165.

[29] H. Yi, L. Wu, W.E. Bentley, R. Ghodssi, G.W. Rubloff, J.N. Culver, et al., Biofabrication with Chitosan. Biomacromolecules. 6 (2005) 2881-2894.

[30] V. Sinha, A.K. Singla, S. Wadhawan, R. Kaushik, R. Kumria, K. Bansal, et al., Chitosan microspheres as a potential carrier for drugs, Int. J. Pharm. 274 (2004) 1-33.

[31] M. Yen, J. Yang, J. Mau, Physicochemical characterization of chitin and chitosan from crab shells. Carbohydr. Polym. 75 (2009) 15-21.

[32] J. Brugnerotto, J. Desbrières, G. Roberts, M. Rinaudo, Characterization of chitosan by steric exclusion chromatography, Polymer. 42 (2001) 09921-09927.

[33] L. Rusu-Balaita, J. Desbrieres, M. Rinaudo, Formation of a biocompatible polyelectrolyte complex: chitosan-hyaluronan complex stability. Polym. Bull. (Berlin, Ger.). 50 (2003) 91-98.

[34] J. Brugnerotto, J. Lizardi, F.M. Goycoolea, W. Arguelles-Monal, J. Desbrieres, M. Rinaudo, An infrared investigation in relation with chitin and chitosan characterization. Polymer. 42 (2001) 3569-3580.

[35] A. Baxter, M. Dillon, K.D. Taylor, G.A. Roberts, Improved method for i.r. determination of the degree of N-acetylation of chitosan, Int J Biol Macromol. 14 (1992) 166-169.

[36] R.A.A. Muzzarelli, R. Rocchetti, Determination of the degree of acetylation of chitosans by first derivative ultraviolet spectrophotometry. Carbohydr. Polym. 5 (1985) 461-472.

[37] M. Rinaudo, D.P. Le, C. Gey, M. Milas, Substituent distribution on O,N-carboxymethylchitosans by 1H and 13C n.m.r, Int J Biol Macromol. 14 (1992) 122-128.

[38] H. Saito, R. Tabeta, K. Ogawa, High-resolution solid-state carbon-13 NMR study of chitosan and its salts with acids: conformational characterization of polymorphs and helical structures as viewed from the conformation-dependent carbon-13 chemical shifts. Macromolecules. 20 (1987) 2424-2430.

[39] L. Raymond, F.G. Morin, R.H. Marchessault, Degree of deacetylation of chitosan using conductometric titration and solid-state NMR. Carbohydr. Res. 246 (1993) 331-336.

[40] A. Pelletier, I. Lemire, J. Sygusch, E. Chornet, R.P. Overend, Chitin/chitosan transformation by thermo-mechano-chemical treatment including characterization by enzymic depolymerization. Biotechnol. Bioeng. 36 (1990) 310-315.

[41] K.M. Vårum, M.W. Antohonsen, H. Grasdalen, O. Smidsrød, Determination of the degree of N-acetylation and the distribution of N-acetyl groups in partially N-deacetylated chitins (chitosans) by high-field n.m.r. spectroscopy, Carbohydrate Research. 211 (1991) 17-23.

[42] K.M. Vårum, M.W. Anthonsen, H. Grasdalen, O. Smidsrød, 13C-N.m.r. studies of the acetylation sequences in partially N-deacetylated chitins (chitosans), Carbohydrate Research. 217 (1991) 19-27.

[43] M. Rinaudo, Main properties and current applications of some polysaccharides as biomaterials. Polym. Int. 57 (2008) 397-430.

[44] J. Zhang, W. Xia, P. Liu, Q. Cheng, T. Tahi, W. Gu, et al., Chitosan modification and pharmaceutical/biomedical applications, Marine drugs. 8 (2010) 1962-1987.

[45] V.K. Thakur, M.K. Thakur, Recent Advances in Graft Copolymerization and Applications of Chitosan: A Review. ACS Sustainable Chem. Eng. 2 (2014) 2637-2652.

[46] F. Shahidi, J.K.V. Arachchi, Y. Jeon, Food applications of chitin and chitosans, Trends Food Sci. Technol. 10 (1999) 37-51.

[47] M.S. Benhabiles, R. Salah, H. Lounici, N. Drouiche, M.F.A. Goosen, N. Mameri, Antibacterial activity of chitin, chitosan and its oligomers prepared from shrimp shell waste. Food Hydrocolloids. 29 (2012) 48-56.

[48] Y.J. Jing, Y.J. Hao, H. Qu, Y. Shan, D.S. Li, R.Q. Du, Studies on the antibacterial activities and mechanisms of chitosan obtained from cuticles of housefly larvae, Acta Biol Hung. 58 (2007) 75-86.

[49] A.P. Martínez-Camacho, M.O. Cortez-Rocha, J.M. Ezquerra-Brauer, A.Z. Graciano-Verdugo, F. Rodriguez-Félix, M.M. Castillo-Ortega, et al., Chitosan composite films: Thermal, structural, mechanical and antifungal properties, Carbohydrate Polymers. 82 (2010) 305-315.

[50] H. Möller, S. Grelier, P. Pardon, V. Coma, Antimicrobial and physicochemical properties of chitosan– hpmc-based films, J. Agric. Food Chem. 52 (2004) 6585-6591.

[51] E.I. Rabea, M.E. Badawy, C.V. Stevens, G. Smagghe, W. Steurbaut, Chitosan as antimicrobial agent: applications and mode of action, Biomacromolecules. 4 (2003) 1457-1465.

[52] S. Roller, N. Covill, The antifungal properties of chitosan in laboratory media and apple juice, International Journal of Food Microbiology. 47 (1999) 67-77.

[53] I. Helander, E. Nurmiaho-Lassila, R. Ahvenainen, J. Rhoades, S. Roller, Chitosan disrupts the barrier properties of the outer membrane of Gram-negative bacteria, Int. J. Food Microbiol. 71 (2001) 235-244.

[54] M. Másson, J. Holappa, M. Hjálmarsdóttir, ÖV. Rúnarsson, T. Nevalainen, T. Järvinen, Antimicrobial activity of piperazine derivatives of chitosan, Carbohydr. Polym. 74 (2008) 566-571.

[55] V. Coma, A. Martial-Gros, S. Garreau, A. Copinet, F. Salin, A. Deschamps, Edible antimicrobial films based on chitosan matrix, J. Food Sci. 67 (2002) 1162-1169.

[56] Assis, Odílio Benedito Garrido de, R. Bernardes-Filho, D.d.C. Vieira, S.C. Filho, AFM characterization of chitosan self-assembled films, Int. J. Polym. Mater. 51 (2002) 633-638.

[57] H.K. No, N.Y. Park, S.H. Lee, S.P. Meyers, Antibacterial activity of chitosans and chitosan oligomers with different molecular weights, Int. J. Food Microbiol. 74 (2002) 65-72.

[58] L. Zheng, J. Zhu, Study on antimicrobial activity of chitosan with different molecular weights, Carbohydr. Polym. 54 (2003) 527-530.

[59] A.B. Vishu Kumar, M.C. Varadaraj, L.R. Gowda, R.N. Tharanathan, Characterization of chito-oligosaccharides prepared by chitosanolysis with the aid of papain and Pronase, and their bactericidal action against Bacillus cereus and Escherichia coli, Biochem. J. 391 (2005) 167-175.

[60] P. Srinivasa, R. Tharanathan, Chitin/chitosan—Safe, ecofriendly packaging materials with multiple potential uses, Food Rev. Int. 23 (2007) 53-72.

[61] H. No, S.P. Meyers, W. Prinyawiwatkul, Z. Xu, Applications of chitosan for improvement of quality and shelf life of foods: a review, J. Food Sci. 72 (2007) R87-R100.

[62] M. Dash, F. Chiellini, R.M. Ottenbrite, E. Chiellini, Chitosan—A versatile semi-synthetic polymer in biomedical applications, Progress in polymer science. 36 (2011) 981-1014.

[63] S. Islam, M.R. Bhuiyan, M. Islam, Chitin and chitosan: structure, properties and applications in biomedical engineering, Journal of Polymers and the Environment. 25 (2017) 854-866.

[64] H.K. No, S.P. Meyers, Application of chitosan for treatment of wastewaters, Reviews of environmental contamination and toxicology, Springer, 2000, pp. 1-27.

[65] S.K. Yong, M. Shrivastava, P. Srivastava, A. Kunhikrishnan, N. Bolan, Environmental Applications of Chitosan and Its Derivatives. Rev. Environ. Contam. Toxicol. 233 (2015) 1-43.

[66] D.J. Macquarrie, J.J. Hardy, Applications of functionalized chitosan in catalysis, Ind Eng Chem Res. 44 (2005) 8499-8520.

[67] A.K. Singla, M. Chawla, Chitosan: some pharmaceutical and biological aspects-an update. J. Pharm. Pharmacol. 53 (2001) 1047-1067.

[68] L. Ma, C. Gao, Z. Mao, J. Zhou, J. Shen, X. Hu, et al., Collagen/chitosan porous scaffolds with improved biostability for skin tissue engineering. Biomaterials. 24 (2003) 4833-4841.

[69] M. Ho, D. Wang, H. Hsieh, H. Liu, T. Hsien, J. Lai, et al., Preparation and characterization of RGD-immobilized chitosan scaffolds. Biomaterials. 26 (2005) 3197-3206.

[70] K.G. Ramawat, J. Mérillon, Polysaccharides: bioactivity and biotechnology, Springer 2015.

[71] C. Peniche, W. Arguelles-Monal, H. Peniche, N. Acosta, Chitosan: An attractive biocompatible polymer for microencapsulation. Macromol. Biosci. 3 (2003) 511-520.

[72] K. Kofuji, C. Qian, M. Nishimura, I. Sugiyama, Y. Murata, S. Kawashima, Relationship between physicochemical characteristics and functional properties of chitosan, European Polymer Journal. 41 (2005) 2784-2791.

[73] I. Jabbal-Gill, P. Watts, A. Smith, Chitosan-based delivery systems for mucosal vaccines, Expert opinion on drug delivery. 9 (2012) 1051-1067.

[74] S. Hirano, M. Zhang, M. Nakagawa, T. Miyata, Wet spun chitosan-collagen fibers, their chemical N-modifications, and blood compatibility. Biomaterials. 21 (2000) 997-1003.

[75] Y. Suzuki, K. Miyatake, Y. Okamoto, E. Muraki, S. Minami, Influence of the chain length of chitosan on complement activation, Carbohydrate Polymers. 54 (2003) 465-469.

[76] G. Brandenberg, L.G. Leibrock, R. Shuman, W.G. Malette, H. Quigley, Chitosan: a new topical hemostatic agent for diffuse capillary bleeding in brain tissue, Neurosurgery. 15 (1984) 9-13.

[77] G. Galed, M.E. Fernandez-Valle, A. Martinez, A. Heras, Application of MRI to monitor the process of ripening and decay in citrus treated with chitosan solutions. Magn. Reson. Imaging. 22 (2004) 127-137.

[78] I. Leceta, S. Molinaro, P. Guerrero, J.P. Kerry, K. de la Caba, Quality attributes of map packaged ready-to-eat baby carrots by using chitosan-based coatings, Postharvest Biology and Technology. 100 (2015) 142-150.

[79] A. Alishahi, M. Aïder, Applications of chitosan in the seafood industry and aquaculture: a review, Food and Bioprocess Technology. 5 (2012) 817-830.

[80] N. Bordenave, S. Grelier, F. Pichavant, V. Coma, Water and moisture susceptibility of chitosan and paper-based materials: Structure–property relationships, J. Agric. Food Chem. 55 (2007) 9479-9488.

[81] M. Friedman, V.K. Juneja, Review of antimicrobial and antioxidative activities of chitosans in food, J. Food Prot. 73 (2010) 1737-1761.

[82] R. Morsy, S.S. Ali, M. El-Shetehy, Development of hydroxyapatite-chitosan gel sunscreen combating clinical multidrug-resistant bacteria, Journal of Molecular Structure. 1143 (2017) 251-258.

[83] M. Vakili, M. Rafatullah, B. Salamatinia, A.Z. Abdullah, M.H. Ibrahim, K.B. Tan, et al., Application of chitosan and its derivatives as adsorbents for dye removal from water and wastewater: A review. Carbohydr. Polym. 113 (2014) 115-130.

[84] P.O. Boamah, Y. Huang, M. Hua, Q. Zhang, J. Wu, J. Onumah, et al., Sorption of heavy metal ions onto carboxylate chitosan derivatives-A mini-review. Ecotoxicol. Environ. Saf. 116 (2015) 113-120.

[85] V.S. Tran, H.H. Ngo, W. Guo, J. Zhang, S. Liang, C. Ton-That, et al., Typical low cost biosorbents for adsorptive removal of specific organic pollutants from water. Bioresour. Technol. 182 (2015) 353-363.

[86] G.Z. Kyzas, D.N. Bikiaris, Recent modifications of chitosan for adsorption applications: a critical and systematic review. Mar. Drugs. 13 (2015) 312-337, 26.

[87] R.A. Muzzarelli, M. Weckx, O. Filippini, F. Sigon, Removal of trace metal ions from industrial waters, nuclear effluents and drinking water, with the aid of cross-linked N-carboxymethyl chitosan, Carbohydr. Polym. 11 (1989) 293-306.

[88] J.R. Deans, B.G. Dixon, Uptake of Pb2+ and Cu2+ by novel biopolymers, Water Research. 26 (1992) 469-472.

[89] S.Y. Park, K.S. Marsh, J.W. Rhim, Characteristics of different molecular weight chitosan films affected by the type of organic solvents. J. Food Sci. 67 (2002) 194-197.

[90] J. Nunthanid, S. Puttipipatkhachorn, K. Yamamoto, G.E. Peck, Physical properties and molecular behavior of chitosan films, Drug Dev. Ind. Pharm. 27 (2001) 143-157.

[91] Y. Jeon, J.Y. Kamil, F. Shahidi, Chitosan as an edible invisible film for quality preservation of herring and Atlantic cod, J. Agric. Food Chem. 50 (2002) 5167-5178.

[92] J. Antoniou, F. Liu, H. Majeed, H.J. Qazi, F. Zhong, Physicochemical and thermomechanical characterization of tara gum edible films: effect of polyols as plasticizers, Carbohydr. Polym. 111 (2014) 359-365.

[93] M.G.A. Vieira, M.A. da Silva, L.O. dos Santos, M.M. Beppu, Natural-based plasticizers and biopolymer films: A review, European Polymer Journal. 47 (2011) 254-263.

[94] M. Zhang, X.H. Li, Y.D. Gong, N.M. Zhao, X.F. Zhang, Properties and biocompatibility of chitosan films modified by blending with PEG, Biomaterials. 23 (2002) 2641-2648.

[95] K. Ziani, J. Oses, V. Coma, J.I. Maté, Effect of the presence of glycerol and Tween 20 on the chemical and physical properties of films based on chitosan with different degree of deacetylation, LWT - Food Science and Technology. 41 (2008) 2159-2165.

[96] N.E. Suyatma, L. Tighzert, A. Copinet, V. Coma, Effects of hydrophilic plasticizers on mechanical, thermal, and surface properties of chitosan films, J. Agric. Food Chem. 53 (2005) 3950-3957.

[97] M.A. Haq, A. Hasnain, M. Azam, Characterization of edible gum cordia film: Effects of plasticizers, LWT-Food Science and Technology. 55 (2014) 163-169.

[98] M. Darder, M. Colilla, E. Ruiz-Hitzky, Biopolymer– clay nanocomposites based on chitosan intercalated in montmorillonite, Chemistry of Materials. 15 (2003) 3774-3780.

[99] S.F. Wang, L. Shen, Y.J. Tong, L. Chen, I.Y. Phang, P.Q. Lim, et al., Biopolymer chitosan/montmorillonite nanocomposites: Preparation and characterization, Polymer Degradation and Stability. 90 (2005) 123-131.

[100] E. Günister, D. Pestreli, C.H. Ünlü, O. Atıcı, N. Güngör, Synthesis and characterization of chitosan-MMT biocomposite systems, Carbohydr. Polym. 67 (2007) 358-365.

[101] D.F. Xie, V.P. Martino, P. Sangwan, C. Way, G.A. Cash, E. Pollet, et al., Elaboration and properties of plasticised chitosan-based exfoliated nano-biocomposites, Polymer. 54 (2013) 3654-3662.

[102] Q. Li, J. Zhou, L. Zhang, Structure and properties of the nanocomposite films of chitosan reinforced with cellulose whiskers, Journal of Polymer Science Part B: Polymer Physics. 47 (2009) 1069-1077.

[103] H.M. Azeredo, L.H.C. Mattoso, R.J. Avena-Bustillos, G.C. Filho, M.L. Munford, D. Wood, et al., Nanocellulose reinforced chitosan composite films as affected by nanofiller loading and plasticizer content, J. Food Sci. 75 (2010) N1-N7.

[104] S. Wang, L. Shen, W. Zhang, Y. Tong, Preparation and mechanical properties of chitosan/carbon nanotubes composites, Biomacromolecules. 6 (2005) 3067-3072.

[105] C. Tang, L. Xiang, J. Su, K. Wang, C. Yang, Q. Zhang, et al., Largely improved tensile properties of chitosan film via unique synergistic reinforcing effect of carbon nanotube and clay, The Journal of Physical Chemistry B. 112 (2008) 3876-3881.

[106] Y. Liu, W. Chen, Y. Chang, Preparation and properties of chitosan/carbon nanotube nanocomposites using poly(styrene sulfonic acid)-modified CNTs, Carbohydr. Polym. 76 (2009) 232-238.

[107] X. Yang, Y. Tu, L. Li, S. Shang, X. Tao, Well-dispersed chitosan/graphene oxide nanocomposites, ACS applied materials & interfaces. 2 (2010) 1707-1713.

[108] H. Fan, L. Wang, K. Zhao, N. Li, Z. Shi, Z. Ge, et al., Fabrication, mechanical properties, and biocompatibility of graphene-reinforced chitosan composites, Biomacromolecules. 11 (2010) 2345-2351.

[109] D. Han, L. Yan, W. Chen, W. Li, Preparation of chitosan/graphene oxide composite film with enhanced mechanical strength in the wet state, Carbohydr. Polym. 83 (2011) 653-658.

[110] Y. Pan, T. Wu, H. Bao, L. Li, Green fabrication of chitosan films reinforced with parallel aligned graphene oxide, Carbohydr. Polym. 83 (2011) 1908-1915.

[111] H. Lim, N. Huang, C. Loo, Facile preparation of graphene-based chitosan films: Enhanced thermal, mechanical and antibacterial properties, J. Non Cryst. Solids. 358 (2012) 525-530.

[112] R. Justin, B. Chen, Characterisation and drug release performance of biodegradable chitosan–graphene oxide nanocomposites, Carbohydr. Polym. 103 (2014) 70-80.

[113] H. Bao, Y. Pan, Y. Ping, N.G. Sahoo, T. Wu, L. Li, et al., Chitosan-functionalized graphene oxide as a nanocarrier for drug and gene delivery, Small. 7 (2011) 1569-1578.

[114] V.K. Rana, M. Choi, J. Kong, G.Y. Kim, M.J. Kim, S. Kim, et al., Synthesis and drug-delivery behavior of chitosan-functionalized graphene oxide hybrid nanosheets, Macromolecular Materials and Engineering. 296 (2011) 131-140.

[115] R. Justin, B. Chen, Strong and conductive chitosan–reduced graphene oxide nanocomposites for transdermal drug delivery, Journal of Materials Chemistry B. 2 (2014) 3759-3770.

[116] T.Y. Ko, S.Y. Kim, H.G. Kim, G. Moon, I. In, Antibacterial activity of chemically reduced graphene oxide assembly with chitosan through noncovalent interactions, Chem. Lett. 42 (2012) 66-67.

[117] M. Fang, J. Long, W. Zhao, L. Wang, G. Chen, pH-responsive chitosan-mediated graphene dispersions, Langmuir. 26 (2010) 16771-16774.

[118] J.H. Lee, J. Marroquin, K.Y. Rhee, S.J. Park, D. Hui, Cryomilling application of graphene to improve material properties of graphene/chitosan nanocomposites, Composites Part B: Engineering. 45 (2013) 682-687.

[119] Z. Yenier, Y. Seki, İ Şen, K. Sever, Ö Mermer, M. Sarikanat, Manufacturing and mechanical, thermal and electrical characterization of graphene loaded chitosan composites, Composites Part B: Engineering. 98 (2016) 281-287.

[120] J. Jagiello, J. Judek, M. Zdrojek, M. Aksienionek, L. Lipinska, Production of graphene composite by direct graphite exfoliation with chitosan, Materials Chemistry and Physics. 148 (2014) 507-511.

[121] C. Demitri, A. Moscatello, A. Giuri, M.G. Raucci, C. Esposito Corcione, Preparation and characterization of eg-chitosan nanocomposites via direct exfoliation: A green methodology, Polymers. 7 (2015) 2584-2594.

[122] T. Sreeprasad, M.S. Maliyekkal, K. Deepti, K. Chaudhari, P.L. Xavier, T. Pradeep, Transparent, luminescent, antibacterial and patternable film forming composites of graphene oxide/reduced graphene oxide, ACS applied materials & interfaces. 3 (2011) 2643-2654.

[123] D.S. Kim, V. Dhand, K.Y. Rhee, S. Park, Study on the effect of silanization and improvement in the tensile behavior of graphene-chitosan-composite, Polymers. 7 (2015) 527-551.

[124] Y. Pan, H. Bao, L. Li, Noncovalently functionalized multiwalled carbon nanotubes by chitosan-grafted reduced graphene oxide and their synergistic reinforcing effects in chitosan films, ACS applied materials & interfaces. 3 (2011) 4819-4830.

[125] Y. Wang, Y. Li, L. Tang, J. Lu, J. Li, Application of graphene-modified electrode for selective detection of dopamine, Electrochemistry Communications. 11 (2009) 889-892.

[126] H. Xu, H. Dai, G. Chen, Direct electrochemistry and electrocatalysis of hemoglobin protein entrapped in graphene and chitosan composite film, Talanta. 81 (2010) 334-338.

[127] S. Sayyar, E. Murray, B. Thompson, J. Chung, D.L. Officer, S. Gambhir, et al., Processable conducting graphene/chitosan hydrogels for tissue engineering, Journal of Materials Chemistry B. 3 (2015) 481-490.

[128] Y. Wang, Z. Shi, J. Yin, Facile synthesis of soluble graphene via a green reduction of graphene oxide in tea solution and its biocomposites, ACS applied materials & interfaces. 3 (2011) 1127-1133.

[129] P. Li, K. Cheng, X. Zheng, P. Liu, X. Xu, Facile synthesis of water-soluble graphene-based composite: Non-covalently functionalized with chitosan-ionic liquid conjugation, Functional Materials Letters. 9 (2016) 1650045.

[130] X. Wang, H. Bai, Z. Yao, A. Liu, G. Shi, Electrically conductive and mechanically strong biomimetic chitosan/reduced graphene oxide composite films, Journal of Materials Chemistry. 20 (2010) 9032-9036.

[131] Z. Tang, C. Zeng, Y. Lei, B. Guo, L. Zhang, D. Jia, Fluorescent whitening agent stabilized graphene and its composites with chitosan, Journal of Materials Chemistry. 21 (2011) 17111-17118.

[132] M. Muralidharan, K. Shinu, A. Seema, Optically triggered actuation in chitosan/reduced graphene oxide nanocomposites, Carbohydr. Polym. 144 (2016) 115-121.

[133] Y. Si, J. Liu, A. Wang, S. Niu, J. Wan, A chitosan-graphene electrochemical sensor for the determination of copper (II), Instrum Sci Technol. 43 (2015) 357-368.

[134] P. Deng, Z. Xu, Y. Kuang, Electrochemical determination of bisphenol A in plastic bottled drinking water and canned beverages using a molecularly imprinted chitosan–graphene composite film modified electrode, Food Chemistry. 157 (2014) 490-497.

[135] W. Sun, J. Liu, X. Wang, T. Li, G. Li, J. Wu, et al., Electrochemical oxidation of adenosine-5'-triphosphate on a chitosan–graphene composite modified carbon ionic liquid electrode and its determination, Materials Science and Engineering: C. 32 (2012) 2129-2134.

[136] Q. Wang, Y. Wang, S. Liu, L. Wang, F. Gao, F. Gao, et al., Voltammetric detection of bisphenol a by a chitosan–graphene composite modified carbon ionic liquid electrode, Thin Solid Films. 520 (2012) 4459-4464.

[137] M.H. Ottey, K.M. Vårum, O. Smidsrød, Compositional heterogeneity of heterogeneously deacetylated chitosans, Carbohydrate Polymers. 29 (1996) 17-24.

[138] S.F. Tanner, H. Chanzy, M. Vincendon, J.C. Roux, F. Gaill, High-resolution solid-state carbon-13 nuclear magnetic resonance study of chitin, Macromolecules. 23 (1990) 3576-3583.

[139] L. Heux, J. Brugnerotto, J. Desbrieres, M. Versali, M. Rinaudo, Solid state NMR for determination of degree of acetylation of chitin and chitosan, Biomacromolecules. 1 (2000) 746-751.

[140] G. Lawrie, I. Keen, B. Drew, A. Chandler-Temple, L. Rintoul, P. Fredericks, et al., Interactions between alginate and chitosan biopolymers characterized using FTIR and XPS, Biomacromolecules. 8 (2007) 2533-2541.

[141] K.H. Prashanth, F. Kittur, R. Tharanathan, Solid state structure of chitosan prepared under different N-deacetylating conditions, Carbohydr. Polym. 50 (2002) 27-33.

[142] K. Ogawa, S. Hirano, T. Miyanishi, T. Yui, T. Watanabe, A new polymorph of chitosan, Macromolecules. 17 (1984) 973-975.

[143] I. Quijada-Garrido, V. Iglesias-González, J. Mazón-Arechederra, J. Barrales-Rienda, The role played by the interactions of small molecules with chitosan and their transition temperatures. Glass-forming liquids: 1, 2, 3-Propantriol (glycerol), Carbohydr. Polym. 68 (2007) 173-186.

[144] M. Bengisu, E. Yilmaz, Oxidation and pyrolysis of chitosan as a route for carbon fiber derivation, Carbohydr. Polym. 50 (2002) 165-175.

[145] A. Pawlak, M. Mucha, Thermogravimetric and FTIR studies of chitosan blends, Thermochimica acta. 396 (2003) 153-166.

[146] G. Cardenas, S.P. Miranda, FTIR and TGA studies of chitosan composite films, Journal of the Chilean Chemical Society. 49 (2004) 291-295.

[147] T. Wanjun, W. Cunxin, C. Donghua, Kinetic studies on the pyrolysis of chitin and chitosan, Polym. Degrad. Stab. 87 (2005) 389-394.

[148] A. Azeez, K. Rhee, S. Park, H. Kim, D. Jung, Application of cryomilling to enhance material properties of carbon nanotube reinforced chitosan nanocomposites, Composites Part B: Engineering. 50 (2013) 127-134.

[149] L. He, L. Yao, D. Yang, Q. Cheng, J. Sun, R. Song, et al., Preparation and characterization of chitosan-blended multiwalled carbon nanotubes, Journal of Macromolecular Science, Part B. 50 (2011) 2454-2463.

[150] C. Tang, N. Chen, Q. Zhang, K. Wang, Q. Fu, X. Zhang, Preparation and properties of chitosan nanocomposites with nanofillers of different dimensions, Polym. Degrad. Stab. 94 (2009) 124-131.

[151] A. Hussein, S. Sarkar, D. Oh, K. Lee, B. Kim, Epoxy/p-phenylenediamine functionalized graphene oxide composites and evaluation of their fracture toughness and tensile properties, J Appl Polym Sci. 133 (2016).

[152] S. Morimune, T. Nishino, T. Goto, Poly (vinyl alcohol)/graphene oxide nanocomposites prepared by a simple eco-process, Polym. J. 44 (2012) 1056.

[153] X. Yang, S. Shang, L. Li, Layer-structured poly (vinyl alcohol)/graphene oxide nanocomposites with improved thermal and mechanical properties, J Appl Polym Sci. 120 (2011) 1355-1360.

[154] A. Ashori, Effects of graphene on the behavior of chitosan and starch nanocomposite films, Polymer Engineering & Science. 54 (2014) 2258-2263.

[155] E.F. Morgan, T.M. Keaveny, Dependence of yield strain of human trabecular bone on anatomic site, Journal of Biomechanics. 34 (2001) 569-577.

[156] T.A. Khan, K.K. Peh, H.S. Ch'ng, Mechanical, bioadhesive strength and biological evaluations of chitosan films for wound dressing. J. Pharm. Pharm. Sci. 3 (2000) 303-311.

[157] K. Liao, Y. Lin, C.W. Macosko, C.L. Haynes, Cytotoxicity of graphene oxide and graphene in human erythrocytes and skin fibroblasts, ACS applied materials & interfaces. 3 (2011) 2607-2615.

[158] Y. Zhang, S.F. Ali, E. Dervishi, Y. Xu, Z. Li, D. Casciano, et al., Cytotoxicity effects of graphene and single-wall carbon nanotubes in neural phaeochromocytoma-derived PC12 cells, ACS nano. 4 (2010) 3181-3186.

[159] G. Lalwani, M. D'Agati, A.M. Khan, B. Sitharaman, Toxicology of graphene-based nanomaterials, Advanced Drug Delivery Reviews. 105 (2016) 109-144.

[160] N. Guitian Oliveira, T. Sirgado, L. Reis, L.F.V. Pinto, C.L. da Silva, F.C. Ferreira, et al., In vitro assessment of three dimensional dense chitosan-based structures to be used as bioabsorbable implants, Journal of the Mechanical Behavior of Biomedical Materials. 40 (2014) 413-425.

[161] M. Lavorgna, F. Piscitelli, P. Mangiacapra, G.G. Buonocore, Study of the combined effect of both clay and glycerol plasticizer on the properties of chitosan films, Carbohydr. Polym. 82 (2010) 291-298.

[162] D. Adame, G.W. Beall, Direct measurement of the constrained polymer region in polyamide/clay nanocomposites and the implications for gas diffusion, Appl. Clay. Sci. 42 (2009) 545-552.

[163] Y. Rao, J.M. Pochan, Mechanics of polymer– clay nanocomposites, Macromolecules. 40 (2007) 290-296.

[164] J.B. Marroquin, K.Y. Rhee, S.J. Park, Chitosan nanocomposite films: Enhanced electrical conductivity, thermal stability, and mechanical properties, Carbohydrate Polymers. 92 (2013) 1783-1791.

[165] T. Zhou, X. Qi, H. Bai, Q. Fu, The different effect of reduced graphene oxide and graphene oxide on the performance of chitosan by using homogenous fillers, RSC Advances. 6 (2016) 34153-34158.

[166] W. Bauhofer, J.Z. Kovacs, A review and analysis of electrical percolation in carbon nanotube polymer composites, Composites Science and Technology. 69 (2009) 1486-1498.

[167] J.R. Potts, D.R. Dreyer, C.W. Bielawski, R.S. Ruoff, Graphene-based polymer nanocomposites, Polymer. 52 (2011) 5-25.

[168] F.H. Gojny, M.H.G. Wichmann, B. Fiedler, I.A. Kinloch, W. Bauhofer, A.H. Windle, et al., Evaluation and identification of electrical and thermal conduction mechanisms in carbon nanotube/epoxy composites, Polymer. 47 (2006) 2036-2045.

[169] P. Fernandez-Saiz, J. Lagaron, M. Ocio, Optimization of the film-forming and storage conditions of chitosan as an antimicrobial agent, J. Agric. Food Chem. 57 (2009) 3298-3307.

[170] H.K. No, S.H. Kim, S.H. Lee, N.Y. Park, W. Prinyawiwatkul, Stability and antibacterial activity of chitosan solutions affected by storage temperature and time, Carbohydr. Polym. 65 (2006) 174-178.

CHAPTER 4

POLY(VINYL ALCOHOL)/GRAPHENE NANOCOMPOSITES

In the last chapter, the reinforcing effect of GO and GS on the chitosan polymer matrix was discussed. The properties of the unplasticized and plasticized nanocomposite films were altered depending on the type and content of the fillers. In the same manner, this chapter will assess the structural, thermal, mechanical, permeability and water absorption analysis of the poly(vinyl alcohol)/graphene-based nanocomposites. Specifically, glycerol-plasticized and unplasticized nanocomposites containing GO were prepared, as well as nanocomposites with chemically reduced graphene (GS), achieved by in situ reduction of GO in a PVA solution using L-AA as an environmentally friendly reducer. Furthermore, in order to provide the PVA matrix with antimicrobial character, PVA/silver nanoparticles-graphene oxide nanocomposites (PVA/AgNPs-GO) were also developed and studied. For the synthesis, one-step process was used (with L-AA as a reducing agent and AgNO₃), and also a solution casting method incorporating a partially reduced graphene oxide decorated with silver nanoparticles (GO-AgNPs) hybrid as a reinforcing filler (the hybrid synthetized and described in Chapter 2). Thus, exhaustive antimicrobial assays were conducted to examine the antibacterial activity of the films against *Staphylococcus aureus* and *Escherichia coli*.

Part of the results presented in this chapter have allowed the publication of three different papers in the following journals: Nanomaterials (2018), Carbon (2019) and Polymers (2020).

INDEX

4.1. Introduction

Poly(vinyl alcohol) (PVA) is a synthetic and highly hydrophilic polymer whose chemical structure contains mainly 1,3-diol units (Figure 4.1). Being a polyhydroxy, polymer chains are capable of undergoing both intra and intermolecular hydrogen bonding. The small size and the strong hydrogen bond interactions of the hydroxyl groups force the polymer chains into a crystal lattice resulting in partially crystalline PVA. Over the last decade, much attention has been recorded in PVA as biocompatible, low cytotoxic and biodegradable (under both aerobic and anaerobic conditions) polymer for biomedical and biomaterial research fields.
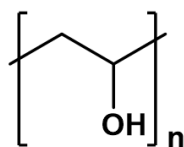
Figure 4.1. Chemical structure of PVA.

PVA is unique among polymers in the sense that it cannot be synthesized directly by traditional polymerization because its monomer, vinyl alcohol, is not stable and tautomerizes to more stable acetaldehyde (Figure 4.2A). This polymer was first synthesized in 1924 by Hermann and Haehnel *via* saponification of poly(vinyl ester) with a sodium hydroxide solution [1]. However, the conventional method for the synthesis consists of two-step process, being the first the synthesis of the precursor, poly(vinyl acetate) (PVAc), and the second, the conversion of PVAc to PVA (Figure 4.2B). The method used is free radical polymerization of vinyl acetate, followed by different conversion methods to reach PVA. Conversion involves partial or total replacement of the ester group of vinyl acetate by hydroxyl groups. Finally, PVA is washed and dried.

Polyvinyl acetate can be converted to PVA by transesterification, hydrolysis or aminolysis (Figure 4.2C) [2]. Transesterification and hydrolysis can be either base or acid catalyzed. The usual base catalysts are sodium or potassium hydroxide and sodium methoxide, while the acid catalysts are hydrochloric and sulphuric acids. The degree of hydrolysis achieved depends on the amount of catalyst/hydrolyser, the duration and temperature of the reaction.
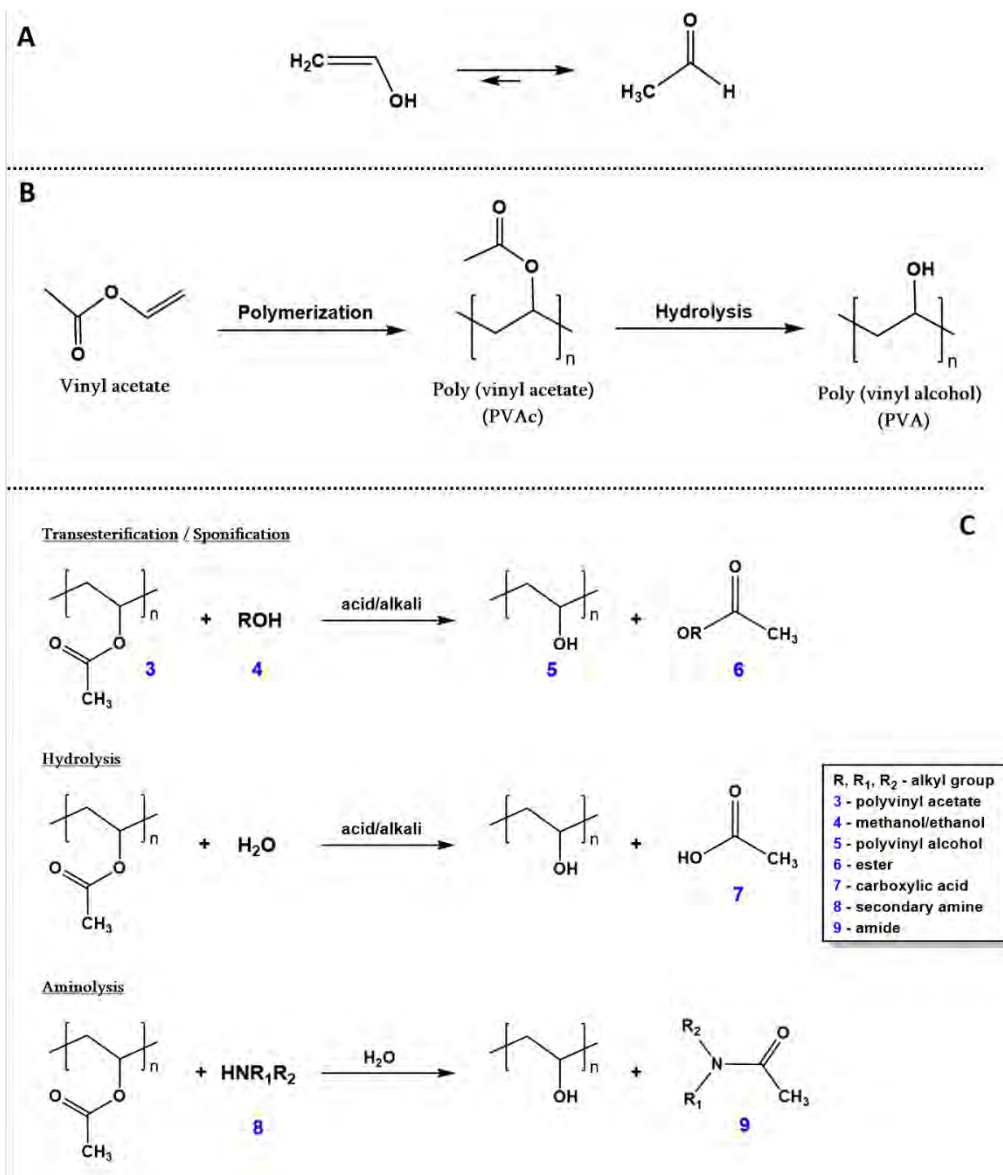
Figure 4.2. (A) Tautomerization of vinyl alcohol to acetaldehyde. (B) Conventional method for the synthesis of PVA. (C) Conversion of poly(vinyl acetate) to poly(vinyl alcohol).

In the field of chemistry, PVA is used for the synthesis of poly(vinyl butyral) (PVB) and vinyl fibers. PVB is a low-cost flexible thermoplastic that is employed as a strong adhesive in many applications. Vinyl is a heat and chemical resistant fiber that is widely used in textiles, quilting and rope.

4.1.1. Physical and chemical properties of PVA

Poly(vinyl alcohol) is one of the few linear non-halogenated aliphatic polymers with excellent film forming, emulsifying, stabilizing and adhesive properties [3]. Also, it is odorless, nontoxic and biocompatible. This polymer is an example of semi-crystalline synthetic water-soluble polymer. However, it is slightly soluble in ethanol and insoluble in other organic solvents. PVA is a cheap polymer and easily available in white powder form.

The physical properties as water solubility, mechanical strength, gas permeability, adhesion, diffusion, thermal and stabilizing properties of PVA vary significantly with the degree of crystallinity, which is heavily dependent on the degree of hydrolysis (DH) and degree of polymerization (DP) or what is the same, the length of the chain. The molecular weight of PVA generally ranging between 20,000-400,000 g/mol [1].

Polyvinyl alcohols are usually classified according to their DH into fully (98-98.8 mol%), intermediate (90-97 mol%), and partially (87-89 mol%) hydrolyzed grades. However, commercially PVA is classified as fully or partially hydrolyzed (Figure 4.3). Commonly is considered quite high DH above 70%, otherwise it would be closer to the original. Since this chemical modification often is uncompleted the name PVA can also be found as the abbreviation for the copolymer of vinyl acetate and vinyl alcohol, P(VAc-co-VA).
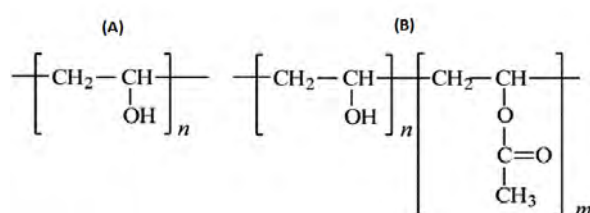
Figure 4.3. (A) PVA structure completely hydrolyzed and (B) partially hydrolyzed PVA.

Regarding thermal characterization, the glass transition (T_g) of PVA changes with the degree of hydrolysis. Temperatures around 85 °C are known for 98-98.8% hydrolyzed PVA and 58 °C for 87-89% hydrolyzed PVA [4]. Generally, an increase in relative humidity leads to a linear decrease in the T_g of PVA as a result of the plasticizing effect of water on the polymer structure. The melting

point of fully hydrolyzed PVA is higher than that of partially hydrolyzed PVA, 230 °C and 180-190 °C respectively [5-7]. Generally, completely hydrolyzed PVA is not considered a thermoplastic polymer because its melting temperature is very close to the degradation temperature. Therefore, plasticizers are often used with PVA to control the melting temperature, fluidity and thermal stability, mainly for screw extrusion and injection molding processes widely used in packaging applications [8-10]. However, the strong inter and intramolecular hydrogen bonds between the hydroxyl groups generally make fusion processing difficult, so PVA is mainly processed from aqueous solutions.

Thermal degradation of PVA can be described taking into account the state of the polymer: molten or solid state [11]. In the melt state, the degradation process is explained as a random chain splitting resulting in volatile products such as acetaldehyde in addition to ketones. Nevertheless, in the solid state the degradation process is described by the removal of water at a temperature below the melting point to produce carboxylic groups in addition to water. In general, the PVA thermal degradation is detailed with different stages. In the first stage, water loss is observed at around 100 °C. In the second stage between 206 °C and 357 °C, PVA loses approximately 80% of its weight due to dehydration, chain excision and decomposition. Finally, degradation of the by-product takes place at 387-450 °C to complete the degradation process [12].

The crystallization capacity of PVA is affected by the presence of acetate groups, and therefore partially hydrolyzed PVA is more difficult to crystallize. The high crystallization of PVA compared to PVAc can be attributed to the fact that the hydroxyl groups are sufficiently small to allow the chains to adopt a planar zig-zag conformation [13,14].

PVA water solubility mentioned above, depends on the degree of hydrolysis, molecular weight, crystallinity and temperature. Fully hydrolyzed PVA requires high temperatures to dissolve in water, above 90 °C, due to the strong intramolecular and intermolecular hydrogen bonds between the hydroxyl groups in the chain. In partially hydrolyzed PVA, the residual acetate groups weaken the hydrogen bonds and are therefore more soluble at low temperatures. A higher degree of hydrolysis and a higher degree of PVA polymerization mean a lower solubility in cold water [15].

In addition to DH and DP, the viscosity of PVA solution depends on polymer concentration, temperature, stereo-regularity of polymer chains, and thermal history [11]. Moreover, a 5% solution of polyvinyl alcohol exhibits a pH in the range of 5.0 to 6.5. Figure 4.4 summarizes how the properties of PVA based materials vary depending on the degree of hydrolysis and molecular weight.
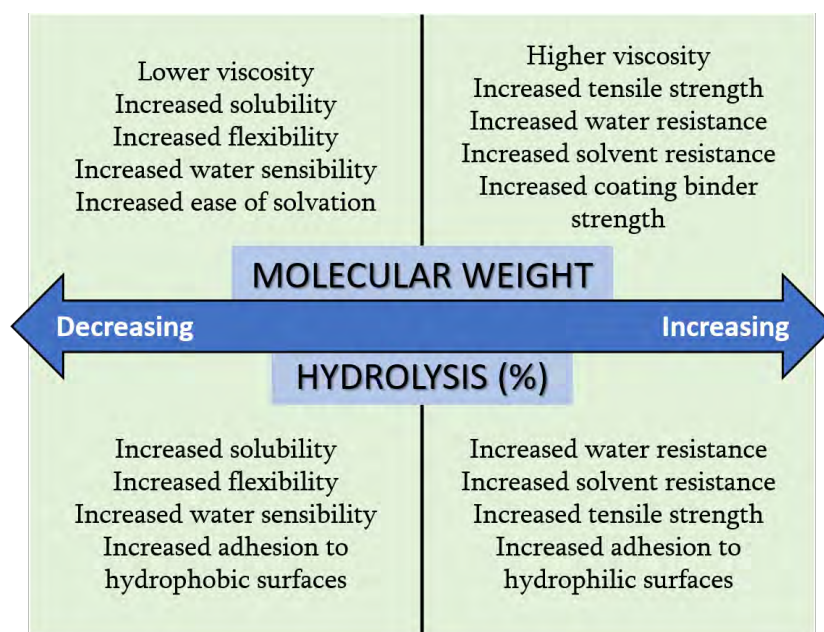
Figure 4.4. PVA properties according to the molecular weight and hydrolysis level [8].

It is worth highlighting that PVA has excellent mechanical and thermal properties, excellent oxygen barrier properties, oil, grease and organic solvent resistance, low moisture permeability, odorless, high heat resistance, UV and IR radiation stability and excellent film forming properties. Furthermore, it is defined as biodegradable and non-toxic due to its poor gastrointestinal absorption and high lethal dose (LD_{50}), between 15 to 20 g/kg [16]. Therefore, PVA does not accumulate in the body after oral administration, has no adverse effects and is not mutagenic, making it suitable for pharmaceutical and biomedical applications.

PVA is considered a biodegradable polymer because it has the ability to self-decompose in non-toxic carbonaceous solids, water or carbon dioxide in the environment through natural biological processes. This behavior involves the enzymatic oxidation of hydroxyl groups to carbonyl groups in the polymer

backbone, followed by hydrolysis of the carbonyl groups, resulting in the breakdown of the polymer chain and a decrease in molecular weight. However, the biodegradability of PVA is low compared to other biodegradable polymers such as poly(lactic acid) and poly(ε-caprolactone) [17]. The biodegradation process of pure PVA is quite slow, particularly under anaerobic conditions [18]. Degradation rate strongly depends on the residual acetate groups [19]. It has been shown that PVA may not be fully biodegradable in certain environments where some of the necessary conditions are lacking, such as temperature, certain microorganisms, pH level and relative humidity [20]. The biodegradability rate of PVA can be enhanced by blending it with polysaccharide polymers such as starch and cellulose.

PVA is considered a completely transparent polymer with a transparency level of approximately 91% to visible light, although this value might decrease when PVA is blended or reinforced with additives or fillers [21,22]. The transparency of polymers is a function of their crystallinity, thus, the increase in crystallinity results in a decrease in transparency [23].

4.1.2. Morphologies of PVA

PVA can be found in different morphologies depending on its final application [24].

- **Bulk:** The commercially available PVA form.

- **Hydrogels:** Cross-linked polymeric materials in the form of a three-dimensional network that in contact with water have the ability to swell and form elastic, soft, flexible compounds that also retain a significant amount of water inside, but without dissolving. PVA hydrogels can be obtained from chemical crosslinkers such as glutaraldehyde, formaldehyde, acetaldehyde or other monoaldehydes [25,26] and physical crosslinkers by freezing/thawing for different purposes [27,28].

- **Beads:** PVA beads are used to immobilize bacteria, yeasts or compounds, which are used mainly in water purification [29]. The beads are obtained from a saturated solution of boric acid (crosslinker) and by esterification of the PVA with phosphate for solidification.

• **Fibers:** PVA fibers can be acquired by means of electrospining technique. The literature includes graphene-filled PVA nanofibers with excellent mechanical and optical properties [30,31]. Thus, fibers are widely used in flexible photocells, photonic crystals, optoelectronic devices, microelectronics, protective clothing, composite materials, and filter media [32].

• **Films:** Uniform PVA films of high optical quality are used in the manufacture of non-linear optical devices and optical sensors. Several studies have observed luminescence properties of PVA films under different conditions in the wavelength of 400–600 nm [33]. Likewise, other studies have prepared PVA–ZnO nanocomposite films using the casting method to investigate dielectric and charge transport properties [34]. Generally, PVA films are too brittle because of high crystallinity. To overcome these drawbacks **plasticizers** have been incorporated into PVA [2,35-38]. Although water is the most effective plasticizer for PVA, **glycerol** has been widely used due to its low toxicity, environmental friendliness, and its low vapor pressure compared to water or other polyols such as ethylene glycol. Plasticizers form strong hydrogen bonding with the hydroxyl groups of PVA and reduce the inter and intra-molecular hydrogen bonding between PVA chains, which leads to an increase of free volume and chain movements, reducing the melting point, improving flexibility, and handling of films and preventing cracks in the polymeric matrix.

• **Membranes:** PVA matrix plays an essential role in the construction of membranes for fuel cells, the alternative for converting chemical energy into electrical energy [39]. The combination of PVA and polyethyleneimine (PEI) has been used to obtain electrospun membranes employed for the removal of metal ions [40].

• **Scaffolds:** PVA-based microporous 3D scaffolds (three-dimensional porous solid structures) are potential materials used in drug delivery, purification and tissue regeneration processes. An example would be those scaffolds coated with polydopamine (pDA) which showed constructive synergistic interactions between cells and materials promoting healthy stem cell adhesion and viability, or those made with GO to improve the mechanical resistance of PVA [41,42].

4.1.3. <u>PVA blends</u>

At the end of 1960, the commercial development of polymer blends experienced a rapid growth due to the great interest of many researches and especially of the materials industry, since polymer blends offer a great number of different commercial products with desirable properties [43]. The main reason for mixing is to find the required properties for the final applications of the materials, and at the same time, to adjust the cost-benefit balance. In addition, polymer blends provide a useful and economical mean of upgrading recycled polymers. Currently, the development of environmentally friendly polymeric materials is the focus a lot of research. In this sense, PVA has been widely used in the preparation of mixtures and compounds with various natural and renewable polymers.

PVA can be described as an excellent candidate for the preparation of blends due to its ability to produce highly resistant films. The literature includes extensive research into the rheological and structural characterization of materials obtained by mixing PVA, either in solution or in melt, with various natural polymers of plant, animal and marine origin, such as cellulose, lignin, starch, silk, chitin, chitosan and poly(lactic acid). For instance, the strength and flexibility of starch can be significantly improved by co-processing with PVA. However, PVA/starch blend films still have some limitations, such as high hydrophilicity and weak mechanical properties. In general, PVA and starch in the presence of plasticizers have an acceptable compatibility. The use of plasticizers could reduce the tensile strength and Young's modulus of PVA/starch blends, but increase their elongation at break and flexibility [44,45]. Starch is mainly used as a matrix of biopolymers to reduce environmental pollution by improving the biodegradation of other polymers such as PVA [46].

The combination of good mechanical properties and hydrophilicity of PVA and the biological activity of chitosan offers a good opportunity to produce useful hydrogels or blending films with high antimicrobial effects, good strength and high barrier properties to be used in wound dressing [47-50]. However, elongation at break can be a limitation for packaging and other medical applications. In order to improve the properties of PVA/chitosan blends, some studies have added different nanofillers such as montmorillonite and halloysite nanotubes [51-53].

Poly(lactic-acid) (PLA) is a natural, biodegradable, biocompatible and non-toxic aliphatic polyester that can be synthesized from renewable resources such as corn, potato and sugar beet making it an outstanding candidate for blends development [54]. A promising option for high performance packaging applications is PVA/PLA blend as it has good mechanical properties and thermoplasticity [55]. Studies have shown that tensile strength increases significantly with increasing amounts of PVA in mixtures, which is attributed to the increased hydrogen bonds and chemical interactions between the two polymers. The addition of PLA to PVA/starch films is another strategy used to improve their miscibility as well as their mechanical and thermal properties and reduce their water absorption [56].

Poly(ethylene oxide) (PEO), a synthetic polymer, is also used for the production of PVA blends. Particularly, compatibilized PVA/PEO blends are employed to prepare packaging films and bottles, since PEO is a nonpolar polymer with good barrier properties against water, in contrast to PVA films with low permeability to water but high permeability to oxygen [57].

4.1.4. PVA nanocomposites

The dispersion of nanoscale fillers (ranging from 0.1 nm to 100 nm) is the most characteristic property of polymer nanocomposites. These new composite materials have attracted a lot of interest in the last decade, since a synergy can be achieved between fillers and polymer chains, and therefore materials with improved properties can be obtained [58,59]. These improved properties can only be accomplished if the nanofiller is well dispersed in the polymer matrix. PVA is one of the most popular biodegradable polymers reinforced with nanofillers in order to enhance its thermal and barrier properties, especially for food packaging [60]. PVA nanocomposites may include nanofillers of the following types: metal, metal oxides [61], metal sulphides, non-metallic, inorganic or nanofillers of a silicon–oxygen structure bonded to organic groups such as oligomeric polyhedral silsesquioxanes (POSS) [62]. Among inorganic nanofillers, carbon nanofibers, carbon nanotubes, graphene, clays and silicates can be highlighted [39,63]. Considering the amount of different nanofillers, this part of the chapter will focus mainly on PVA metal nanocomposites and PVA/graphene-based nanocomposites.

4.1.4.1. <u>PVA/Metal nanocomposites</u>

According to section 2.1.4.1 in the second chapter, metallic nanoparticles (NPs) have excellent properties that lead to their application in different fields. In particular, silver nanoparticles due to their biological properties, have emerged as the most exploited nano-antimicrobial agents in a variety of applications, for instance, nanocrystalline silver dressings, creams and gels that have effectively reduced bacterial infections in chronic wounds [64].

Poly(vinyl alcohol) can be employed as a stabilizing agent in the synthesis of AgNPs playing a vital role in the formation of nanoparticles with a controlled size and well-defined shape. The preparation and characterization of PVA nanocomposites with different silver contents is reported in several works of research. PVA/AgNPs nanocomposites can be obtained by *ex situ* processes such as mixing a colloidal solution composed of Ag nanoparticles with the appropriate amount of PVA [65], or by *in situ* processes employing gamma irradiation or reducing agents to achieve silver atoms (Ag^0) from silver ions (Ag^+) in an aqueous PVA solution [66,67].

4.1.4.2. <u>PVA/Graphene-based nanocomposites</u>

Several studies have reported the effect of loading of graphene or its derivatives on the properties of PVA-based composites [68-90]. In general, it is known that graphene provides significant improvements in the properties of nanocomposites at low filler content. However, some disparities in thermal and mechanical property values have been reported. These variations are the result of different degrees of interaction between graphene sheets and PVA molecules through hydrogen bonding. The properties of polymer nanocomposites are highly related to the microstructures. A uniform dispersion of nanofiller and absence of agglomerates in the polymer matrix is required to achieve an improvement in the properties.

According to chapter two, graphene is hydrophobic in nature, while PVA is hydrophilic, so the dispersion of the sheets in the polymer is difficult and the formation of agglomerations in the matrix takes place. On the contrary, graphene oxide is hydrophilic, but during the reduction process, GO sheets become more hydrophobic and tend to agglomerate rapidly into flakes of monolayered sheets,

to restack to form graphite. Therefore, the *in situ* reduction of GO dispersed in a polymer matrix is one of the most effective strategies employed to accomplish stable dispersions of graphene [91]. Zhao *et al.* [75] reported the preparation of fully exfoliated graphene/PVA nanocomposites by means of chemical reduction of GO in an aqueous solution containing PVA and dodecylbenzene sulfonate (SDBS) as a stabilizer. The excellent dispersion of graphene in PVA was confirmed due to the disappearance of graphene XRD peak. Also, tensile strength was enhanced by 150% at 1.8 vol% of graphene in the PVA matrix. Yang *et al.* [73] manufactured PVA-graphene nanocomposite films aligned in layers through chemical reduction of GO, adding hydrazine to the PVA/GO solution. The addition of 3.5 wt% graphene in PVA increased tensile strength, Young's modulus and glass transition temperature. However, crystallinity, melting temperature and crystallization temperature decreased.

The main strategy for the preparation of PVA/GO nanocomposites is the solution casting technique, however, there are other ways such as *in situ* intercalative polymerization or melt intercalation. Morimune *et al.* [80] fabricated PVA/GO films *via* ordinary solution casting process. Young's modulus, tensile strength, thermal and barrier properties were significantly improved increasing GO nanofillers content. Jiaojiao *et al.* [87] reported the one-step *in situ* polymerization process that resulted in fully intercalated, highly dispersed and oriented GO along the surface of the nanocomposite film. The mechanical properties were strikingly enhanced at extremely low loadings of GO. Putz *et al.* [72] achieved a highly ordered, homogeneous polymer film of layered graphene oxide using a vacuum-assisted self-assembly (VASA) technique, which has allowed for the recognition that hydrogen bonding plays a crucial role in the mechanical properties. Qi *et al.* [81] used electrospinning technique to prepare PVA/GO scaffolds. The results showed the great potential of PVA/GO nanocomposites to be used in tissue engineering and drug delivery systems.

The research on PVA/graphene based nanocomposites is very extensive, however reported studies related to PVA nanocomposites through the addition of graphene oxide decorated with silver nanoparticles have been limited [92-95]. Briefly, PVA/GO–AgNPs composites can be prepared through two main routes, *in situ* and *ex situ* methods. The *in situ* approach is a one-step method that consists of chemical reduction of both metal precursor and GO sheets in the presence of

the polymer. The *ex situ* method is based on the incorporation of previously synthesized GO–AgNPs hybrids into the polymer by melt compounding or solution blending. According to these methods, Li *et al.* [92] prepared PVA composites with incorporation of Ag nanoparticle-reduced graphene oxide (Ag-rGO/PVA) *via ex situ*, and investigated the thermal conductivity of the resulting composites. Compared to rGO/PVA composites, Ag-rGO/PVA composites showed greater enhancement in thermal conductivity. Surudžić *et al.* [93] synthesized silver/poly(vinyl alcohol) and silver/poly(vinyl alcohol)/graphene nanocomposites by electrochemical reduction of silver ions at constant current density, and investigated their thermal stability, mechanical characteristics, and antibacterial activity. They found enhanced thermal stability, mechanical properties and antibacterial activity against *Staphylococcus aureus* and *Escherichia coli* for Ag/PVA/graphene nanocomposites compared with Ag/PVA nanocomposites. Nešović *et al.* [94] incorporated AgNPs into a PVA/graphene hydrogel using an *in situ* electrochemical method of silver ion reduction inside the PVA/graphene matrix at constant voltage, and evaluated the biological properties. This study demonstrated that the graphene-based composite hydrogel with incorporated spherical AgNPs was a non-toxic biomaterial with antibacterial activity against *Staphylococcus aureus* and *Escherichia coli*. Another research performed by Usman *et al.* [95] reported on the one-step synthesis of PVA/GO/starch/silver nanocomposites.

However, to the best of our knowledge there are no other reports on the *in situ* chemical approach to develop PVA/Ag-GO nanocomposites. Therefore, the *in situ* synthesis of PVA/AgNPs-GO nanocomposites by chemical reduction of silver ions in the presence of GO dispersed in PVA will be one of the synthesis studied in this chapter.

4.1.5. PVA applications

PVA is commonly used in textile industry as fibers for dressmaking, as blinders in paper products manufacturing, in food packaging industry and in medicine [2,49,50,96-99]. Regarding food packaging systems, PVA films exhibit excellent barrier properties and FDA (Food and Drug Administration) has approved PVA to be in close contact with food products [100]. In medical devices,

PVA is used as a biomaterial due to its biocompatible, nontoxic, no-carcinogenic, and swelling properties [25]. In addition, PVA has proven to be an ideal candidate for development of drug delivery systems because of its good film forming ability, long term temperature stability and pH stability [101-103]. Likewise, considering all the properties that it presents, PVA can be used in adhesives [104], colloids in emulsion polymerization [105], blends [99] and membranes [106,107].

For different applications PVA can be reticulated to form hydrogels. Physical or chemical crosslinks provide the structural stability that hydrogel needs after swelling in the presence of water or biological fluids. The degree of crosslinking determines the amount of fluid uptake, and thus, the physical, chemical, and diffusional properties of the polymer, as well as its biological properties. PVA gels show a high degree of swelling in aqueous solutions, a rubber-like elasticity and no adhesion to surrounding tissue. Therefore, PVA is capable of simulating natural tissue and can be readily accepted into the body [108]. PVA hydrogels have potential applications as tissue replacements [109-111], articular cartilage [108,112], catheters, artificial skin, membranes for the encapsulation of live metabolic cells to prevent immune rejection after tissue transplantation [113,114] and hemodialysis membranes [115]. In the field of ophthalmology, the high water content, oxygen permeability, optical clarity, and low protein adsorption of the PVA hydrogels have led to new applications in the manufacturing of soft contact lenses. PVA extend wearing time without inducing hypoxia to the cornea [116].

The elastic physical properties and the possibility of developing hydrogels with certain tensile strength and compressive modulus, make PVA an appropriate artificial candidate for cartilage replacement. Depending on the concentration of the polymer and the number of cycles tested, PVA hydrogels can be prepared with a resistance range and compression module required for this particular application, 1-17 MPa and 0.0012-0.85 MPa, respectively [117,118]. Another example of replacement might be the use of PVA implants in meniscus. Kobayashi *et al.* [109,111] studied PVA hydrogel for meniscus replacement using a rabbit model where five rabbits were examined after 2 years and the rest at earlier time points. The results of this study showed that the PVA hydrogel implants were intact, with no wear or dislocation seen; implants were stable inside the body.

Kokabi *et al.* [119] prepared PVA–clay nanocomposite hydrogel by the freezing–thawing process to be used as wound dressings. According to the results, PVA–clay nanocomposite hydrogels showed excellent physical and mechanical properties which met the essential requirements of ideal wound dressings. Based on swelling measurements, hydrogels exhibited high capability in absorbing fluid, so recommended for exudative wounds. Additionally, Kenawy *et al.* [120] described PVA/hydroxyethyl starch (HES) blend gel membranes with ampicillin as a novel approach for wound dressing purposes and drug delivery system. The addition of HES into PVA hydrogels improves the physicochemical, morphological, mechanical and thermal properties as well as their degradation, and release profile, which is expected to improve their usefulness as hydrogels.

As a promising biomaterial, several studies have focused on the efficacy of PVA and its nanocomposites for pharmaceutical applications [49,50,121,122]. The semi-crystalline structure of the PVA hydrogels shows a controlled dissolution behavior of the drugs. On the basis of this property, PVA has been extensively studied in pharmaceutical applications as a drug delivery system [123-127].

4.2. Experimental section

4.2.1. Materials

Poly(vinyl alcohol) (PVA) (M_w= 61,000 Da; degree of hydrolysis 98.0–98.8 mol%), glycerol, silver nitrate (AgNO$_3$), L-ascorbic acid (L-AA), phosphate-buffered saline (PBS), and RPMI were supplied by Sigma-Aldrich, while ammonium hydroxide (NH$_4$OH) was acquired from Panreac. All chemicals were used as received without further purification.

4.2.2. Preparation of PVA film

An aqueous solution (2.5 wt%) was prepared by dissolving PVA powder in deionized water at 100 °C for one hour under constant stirring. After that, the solution was poured into a levelled plastic plate that was left at room temperature for drying until its weight equilibrated. The as-prepared film was dried under vacuum at 60 °C for three days before use.

4.2.3. Preparation of PVA/GO nanocomposite films

These types of nanocomposites were prepared following two different procedures in which the type of sonication mainly differs.

4.2.3.1. PVA/GO nanocomposites in the same conditions as PVA/GS nanocomposites

Graphene oxide homogeneous suspension was prepared by dispersing the desired amount of GrO in 30 mL of deionized water under a tip sonicator for 15 min. Separately, a 5 wt% aqueous solution of PVA was prepared at 100 °C upon stirring for 1 h, and subsequently cooled. The GO dispersion was then added to PVA solution while stirring and held for 1 h in constant agitation. Finally, obtained mixture was cast onto a levelled plastic Petri dish, which was allowed to dry at room temperature. The as-prepared films were dried under vacuum at 60 °C for three days before use. The same procedure was followed for the preparation of films containing plasticizer, by adding 20% weight glycerol to the PVA solution. The nanocomposites were denoted as PVA/GO-x, where x indicates the weight percentage of GO.

4.2.3.2. <u>PVA/GO nanocomposites in the same conditions as PVA/AgNPs-GO nanocomposites</u>

The desired amount of GrO was suspended in 50 mL of deionized water. In this case, the suspension was dispersed by <u>bath sonication for 1 h</u>, instead of tip sonicator, to obtained GO sheets. PVA polymer solution was prepared by dissolving 5 wt% PVA in deionized water and vigorously stirred at 100 °C for one hour. Then, under steady stirring, GO suspension was gently added to the prepared PVA solution at 50 °C while stirring for one hour, followed by sonication for another 1 h at room temperature in a bath-type ultrasound sonicator. The resultant solution was 2.5 wt% PVA. Finally, the mixture was cast onto a levelled plastic Petri dish and allowed to dry at room temperature. The films were also vacuum dried at 60 °C for three days and kept in desiccators. The graphene oxide content of the samples prepared through this procedure was 1 and 2 wt%, and were named PVA/GO1 and PVA/GO2.

4.2.4. <u>Synthesis of PVA/Graphene nanocomposite by *in situ* method.</u>

As in previous procedures, graphene oxide sheets were achieved by treatment of 30 mL of GrO aqueous suspensions with <u>a tip sonicator for 15 min.</u> Next, the dispersion was added to the PVA solution which had previously been obtained by dissolving 5 wt% PVA in deionized water at 100 °C for one hour. The mixture was left stirring overnight and then heated at 60 °C using an oil bath and the desired amount of a water solution of L-AA was added (ratio of L-AA to GO was 3.5) under vigorous stirring. To reduce the graphene oxide sheets into graphene sheets (GS), the mixture was maintained at 60 °C for 6 h with constant stirring and in the absence of light. To obtain free-standing PVA/GS films, the mixture was cast onto a plastic Petri dish and left to dry at room temperature. Prior to characterization, the films were dried under vacuum at 60 °C for three days and kept in desiccators. The same procedure was followed for the preparation of films containing plasticizer, by adding 20% weight glycerol to the PVA solution. The nanocomposites were denoted as PVA/GS-x, where x indicates the weight percentage of GS.

4.2.5. Synthesis of PVA/Graphene nanocomposite by *ex situ* method.

Ex situ PVA/graphene nanocomposite film was prepared by blending PVA with chemically reduced GO (GS). The desired amount of chemically reduced graphene oxide powder by L-AA was dispersed in 30 mL of deionized water by ultrasonication for 1 h, to get exfoliated graphene sheets. The GS dispersion was then mixed with a PVA solution prepared as described above and ultrasonicated for an additional 1 h. The film was prepared with 1 wt% of GS loading.

4.2.6. Synthesis of PVA/AgNPs-GO nanocomposite by *in situ* method

The preparation of PVA/AgNPs-GO nanocomposite films was performed *via in situ* reduction of silver ions in the mixture PVA/GO by using L-AA as green reducing agent. PVA solution was prepared by dissolving 2.5 g of PVA in 45 mL deionized water and vigorously stirred at 100 °C for 1 h. GO suspension was prepared by dispersing the desired amount of GrO (25 mg or 50 mg) in 45 ml deionized water under bath sonication. After one hour, ammonium hydroxide was added until the pH value reached 10. Subsequently, GO suspension was gently added to the prepared PVA solution at 50 °C while stirring for one hour, followed by sonication for another 1 h at room temperature in an ultrasonic bath. Then, the mixture solution was placed in an oil bath that was heated to 60 °C with stirring. In order to maintain the weight relationship between $AgNO_3$ and GO fixed at 0.51, the desired amount of a water solution of $AgNO_3$ (to reach 0.75 mM or 1.5 mM) was slowly added to the PVA/graphene oxide sheets mixture, under vigorous stirring and in the absence of light. Next, the desired amount of a water solution of L-AA (to reach 1.5 mM or 3.0 mM) was added to it. The resultant solution was 2.5 wt% PVA. The reaction was then maintained at 60 °C for 1 h with constant stirring and in the absence of light. The original brown color of the solution, due to the GO, immediately turned dark blue, suggesting that Tollen's reagent, $[Ag(NH_3)_2]^+$, formed when mixing the aqueous solution containing PVA, GO and ammonia with the aqueous silver nitrate solution, led to metallic silver in the presence of L-AA. Finally, the reaction mixture was cooled and dialyzed in water for one week to remove residual salts. The suspension was then cast onto a

levelled plastic plate, left to dry at room temperature and subsequently peeled off as a free-standing film. The film was dried under vacuum at 60 °C for three days before use. These experiments were carried out with silver precursor and graphene oxide concentrations of 0.5 and 1 wt% (PVA/ AgNPs-GO1), and 1 and 2 wt% (PVA/AgNPs-GO2), relative to the weight of PVA. One experiment was carried out where no reducing agent was used. In both syntheses, the weight relationship between silver precursor, reducing agent and the GO were the same as in the Chapter 2 for the synthesis of the GO-AgNPs-A hybrid: the ratio of AgNO$_3$ to GO was 0.51, and between L-AA and AgNO$_3$ was 2.07.

4.2.7. Synthesis of PVA/GO-AgNPs nanocomposite by *ex situ* method

PVA/GO-AgNPs nanocomposite films were prepared by blending PVA with previously synthetized graphene-silverNPs hybrid (at 60 °C, with 1.50 mM of AgNO$_3$). For this purpose, an aqueous solution of PVA (5 wt%) was prepared at 100 °C upon stirring for 1 h, and afterward cooled to room temperature. The desired amount of GO-AgNPs powder was dispersed in 30 mL of deionized water by bath sonication for 1 h to get exfoliated sheets. The dispersion was then mixed with PVA solution and ultrasonicated for an additional 1 h. The mixture was then cast as film at room temperature. The as-prepared films were heated at 60 °C under vacuum for three days before use. The nanocomposites were named PVA/GO-AgNPs-x, where *x* denotes the weight percentage of GO-AgNPs-A.

4.2.8. Summary of prepared nanocomposites

Table 4.1. Summary of the synthesized samples.

Samples	Experimental details
PVA/GO-x	Tip sonicator as PVA/GS-x samples. *x = GO percentage.*
PVA/GO1 and PVA/GO2	Bath sonication.
PVA/GS-x	Tip sonicator and *in situ* synthesis. *x = GS percentage.*
PVA/GS1	Prepared by *ex situ* method.
PVA/AgNPs-GO*x*	By *in situ* synthesis. *x = GO percentage.*
PVA/GO-AgNPs-x	By *ex situ* method. *x = GO-AgNPs-A percentage.*

4.2.9. Characterization

The structure and the morphology of the synthetized nanocomposite films were examined by FTIR spectroscopy, Ultraviolet-visible absorption spectroscopy (UV-Vis), X-ray photoelectron spectroscopy (XPS), Raman spectroscopy, X-ray diffraction (XRD), scanning electron microscopy (SEM) and transmission electron microscopy (TEM). Thermal characterization was realized by thermogravimetric analysis (TGA) and differential scanning calorimetry (DSC). The mechanical characterization was carried out by means of tensile test (MTS). Water vapor permeability (WVP) was determined according to the ASTM E96 standard, using the upright cup method (UCM) and water absorption capacity (WAC) was calculated by applying a specific equation. Details of the equipment and protocols of the characterization are shown in Appendix I. The following Table 4.2 details the section of each technique or method performed.

Table 4.2. Characterization methods used for the analysis of PVA-based nanocomposites.

Analysis	Technique or Method	Appendix Section
Formation of AgNPs	UV-Vis	I.1.2
Chemical structure	FTIR	I.1.3
Surface chemistry	XPS	I.1.4
Chemical structure	Raman	I.1.5
Crystalline structure	XRD	I.1.6
Nanostructure and morphology	SEM	I.1.8
	TEM	I.1.9
Thermal behavior	TGA	I.2.1
	DSC	I.2.2
Mechanical Properties	MTS	I.3
Permeability	UCM	I.5
Water Absorption	WAC	I.6

4.2.10. Antimicrobial activity

4.2.10.1. Microbial strains and culture

Gram-negative *Escherichia coli* ATCC 25922 and *Gram-positive Staphylococcus aureus* ATCC 25923 were selected to evaluate the antibacterial activity of PVA-based nanocomposites. Microorganisms were stored frozen at -80 °C in cryoballs (Microbank, Biolab Diagnostics). Bacteria were cultured on Plate Count Agar (PCA) for 24 h at 37 °C, and inoculum was prepared from single colonies grown to stationary phase in Brain Heart Infusion (BHI) broth at 37 °C overnight in an orbital incubator under 100 rpm. Broths were centrifuged (3000 x g, 10 min) and washed twice with Phosphate-Buffered Saline (PBS). A cell suspension adjusted to a cell density equivalent to 0.5 McFarland (representing approximately 1-5 x 10^8 cells/mL) was prepared using sterile saline buffer. Viable counts were enumerated after overnight incubation at 37 °C onto PCA.

4.2.10.2. Antimicrobial activity assays

A modification of the EUCAST dilution method was used to assess the antibacterial activity [128]. The antibacterial properties of PVA-based nanocomposite films in direct contact with bacterial cells and the leaching from the films after their immersion in PBS at 37 °C for 24 h were evaluated.

The assays were performed in 96-well microtiter plates with a volume of 100 μL of Mueller-Hinton Broth (MHB) at twice the desired final concentration. The inoculum was diluted 1:10 with sterile water and each well was inoculated with 100 μL to give a final concentration of 5 x 10^6 CFU/mL. The nanocomposite films were cut to a size of 0.6 cm in diameter, sterilized with ultraviolet light and placed in the wells of the plate in triplicate for each material and for each day. The plates were then incubated at 37 °C, and every 24 h the samples were removed with sterile clamps until 72 h. The absorbance of the culture monitored with a microplate reader (BioRad, USA) at 450 nm, and the quantification of colony-forming units (CFU) present in the wells after dilution and seeding on PCA were used to determine bacterial growth in each well. This experiment was repeated three times during different weeks.

On the other hand, an antibacterial activity assay was performed to determine whether the lixiviates from PVA/GO–AgNPs composite films showed a growth inhibitory effect against *E. coli* and *S. aureus*. The test was carried out in 100-well microtiter plates at 37 °C. Nanocomposite films cut to a size of 0.6 cm in diameter were sterilized under UV light, placed in the plate wells in triplicate for each material and 100 μL of PBS was added to each well. Plates were incubated for 24 h at 37 °C. Then nanocomposite films were removed aseptically with a clamp and other 100 μL of inoculum were added. The microtiter plates were then placed in a microplate reader (Bioscreen C), which was set up to measure the bacterial growth by monitoring the absorbance at 450 nm every hour for 72 h at 37 °C. The experiment was performed in triplicate and differences between PVA (used as control with no antibacterial activity) and PVA/GO–AgNPs nanocomposite films were evaluated.

Bacterial growth was presented as the mean of the logarithm of colony-forming units (CFU) per milliliter. Data were analyzed using analysis of variance (ANOVA) followed by Tukey or Games-Howell's correction depending on the homogeneity of variances (tested by Levene test) and significant differences between neat PVA and nanocomposites were determined (p value < 0.05). Calculations were performed with statistical software SPSS 24.

4.2.10.3. SEM analysis of surfaces after antibacterial assay

SEM analysis was performed for PVA, PVA/AgNPs-GO2 and PVA/GO2 nanocomposites. Briefly, sample discs were fixed one hour with 2% glutaraldehyde in PBS at room temperature. Then, the samples were washed with a phosphate buffer and treated in a graded series of ethanol followed by a coating with gold under an argon atmosphere and finally the discs were observed with a scanning electron microscope Hitachi S4800 operating at 10 kV.

4.3. Results and discussion

4.3.1. Structural and morphological characterization

UV–vis spectroscopy

UV-Vis spectroscopy was used to follow the formation of AgNPs in the synthesis of PVA/AgNPs-GO nanocomposites by *in situ* method. Figure 4.5 compares the absorption spectra of prepared GO, PVA/GO after treatment with $AgNO_3$ in the absence of L-AA, and PVA/AgNPs-GO samples. The GO content was the same for GO, PVA/GO after treatment with $AgNO_3$ in the absence of L-AA and PVA/AgNPS-GO2 samples, whereas for PVA/AgNPS-GO1 it was lower. According to Chapter 2, the spectrum of GO dispersion exhibited a maximum at 230 nm, which is attributed to $\pi \to \pi^*$ transitions of aromatic C-C bonds, and a shoulder at ~300 nm ascribed to $n \to \pi^*$ transitions of C=O bonds. Compared to GO, in the absorption spectra of PVA/AgNPs-GO solutions it can be observed the red shift in the characteristic absorption peak of GO, from 230 to 265 nm. This indicates that GO was simultaneously reduced at a certain extent during the synthesis of PVA/AgNPs-GO nanocomposites, suggesting that the electronic conjugation within the graphene sheets was partially restored.
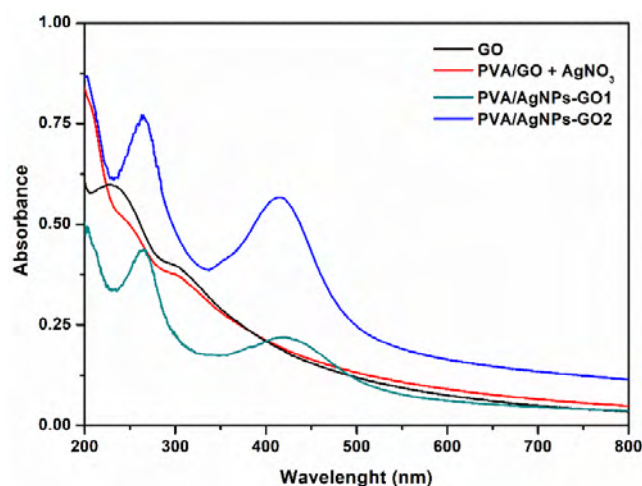
Figure 4.5. UV-Vis absorption spectra of GO, PVA/GO after treatment with $AgNO_3$ in the absence of L-AA, PVA/AgNPs-GO1, and PVA/AgNPs-GO2 suspensions.

Moreover, PVA/AgNPs-GO solutions exhibited surface plasmon resonance (SPR) absorption band, with an absorption peak at 415 and 417 nm for nanocomposites with 2 wt% and 1 wt% GO, respectively, indicating the reduction of silver nitrate to AgNPs [129]. As mentioned in the second chapter, particle size, shape, state of aggregation and the dielectric constant of the surrounding medium influence the intensity, wavelength and shape of the SPR absorption band [130]. The position of the peaks found for PVA/AgNPs-GO is characteristic of small roughly spherical AgNPs [131]. The intense SPR band is responsible for the bluish colour of the mixtures of the PVA, $[Ag(NH_3)_2]^+$ and GO solution after adding L-AA. As can be seen in Figure 4.5, the absorbance peak for the PVA/AgNPs-GO2 sample becomes sharper and of higher intensity than that of the PVA/AgNPs-GO1 sample. The increase in intensity can be due to an increase in the number of nanoparticles formed, and the sharpness reveals the formation of smaller sized AgNPs. On the contrary, UV–vis spectrum of PVA/GO after treatment with AgNO$_3$ in the absence of L-AA did not exhibit the absorption band of metal nanoparticles, indicating that Ag$^+$ ions were not reduced to metallic AgNPs.

Fourier-transform infrared (FTIR) spectroscopy

The FTIR spectra of pure PVA, PVA/GO and PVA/ AgNPs-GO nanocomposite films are compared in Figure 4.6A. The FTIR spectrum of PVA film cast from aqueous solution exhibits the broad O–H stretch band, in the region 3650–3000 cm^{-1}, due to the intermolecular and intramolecular hydrogen bonds. The band between 3000 and 2800 cm^{-1} is assigned to stretching of C–H from alkyl groups and the peaks from 1780–1600 cm^{-1} due to stretching of C=O and C–O from the residual acetate groups in PVA, and peaks attributed to the vibration of CH$_2$ (1418, 1326 cm^{-1}), CH (1237 cm^{-1}), and C–O (1087 cm^{-1}). Compared to neat PVA, the -OH stretching band shifts slightly to a higher wavenumber in the PVA/GO nanocomposites, from 3260 to 3265 cm^{-1}, indicating the formation of hydrogen bonds between oxygen-containing functional groups of GO and the hydroxyl groups in PVA [132]. The PVA/AgNPs-GO films present a similar spectrum to that of PVA. With respect to glycerol plasticized PVA, the FTIR spectrum shows an additional band at 1042 cm^{-1} characteristic of C–O stretching (Figure 4.6B), and the –OH stretching peak shifts to a higher wavenumber due to the hydrogen bonding between the hydroxyl groups of PVA and glycerol. As with

PVA/GO nanocomposites, in the FTIR spectra of unplasticized and plasticized PVA/GS nanocomposites it can be seen that the peak associated with OH stretching is shifted to a higher wavenumber due to the bonding of hydrogen with residual GS oxygen groups.
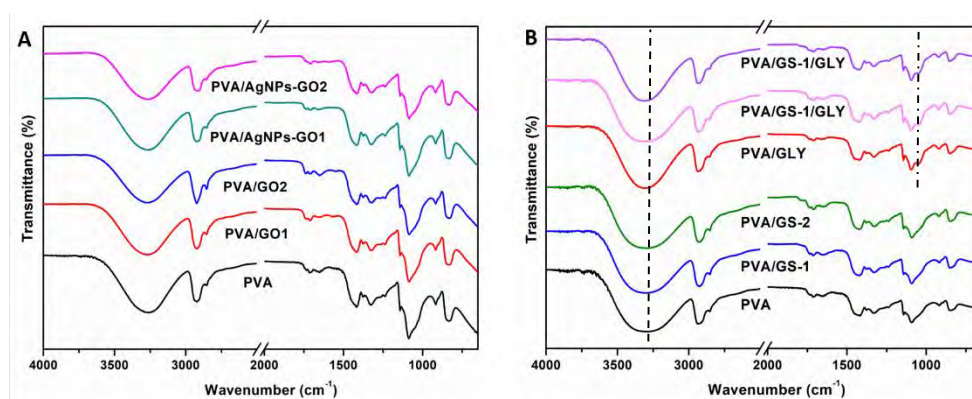
Figure 4.6. FTIR spectra of: (A) neat PVA, PVA/GO and PVA/AgNPs-GO nanocomposites, and (B) unplasticized and glycerol plasticized PVA/GS nanocomposites.

X-ray photoelectron spectroscopy (XPS)

According to chapter 2, an XPS analysis was performed to prove the formation of AgNPs during the *in situ* synthesis. Figure 4.7 shows the high resolution Ag3d spectra of the PVA/AgNPs-GO composites. The spectra show the $Ag3d_{3/2}$ and $Ag3d_{5/2}$ bands at 373.8 and 367.9 eV, respectively, suggesting the formation of metallic AgNPs.
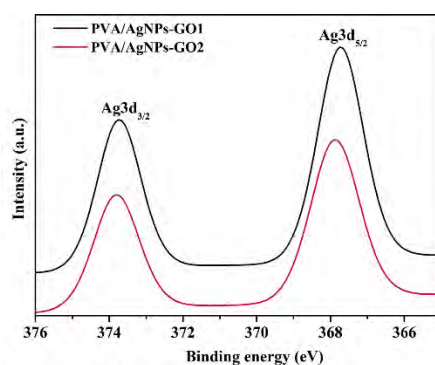
Figure 4.7. High resolution XPS spectra of Ag3d in PVA/AgNPs-GO composites.

Raman spectroscopy

Raman spectroscopy was used to provide structural information of the PVA/GO and PVA/AgNPs-GO nanocomposite samples (Figure 4.8). In order to investigate spectral reproducibility, Raman spectra were collected from different positions on each sample and the mean of the data are shown in Table 4.3. For PVA (Figure 4.8A) the most intense band centered at 2909 cm^{-1} is ascribed to the stretching vibration of $-CH_2$, the other peaks at 1441 and 1100 cm^{-1} are assigned to the stretching vibrations of CH and OH, respectively [133]. The Raman spectrum of the PVA/GO and PVA/AgNPs-GO samples displays the characteristic bands of GO (D, G, 2D, D+G and 2G bands) (Figure 4.8B).
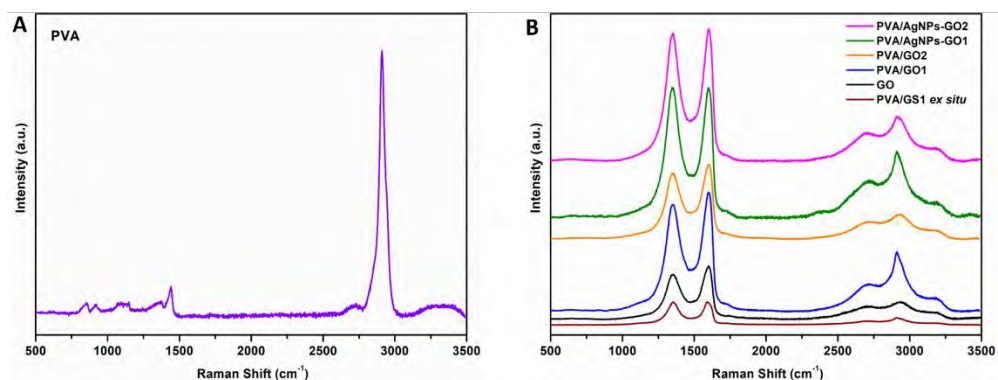
Figure 4.8. Raman spectra of: (A) PVA and (B) GO, PVA/GS *ex situ,* PVA/GO and PVA/AgNPs-GO composites.

The intensity ratio of the D and G peaks (I_D/I_G) for PVA/AgNPs-GO samples increased to 0.99 ± 0.03 as compared to GO (0.85 ± 0.01). This can be attributed to the increase in the number of sp^2 carbon domains with a smaller average size in GO matrix due to its partial reduction during the synthesis of the composites [134]. Additionally, the intensity of these bands increased considerably, which is attributed to the surface-enhanced Raman scattering (SERS) effect of Ag nanoparticles that results from the intense local electromagnetic fields of Ag nanoparticles [135].

Table 4.3. Raman peak position for GO and PVA nanocomposites and I_D/I_G intensity ratios.

Material	D (cm⁻¹)	G (cm⁻¹)	2D (cm⁻¹)	D+G (cm⁻¹)	2G (cm⁻¹)	I_D/I_G
GO	1351	1596	2743	2935	3179	0.85±0.01
PVA/GO1	1352	1602	2731	2912	3186	0.89±0.01
PVA/GO2	1354	1603	2741	2918	3187	0.86±0.03
PVA/AgNPs-GO1	1349	1603	2728	2912	3185	0.99±0.01
PVA/AgNPs-GO2	1352	1603	2721	2915	3187	0.99±0.03
PVA/GS1	1355	1592	2823	2927	3204	0.94±0.08

X-ray diffraction (XRD)

X-ray diffractograms of unplasticized and plasticized PVA, and PVA/GO nanocomposite films measured in the range of $2\theta = 5°\text{-}50°$ are presented in Figure 4.9. The XRD patterns of neat unplasticized and glycerol plasticized PVA films show a main diffraction peak at $2\theta = 19.9°$, and another one at $2\theta = 40.8°$ which correspond to (101) and (111) planes, respectively [136]. Unplasticized and glycerol plasticized PVA/GO nanocomposites show the same spectrum profile and peaks as PVA. The characteristic peak of GO at $2\theta = 11.1°$ (Chapter 2, Figure 2.22) is not detected in nanocomposites, indicating a homogeneous dispersion of GO films in the polymer matrix. The addition of GO to the PVA matrix does not result in noticeable changes in X-ray results.
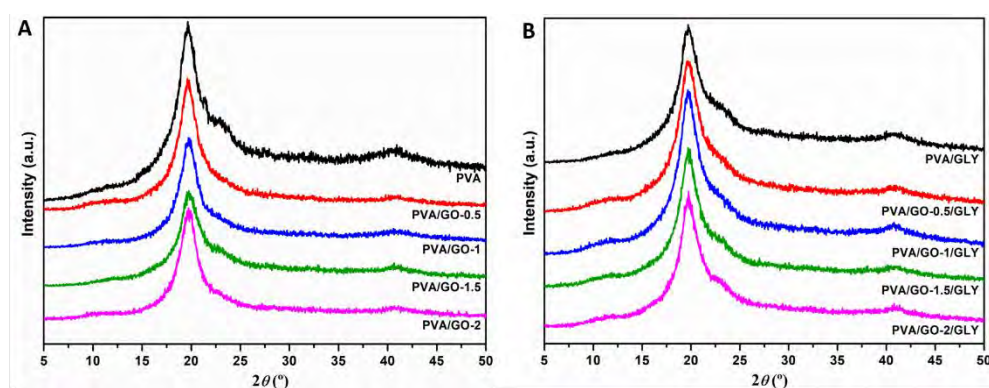
Figure 4.9. XRD patterns of: (A) unplasticized PVA/GO nanocomposites and (B) plasticized PVA/GO nanocomposites.

The X-ray diffraction spectra of unplasticized and plasticized PVA prepared under the same conditions as GS *in situ* nanocomposites (maintained 6 h at 60 °C) and PVA/GS nanocomposites in the range $2\theta = 5°\text{-}50°$ are shown in Figure 4.10. According to the previous PVA, both plasticized and unplasticized heated-PVA films show a main diffraction peak at $2\theta = 19.9°$, and another at $2\theta = 40.8°$ corresponding to (101) and (111) planes, respectively. Compared to heated-PVA, the nanocomposite samples only show peaks at $2\theta = 19.6°$ and $40.8°$, while the broad GS peak at $2\theta = 24.3°$ disappears (Chapter 2, Figure 2.22), suggesting that the GS sheets are homogeneously dispersed in the polymer matrix and not aggregated and restacked together. The intensity of the diffraction peak at $2\theta = 19.9°$ decreases as the GS content increases, indicating a decrease in the crystallinity of the PVA. The reduction in the crystallinity of PVA after the incorporation of GS can be due to the reduction in polymer chain mobility, that can be explained by the formation of a constrained polymer region [137]. This region located around the filler surface adjacent to the interface region exhibits different characteristics than those of neat polymer due to the interfacial interactions between the polymer matrix and the surface of the filler. The mobility of the polymer chains within this region is greatly hampered, and the degree of restriction of the mobility of the polymer chains is affected by the filler content [138]. On this basis, it may be inferred that the interactions through hydrogen bonding between residual oxygen functionalities of GS and the –OH groups of PVA restrict the polymer motion resulting in a decrease in the crystallinity of PVA in the presence of GS.
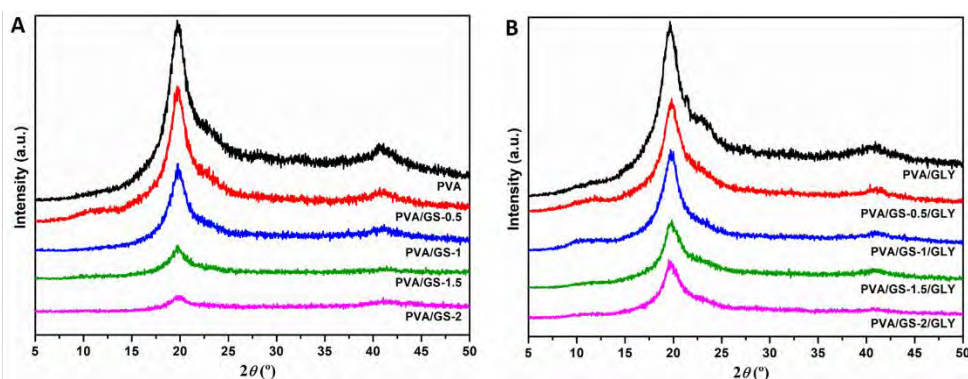
Figure 4.10. XRD patterns of: (A) unplasticized PVA/GS nanocomposites and (B) plasticized PVA/GS nanocomposites.

Figure 4.11 shows X-ray diffraction pattern of neat PVA, PVA/GO2 and *ex situ* and *in situ* PVA nanocomposites with 2 wt% of GO–AgNPs. The pattern of PVA/AgNPs-GO2 *in situ* and PVA/GO-AgNPs-2 *ex situ* composite films shows two additional peaks at $2\theta = 38.3°$ and $44.2°$, corresponding to the (111) and (200) crystal planes of the face-centred cubic crystal structure of AgNPs, respectively [139]. Thus, XRD analysis showed the presence of AgNP in the polymer matrix.
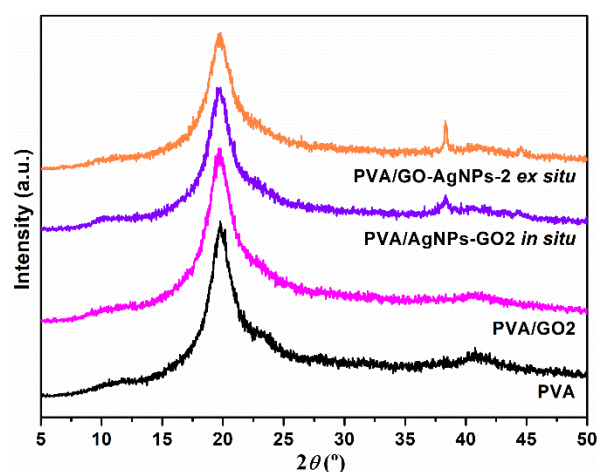
Figure 4.11. XRD patterns of PVA, PVA/GO2, PVA/AgNPs-GO2 *in situ* and PVA/GO-AgNPs-2 *ex situ.*

Nanostructure and morphology

Morphological features of the different PVA-based nanocomposites was analyzed by SEM and TEM. Figure 4.12 displays SEM images of fractured surfaces of plasticized and unplasticized PVA, PVA/GO, PVA/GS with 1 and 2 wt% filler and PVA/AgNPs-GO2 films, as well as PVA/GS1 and PVA/GO-AgNPs-2 prepared through the *ex situ* procedure. SEM micrographs of PVA and PVA/GLY have a clean and smooth surface. The cross-sectional image of unplasticized PVA/GO nanocomposites shows a rough fractured surface without any aggregates of GO, and has a wave-like morphology. The roughness of the fracture surface increases when plasticizer is present and with the increase of GO content. This result indicates a uniform dispersion of GO in PVA matrix. The rougher fracture surface is attributed to the interfacial adhesion and compatibility between polymer matrix and GO sheets.
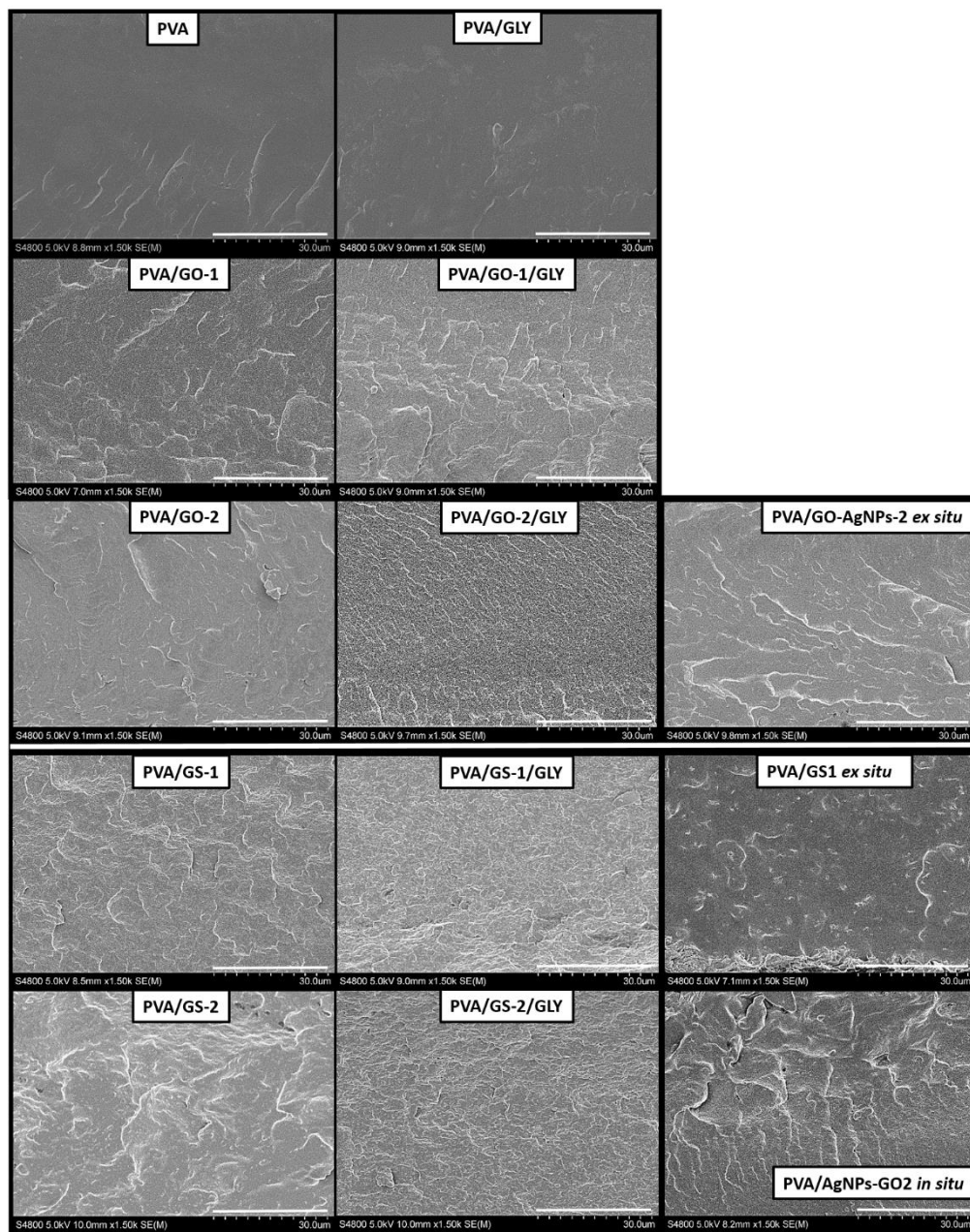
Figure 4.12. SEM images of the fractured surface of: plasticized and unplasticized PVA, PVA/GO and PVA/GS with 1 and 2 wt% filler content, PVA/GS1 *ex situ*, PVA/AgNPs-GO2 *in situ* and PVA/GO-AgNPs-2 *ex situ* nanocomposites.

Likewise, the images of PVA/GS, prepared by *in situ* reduction, with 1 and 2 wt% GS content exhibit a rougher fractured surface with no aggregates of GS, and a wave-like morphology. According to the behavior described above, the roughness of the fracture surface increases when the plasticizer is present, which confirms an improvement in the dispersion of GS in the PVA matrix. The increased GS content also increases the roughness slightly, because there are more points of interfacial interaction between the polymer matrix and filler. On the contrary, the micrograph of the nanocomposite obtained by the *ex situ* method shows a cleaner and smoother surface than its *in situ* obtained counterpart, indicative of poor dispersion of GS due to the lack of interfacial interaction and adhesion of GS to PVA. In the case of nanocomposites with AgNPs, both fractures images show a rough surface, but it is smoother when the film is prepared through the *ex situ* process, which indicates a worse adhesion of the filler with the polymer matrix.

TEM images of unplasticized and glycerol plasticized PVA/GO and PVA/GS nanocomposites with 1 and 2 wt% of filler presented in Figure 4.13 evidence the good dispersion state of GO or chemically reduced graphene sheets (GS) throughout PVA. Single dispersed GO or GS sheets and aggregated nanosheets with thickness between 7-10 nm and ≈12 nm, respectively, coexist. However, a better degree of dispersion is achieved in the plasticized nanocomposites. From TEM and SEM analysis, and XRD patterns it can be inferred an exfoliated morphology for the PVA/GS samples prepared by the *in situ* method. For the nanocomposite sample obtained by the *ex situ* method, a poor dispersion and exfoliation of graphene sheets is observed.

Figure 4.14 displays TEM images of PVA/GO-AgNPs *ex situ* and PVA/AgNPs-GO *in situ* nanocomposites with different amounts of filler. Comparing the preparation processes, it can be highlighted that the best dispersion is achieved in the nanocomposites prepared through *in situ* synthesis, since GO nanosheets are better dispersed throughout the polymer matrix. In *ex situ* PVA/GO-AgNPs nanocomposite images the dark lines are the side views of GO sheets. In Figures 4.14c,f, the black dots indicate the presence of AgNPs, and it can be seen that they are located at the edge of GO sheets, suggesting that they are associated with the GO sheets.
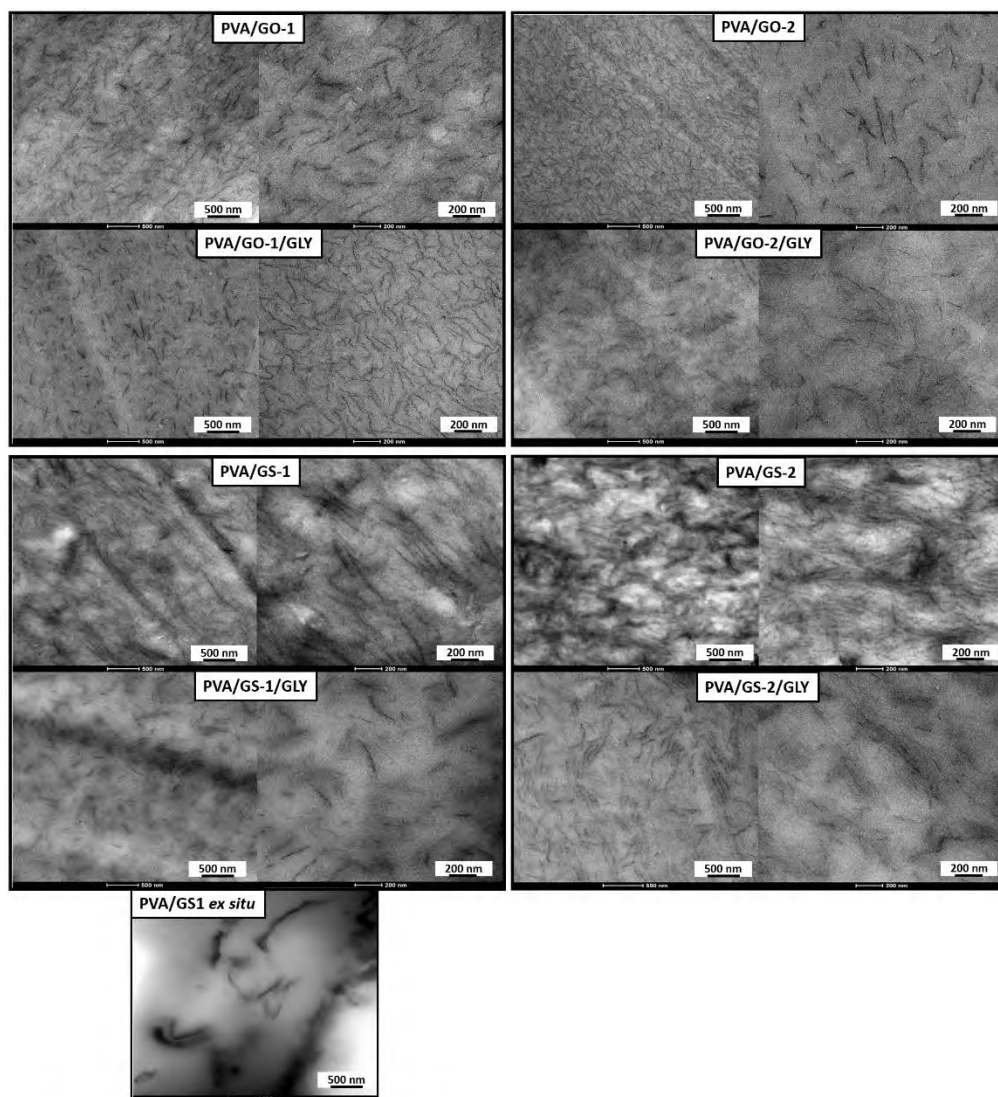
Figure 4.13. TEM images of: plasticized and unplasticized PVA/GO and PVA/GS nanocomposite films filled with 1 and 2 wt% of GO or GS at different magnifications, and PVA/GS1 *ex situ* nanocomposite.
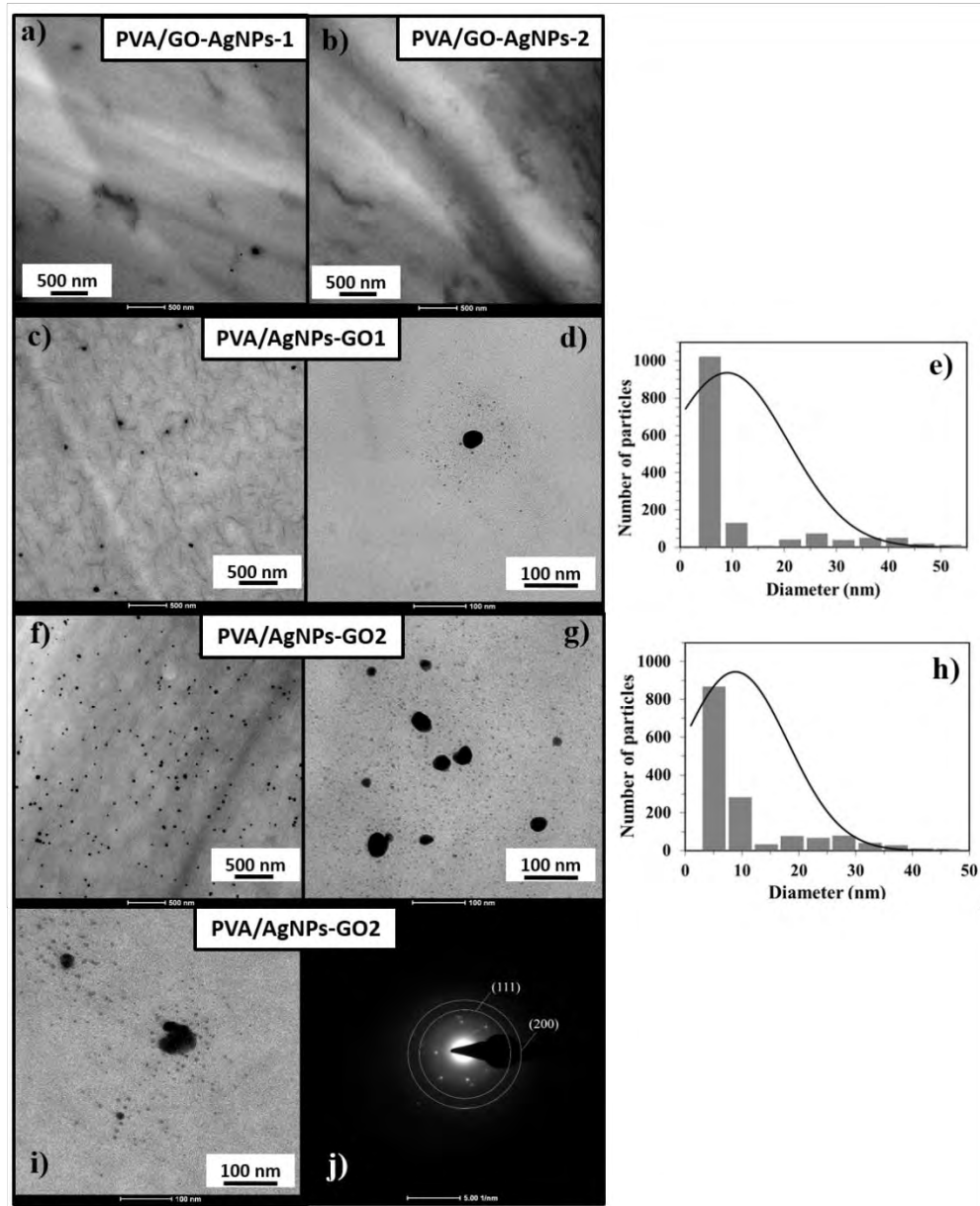
Figure 4.14. TEM images of: (a,b) PVA/GO-AgNPs *ex situ* nanocomposites and (c,d,f,g,i) PVA/AgNPs-GO *in situ* nanocomposites at different magnifications, (e,h) particle size distributions of AgNPs on PVA/AgNPs-GO nanocomposites and (j) the selected area electron diffraction (SAED) patterns of silver nanoparticles.

Moreover, from Figures 4.14c,f, it can be observed that the number of silver nanoparticles increases as the precursor content increases from 0.5 to 1 wt%. On the other hand, in high magnification TEM images (Figures 4.14d,g,i), the large and small spherical black dots correspond to the generated AgNPs, and the dispersed GO sheets are more difficult to observe due to the large black AgNPs, appearing as lighter shaded substrate. In these images, some large particles show a non-spherical shape that can be attributed to aggregation of smaller particles. The selected area electron diffraction (SAED) pattern of AgNPs in the PVA/AgNPs-GO2 approves the crystalline of nature of the *in situ* generated silver nanoparticles (Figure 4.14j). The lattice spacing of ≈ 0.232 nm and ≈ 0.200 nm, corresponds to (111) and (200) planes of the AgNPs, respectively, which confirms that the particles present on the surface of the films are silver nanoparticles. The AgNPs sizes were estimated by counting 1500 nanoparticles in several PVA/AgNPs-GO TEM micrographs. It was found a diameter range of ≈ 0.5-51 for a 1 wt% GO content and silver precursor content of 0.5 wt%, although about 79% of the counted Ag nanoparticles were less than 10 nm in diameter, with a mean size of 9.0 nm (Figure 4.14e). As the GO content further increased to 2 wt% and $AgNO_3$ content to 1 wt%, the histogram indicates a little narrower size distribution, with most of nanoparticles (77%) in the range of 0.5-10 nm, and with a mean size of 8.8 nm. These nanoparticle sizes are much smaller than that of AgNPs synthesized in the absence of GO and PVA (60 nm) [140]. These results indicate the stabilizing role played by both GO and PVA for preventing the formation of large aggregates.

4.3.2. Thermal characterization of PVA nanocomposites

Thermogravimetric analysis (TGA)

The influence of the different graphene-based fillers on the thermal stability of PVA was evaluated by TGA. Thermogravimetric (TG) and derivative thermogravimetric (DTG) curves of plasticized and unplasticized PVA/GO nanocomposites in inert atmosphere are displayed in Figure 4.15, and Table 4.4 summarizes the data collected from these curves. Two stages are observed in the thermal decomposition of PVA, which occur in the following temperature regions: the first one in the range between 200 and 400 °C, and the second one

between 400 and 500 °C (Figure 4.15A). It is during the first step when the greatest weight loss occurs, more than 80%. In this stage the side groups (-OH) are eliminated from PVA and chain scission reactions take place, while in the second one the breakdown of the polymer backbone occurs [141]. About 3% of the initial weight remained at 800 °C as carbon residue. From the DTG curve of the PVA two superimposed processes can be observed during the first decomposition phase (Figure 4.15B), with peaks appearing at 302 and 350 °C. The intensity of both peaks is quite similar. As for the addition of glycerol, the TGA and DTG profiles of PVA and plasticized PVA are similar, except that a new step appears between 100 °C and 235 °C, which corresponds to the evaporation of the plasticizer. The thermal stability of plasticized PVA is slightly lower than that of pure PVA.
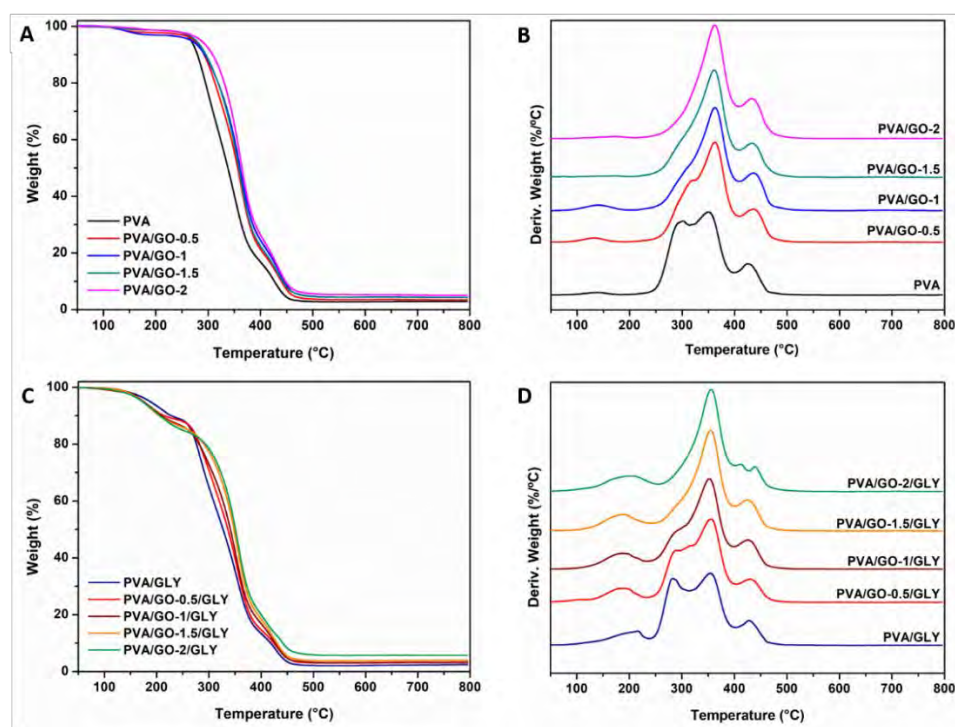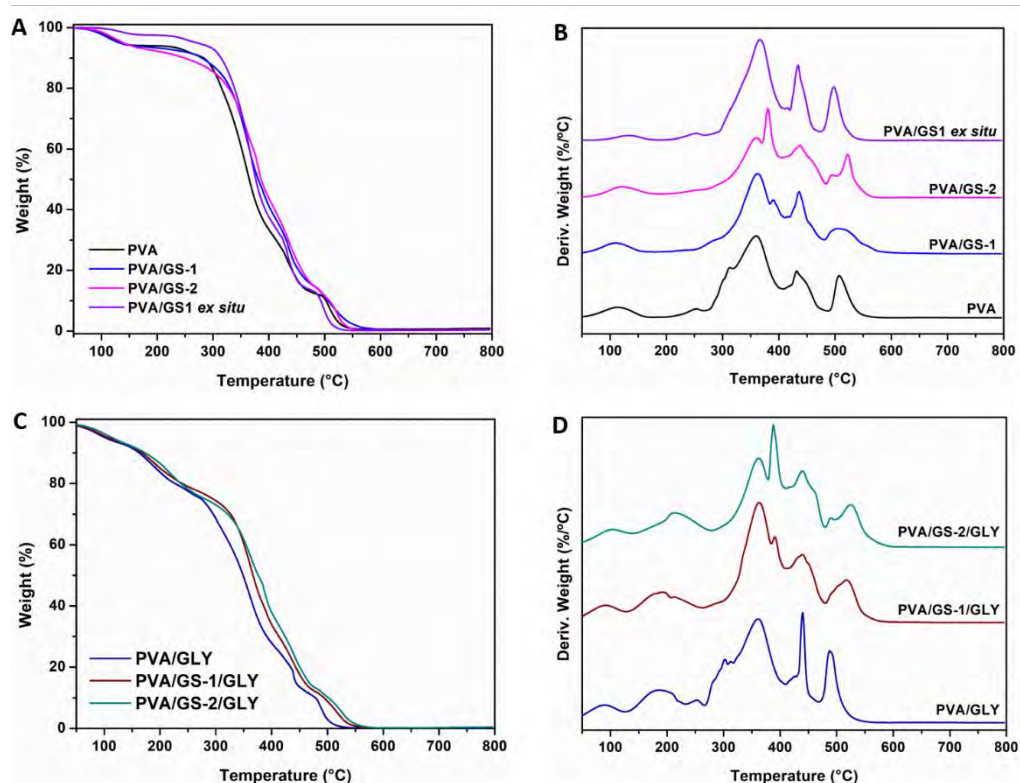

Figure 4.15. TG (A,C) and DTG (B,D) curves of unplasticized and plasticized PVA/GO nanocomposites in nitrogen atmosphere.

The presence of GO significantly alters the degradation of PVA, as the degradation profile of PVA/GO nanocomposites in the DTG curve changes in shape compared to pure PVA (Figure 4.15B). The first stage of PVA decomposition

exhibits two peaks in the DTG curve, while after the addition of GO, the first peak disappears and the intensity of the second peak increases. The two peaks merge with GO contents above 0.5 wt% by weight.

Table 4.4. TGA data for unplasticized and plasticized PVA/GO nanocomposites in inert atmosphere and in air.

Samples (in N_2)	$T_{5\%}$ (°C)	$T_{50\%}$ (°C)	T_{max} (°C) (a)	(b)	(c)	Residue (%)
PVA	271	339	302	350	425	2.9
PVA/GO-0.5	274	356	320*	363	436	3.5
PVA/GO-1	267	361	-	362	439	4.4
PVA/GO-1.5	277	359	-	361	437	4.4
PVA/GO-2	286	365	-	362	437	5.1
PVA/GLY	188	327	283	355	430	2.5
PVA/GO-0.5/GLY	176	336	290*	357	431	3.2
PVA/GO-1/GLY	176	341	-	352	426	3.3
PVA/GO-1.5/GLY	174	348	-	355	426	4.1
PVA/GO-2/GLY	175	351	-	357	440	5.7
Samples (in O_2)	$T_{5\%}$ (°C)	$T_{50\%}$ (°C)	T_{max} (°C) (a)	(b)	(c)	Residue (%)
PVA	136	367	359	427	489	0.34
PVA/GO-1	141	372	360	435	497	1.64
PVA/GO-2	140	382	365	446	503	0.59
PVA/GLY	168	360	360	427	490	0.30
PVA/GO-1/GLY	107	363	361	450	503	0.56
PVA/GO-2/GLY	111	375	381	457	518	0.38

(a) 1st stage; (b) 2nd stage; (c) 3rd stage

The elimination of the side groups (–OH) is slower in the presence of GO, being slower with 2 wt% of GO. The $T_{5\%}$ and $T_{50\%}$ (temperatures corresponding

to 5% and 50% weight loss) increase with the addition of GO, reaching an increase of 15 °C and 26 °C, respectively for PVA/GO-2 nanocomposite when compared to pure PVA. The PVA/GO nanocomposites leave higher char residue than pure PVA at 800 °C and the amount of residue increases with the GO content.

In the case of plasticized PVA/GO nanocomposites, $T_{5\%}$ decreases with increasing GO content, while $T_{50\%}$ increases. The degradation process starts somewhat earlier with the addition of GO, concretely 14 °C for PVA/GO-1.5/GLY compared to PVA/GLY. This behavior could be explained by the water absorption (atmospheric humidity) through the hydrogen bonds. Considering the amounts of each component (the weight of PVA and plasticizer is the same in all the nanocomposites), the number of polar functional groups that can act as an anchor to fix water molecules increases with the addition of GO to PVA/GLY. As a result, in the decomposition process, the loss of humidity-water that occurs at the beginning of the process will be greater with increasing GO content. In the absence of a plasticizer this behavior is not appreciated because functional groups of GO interact with the hydroxyl groups of PVA and also the total number of -OH groups that could interact with water is lower. With regard to $T_{50\%}$, an increase of 24 °C is obtained for the plasticized nanocomposite containing 2 wt% GO. Considering the whole degradation process, the thermal stability of PVA and PVA/GLY is improved by increasing the GO content, since the maximum stabilization is observed at the temperature at which the highest weight loss rate takes place.

TG and DTG curves of unplasticized and plasticized PVA/GO nanocomposites obtained under oxygen are shown in Figure 4.16 and the data compiled are in Table 4.4. The thermogram of PVA reveals, in addition to the loss of physically adsorbed water around 100 °C, another four steps. The first stage with maximum rate at 300 °C assigned to the partial dehydration of polymer chains followed by the polyene formation, and the second one with maximum rate at 360 °C attributed to the polyene decomposition to form macroradicals. The third stage with maximum rate at 427 °C is the result of intramolecular cyclization and condensation of polyconjugated aromatic structures formed from the decomposition of polyene macroradicals, and the last step with maximum rate at 489 °C is due to the thermo-oxidation of carbonized residue [142]. As in the case of inert atmosphere, the plasticized PVA exhibits another decomposition step

between 150 °C and 250 °C due to the glycerol evaporation. The $T_{5\%}$ and $T_{50\%}$ of unplasticized PVA/GO nanocomposites are higher than those of neat PVA. Therefore, GO increases the thermo-oxidative stability of PVA. However, in the presence of glycerol as in the inert atmosphere, $T_{5\%}$ decreases with the addition of GO, while $T_{50\%}$ increases, thereby delaying the partial dehydration of the polymer.
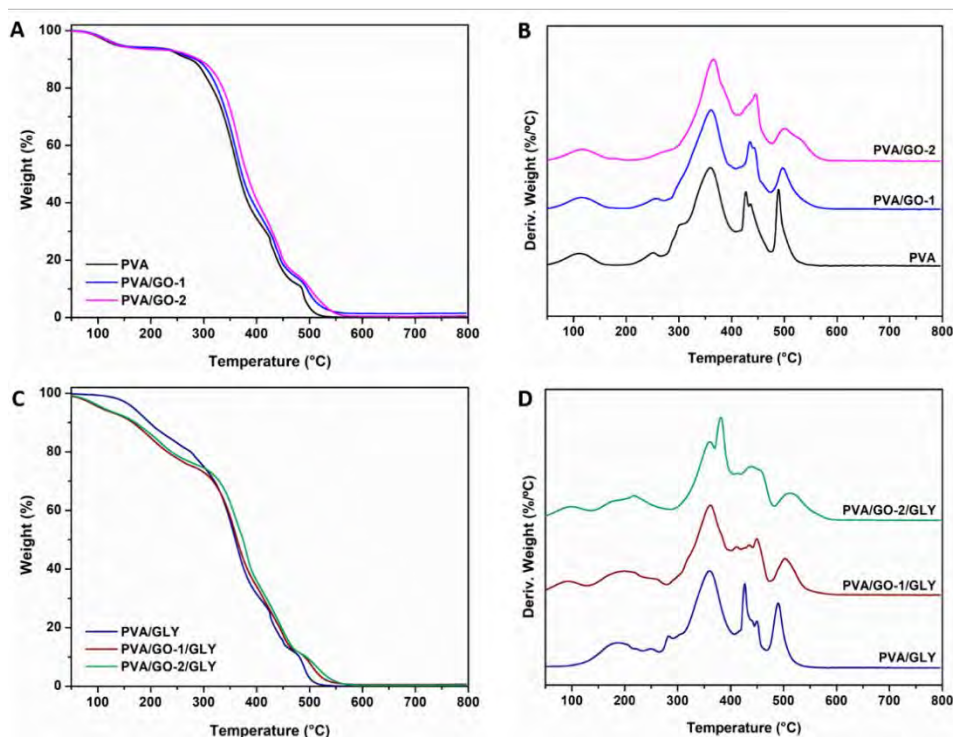
Figure 4.16. TG (A,C) and DTG (B,D) curves of unplasticized and plasticized PVA/GO nanocomposites in air atmosphere.

The effect of GS and glycerol on the thermal and thermo-oxidative stability of PVA films was also evaluated. TG and DTG curves for PVA and glycerol-plasticized PVA, both maintained at 60 °C for 6 h (the same conditions as for the synthesis of the nanocomposites), and their GS nanocomposites are shown in Figure 4.17 and Figure 4.18. The thermal degradation characteristics $T_{5\%}$, $T_{50\%}$, T_{max} (maximum loss rate temperature) and the solid residue fraction at 800 °C are summarized in Table 4.5. The degradation profiles of heated PVA and PVA/GLY do not change compared to their unheated counterparts.
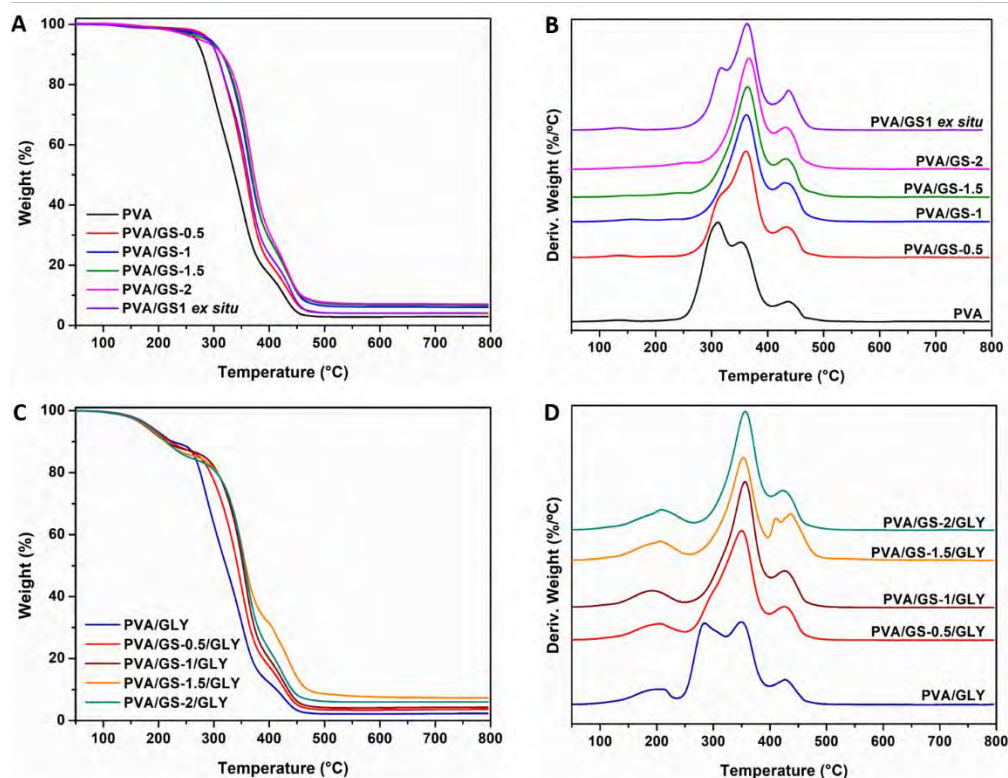
Figure 4.17. TG (A,C) and DTG (B,D) curves of unplasticized and plasticized PVA/GS nanocomposites in nitrogen atmosphere.

Similar to what was happening with graphene oxide, the presence of GS has an effect on PVA degradation, there is a significant change in the shape of the DTG curve of PVA/GS nanocomposites compared to PVA (Figure 4.17B). The first stage of PVA decomposition has two peaks in the DTG curve, while after the addition of GS, the first peak disappears and the intensity of the second peak increases. The two peaks merge at GS contents above 0.5% by weight. $T_{5\%}$ and $T_{50\%}$ increase with the addition of GS, obtaining for nanocomposites with 0.5 wt% and 1 wt% GS increases of 20 and 27 °C, respectively, when compared to pure PVA. The nanocomposite with 1 wt% of GS exhibits the highest thermal stability. The PVA/GS nanocomposites leave higher char residue at 800 °C as compared to neat PVA. In the case of the nanocomposite PVA/GS1 prepared by the *ex situ* method, the $T_{5\%}$ and $T_{50\%}$ values are higher than those of PVA, but slightly lower than the values for the *in situ* prepared sample. In the DTG curve of the blend

prepared by the *ex situ* method, unlike what had happened with the blend prepared by *in situ* method, the first peak due to the side groups elimination does not disappear, although its intensity is reduced.

Table 4.5. TGA data for unplasticized and plasticized PVA/GS nanocomposites in inert atmosphere and in air.

Samples (in N_2)	$T_{5\%}$ (°C)	$T_{50\%}$ (°C)	T_{max} (°C) (a)	(b)	(c)	Residue (%)
PVA	273	338	312	352	439	2.9
PVA/GS-0.5	293	358	318*	362	433	4.1
PVA/GS-1	300	367	-	364	435	6.0
PVA/GS-1.5	295	368	-	364	434	6.6
PVA/GS-2	287	372	-	366	435	7.1
PVA/GS1 *ex situ*	295	361	322	362	434	4.1
PVA/GLY	185	322	284	348	427	2.3
PVA/GS-0.5/GLY	184	343	-	350	426	3.7
PVA/GS-1/GLY	177	353	-	355	428	4.3
PVA/GS-1.5/GLY	180	358	-	353	430	7.3
PVA/GS-2/GLY	182	355	-	356	426	6.0
Samples (in O_2)	$T_{5\%}$ (°C)	$T_{50\%}$ (°C)	T_{max} (°C) (a)	(b)	(c)	Residue (%)
PVA	137	365	360	432	508	0.9
PVA/GS-1	133	381	361	436	507	0.4
PVA/GS-2	141	386	380	438	522	0.5
PVA/GS1 *ex situ*	269	376	367	435	499	0.4
PVA/GLY	103	349	360	440	488	0.3
PVA/GS-1/GLY	108	367	362	441	519	0.5
PVA/GS-2/GLY	115	376	388	441	526	0.5

[a] 1st stage; [b] 2nd stage; [c] 3rd stage

In the case of the plasticized PVA/GS nanocomposites, $T_{5\%}$ remains practically unchanged with the addition of GS to plasticized PVA (Table 4.5), while the $T_{50\%}$ increases by 36 °C with 1.5 wt% of GS when compared with neat PVA. Considering all these values, the thermal stability of PVA or PVA/GLY is improved with the addition of GS.

Figure 4.18. TG (A,C) and DTG (B,D) curves of unplasticized and plasticized PVA/GS nanocomposites in air atmosphere.

The higher thermal stability of graphene filled PVA can be attributed to the high thermal stability of GS, to the mass transport barrier effect of uniformly dispersed graphene sheets to volatile degradation products [143], and also to char formation. The diffusion of volatile gas evolved during the thermal decomposition is hindered, the oxygen diffusion into the polymer matrix is prevented. The presence of GS in the PVA matrix inhibits the side groups elimination due to the absorption of free-radicals generated during polymer decomposition by the

carbon surface [144], to the interaction of oxygen functionalities of GS with –OH groups of PVA and to the tortuous path formed by the GS homogeneously distributed in the PVA matrix, that prevents the gas scape. In the case of the sample prepared by the *ex situ* method the distribution is non-uniform and the interfacial interactions are weaker.

The decomposition process in the air atmosphere (Figure 4.18) differs from that in an inert environment. DTG curves of the unplasticized and plasticized PVA/GS nanocomposites reveal the loss of physically adsorbed water around 100 °C (Figures 4.18C,D), which has generated that the values of $T_{5\%}$ in the thermo-oxidative degradation have been low. However, the $T_{5\%}$ values increase for all GS nanocomposites with an increasing GS content. Likewise, $T_{50\%}$ of both unplasticized and glycerol plasticized PVA/GS nanocomposites are higher than that of neat PVA. Therefore, GS increases the thermo-oxidative stability of PVA. The enhancement of thermal stability can be attributed to the physical protective barrier of GS in the PVA matrix, retarding the escape of volatile degradation products. Besides blocking the dehydration of polymer, GS retards the thermo-oxidation of carbonized residue (Figures 4.18C,D) which can be attributed to the barrier effect of GS that makes it more difficult for oxygen to reach the polymer.

In the same way as for GO and GS, the TGA has also been used to evaluate the effect of the AgNPs-GO hybrid on the thermal stability of PVA. The TG and DTG curves obtained for PVA, PVA/GO samples (prepared under the same conditions as PVA/AgNPs-GO nanocomposites) and *in situ* PVA/AgNPs-GO nanocomposite samples in an inert atmosphere are shown in Figures 4.19A,B, and the *ex situ* PVA/GO-AgNPs nanocomposites in Figures 4.19C,D. Similar to the PVAs shown above, the decomposition pattern of this two PVA also reveals that this polymer degrades in a two-stage process. The first step is the predominant degradation process, which is attributed to the dehydration, chain scission and decomposition of PVA backbone.

As shown in Figure 4.19B, for PVA/GO samples, two overlapping processes occur in the first stage of decomposition, with peaks at 286 °C and 298 °C for PVA/GO1 and PVA/GO2, respectively, while the second peak (332 °C and 330 °C for PVA/GO1 and PVA/GO2, respectively) seems to correspond to the shoulder (at 305 °C) on the PVA curve. Therefore, the presence of GO leads to a decrease

of the first peak and an increase of the second peak. The DTG curves of *in situ* PVA/AgNPs-GO nanocomposites showed similar pattern than that of PVA/GO nanocomposites, but with considerably higher intensity of the second peak and shifted toward a higher temperature, ≈353 ℃. It can be inferred that the presence of GO and AgNPs-GO slows down the dehydration reaction of PVA, but the slowdown is more significant in the last case. This behavior could be related to the reduction of the GO during the synthesis of the PVA/AgNPs-GO nanocomposites, and may be attributed to the absorption of free radicals generated during the PVA decomposition by carbon surface [144].
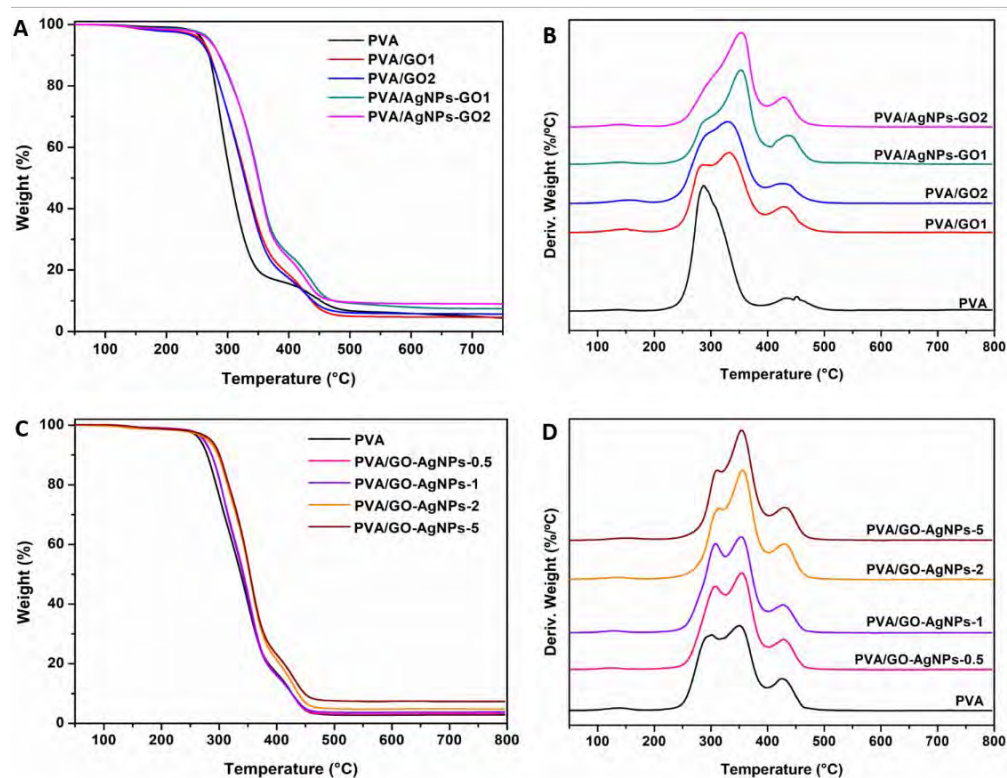
Figure 4.19. TG (A,C) and DTG (B,D) curves of: PVA/AgNPs-GO *in situ* nanocomposites accompanied by PVA and PVA/GO counterparts, and PVA/GO-AgNPs *ex situ* nanocomposites in nitrogen atmosphere.

TGA data collected from TG and DTG curves of nanocomposites containing silver NPs-graphene oxide hybrid are recorded in Table 4.6. The $T_{5\%}$ and $T_{50\%}$ obtained in nitrogen are shifted to higher temperatures for all nanocomposites

relative to pure PVA. For *in situ* PVA/AgNPs-GO nanocomposites the increase in $T_{5\%}$ and $T_{50\%}$ was about 17 °C and 46 °C, respectively, a higher increase than for PVA/GO nanocomposites (6 °C and 25 °C). These results reveals that PVA thermal stability is mainly improved with the incorporation of the AgNPs-GO hybrid synthesized through the *in situ* method.

E*x situ* PVA/GO–AgNPs samples show a decomposition pattern similar to that displayed by neat PVA (Figure 4.19C). The DTG curves, however, show that the intensity of the peak at around 355 °C increases with respect to that of the peak at around 310 °C as the content of the hybrid increases beyond 1 wt%. The second peak shifts to a higher temperature, between 6 and 12 °C. As in the *in situ* hybrids, thermal decomposition temperatures for 5% and 50% weight loss increase after incorporation of the GO–AgNPs hybrid, achieving the most significant increase with 2 and 5 wt% of GO-AgNPs, 9–15 °C and 14–16 °C, respectively.

Table 4.6. TGA data for PVA (according to the preparation conditions), PVA/GO nanocomposites (prepared as their *in situ* counterparts), PVA/AgNPs-GO *in situ* and PVA/GO-AgNPs *ex situ* nanocomposites in inert atmosphere.

Samples (in N₂)	$T_{5\%}$ (°C)	$T_{50\%}$ (°C)	T_{max} (°C) (a)	(b)	(c)	Residue (%)
PVA *(in situ synthesis conditions)*	259	305	287	310*	432	3.9
PVA/GO1	265	330	287	332	428	4.6
PVA/GO2	262	328	298*	330	425	5.6
PVA/AgNPs-GO1	276	351	293	353	435	7.4
PVA/AgNPs-GO2	276	350	304	353	428	9.0
PVA *(ex situ synthesis conditions)*	271	339	302	350	425	2.9
PVA/GO-AgNPs-0.5	274	343	308	355	428	3.2
PVA/GO-AgNPs-1	273	341	308	353	428	3.8
PVA/GO-AgNPs-2	280	353	314	357	429	4.9
PVA/GO-AgNPs-5	285	354	312	356	431	7.4

(a) 1st stage; (b) 2nd stage; (c) 3rd stage

The improved thermal stability of PVA/AgNPs-GO composites as compared to PVA/GO can be attribute to the reduction of GO during the synthesis of PVA/AgNPs-GO nanocomposites or GO-AgNPs hybrid, as reduced graphene oxide has higher thermal stability than GO. From Figure 4.19B, it can be inferred that the addition of AgNPs-GO retards the decomposition of PVA backbone, because the maximum stabilization is analyzed at the temperature at which the highest rate of weight loss occurs. The residue at 800 °C was found to be higher for PVA/AgNPs-GO nanocomposites than for PVA/GO samples, which can be attributed to the incorporation of silver nanoparticles. The PVA/AgNPs-GO sample prepared with higher content of GO and silver nitrate displayed the highest residue. The thermo-oxidative analysis for these nanocomposites has not been performed.

Differential scanning calorimetry (DSC)

Thermal transitions behavior of the different PVA-based nanocomposites was investigated by DSC. First cooling and second heating scans for unplasticized PVA and PVA/GO nanocomposites are shown in Figure 4.20, as well as of their glycerol counterparts. The DSC data for these samples are summarized in Table 4.7. The crystallization temperature (T_c) and crystallization enthalpy (ΔH_c) were determined from the first cooling scan, whereas the glass transition temperature (T_g), melting temperature (T_m) and melting enthalpy (ΔH_m) were determined from the second heating scan. The degree of crystallinity (X_c) was calculated from the second heating scan and using equation I.2.2 shown in the differential scanning calorimetry section of the Appendix I.

The DSC cooling thermograms of neat unplasticized and plasticized PVA (Figures 4.20A,C) show an exotherm peak at 197.7 °C and 188.7 °C, respectively, due to crystallization (Table 4.7). The presence of plasticizer causes the lowering of T_c since it forms hydrogen bonds with PVA and acts as a diluent for the PVA chains [145]. In the second heating (Figures 4.20B,D), unplasticized PVA has an endothermic peak at 221.7 °C that corresponds to the melt of crystalline phase of PVA with a heat of fusion of 76.2 J/g, whereas when PVA is plasticized with glycerol the endotherm broadens and shifts toward lower temperature, at 216 °C, and the heat of fusion (49.8 J/g) significantly diminishes. This variation in T_m and enthalpy of fusion values is attributed to the hydrogen-bonding interaction

between the glycerol and PVA, the inter- and intra-hydrogen bonds in PVA chains are weakened and the molecular motions are eased. The percentage crystallinity decreases after plasticization of PVA with 20 wt% glycerol, from 53.7 to 35.1%. Likewise, the glass transition temperature (T_g) of neat PVA decreases upon addition of glycerol from 76.1 °C to 42.5 °C, indicating an enhancement of chain segment mobility.
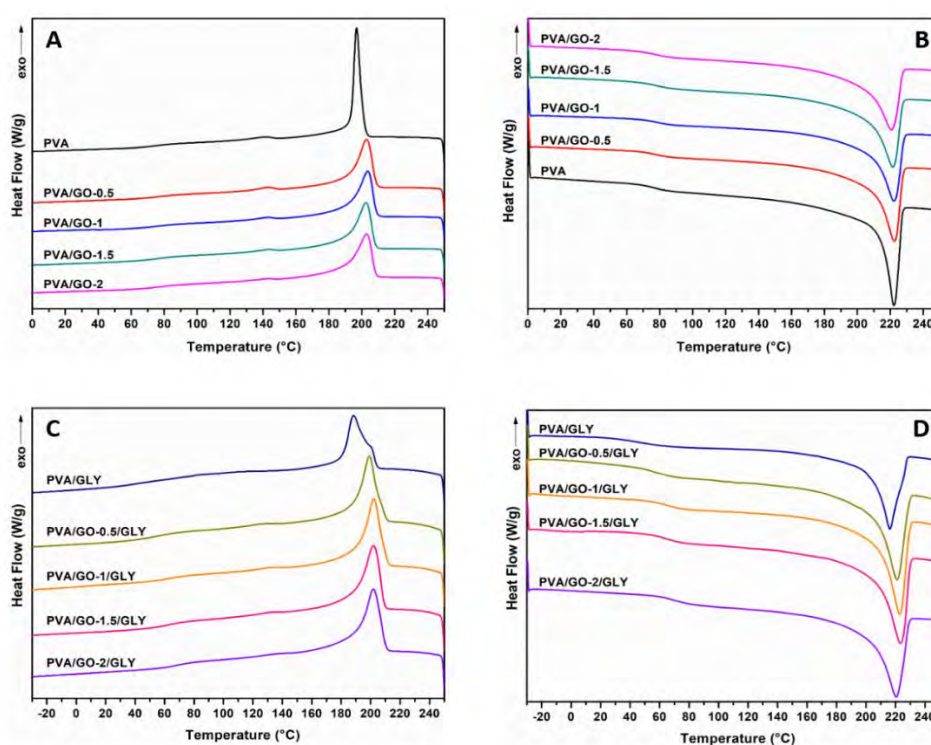
Figure 4.20. DSC thermograms. (A,C) First cooling and (B,D) second heating for unplasticized (A,B) and plasticized (C,D) PVA and PVA/GO nanocomposites.

As far as PVA/GO nanocomposites are concerned, the crystallization temperature is almost unaffected by the incorporation of GO (Figure 4.20). The addition of 0.5 wt% GO to unplasticized PVA increases T_c by ≈6 °C, while in plasticized PVA increases ≈11 °C. A further increase in GO content keeps the crystallization temperature at ≈203 °C for unplasticized and at 202 °C for plasticized nanocomposites. This behavior suggests that GO acts as a nucleating agent.

Table 4.7. DSC data for unplasticized and plasticized PVA and PVA/GO nanocomposites.

Samples	T_g (°C)	T_m (°C)	ΔH_m (J/g)	T_c (°C)	ΔH_c (J/g)	X_c (%)
PVA	76.1	221.7	76.2	197.7	66.5	53.7
PVA/GO-0.5	77.3	222.1	72.5	203.2	60.1	51.4
PVA/GO-1	78.3	221.9	69.8	203.9	60.7	49.6
PVA/GO-1.5	77.8	221.2	70.5	202.9	60.3	50.4
PVA/GO-2	77.8	220.4	70.0	203.2	60.4	50.3
PVA/GLY	42.5	216.0	49.8	188.7	47.7	35.1
PVA/GO-0.5/GLY	55.8	221.0	59.5	199.4	57.7	42.2
PVA/GO-1/GLY	64.0	222.6	61.2	202.4	58.6	43.5
PVA/GO-1.5/GLY	65.0	223.3	61.4	202.3	57.4	43.9
PVA/GO-2/GLY	70.3	220.3	61.8	202.1	57.6	44.4

The incorporation of different amounts of GO does not alter the T_m values of unplasticized and plasticized PVA. However, the enthalpy of fusion slightly decreases for unplasticized PVA/GO nanocomposites. GO contents above 0.5 wt% decrease ΔH_m from 76.2 to approximately 70 J/g. For plasticized PVA/GO, the melt enthalpy increases with GO content, the highest value being obtained for 2 wt% GO content. The crystallinity of unplasticized nanocomposites remains constant with the incorporation of GO, but in plasticized nanocomposites increases with the addition of 0.5 wt% GO from 35.1 to 42.2% and the higher value is achieved with 2.0 wt% of GO (44.4%). Glass transition temperature increases gradually as the filler content increases due to the hydrogen bonding interactions between GO and PVA. Those interactions make the nanocomposite matrix more rigid. Plasticized PVA/GO nanocomposites show a larger increase than unplasticized counterparts suggesting more interactions in the presence of glycerol.

The thermal transition temperatures and enthalpies of unplasticized and plasticized PVA/GS nanocomposites are given in the Table 4.8 and the corresponding DSC thermograms are shown in the Figure 4.21.
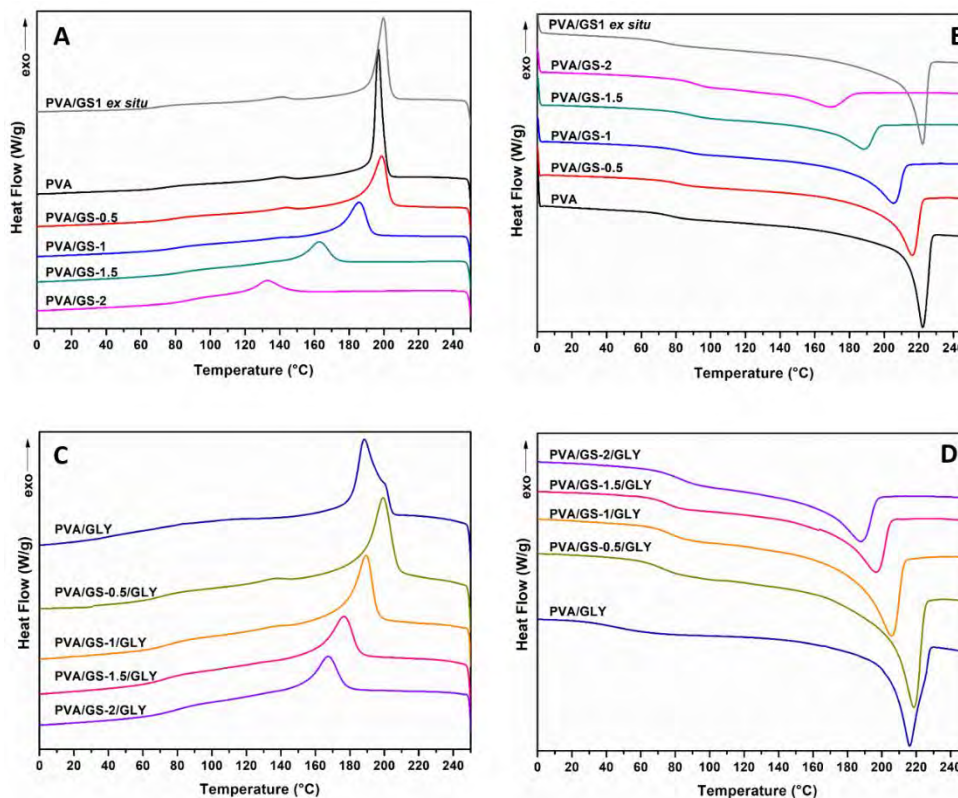
Figure 4.21. DSC thermograms. (A,C) First cooling and (B,D) second heating for unplasticized (A,B) and plasticized (C,D) PVA and PVA/GS nanocomposites.

Analyzing the first cooling it can be inferred that T_c is almost unaffected by the incorporation of 0.5 wt% of GS to unplasticized PVA, and a further increase of GS content leads to lower T_c values, indicating that crystallization is retarded (Figure 4.21A). T_c value of plasticized PVA increases by adding 0.5 wt% of GS; it is almost unaffected by the presence of 1 wt% of GS, whilst decreases with a further increase in GS loading. At a loading of 0.5 wt% GS the nanofiller may act as nucleating agent which results in a higher T_c value, while the lower T_c values attained at GS loadings higher than 0.5 wt% are attributed to the hydrogen bonding between PVA and GS. The T_c value of the blend of PVA with 1 wt% of GS prepared by the *ex situ* method is almost unaffected as compared with that of neat PVA, and 14 °C higher than the value of the sample prepared by *in situ* process.

Table 4.8. DSC data for unplasticized and plasticized PVA and PVA/GS nanocomposites.

Samples	T_g (°C)	T_m (°C)	ΔH_m (J/g)	T_c (°C)	ΔH_c (J/g)	X_c (%)
PVA	76.1	221.7	76.2	197.7	66.5	53.7
PVA/GS-0.5	80.3	215.9	67.9	199.2	51.6	48.1
PVA/GS-1	84.4	205.2	53.8	186.0	39.8	38.3
PVA/GS-1.5	88.0	188.2	34.1	163.0	28.3	24.4
PVA/GS-2	91.9	169.2	21.0	133.0	21.6	15.1
PVA/GS1 *ex situ*	75.0	221.9	75.7	200.1	60.1	53.9
PVA/GLY	42.5	216.0	49.8	188.7	47.7	35.1
PVA/GS-0.5/GLY	72.0	218.3	58.8	199.6	50.1	41.6
PVA/GS-1/GLY	77.0	205.5	48.8	189.5	39.2	34.7
PVA/GS-1.5/GLY	73.6	196.6	33.8	176.8	28.2	24.2
PVA/GS-2/GLY	83.6	187.9	31.7	167.6	21.2	22.8

In the second heating (Figures 4.21B,D), the incorporation of different amounts of GS, in both unplasticized and glycerol plasticized PVA, important changes are observed in the T_m values as compared with neat PVA (Table 4.8). Melting temperature decreases gradually as the GS content increases in unplasticized PVA, and the same trend is observed in the case of the enthalpy of fusion. As for plasticized PVA T_m value is almost unaffected by the incorporation of 0.5 wt% of GS, whereas the enthalpy of fusion increases. GS contents higher than 0.5 wt% cause a lowering in the T_m and ΔH_m values. This behavior is attributed to the interaction between GS and PVA. These results are consistent with those found in previous studies on PVA/reduced GO nanocomposites obtained by reducing GO with hydrazine in the presence of PVA [68], although in our study the changes in T_c and T_m are significantly higher.

The incorporation of GS also causes a remarkable decrease in the degree of crystallinity of unplasticized PVA, from ≈54% for PVA to 15% for the sample containing 2 wt% GS, whereas in the case of plasticized PVA the incorporation of 0.5 wt% of GS leads to a slight increase in crystallinity and then a higher amount

of GS causes a decrease. This reduction of the crystallinity in the nanocomposites, that can be explained by the formation of a constrained polymer region [137], indicates some interaction between the polymer chains and the filler. The crystallinity changes induced by the incorporation of GS are in good agreement with the XRD results and previous studies on PVA/graphene nanocomposites synthesized by reducing GO in the presence of the polymer matrix [68].

When GS is incorporated both in unplasticized and in glycerol plasticized PVA, T_g increases gradually as the nanofiller content increases, as a result of the hydrogen bonding interactions between GS and PVA [146]. As with GO, the interfacial interactions between GS and PVA make the polymer matrix more rigid. Similar results have been reported by other authors in their studies on PVA/graphene nanocomposites prepared by *in situ* reduction of GO [68,77]. Plasticized PVA/GS nanocomposites show a larger T_g increase than their unplasticized counterparts, indicating that there are more interactions in the presence of plasticizer.

T_m, ΔH_m, degree of crystallinity and T_g were not affected upon the incorporation of previously prepared GS to PVA (Table 4.8), indicating that there are not enough interactions between graphene and polymer chains to change the thermal behavior of PVA if the film is prepared by the *ex situ* method.

The effect of GO–AgNPs hybrid on the thermal transitions of the PVA matrix can be seen in the data displayed in Table 4.9. The corresponding DSC thermograms are shown in Figure 4.22. Glass transition temperature increases by 5 °C for the *in situ* PVA/AgNPs-GO2 nanocomposite. The addition of previously synthetized GO–AgNPs hybrid to the PVA matrix also increases the T_g, and the higher the hybrid content, the higher the T_g value. Neat PVA displays a T_g of 76.1 °C, while for PVA/GO–AgNPs-5 composite film, the T_g rises to 83.0 °C, with an increment of 6.5 °C. However, the *in situ* counterparts show higher T_g values as a result of better dispersion of the hybrid in the polymer matrix. The enhanced T_g can be explained by the reduced polymer chain mobility due to the interfacial interactions between the hybrid and PVA. The presence of GO–AgNPs hybrid also results in a slight increase in crystallization temperature, which can be due to the nucleating effect of GO–AgNPs on the PVA crystallization. However, T_c values are higher for *in situ* nanocomposites. The melting endothermic peak of

PVA is unaffected in the nanocomposites, except in the case of *in situ* PVA/AgNPs-GO1, that is slightly increased. The crystallization and melting enthalpy decrease somewhat. In *ex situ* nanocomposites, the melting peak temperature also remains unchanged by the addition of the hybrid, but heat enthalpy and crystallization degree slightly reduced upon increasing the content of the hybrid, with a greater reduction than for *in situ* nanocomposites.
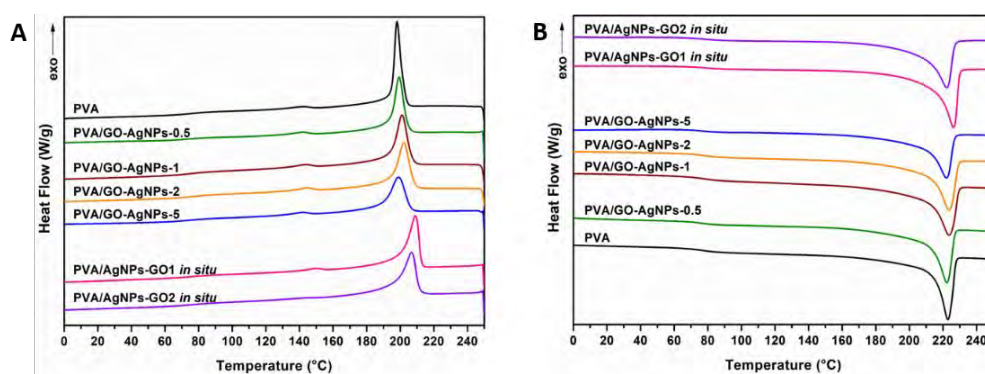
Figure 4.22. DSC thermograms. (A) First cooling and (B) second heating for in situ synthetizes PVA/AgNPs-GO nanocomposites and ex situ PVA/GO-AgNPs.

Table 4.9. DSC data for *in situ* synthetized PVA/AgNPs-GO nanocomposites and *ex situ* PVA/GO-AgNPs.

Samples	T_g (°C)	T_m (°C)	ΔH_m (J/g)	T_c (°C)	ΔH_c (J/g)	X_c (%)
PVA	76.1	221.7	76.2	197.7	66.5	53.7
PVA/GO-AgNPs-0.5	78.3	222.8	70.0	201.8	57.9	49.6
PVA/GO-AgNPs-1	78.6	223.8	61.5	201.8	50.4	43.8
PVA/GO-AgNPs-2	79.6	224.6	61.8	202.5	53.5	44.4
PVA/GO-AgNPs-5	83.0	223.5	59.3	202.8	48.2	44.0
PVA/AgNPs-GO1 *in situ*	79.1	228.1	74.3	210.6	65.6	52.9
PVA/AgNPs-GO2 *in situ*	81.1	222.9	73.1	209.3	65.2	52.5

4.3.3. Mechanical characterization

Tensile tests were used to determine mechanical properties. Typical stress-strain curves of unplasticized and plasticized PVA and PVA/GO nanocomposites are presented in Figure 4.23. The unplasticized nanocomposites (Figure 4.23A) show a ductile behavior since the deformations are moderate and exhibit yield stress. During the tensile test these samples subjected to a continuous stress above the limit of elasticity, experienced the phenomenon of cold drawing. At yield point, a neck was formed at one point in the sample. As the deformation continued, the neck region lengthened until the whole sample had been drawn into the new shape with a cross-sectional area equal to that of the neck zone. On the contrary, plasticized nanocomposites (Figure 4.23B) present an elastomeric behavior with high deformations and moderate maximum-stress, as well as relatively low elastic module values.
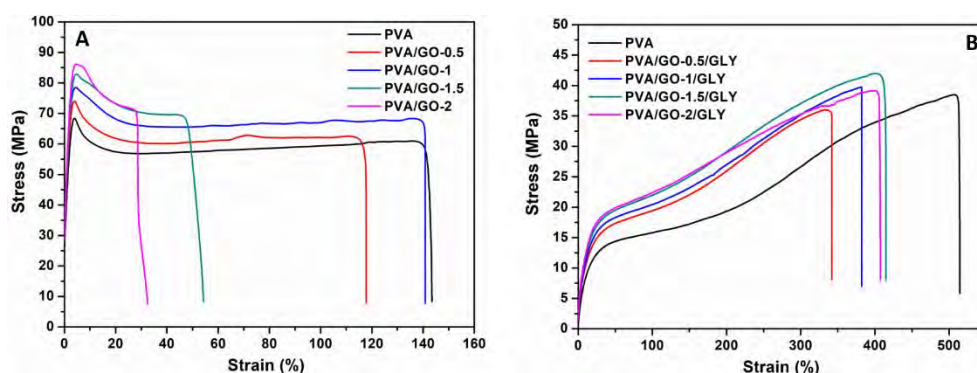
Figure 4.23. Stress–strain curves of (A) unplasticized and (B) glycerol plasticized PVA and PVA/GO nanocomposites.

The data of Young´s modulus, yield stress, break stress and the elongation at break for PVA/GO nanocomposites are given in Table 4.10 and their representation is shown in Figure 4.24. Additionally, Figure 4.25 shows the rate change of mechanical properties for unplasticized and plasticized PVA/GO and PVA/GS nanocomposites calculated from equation I.3 explained in the section concerning mechanical characterization in Appendix I.

The mechanical properties of PVA change considerably with the addition of glycerol. The Young's modulus and break stress of the PVA film decrease, 96% and 34% respectively, upon incorporation of glycerol, whereas the elongation

increases enormously, exceeding 250%, indicating that PVA film becomes less strong and more ductile. Glycerol destroys the inter and intra-molecular hydrogen bonds in PVA chains, facilitating the molecular motions of polymer chains, making PVA films more flexible. Changes in the degree of crystallinity due to the presence of plasticizer must also be taken into account (Table 4.7). The decrease in the Young´s modulus and break stress can be ascribed to the lower crystallinity of plasticized PVA with respect to the unplasticized polymer.
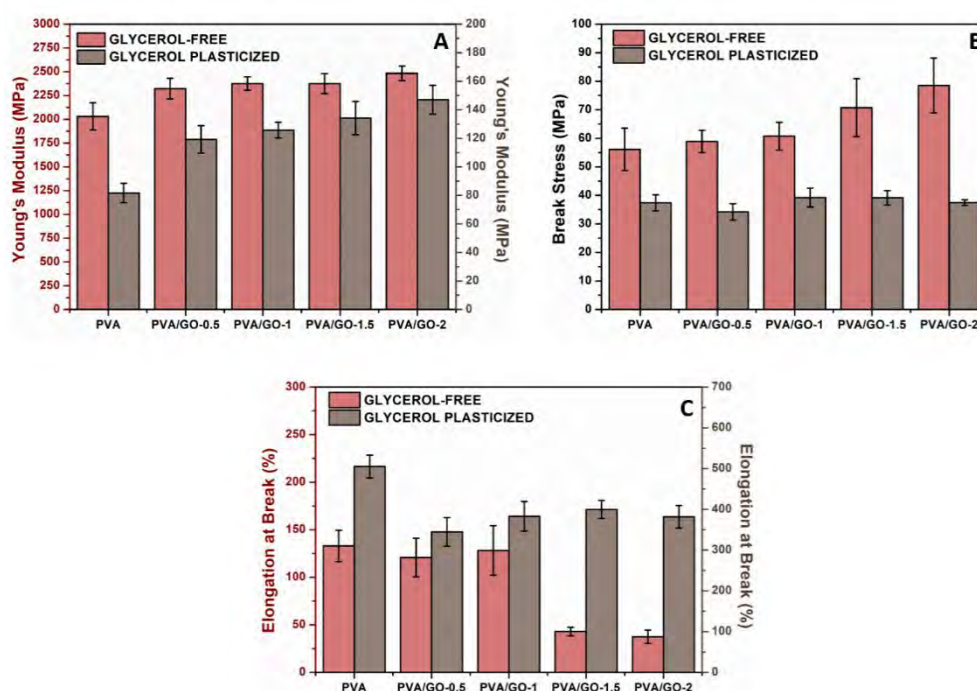
Figure 4.24. Mechanical properties of PVA/GO nanocomposites: (A) Young's modulus, (B) break stress and (C) elongation at break.

The addition of GO into the unplasticized and plasticized PVA matrix leads to an increase in the elastic modulus of PVA/GO nanocomposites, which in turn, is affected by the filler content (Figure 4.24A). In particular, the addition of 2 wt% GO to unplasticized PVA results in a 22% increase in the elastic modulus, the greatest variation among the filler contents tested. However, the GO effect is more outstanding in plasticized nanocomposites (Figure 4.25A). In plasticized PVA/GO films, Young's modulus increases gradually with increasing GO content,

achieving the maximum increase in the nanocomposite that contents 2 wt% of GO, about 79%, compared to PVA/GLY. These results suggest that in the presence of glycerol, GO leads to an increase in the stiffness of the PVA.

Table 4.10. Mechanical properties data of unplasticized and glycerol-plasticized PVA and PVA/GO nanocomposites.

Sample	Young's modulus (MPa)	Yield stress (MPa)	Break Stress (MPa)	Elongation at break (%)
PVA	2031±144	59.0±7.8	56.1±7.4	133.0±16.5
PVA/GO-0.5	2323±109	72.6±6.3	58.9±3.9	120.7±20.4
PVA/GO-1	2375±71	74.3±5.8	60.7±4.9	128.1±26.1
PVA/GO-1.5	2376±105	81.1±4.7	70.7±10.2	43.0±4.5
PVA/GO-2	2483±77	84.7±3.4	78.5±9.6	37.4±7.0
PVA/GLY	82±7	-	37.4±2.8	505.1±27.9
PVA/GO-0.5/GLY	119±10	-	34.2±2.9	344.7±35.0
PVA/GO-1/GLY	126±6	-	39.2±3.3	382.9±36.2
PVA/GO-1.5/GLY	134±12	-	39.1±2.5	399.8±22.3
PVA/GO-2/GLY	147±10	-	37.5±1.0	381.7±27.6

Yield and break stress also increases with respect to PVA, but in glycerol-plasticized nanocomposites the achieved break stress variation is practically within the experimental error (Table 4.10). For unplasticized films yield and break stress increased gradually as the GO content increased, making PVA more strong. The addition of 2 wt% of GO to unplasticized PVA leads to an increase of about 44% and 40% in yield and break stress, respectively, compared to PVA (Figures 4.25B,C). On the contrary, the plasticized counterpart has nearly the same break stress value as PVA/GLY (Figure 4.24B). The yield stress points of the plasticized nanocomposites were not determined due to the shape of their stress-strain curves, in which the limits of the elastic behavior and the beginning of the plastic behavior could not be precisely detected by the MTS TestWorks 4 software. The elongation at break of unplasticized and plasticized PVA decreases

with the addition of GO (Figure 4.24C). The lowest elongation at break is obtained for unplasticized films with 2 wt% of GO in comparison with neat PVA, the reduction is about 72% (Figure 4.25D). In glycerol-plasticized nanocomposites the addition of GO affects to a lesser extent the elongation, giving the maximum decrease (31%) with the addition of 0.5 wt% of GO compared to PVA/GLY and remaining constant with higher GO contents (≈18%). These results indicate that the addition of GO results in more brittle materials when compared with PVA.
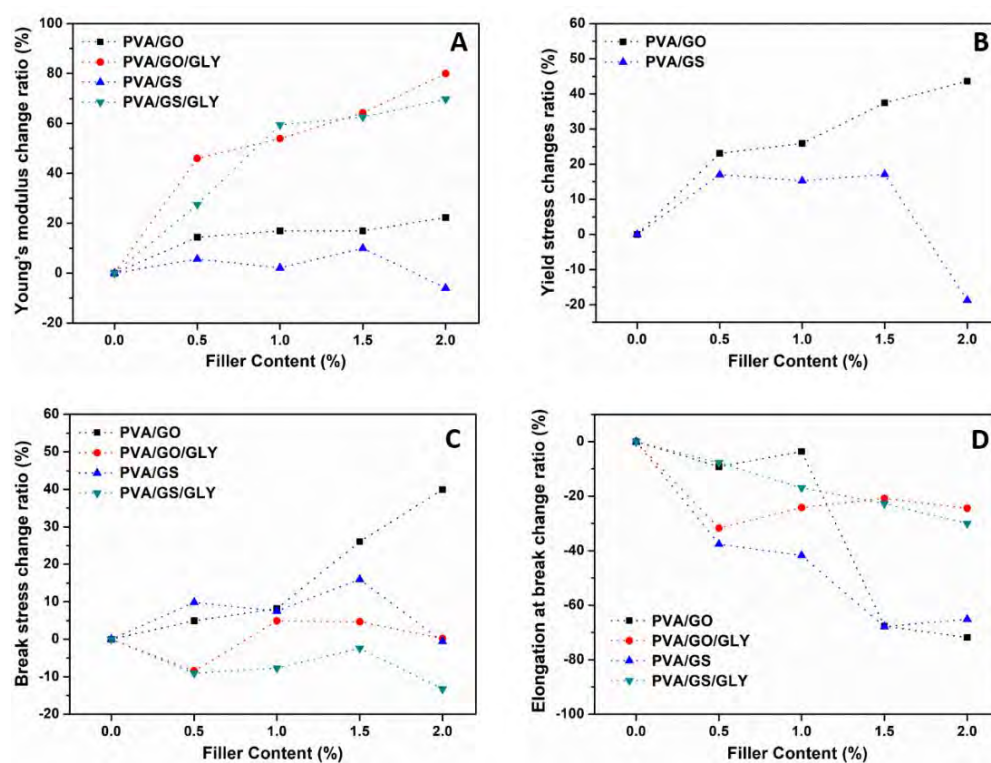
Figure 4.25. Change ratio of: (A) Young's modulus, (B) yield stress, (C) break stress and (D) elongation at break for unplasticized and plasticized PVA/GO and PVA/GS nanocomposites.

In short, the enhanced mechanical properties for PVA/GO nanocomposites can be attributed to the high elastic modulus and tensile strength of GO [147,148], the good dispersion of graphene oxide sheets throughout the PVA matrix, and the presence of strong interfacial interaction between polymer chains and GO, which make possible to increase the efficiency of stress transfer from the PVA to the filler at the interface, as well as the adhesion of both with the glycerol.

As far as PVA/GS nanocomposites are concerned, the stress-strain curves of unplasticized and plasticized nanocomposites are shown in Figure 4.26, the mechanical properties data values in Table 4.11 and their graphics in Figure 4.27. Similar to the previous GO nanocomposites, unplasticized PVA/GS films can be classified as ductile materials, while plasticized nanocomposites as elastomeric-type materials. On the other hand, the difference in the values of tensile properties of PVA and PVA/GLY specified in Table 4.10 and Table 4.11 can be attributed to the heat treatment realized in accordance with the synthesis of unplasticized and plasticized PVA/GS nanocomposites.
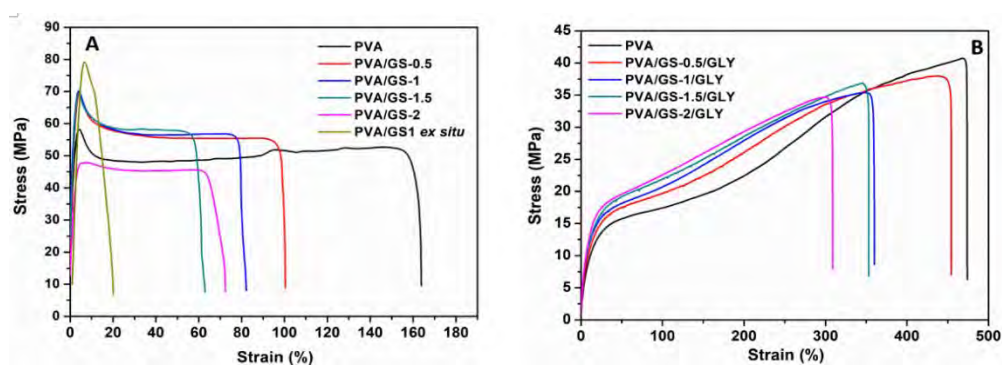
Figure 4.26. Stress–strain curves of (A) unplasticized and (B) glycerol plasticized PVA and PVA/GO nanocomposites.

The presence of GS has no effect on the elastic modulus of unplasticized PVA (Figure 4.27A), the changes in Young's modulus found for unplasticized nanocomposite films are within the experimental error (Table 4.11), except for the addition of 1.5 wt% GS which enhances the elastic modulus at least in a 10%. In contrast, in plasticized nanocomposites the modulus increases with GS content; the maximum increment attained is 70% at 2 wt% of GS loading (Figure 4.25A). The reinforcing action of GS is stronger in the presence of glycerol due to the better interfacial contact of the filler with PVA matrix, which is in good agreement with SEM and TEM results.

The yield and break stress of unplasticized nanocomposite films increases somewhat up to 1.5 wt% GS of content (Table 4.11). However, in the case of plasticized films, break stress decrease slightly (5-10%) and remain almost constant after the incorporation of GS contents (Figure 4.27B). As with GO

nanocomposites, the yield stress points of plasticized PVA/GS nanocomposites could not be precisely detected by the MTS TestWorks 4 software. The elongation at break value of both unplasticized and plasticized films decreases as the GS content increases (Figure 4.27C), being the highest reduction in the case of the unplasticized nanocomposites, 65% for the unplasticized film containing 2 wt% GS and 30% for the glycerol plasticized counterpart (Figure 4.25D) indicating that the graphene increases the brittleness of the films. The degree of crystallinity is an important parameter for semi-crystalline polymers that has effect on their mechanical properties. PVA crystallinity decreases as GS content increases, however the reduction in the degree of crystallinity has not drastically affected the mechanical behavior of PVA/GS nanocomposites, which can be attributed to the interfacial interaction between PVA and graphene.
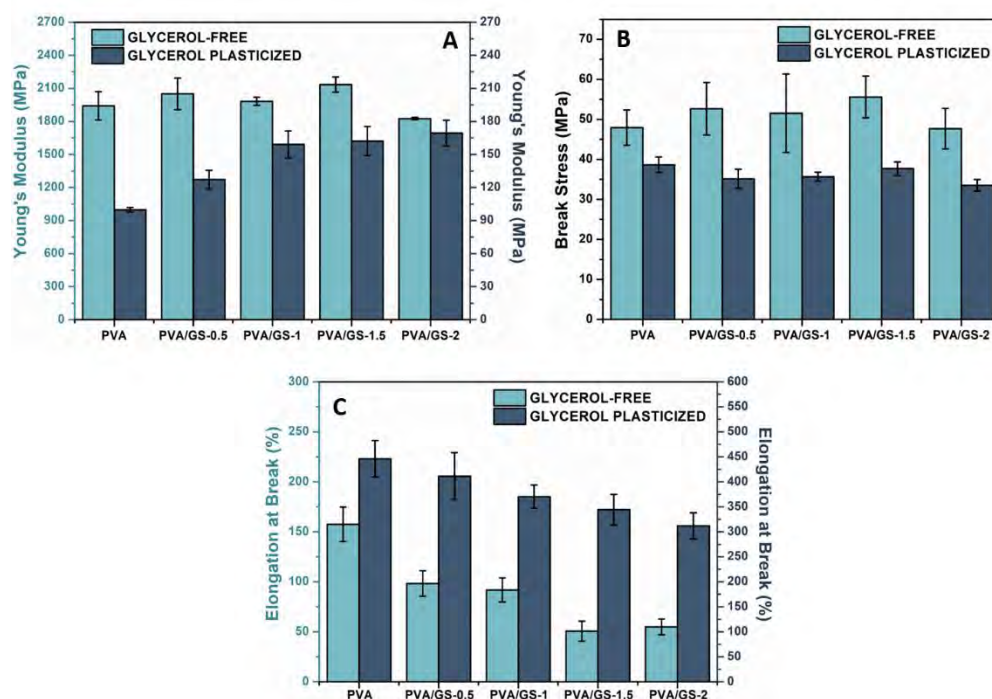
Figure 4.27. Mechanical properties of PVA/GS nanocomposites: (A) Young's modulus, (B) break stress and (C) elongation at break.

The value of the elastic modulus of the nanocomposite containing 1 wt% GS prepared by the *ex situ* method is similar to that of PVA. The yield and break stress values point to an increase of 31% and 56% respectively, whereas the elongation at break decreases drastically from 158 to 12%, implying a decrease of 92% with respect to the values for PVA (Table 4.11). In the case of this film, it must be taken into account that the degree of crystallinity remains unchanged as compared with PVA (Table 4.8).

Table 4.11. Mechanical properties data of unplasticized and glycerol-plasticized PVA and PVA/GS nanocomposites.

Sample	Young's modulus (MPa)	Yield stress (MPa)	Break Stress (MPa)	Elongation at break (%)
PVA (6 h at 60 °C)	1941±129	60.4±6.3	47.9±4.4	157.6±17.2
PVA/GS-0.5	2051±144	70.7±5.2	52.6±6.5	98.3±12.7
PVA/GS-1	1982±37	69.6±7.6	51.5±9.8	91.8±12.0
PVA/GS-1.5	2235±69	70.7±5.0	55.6±5.2	50.6±10.1
PVA/GS-2	1825±11	49.1±3.1	47.7±5.1	55.0±7.9
PVA/GS1 *ex situ*	1998±158	79.2±7.6	74.9±7.6	12.0±3.1
PVA/GLY (6 h at 60 °C)	100±1	-	38.6±1.9	446.0±36.4
PVA/GS-0.5/GLY	127±8	-	35.1±2.4	411.3±47.1
PVA/GS-1/GLY	159±12	-	35.7±1.1	370.4±23.2
PVA/GS-1.5/GLY	162±13	-	37.7±1.7	344.5±30.5
PVA/GS-2/GLY	169±12	-	33.5±1.5	312.1±26.0

The lower elongation at break of the PVA/graphene nanocomposites compared to neat PVA indicates that the incorporation of GS into PVA increases the brittleness of the composite, especially in the case of the unplasticized composite prepared by the *ex situ* method. This can be due to the poorer dispersion of GS in PVA matrix as compared with the nanocomposite film prepared by *in situ* process. The presence of GS aggregates which act as stress concentrators leads to premature break of the material.

Following the same procedure, the mechanical properties of nanocomposites containing AgNPs prepared through *in situ* and *ex situ* synthesis are analyzed, as well as their GO counterparts. PVA, PVA/GO and PVA with AgNPs films undergo elastic deformation and a yielding behavior (Figure 4.28).
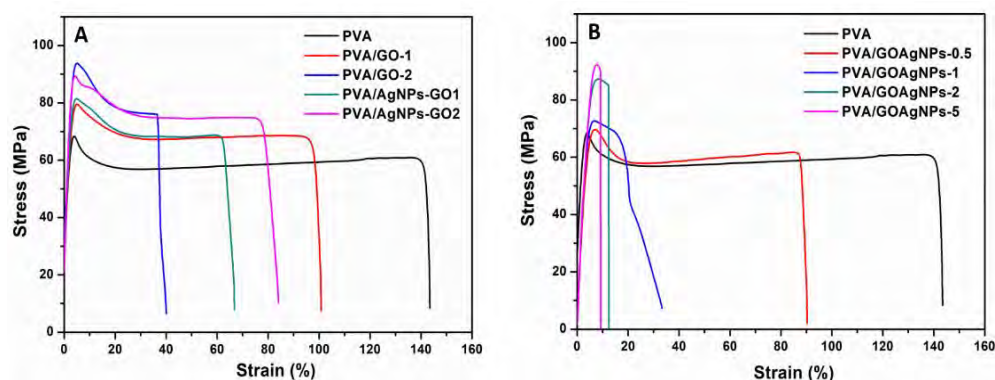
Figure 4.28. Stress–strain curves of: (A) PVA, PVA/GO and *in situ* PVA/AgNPs-GO nanocomposites and (B) *ex situ* PVA/GO-AgNPs nanocomposites.

Experimental data of the mechanical properties are shown in Table 4.12 and Figure 4.29. The incorporation of GO and AgNPs-GO through *in situ* synthesis resulted in an increase of Young´s modulus, yield and break stress, and in a reduction of elongation at break. Compared to the values shown in Table 4.10, it can be inferred that this group of PVA/GO samples prepared with an ultrasonic bath (under the same conditions as for the *in situ* synthesis) shows some changes in the mechanical properties with the addition of GO, very similar to those shown above. A 24%, 53% and 34% increase of elastic modulus, yield and break stress, respectively, is achieved at 2 wt% GO compared to PVA. However, elongation at break is found to decrease at both GO loadings, but the reduction is more pronounced in the higher GO content (Figure 4.29).

The enhancement in elastic modulus is more significant when AgNPs are incorporated through *in situ* synthesis, especially at 2 wt% GO, where a 47% increase is observed as compared with neat PVA. In this sample, the improvement in yield stress and break stress are 52% and 40% respectively and the reduction in elongation at break is about 50%. The *ex situ* counterparts show slightly higher Young's modulus values than those obtained for pure PVA, but lower than the values achieved with the *in situ* samples. Yield stress and break stress increase a

49% and 42%, respectively, in the sample with 2 wt% of filler, being similar to the improvement of the *in situ* sample. The elongation at break decreases dramatically by 90% with the addition of 2 wt% GO-AgNPs through the *ex situ* method. The decrease in elongation at break is not as sharp in the *in situ* samples as it was in the *ex situ* samples.

Table 4.12. Mechanical properties data of PVA and PVA with AgNPs nanocomposites.

Sample	Young's modulus (MPa)	Yield stress (MPa)	Break Stress (MPa)	Elongation at break (%)
PVA	2031±144	59.0±7.8	56.1±7.4	133.0±16.5
PVA/GO1	2322±141	79.1±5.1	61.7±6.1	103.9±18.8
PVA/GO2	2519±113	90.3±4.4	75.0±5.2	36.8±5.3
PVA/AgNPs-GO1	2533±101	81.7±5.5	69.4±6.7	63.3±8.8
PVA/AgNPs-GO2	2982±132	90.1±5.1	78.7±7.9	68.3±12.5
PVA/GO-AgNPs-0.5	2212±198	70.3±7.2	64.3±3.4	108.0±18.7
PVA/GO-AgNPs-1	2230±33	72.4±5.4	65.0±2.5	21.4±4.1
PVA/GO-AgNPs-2	2329±203	88.1±2.2	79.8±9.5	13.7±2.9
PVA/GO-AgNPs-5	2332±111	89.7±5.3	85.1±6.0	9.0±0.5

The comparison between PVA/AgNPs-GO1 and PVA/AgNPs-GO2 shows an improvement in Young's modulus (18%), but no notable differences in the other properties. Likewise, the evaluation between *ex situ* nanocomposites reveals a slight increase with the increase of the filler content, achieving the highest value of the elastic modulus with 5 wt% of GO-AgNPs. This filler content also causes an increase of about 52% in yield and break stress when compared to pure PVA. Moreover, a severe and gradually decrease in the elongation at break is observed after the addition of GO–AgNPs hybrid, being the most important drop also for PVA/GO-AgNPs-5 nanocomposite, about 93%. The improved mechanical properties are attributed to the superior mechanical properties of GO and the reinforcement effect of AgNPs. Usman *et al.* [95] reported an enhancement in the modulus of PVA in the presence of Ag or GO, and further improvement with the incorporation of GO-Ag. The constrained polymer chain mobility due to the

interfacial interaction between PVA and GO–AgNPs hybrid leads to highly brittle PVA/GO–AgNPs composites.
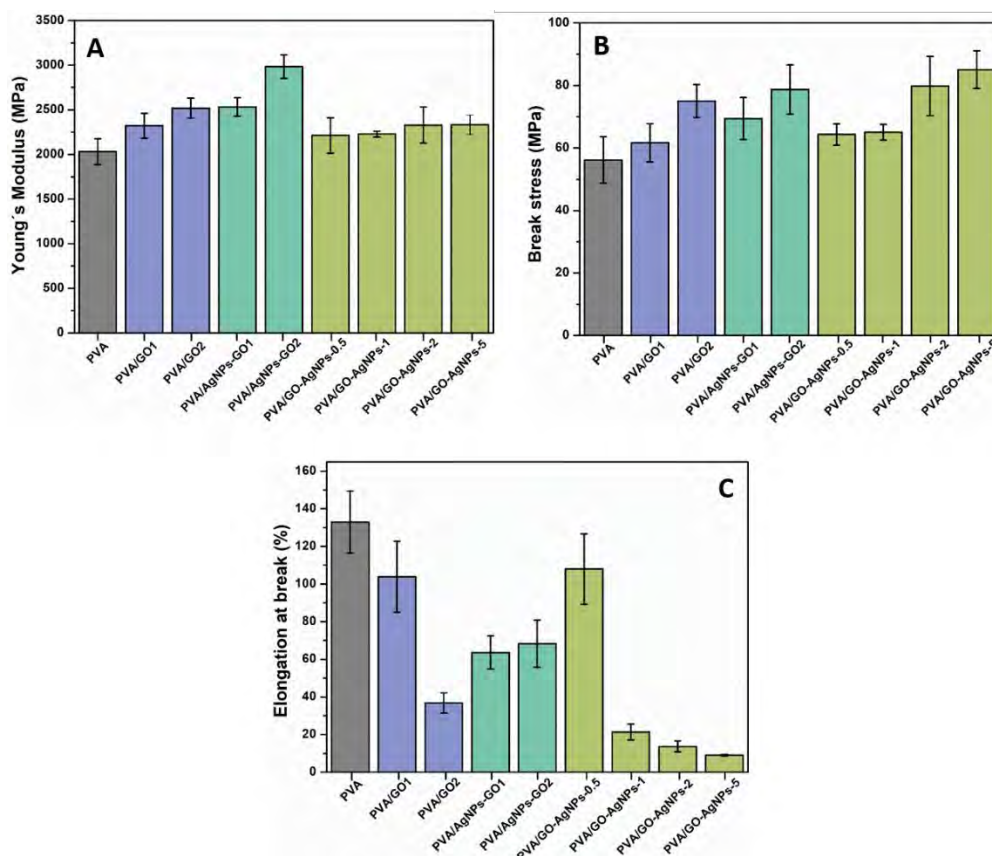
Figure 4.29. Mechanical properties of PVA, PVA/GO and PVA with AgNPs nanocomposites: (A) Young's modulus, (B) Yield stress and (C) Break stress.

In previous studies on polymer/graphene nanocomposites improvements in mechanical properties have been reported [71,75,149-152]. Liang *et al.* [71] developed nanocomposite thin films of PVA/GO with GO up to 0.7 wt% that presented a significant increase in the tensile strength and tensile modulus, and a reduction in the elongation at break. Yang *et al.* [151] produced PVA/GO nanocomposites by solution casting with a wide range of GO contents up to 3.5 wt%, verifying that the presence of GO enhanced the tensile strength and modulus, but decreased significantly the elongation at break. Yang *et al.* [73] and Zhao *et al.* [75] reported the preparation of PVA/graphene composites by a

reduction process of graphene oxide/PVA solution using hydrazine. The authors also verified the increase in the elastic modulus and tensile strength with increasing graphene content, and the significant decrease in elongation at break. Bao *et al.* [152] have also reported the preparation of PVA/GO nanocomposites through solution mixing and PVA/graphene *via* chemical reduction of GO in the presence of polymer at low GO loadings with improved mechanical properties. Manna *et al.* reported the improvement of mechanical properties of poly(vinylidene fluoride) when filled with AgNPs [153]. Mbhele *et al.* studied the mechanical properties of AgNPs-filled PVA and observed that its incorporation increased the elastic modulus and the stress at break of PVA [65]. Liu *et al.* studied the effect of GO–AgNPs hybrids on the tensile mechanical behavior of PLA. The authors observed that PLA/GO–AgNPs composites had higher tensile modulus and tensile strength than PLA/GO [154].

Taking all examined results into consideration, it can be concluded that among the employed graphene-based nanostructures, the greatest enhancement in mechanical properties of PVA has been achieved with *in situ* synthetized PVA/AgNPs-GO2 nanocomposite. The good dispersion of the filler throughout the polymer matrix (with strong interfacial interaction between polymer chains and the hybrid), the superior mechanical properties of GO and the reinforcement effect of AgNPs make possible to increase the efficiency of stress transfer from the PVA to the filler at the interface.

4.3.4. Water vapor permeability

Water vapor permeability (WVP) of unplasticized and plasticized PVA/GO and PVA/GS nanocomposites with different contents of fillers was measured at a vapor pressure difference of 100/58% RH (i.e. at a RH gradient of 100/58) across the film. WVP data are shown in Figure 4.30.

In line with the behavior observed in Chapter 3, PVA films show significant differences ($p < 0.05$) with respect to PVA/GLY films. The WVP of PVA and heated-PVA increases, about 89 and 120%, respectively, with the addition of glycerol. The hydrophilic nature of glycerol results in an increase in permeability. Hydroxyl groups of glycerol interact with the hydroxyl groups of PVA, so the intermolecular attractions along the PVA chains decrease and, consequently, the

mobility of the chain increases, facilitating the diffusivity of water vapor through the PVA film and accelerating the transmission of water vapor [155].

The permeability values obtained with the addition of 1 and 2 wt% of GO to unplasticized PVA are not statistically significant ($p > 0.05$) compared to pure polymer, and the same behavior is observed with the addition of GO to plasticized PVA. Similarly, the WVP obtained with the addition of GS (1 and 2 wt%) to plasticized and unplasticized PVA are not statistically significant ($p > 0.05$).
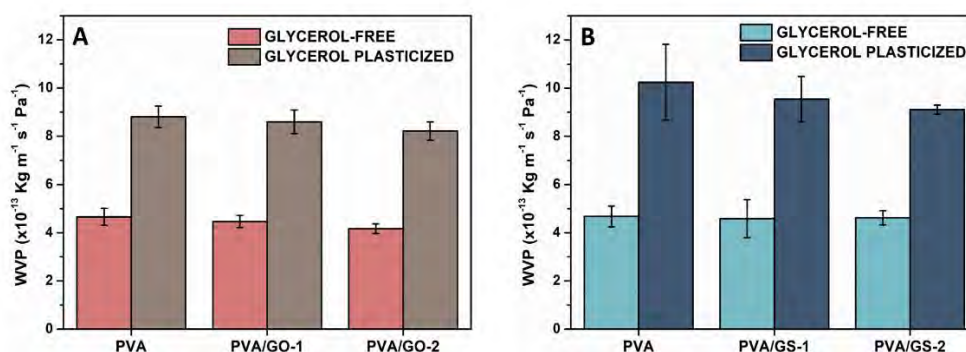
Figure 4.30. Water vapor permeability (WVP) for unplasticized and glycerol plasticized (A) PVA/GO and (B) PVA/GS nanocomposites.

Considering the decreasing trend that can be inferred from the Figure 4.30, higher GO or GS contents could reduce permeability, since the presence of the sheets distributed in the PVA (as good dispersion) leads to a more tortuous path that water molecules require to permeate through the polymeric matrix, leading to lower diffusion process and to lower WVP. However, there would be another factor to consider, the effect of crystallinity on the solubility of water vapor in polymers. PVA/GS nanocomposites exhibit less crystallinity than pure PVA (Table 4.8), and free amorphous regions exhibit less resistance to water vapor permeability than crystalline regions, which would lead to an increase in permeability [156]. In contrast, in this case, despite the reduction in crystallinity with increasing GS content, the effect of good dispersion (more tortuous path) seems to have more impact on permeability.

4.3.5. Water absorption

The water uptake results of unplasticized and glycerol plasticized PVA, PVA/GO and PVA/GS nanocomposites, as well as PVA/AgNPs-GO synthesized via *in situ* and *ex situ* method are displayed in Figure 4.31. Neat unplasticized PVA film exhibits the highest water absorption value, whilst in the presence of glycerol a significant reduction in the water uptake (≈35%) is observed. This reduction can be attributed to the hydrogen bonding between glycerol and PVA. The polar groups of PVA form hydrogen bonds with hydroxyl groups of plasticizer and they are unable to attach water molecules, and therefore the insertion of water molecules is hindered. In the case of heated-PVA (according to PVA/GS nanocomposite synthesis conditions) glycerol addition decreases the water adsorption by 38%, suggesting higher interaction between polymer chains and plasticizer as a result of the heat treatment.

The addition of GO into unplasticized and plasticized PVA (Figure 4.31A) leads to a reduction in the amount of water uptake. The water absorption of PVA/GO nanocomposites decreases by 17.7, 28.1, 31.0 and 40.8%, after incorporation of 0.5, 1, 1.5 and 2 wt% of GS respectively, when compared with neat PVA. Likewise, the addition of the same amounts of GO to the plasticized PVA results in a decrease of 8.7, 20.7, 30.4 and 39.1% water uptake. With respect to PVA/GS nanocomposites, the incorporation of GS by the *in situ* method into unplasticized and plasticized PVA also results in a reduction in the amount of water absorbed (Figure 4.31B). Compared to heated-PVA, 0.5, 1, 1.5 and 2 wt% GS content decreases the water absorption of the nanocomposites by 8.8, 20.7, 30.4 and 39.1% respectively. Similarly, the incorporation of these amounts into glycerol-plasticized PVA reduces water absorption by 8.6, 15.1, 25.7 and 41.1% respectively. In addition, the water absorption value of the unplasticized nanocomposite containing 1 wt% GS prepared by the *ex situ* method is similar to that of the pure PVA film (Figure 4.31B).

Previous studies have revealed that graphene and GO-AgNPs -based PVA nanocomposites show a considerable improvement in water resistance compared to the neat polymer matrix [74]. The presence of GO–AgNPs results in a lower absorbed water content (Figure 4.31C) and a higher GO–AgNPs content leads to a lower amount of water uptake. However, this behavior is not observed in

PVA/AgNPs-GO nanocomposites prepared through *in situ* method, since no statistically significant difference is found for these two samples. Both have a reduction of approximately 46%, greater water resistance than in the case of their *ex situ* counterparts. For the PVA/GO-AgNPs nanocomposites prepared *via ex situ* method, a reduction of the absorbed water between 10% and 50% is observed, specifically a decrease of 27% and 40% with the addition of 1 wt% and 2 wt% GO-AgNPs hybrid.
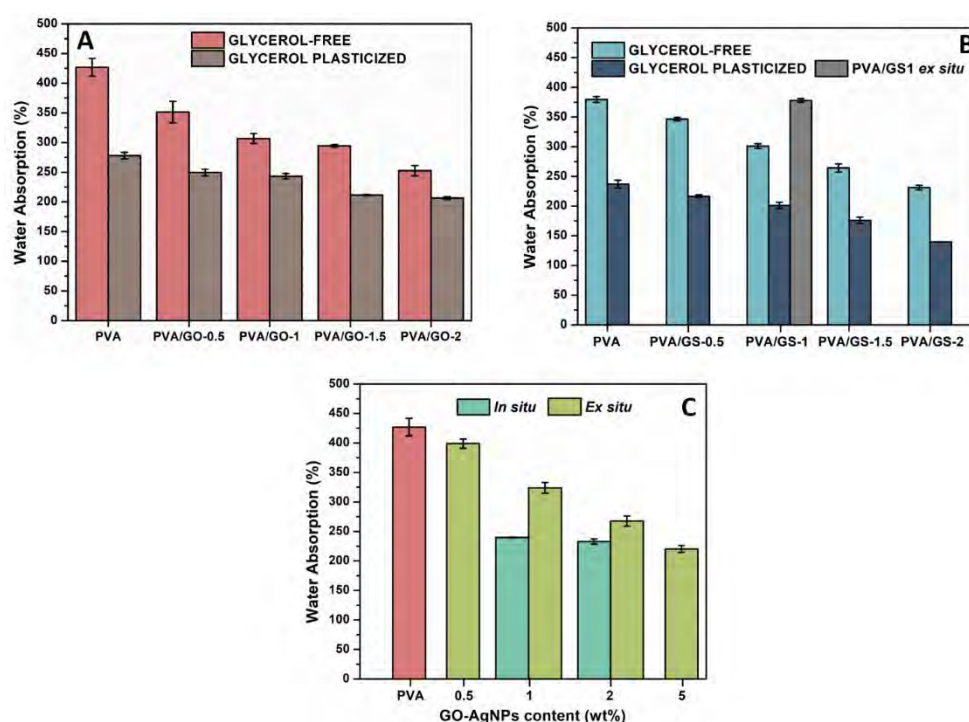
Figure 4.31. Water absorption for unplasticized and glycerol plasticized (A) PVA/GO, (B) PVA/GS nanocomposites and (C) PVA nanocomposites containing GO-AgNPs hybrid synthesized *via in situ* and *ex situ* method.

The water resistance increase found for the PVA nanocomposites is attributed to different factors. First, the strong interfacial adhesion between the polymer matrix and fillers through hydrogen bonding that leads to less free hydrophilic groups, and therefore less absorption sites for lodging of water, and secondly, due to the hydrophobic nature of the filler in the case of GS. For GO-AgNPs, the partial reduction of GO when nanoparticles are synthesized results in

the filler changing to hydrophobic. Finally, because of the interactions between the polymer and the filler, a constrained polymer region is formed in which a restriction of polymer motion occurs, which inhibits the absorption of water [137,157]. The better water-resistance property displayed by *in situ* PVA/AgNPs-GO nanocomposites may be also explained by the existence of more interactions between PVA and fillers when comparing with PVA/GO composites.

4.3.6. Inhibition of bacterial growth by the nanocomposites

Gram negative *E. coli* ATCC 25922 and Gram positive *S. aureus* ATCC 25923 were selected for assessing antibacterial activity of PVA/GO and PVA/AgNPs-GO nanocomposites due to their clinical importance and their wide use as model microorganisms in antimicrobial activity tests [158,159]. Owing to the biocompatibility properties and the lack of antimicrobial activity of PVA [160], it was used as a negative inhibition control in this assay. The bacterial growth inhibition was analyzed using two different methods: measuring bacterial growth by means of absorbance measurements, and counting of CFU. Figures 4.32A,B show the growth kinetics curves of *S. aureus* and *E. coli* in the presence of PVA, PVA/GO2 and *in situ* synthetized PVA/AgNPs-GO discs by measuring the absorbance at 450 nm every 24 h. The cellular viability (in CFU/mL) of *S. aureus* and *E. coli* after different exposure times is represented in Figures 4.32C,D. In these figures, the antibacterial behavior of PVA/GO1 sample is not displayed, since the same behavior was observed for both PVA/GO samples.

As can be seen in Figures 4.32A,B, both *E. coli* and *S. aureus* strains were able to grow in the presence of PVA/GO2 nanocomposite sample, indicating the lack of antibacterial activity of GO against both *E. coli* and *S. aureus* when it is incorporated in PVA matrix with a content up to 2 wt%. These results agree with those presented in Chapter 2 and with the findings of other studies, in which antibacterial activity of graphene based polymer nanocomposites is investigated. Cao *et al.* [161] reported that PVA/graphene nanocomposites did not exhibit antimicrobial activity against *E. coli* and *S. aureus*, and in PLA/GO nanocomposites produced by Liu *et al.* [154] no antibacterial activity was found either against *E. coli*.
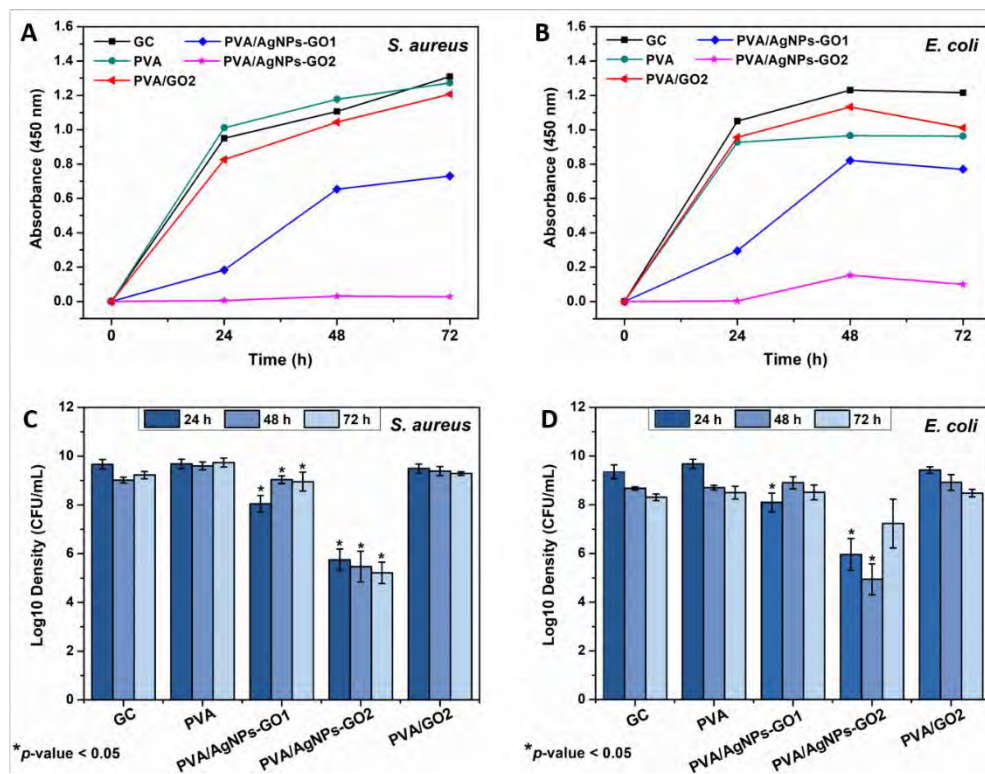
Figure 4.32. Absorbance of (A) *S. aureus* growth curves and (B) *E. coli* growth curves after different times of exposure to PVA, PVA/GO2 and *in situ* PVA/AgNPs-GO nanocomposite films. Viable counts of (C) *S. aureus* and (D) *E. coli*.

In line with the discussion of Chapter 2, graphene-based nanomaterials can show antimicrobial properties, depending on their physicochemical properties, such as sheet size, surface area, purity, structural defects, surface chemical properties, functional groups and degree of oxidation. The toxicity of GO and reduced GO embedded in biodegradable polymer nanocomposites is exposure time and graphenic material concentration dependent as demonstrated by Fran *et al.* [162] and Peña-Bahamonde *et al.* [163]. Their results have shown that the lower the concentration of graphite oxide, the less graphite oxide gets exposed from the films. At low concentrations, microorganisms could only access the nanomaterial, and therefore be inactivated, if the polymer could be degraded to expose GO or reduced GO on the film surface. On the other hand, their studies have confirmed that the time needed to produce microbial inactivation and inhibition of biofilm growth is directly related to the time needed by

microorganisms to degrade the polymer and that the sharp edges of the graphenic material emerge on the surface of the nanocomposite. From these studies it can be concluded that the antimicrobial activity of a graphene-based polymer composite surface depends on the graphene concentration.

Furthermore, the presence of irregularities on the polymer film surface has effect on bacterial adhesion and biofilm deposition. However, the exact influence of the surface roughness is still controversial as it depends on the surface topography and whether it is micro or nano [164]. While some studies have shown an increase in proliferation and adhesion by increasing roughness, others have observed the opposite. There are also research that have reported the existence of an optimal controlled roughness for a minimum microbial proliferation by means of the design of nanopillars in the material surface [165]. Generally, rougher surfaces have more attachments sites for bacteria than smoother ones. It has been reported that the incorporation of GO into polymer matrices changes the topography of the surface, observing an increase in roughness due to the wrinkled geometry of GO nanosheets [154,166,167]. Zou *et al.* [168] observed that the antibacterial effect of GO was stronger when the wrinkle size matched the bacterial diameter. In these cases, the surface topography significantly affects the antimicrobial activity due to the close contact between the cell wall and the GO substrate. Pham *et al.* [169] analyzed the effect of graphene film surface roughness, the density of graphene edges, and stack orientation on bactericidal efficiency. This study demonstrated that the density of the edges of the graphene was the predominant parameter that determines the antibacterial behavior of the graphene nanosheet films.

In the present work, the high purity of GO obtained by exhaustive washings, the reduced amounts of GO used, and the binding of homogeneous dispersed GO sheets with the polymer matrix, along with the fact that the contact of GO with bacteria is hindered due to their coating with PVA, may explain the lack of antibacterial activity of GO when incorporated into the PVA matrix to form PVA/GO nanocomposites.

Figures 4.32A and B reveal that bacterial growth was affected by the presence of the two *in situ* PVA/AgNPs-GO nanocomposite films. However, it can be appreciated that only the PVA/AgNPs-GO2 sample completely prevents

cell division of the bacteria because its absorbance remains stable during the 72 h of the test, showing no growth. For the nanocomposite sample synthesized using less concentration of both GO and silver precursor (PVA/AgNPs-GO1), the growth slows down during 24 h, and then this effect is less noticeable. Both absorbance and viable cell count seem to demonstrate the antibacterial capacity of PVA/AgNPs-GO nanocomposites, where the efficiency is time and AgNPs precursor concentration dependent. In fact, PVA/AgNPs-GO2 nanocomposite exhibits the strongest inhibition of bacterial growth at any time with both bacteria ($p < 0.001$), with exception of the viable cells of *E. coli* after 72 h where no statistically growth inhibition was found (Figure 4.32D). Nevertheless, it showed longer-term antibacterial effectiveness than PVA/AgNPs-GO1, which lost some of its antimicrobial effect after 48 h, especially against *E. coli* where no difference was found compared with PVA control at 48 h and 72 h in both methods (Figures 4.32B,D). Moreover, it should be noted that PVA/AgNPs-GO2 was found to have a bactericidal effect, not only inhibiting bacterial growth, but also by reducing the number of viable cells that were inoculated.

Although all the studied samples present similar antibacterial behavior in both bacteria, the results suggest that *S. aureus* cells are slightly more susceptible to PVA/AgNPs-GO nanocomposites effect than *E. coli* cells. Similar results have been reported by Carpio *et al.* [170], and more recently by Ma *et al.* [171]. This can be explained through the structural differences of the cell wall between the two bacteria [172]. The cell walls of the Gram-positive bacteria (*S. aureus*) is a thick wall containing many peptidoglycan layers. However, Gram-negative bacteria, such as *E. coli*, display two membranes, which structure and composition are different. The inner one is the cytoplasmic cell membrane, the outer one has as a main constituent lipopolysaccharide (LPS), and between them, there is a thin peptidoglycan layer. LPS may act as a protective barrier preventing the penetration of PVA/AgNPa-GO compounds into Gram-negative bacterial cells.

Figure 4.33 displays the effect of *ex situ* PVA/GO–AgNPs composite films with different GO–AgNPs contents on the growth of *S. aureus* and *E. coli* cells. As seen from the representation of the results, the antibacterial properties of the PVA/GO-AgNPs nanocomposite films are also time and GO–AgNPs loading dependent. On the basis of the absorbance measurements, nanocomposite samples with 0.5 and 1 wt% GO–AgNPs displayed no inhibition of *S. aureus* cells over the

time investigated. By increasing the GO–AgNPs content up to 2 wt% a reduction in bacteria growth started to be noticeable, while 5 wt% GO-AgNPs had a remarkable effect on cell growth, since a complete inhibition effect was achieved during the entire sampling time (Figure 4.33A).
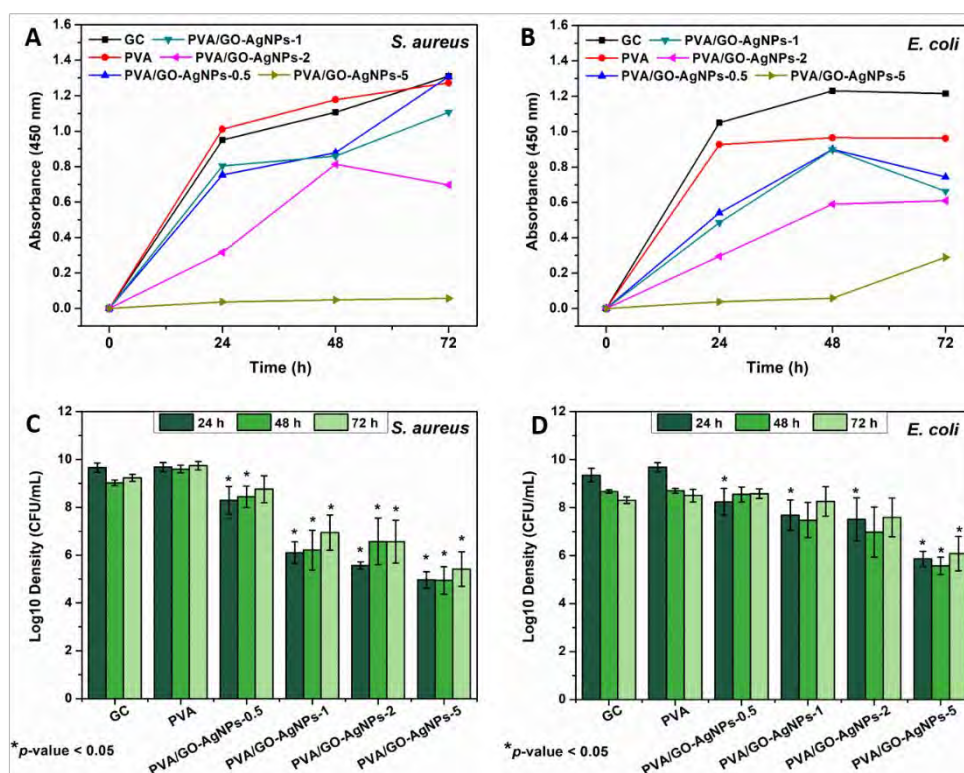
Figure 4.33. Absorbance of (A) *S. aureus* growth curves and (B) *E. coli* growth curves after different times of exposure to *ex situ* PVA/GO–AgNPs nanocomposite films. Viable counts of (C) *S. aureus* and (D) *E. coli*.

The incorporation of 0.5 and 1 wt% GO-AgNPs into the PVA matrix exhibited a moderate reduction in *E. coli* bacterial growth upon 24 h of exposure (Figure 4.33B). Beyond that time not inhibitory effect was observed, suggesting again a slower growth effect. In the case of PVA/GO–AgNPs-2 composite film at 24 h of exposure, an inhibition of cell growth was detected, resulting in a slower growth compared to the growth in the presence of PVA films containing 0.5 and 1 wt% GO–AgNPs. The growth of *E. coli* cell population is completely suppressed after 24 and 48 h of exposure in the presence of PVA films filled with 5 wt% GO-

AgNPs. As can be seen from Figures 4.33C,D, the growth of both *S. aureus* and *E. coli* cell population is reduced, in a greater or lesser extent in the presence of PVA film filled with 0.5 to 5 wt% GO–AgNPs, and the composite sample film with the highest GO–AgNPs content exhibits the strongest bacterial growth inhibitory activity.

Similar to the behavior observed for *in situ* nanocomposites, the *E. coli* strain is more resistant than the *S. aureus* strain to *ex situ* PVA/GO-AgNPs nanocomposite films with any hybrid GO-AgNPs content. Therefore, the presence of hybrid GO-AgNPs in PVA nanocomposite films leads to a higher long-term antibacterial efficacy against *S. aureus* than against *E. coli*.

Leaching of antimicrobial agents from *ex situ* PVA/GO–AgNPs composite films after immersion in PBS (for 24 h at 37 °C) may exert a bacterial growth inhibitory effect. AgNPs and Ag^+ ions are the antimicrobial agents that could leach out of the composite films. The evaluation of the antimicrobial effect of the leaches was estimated by measuring the absorbance at 450 nm and the results are shown in Figure 4.34. As previously, PVA film was used as growth control since it does not release any antimicrobial agent.
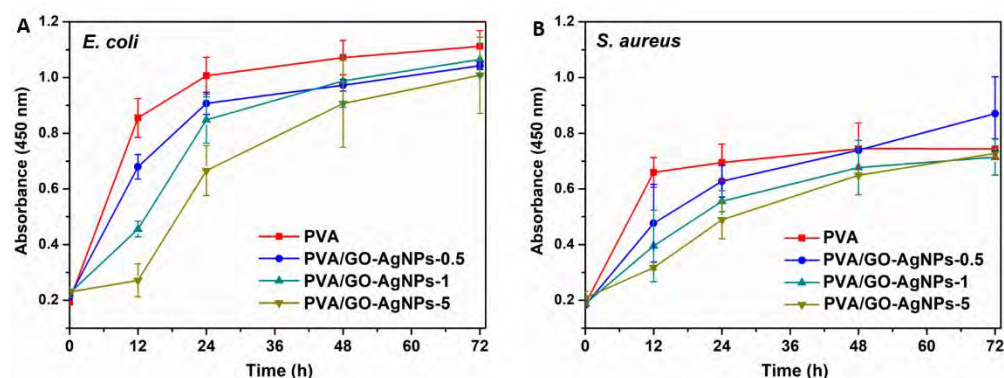
Figure 4.34. Absorbance of (A) E. coli growth curves and (B) S. aureus growth curves after different times of exposure to the leaches from PVA/GO–AgNPs composite films (for 24 hours at 37 °C in PBS).

The lixiviates from all PVA films containing GO–AgNPs showed significant bacterial growth inhibition compared to neat PVA in the first 12 hours in contact with bacteria. PVA/GO-AgNPs-5 film displayed statistically the highest

inhibitory activity against *E. coli* ($p < 0.01$), and after 24 h of exposure, the PVA/GO–AgNPs5 film was the only one that exhibited growth inhibition ($p < 0.01$) (Figure 4.34A). As for *S. aureus*, PVA/GO-AgNPs-0.5 showed no inhibitory effect on this bacterium growth over the period of time studied, and both PVA/GO-AgNPs-1 and PVA/GO-AgNPs-5 did show it up to 24 h exposure ($p < 0.05$), although there were no significant differences between them (Figure 4.34B). After 48 h, none of the tested materials showed statistically significant differences when compared with PVA in both microorganisms ($p > 0.05$).

In order to assess the possible release of silver nanoparticles from the polymer matrix, more leaching experiments were performed. For each PVA/GO-AgNPs sample, specimens with dimensions of 2 cm x 2 cm were immersed in 10 mL deionized water at 25 °C for 24 h. The solutions were then analyzed by UV-Vis spectroscopy for the detection of the Surface Plasmon Resonance absorption band of silver nanoparticles, but in none of the samples was the SPR band observed (Figure 4.35).
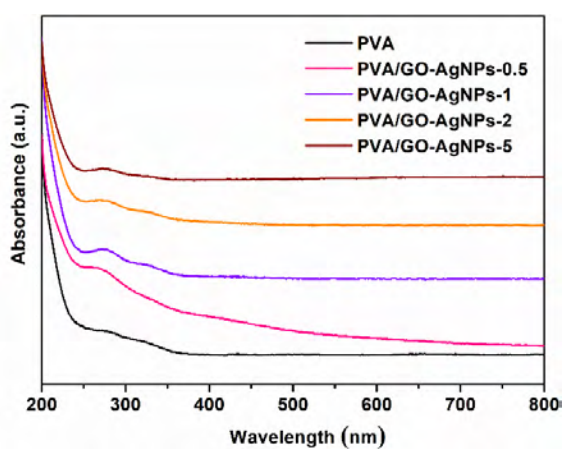
Figure 4.35. UV-Vis absorption spectra of leachates from PVA/GO–AgNPs nanocomposite films after water immersion.

This indicates that there was no AgNPs in solution, suggesting that silver nanoparticles are firmly attached to GO, immobilized, and that a strong interaction has been established between GO–AgNPs hybrid and polymer matrix. Thus, the stability of the hybrid is confirmed. Therefore, it can be inferred that the antibacterial activity observed in the leachates released from the films is due to the leaching of silver ions (Ag^+).

Although the mechanisms of antibacterial activity of AgNPs are not fully understood yet, it has been recognized that the antibacterial effect of AgNPs depends on nanoparticle-cell interactions and/or silver ions interactions. Some authors suggest that the toxic effect is due to particle-only effects [173,174], others, however, attributed it to Ag^+ ions alone [175], whereas there are others that claim that both nanoparticles and ions contribute to the toxicity [176-181]. In the first case, nanoparticles attack bacteria through direct contact with cell wall, since AgNPs can effectively contact microorganisms due to their high surface/volume ratio. After contacting, changes in membrane morphology have been observed, which lead to an increase in permeability, allowing nanoparticles penetration into cell membrane that affects the transport activity through the plasma membrane [182]. As a result, various vital cell functions are obstructed, leading to cell death. Sondi *et al.* [183], Morones *et al.* [173] and Agnihotri *et al.* [184] confirmed the incorporation of AgNPs into the *E. coli* membrane by electron microscopy. Some researchers, however, have claimed that the toxicity of AgNPs is attributed exclusively to the Ag^+ ions released from the oxidized AgNPs surface in aerobic conditions [175]. Ag^+ ions interact with thiol-containing proteins in the cell wall and affect their functions. The properties of nanoparticles such as size and shape indirectly influence the toxicity of AgNPs. The higher the specific surface area, the faster is the rate of silver particle dissolution. Small AgNPs release more Ag^+ ions than the large ones, and according to the study by Sotiriou *et al.* the antibacterial performance of AgNPs with an average size < 10 nm is governed by the Ag^+ ions released from their surface [185].

After 24 h of incubation, the results of the antibacterial experiments (Figures 4.32A,B; Figures 4.33A,B and Figure 4.34) show that the inhibitory effect is higher when bacterial cells are in direct contact with PVA/GO–AgNPs composite films than when they are exposed to leaching of silver ions from PVA/GO–AgNPs composite films. From this result, it can be inferred that both the cell direct contact and penetration of the nanoparticles, together with the released silver ions from the oxidized surface of AgNPs, contribute to the toxic activity. The incorporation of 2 wt% GO to PVA resulted in a composite that lacked antibacterial activity against *E. coli* and *S. aureus* (Figure 4.32). Therefore, AgNPs may be considered the main contributors to the bactericidal effect of the nanocomposite.

In addition, it is worth noting the effect of the exposure of the hybrids on the surface of the films. In PVA/GO–AgNPs nanocomposites, GO–AgNPs hybrid can be emerging on the surface and/or embedded inside. GO–AgNPs sheets exposed at the surface of the film can have a direct contact with the bacteria, while those present in the bulk of the polymer cannot. The only possible mechanism of the antibacterial action of the latter is through the release of Ag^+ ions. The water from the bacteria medium containing dissolved oxygen diffuses into the polymer and reaches the AgNPs embedded in the polymer, allowing their oxidation, and generating Ag^+ ions that diffuse to the surface of the film and attack the adsorbed bacteria.

Furthermore, Figure 4.36 shows SEM images of bacteria growth on the different nanocomposite samples. PVA/AgNPs-GO2 nanocomposite did not present any cells adhered to the surface when compared with control PVA in both *S. aureus* and *E. coli*. Likewise, the PVA/GO sample seems to allow the development of a dense biofilm, supporting the results in microtiter plates where no antimicrobial activity was found.
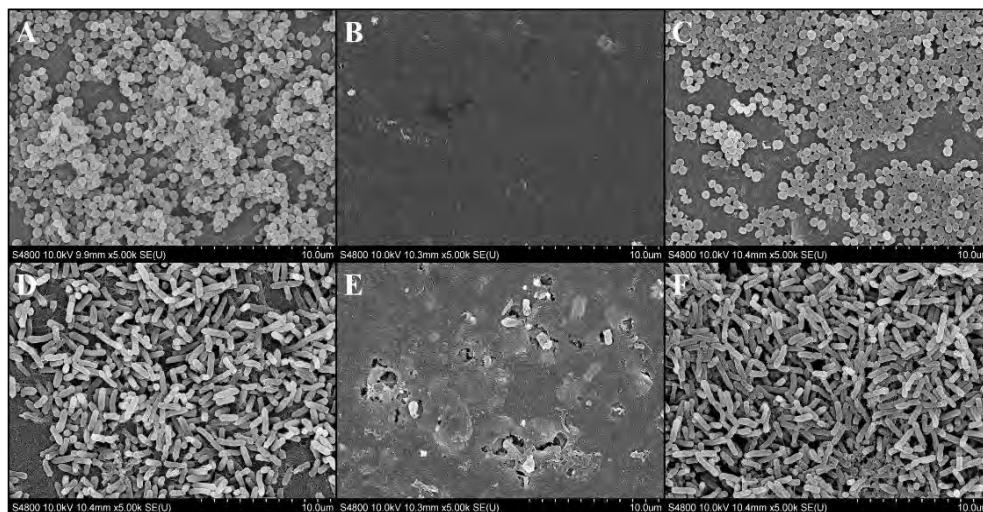
Figure 4.36. Representative SEM micrographs of nanocomposites after incubation with *S. aureus* and *E. coli* for 48 h. (A) PVA with *S. aureus*. (B) PVA/AgNPs-GO2 with *S. aureus*. (C) *S. aureus* on PVA/GO2. (D) *E. coli* cells deposited on PVA. (E) PVA/AgNPs-GO2 with *E. coli*. (F) *E. coli* on PVA/GO2.

PVA has been used in biomedical and pharmaceutical applications as mentioned previously, due to its biocompatibility, biodegradability, water solubility, nontoxicity and film forming ability. Graphene derivatives and graphene-inorganic hybrid materials are also used as biomedical materials due to their unique properties [186]. Biomedical applications of these nanomaterials include drug and gene delivery, biosensing and bioimaging systems, tissue engineering and other therapeutic applications.

The cytotoxicity of nanomaterials is of particular concern when it comes to biomedical applications. The interaction of AgNPs with cells is strongly influenced by their size, shape, surface coatings and aggregation [187]. Studies reported in the literature have shown that the specific physicochemical characteristics of graphenic materials, such as surface area, layer number, lateral dimension, surface chemistry and impurities contribute to the toxicity [188]. Moreover, the cytotoxicity of these nanomaterials is affected by the cell type, dose and exposure time. Cytotoxicity increases with the decrease of AgNPs size while the same concentration is maintained [189,190]. Likewise, an increase in dose leads to an increase in cytotoxicity. In contrast, silver nanoparticles embedded in polymer matrices show less cytotoxicity than bared ones. Sowa-Söhle *et al.* [191] found that thermoplastic polyurethane-silver nanoparticle composites with nanosilver concentrations from 0.01 to 1.0 wt% were non-cytotoxic to mouse fibroblast cells, but toxic to bacteria. Oliveira *et al.* [192] reported the preparation of PVA-Ag hydrogel samples with 0.25 and 0.50 wt% silver precursor. The results revealed the non-cytotoxicity of the materials to mouse fibroblast cells and antimicrobial activity towards bacteria and fungi. The concentration of nanoparticles necessary to induce toxicity in human cells is much higher than that needed to exert antimicrobial activity [193,194]. Regarding the cytotoxicity of graphene nanomaterials, it has been demonstrated the reduced cytotoxicity of graphenic materials when incorporated into polymer matrices [171,195]. Ma *et al.* found that the cytotoxicity of PVA/graphene nanocomposite fibers to human cells was low and graphene content dependent [171]. Based on the above-mentioned analysis, and according to the improved physical and antibacterial properties, the developed PVA/GO–AgNPs composite films can be potential materials in the biomedical field as wound dressings for wound healing and infection prevention.

4.4. Conclusions

The solution casting method allowed the successful addition of GO into the unplasticized PVA and glycerol-plasticized matrix, while the *in situ* reduction of GO, in the presence of PVA and L-AA as a reducing agent, was the optimal strategy for the preparation of PVA/GS nanocomposites. In contrast to the *ex situ* incorporation of GS, the *in situ* approach resulted in good dispersion of GS in the polymer matrix due to hydrogen bonding interactions. Regarding nanocomposites containing silver nanoparticles, two different strategies were developed for their preparation: *in situ* (an environmentally friendly one-step chemical reduction method) and *ex situ* (solution casting) methods.

Microstructural and morphological characterization revealed the good dispersion of the fillers (GO, GS and GO-AgNPs) in the polymer matrix, except for the *ex situ* PVA/GS1 nanocomposite due to weak bonding between GS and PVA. Thermogravimetric measurements showed that thermal stability of PVA was greatly improved at low loading of GO, and this improvement was more significant by adding AgNPs-GO. However, GS exerted a greater blocking effect on the elimination of hydroxyl groups of PVA chains during thermal decomposition, delaying its thermal and thermo-oxidative degradation. The content of graphene-based fillers and the presence of glycerol as a plasticizer affected the thermal transitions (T_g, T_m and T_c) and the degree of crystallinity of PVA, with less prominent variations with GO. The mechanical properties of the PVA were differently affected by the presence of different fillers or depending on whether plasticizer was or not present. For PVA/GS nanocomposites, the mechanical properties were not drastically affected by the reduction in PVA crystallinity. Tensile tests revealed the enhancement in the Young's modulus and tensile strength at break of PVA with the addition of GO, GS or GO-AgNPs, being significantly higher in the presence of AgNPs-GO. All nanocomposites types were more brittle than neat PVA. All nanocomposite samples displayed better water resistance than neat PVA, being the PVA/GS-2 nanocomposite the most water resistant material, whereas no change was observed for the *ex situ* prepared PVA/GS nanocomposite. In general, the exfoliated structure of the nanocomposites resulted in increased thermal stability, mechanical properties and water resistance.

PVA films filled with GO–AgNPs through *in situ* or *ex situ* method showed antibacterial effect against *E. coli* and *S. aureus*, being stronger for the *in situ* PVA/AgNPs-GO2 composite and for the *ex situ* PVA/GO-AgNPs with higher GO–AgNPs content. The higher the silver salt concentration the greater the long-term antibacterial efficiency. These nanocomposites caused higher growth inhibition in *S. aureus* compared to *E. coli*. The direct contact of the bacteria with the composite films led a higher bactericidal effect than the contact with the leachates from those films. Surface bacterial biofilm formation of *S. aureus* and *E. coli* was effectively reduced for the PVA/AgNPs-GO samples. GO not only acted as an effective reinforcing filler but also as an excellent platform to support and stabilize silver nanoparticles, and as a synergistic agent on the antibacterial activity of AgNPs. Due to their properties, the PVA nanocomposites synthesized in this work could potentially be applied for biomedical applications such as transdermal drug delivery or as wound dressings.

4.5. References

[1] N.B. Halima, Poly(vinyl alcohol): review of its promising applications and insights into biodegradation, RSC Advances. 6 (2016) 39823-39832.

[2] C.A. Finch, Polyvinyl alcohol: Properties and Applications, Wiley 1973.

[3] J. Wang, L. Ye, Structure and properties of polyvinyl alcohol/polyurethane blends, Composites Part B: Engineering. 69 (2015) 389-396.

[4] D. Feldman, Polymer nanocomposite barriers, Journal of Macromolecular Science, Part A. 50 (2013) 441-448.

[5] Y. Yan, 2 - Developments in fibers for technical nonwovens, Advances in Technical Nonwovens. (2016) 19-96.

[6] K. Khana, M. Nthoiwa, C.A. Diaz, Y. Chaudhari, Vinyl Alcohol Polymers. in: Olabisi O., Adewale K. (Eds.), Handbook of Thermoplastic, Second edition ed., CRC Press, Boca Raton, 2015, pp. 55.

[7] R.C. Rowe, P.J. Sheskey, S.C. Owen, American Pharmacists Association., Handbook of pharmaceutical excipients, APhA/Pharmaceutical Press, London; Chicago, 2009.

[8] X. Tang, S. Alavi, Recent advances in starch, polyvinyl alcohol based polymer blends, nanocomposites and their biodegradability, Carbohydr. Polym. 85 (2011) 7-16.

[9] X. Luo, J. Li, X. Lin, Effect of gelatinization and additives on morphology and thermal behavior of corn starch/PVA blend films, Carbohydr. Polym. 90 (2012) 1595-1600.

[10] P. Yuan, D. Tan, F. Annabi-Bergaya, Properties and applications of halloysite nanotubes: recent research advances and future prospects, Appl. Clay. Sci. 112 (2015) 75-93.

[11] B.J. Holland, J.N. Hay, The thermal degradation of poly(vinyl alcohol), Polymer. 42 (2001) 6775-6783.

[12] A.I. Cano, M. Cháfer, A. Chiralt, C. González-Martínez, Biodegradation behavior of starch-PVA films as affected by the incorporation of different antimicrobials, Polymer Degradation and Stability. 132 (2016) 11-20.

[13] I. Arvanitoyannis, I. Kolokuris, A. Nakayama, N. Yamamoto, S. Aiba, Physico-chemical studies of chitosan-poly(vinyl alcohol) blends plasticized with sorbitol and sucrose, Carbohydr. Polym. 34 (1997) 9-19.

[14] L. Cui, Q. Fu, C. Chang, J. Yeh, The effect of poly(vinyl alcohol) hydrolysis on the properties of its blends with nylon 6, Polymer Engineering & Science. 49 (2009) 1553-1561.

[15] E. Marin, J. Rojas, Y. Ciro, A review of polyvinyl alcohol derivatives: promising materials for pharmaceutical and biomedical applications. Afr. J. Pharm. Pharmacol. 8 (2014) 674-684, 11.

[16] C.C. DeMerlis, D.R. Schoneker, Review of the oral toxicity of polyvinyl alcohol (PVA), Food and Chemical Toxicology. 41 (2003) 319-326.

[17] T. Ishigaki, Y. Kawagoshi, M. Ike, M. Fujita, Biodegradation of a polyvinyl alcohol-starch blend plastic film. World J. Microbiol. Biotechnol. 15 (1999) 321-327.

[18] J. Pseja, H. Charvatova, P. Hruzik, J. Hrncirik, J. Kupec, Anaerobic biodegradation of blends based on polyvinyl alcohol. J. Polym. Environ. 14 (2006) 185-190.

[19] A. Corti, P. Cinelli, S. D'Antone, E. Kenawy, R. Solaro, Biodegradation of poly(vinyl alcohol) in soil environment: influence of natural organic fillers and structural parameters. Macromol. Chem. Phys. 203 (2002) 1526-1531.

[20] M. Kopcilova, J. Hubackova, J. Ruzicka, M. Dvorackova, M. Julinova, M. Koutny, et al., Biodegradability and Mechanical Properties of Poly(vinyl alcohol)-Based Blend Plastics Prepared Through Extrusion Method. J. Polym. Environ. 21 (2013) 88-94.

[21] V. Loryuenyong, C. Saewong, C. Aranchaiya, A. Buasri, The improvement in mechanical and barrier properties of poly(vinyl alcohol)/graphene oxide packaging films, Packaging Technology and Science. 28 (2015) 939-947.

[22] J. Cai, J. Chen, Q. Zhang, M. Lei, J. He, A. Xiao, et al., Well-aligned cellulose nanofiber-reinforced polyvinyl alcohol composite film: Mechanical and optical properties, Carbohydr. Polym. 140 (2016) 238-245.

[23] H.M. Kim, J.K. Lee, H.S. Lee, Transparent and high gas barrier films based on poly(vinyl alcohol)/graphene oxide composites. Thin Solid Films. 519 (2011) 7766-7771.

[24] M. Aslam, M.A. Kalyar, Z.A. Raza, Polyvinyl alcohol: a review of research status and use of polyvinyl alcohol based nanocomposites, Polymer Engineering & Science. (2018).

[25] C.M. Hassan, N.A. Peppas, Structure and applications of Poly(vinyl alcohol) hydrogels produced by conventional crosslinking or by freezing/thawing methods. Adv. Polym. Sci. 153 (2000) 37-65.

[26] H. Liao, Y. Liu, Q. Wang, W. Duan, Structure and properties of porous poly(vinyl alcohol) hydrogel beads prepared through a physical-chemical crosslinking method. J. Appl. Polym. Sci. 135 (2018) n/a.

[27] C.M. Hassan, N.A. Peppas, Structure and applications of poly(vinyl alcohol) hydrogels produced by conventional crosslinking or by freezing/thawing methods, Biopolymers· PVA Hydrogels, Anionic Polymerisation Nanocomposites, Springer, 2000, pp. 37-65.

[28] R. Surkatti, M.H. El-Naas, Biological treatment of wastewater contaminated with p-cresol using Pseudomonas putida immobilized in polyvinyl alcohol (PVA) gel, Journal of Water Process Engineering. 1 (2014) 84-90.

[29] S.K. Jeong, J. Cho, I. Kong, H. Do Jeong, J.K. Kim, Purification of aquarium water by PVA gel-immobilized photosynthetic bacteria during goldfish rearing, Biotechnology and Bioprocess Engineering. 14 (2009) 238-247.

[30] C. Meng, S. Yu, H. Wang, Y. Cao, L. Tong, W. Liu, et al., Graphene-doped polymer nanofibers for low-threshold nonlinear optical waveguiding, Light: Science & Applications. 4 (2015) e348.

[31] K.J. Ramalingam, N. Dhineshbabu, S. Srither, B. Saravanakumar, R. Yuvakkumar, V. Rajendran, Electrical measurement of PVA/graphene nanofibers for transparent electrode applications, Synth. Met. 191 (2014) 113-119.

[32] S. Tang, Y. Zeng, X. Wang, Splashing needleless electrospinning of nanofibers, Polymer Engineering & Science. 50 (2010) 2252-2257.

[33] J. Mieloszyk, R. Drabent, J. Siódmiak, Phosphorescence and fluorescence of Poly(vinyl Alcohol) films, J Appl Polym Sci. 34 (1987) 1577-1580.

[34] A.S. Roy, S. Gupta, S. Sindhu, A. Parveen, P.C. Ramamurthy, Dielectric properties of novel PVA/ZnO hybrid nanocomposite films, Composites Part B: Engineering. 47 (2013) 314-319.

[35] W. Wu, H. Tian, A. Xiang, Influence of polyol plasticizers on the properties of polyvinyl alcohol films fabricated by melt processing, Journal of Polymers and the Environment. 20 (2012) 63-69.

[36] R. Wang, Q. Wang, L. Li, Evaporation behaviour of water and its plasticizing effect in modified poly(vinyl alcohol) systems, Polym. Int. 52 (2003) 1820-1826.

[37] R. Hodge, T. Bastow, G. Edward, G. Simon, A. Hill, Free volume and the mechanism of plasticization in water-swollen poly(vinyl alcohol), Macromolecules. 29 (1996) 8137-8143.

[38] L. Lim, L.S. Wan, The effect of plasticizers on the properties of polyvinyl alcohol films, Drug Dev. Ind. Pharm. 20 (1994) 1007-1020.

[39] S. Moulay, Review: Poly(vinyl alcohol) Functionalizations and Applications. Polym. - Plast. Technol. Eng. 54 (2015) 1289-1319.

[40] X. Wang, M. Min, Z. Liu, Y. Yang, Z. Zhou, M. Zhu, et al., Poly(ethyleneimine) nanofibrous affinity membrane fabricated via one step wet-electrospinning from poly(vinyl alcohol)-doped poly(ethyleneimine) solution system and its application, Journal of Membrane Science. 379 (2011) 191-199.

[41] C. Shuai, P. Feng, C. Gao, X. Shuai, T. Xiao, S. Peng, Graphene oxide reinforced poly(vinyl alcohol): nanocomposite scaffolds for tissue engineering applications, RSC advances. 5 (2015) 25416-25423.

[42] S. Roy, S. Kuddannaya, T. Das, H.Y. Lee, J. Lim, Y.C. Yoon, et al., A novel approach for fabricating highly tunable and fluffy bioinspired 3D poly(vinyl alcohol)(PVA) fiber scaffolds, Nanoscale. 9 (2017) 7081-7093.

[43] L.A. Utracki, C.A. Wilkie, Polymer blends handbook, Springer 2002.

[44] H. Park, S. Chough, Y. Yun, S. Yoon, Properties of starch/PVA blend films containing citric acid as additive. J. Polym. Environ. 13 (2005) 375-382.

[45] J. Zanela, J.B. Olivato, A.P. Dias, M.V.E. Grossmann, F. Yamashita, Mixture design applied for the development of films based on starch, polyvinyl alcohol, and glycerol. J. Appl. Polym. Sci. 132 (2015) n/a.

[46] E.E. Tanase, V.I. Popa, M.E. Popa, M. Rapa, O. Popa, Biodegradation study of some food packaging biopolymers based on PVA. Bull. Univ. Agric. Sci. Vet. Med. Cluj-Napoca, Anim. Sci. Biotechnol. 73 (2016) 1-5.

[47] L. Fan, H. Yang, J. Yang, M. Peng, J. Hu, Preparation and characterization of chitosan/gelatin/PVA hydrogel for wound dressings, Carbohydr. Polym. 146 (2016) 427-434.

[48] W. Yang, E. Fortunati, F. Bertoglio, J. Owczarek, G. Bruni, M. Kozanecki, et al., Polyvinyl alcohol/chitosan hydrogels with enhanced antioxidant and antibacterial properties induced by lignin nanoparticles, Carbohydr. Polym. 181 (2018) 275-284.

[49] E.A. Kamoun, X. Chen, M.S.M. Eldin, E.S. Kenawy, Crosslinked poly(vinyl alcohol) hydrogels for wound dressing applications: A review of remarkably blended polymers, Arabian Journal of chemistry. 8 (2015) 1-14.

[50] E.A. Kamoun, E.S. Kenawy, T.M. Tamer, M.A. El-Meligy, M.S.M. Eldin, Poly(vinyl alcohol)-alginate physically crosslinked hydrogel membranes for wound dressing applications: characterization and bio-evaluation, Arabian Journal of Chemistry. 8 (2015) 38-47.

[51] H. Li, S. Chen, Y. Wang, Preparation and characterization of nanocomposites of polyvinyl alcohol/cellulose nanowhiskers/chitosan. Compos. Sci. Technol. 115 (2015) 60-65.

[52] E. Butnaru, C.N. Cheaburu, O. Yilmaz, G.M. Pricope, C. Vasile, Poly(vinyl alcohol)/chitosan/montmorillonite nanocomposites for food packaging applications: influence of montmorillonite content. High Perform. Polym. 28 (2016) 1124-1138.

[53] W.S. Khoo, H. Ismail, A. Ariffin, Tensile, swelling, and oxidative degradation properties of crosslinked polyvinyl alcohol/chitosan/halloysite nanotube composites. Int. J. Polym. Mater. Polym. Biomater. 62 (2013) 390-396.

[54] M. Murariu, P. Dubois, PLA composites: From production to properties, Advanced Drug Delivery Reviews. 107 (2016) 17-46.

[55] H. Li, S. Chen, Y. Wang, Thermoplastic PVA/PLA Blends with Improved Processability and Hydrophobicity. Ind. Eng. Chem. Res. 53 (2014) 17355-17361.

[56] Y. Hu, Q. Wang, M. Tang, Preparation and properties of Starch-g-PLA/poly(vinyl alcohol) composite film. Carbohydr. Polym. 96 (2013) 384-388.

[57] C. Sawatari, T. Kondo, Interchain Hydrogen Bonds in Blend Films of Poly(vinyl alcohol) and Its Derivatives with Poly(ethylene oxide). Macromolecules. 32 (1999) 1949-1955.

[58] D.R. Paul, L.M. Robeson, Polymer nanotechnology: Nanocomposites, Polymer. 49 (2008) 3187-3204.

[59] A.J. Crosby, J. Lee, Polymer nanocomposites: the "nano" effect on mechanical properties, Polymer reviews. 47 (2007) 217-229.

[60] E. Chiellini, A. Corti, S. D'Antone, R. Solaro, Biodegradation of poly(vinyl alcohol) based materials. Prog. Polym. Sci. 28 (2003) 963-1014.

[61] S. Asghari, S. Ramezani, M. Ahmadipour, M. Hatami, Fabrication and morphological characterizations of immobilized silver-loaded titanium dioxide nanoparticles/polyvinyl alcohol nanocomposites, Designed Monomers and Polymers. 16 (2013) 349-357.

[62] D. Liu, L. Yuan, H. Xu, H. Tian, A. Xiang, PVA grafted POSS hybrid for high performance polyvinyl alcohol films with enhanced thermal, hydrophobic and mechanical properties, Polymer Composites.

[63] Y. Yu, C. Lin, J. Yeh, W. Lin, Preparation and properties of poly(vinyl alcohol)–clay nanocomposite materials, Polymer. 44 (2003) 3553-3560.

[64] M. Ip, S.L. Lui, V.K. Poon, I. Lung, A. Burd, Antimicrobial activities of silver dressings: an in vitro comparison, J. Med. Microbiol. 55 (2006) 59-63.

[65] Z.H. Mbhele, M.G. Salemane, C.G.C.E. van Sittert, J.M. Nedeljkovic, V. Djokovic, A.S. Luyt, Fabrication and Characterization of Silver-Polyvinyl Alcohol Nanocomposites. Chem. Mater. 15 (2003) 5019-5024.

[66] A.N. Krkljes, M.T. Marinovic-Cincovic, Z.M. Kacarevic-Popovic, J.M. Nedeljkovic, Radiolytic synthesis and characterization of Ag-PVA nanocomposites. Eur. Polym. J. 43 (2007) 2171-2176.

[67] N. Eghbalifam, M. Frounchi, S. Dadbin, Antibacterial silver nanoparticles in polyvinyl alcohol/sodium alginate blend produced by gamma irradiation, Int. J. Biol. Macromol. 80 (2015) 170-176.

[68] H.J. Salavagione, G. Martínez, M.A. Gómez, Synthesis of poly(vinyl alcohol)/reduced graphite oxide nanocomposites with improved thermal and electrical properties, Journal of Materials Chemistry. 19 (2009) 5027-5032.

[69] Y. Xu, W. Hong, H. Bai, C. Li, G. Shi, Strong and ductile poly(vinyl alcohol)/graphene oxide composite films with a layered structure. Carbon. 47 (2009) 3538-3543.

[70] H.J. Salavagione, M.A. Gomez, G. Martinez, Polymeric modification of graphene through esterification of graphite oxide and poly(vinyl alcohol), Macromolecules. 42 (2009) 6331-6334.

[71] J. Liang, Y. Huang, L. Zhang, Y. Wang, Y. Ma, T. Guo, et al., Molecular-level dispersion of graphene into poly(vinyl alcohol) and effective reinforcement of their nanocomposites. Adv. Funct. Mater. 19 (2009) 2297-2302.

[72] K.W. Putz, O.C. Compton, M.J. Palmeri, S.T. Nguyen, L.C. Brinson, High-Nanofiller-Content Graphene Oxide-Polymer Nanocomposites via Vacuum-Assisted Self-Assembly. Adv. Funct. Mater. 20 (2010) 3322-3329.

[73] X. Yang, L. Li, S. Shang, X. Tao, Synthesis and characterization of layer-aligned poly(vinyl alcohol)/graphene nanocomposites. Polymer. 51 (2010) 3431-3435.

[74] J. Wang, X. Wang, C. Xu, M. Zhang, X. Shang, Preparation of graphene/poly(vinyl alcohol) nanocomposites with enhanced mechanical properties and water resistance, Polym. Int. 60 (2011) 816-822.

[75] X. Zhao, Q. Zhang, D. Chen, P. Lu, Enhanced mechanical properties of graphene-based poly(vinyl alcohol) composites, Macromolecules. 44 (2011) 2392-2392.

[76] C. Bao, Y. Guo, L. Song, Y. Hu, Poly(vinyl alcohol) nanocomposites based on graphene and graphite oxide: a comparative investigation of property and mechanism. J. Mater. Chem. 21 (2011) 13942-13950.

[77] T. Zhou, F. Chen, C. Tang, H. Bai, Q. Zhang, H. Deng, et al., The preparation of high performance and conductive poly(vinyl alcohol)/graphene nanocomposite via reducing graphite oxide with sodium hydrosulfite. Compos. Sci. Technol. 71 (2011) 1266-1270.

[78] X. Yang, S. Shang, L. Li, Layer-structured poly(vinyl alcohol)/graphene oxide nanocomposites with improved thermal and mechanical properties, J Appl Polym Sci. 120 (2011) 1355-1360.

[79] H. Huang, P. Ren, J. Chen, W. Zhang, X. Ji, Z. Li, High barrier graphene oxide nanosheet/poly(vinyl alcohol) nanocomposite films, J. Membr. Sci. 409 (2012) 156-163.

[80] S. Morimune, T. Nishino, T. Goto, Poly(vinyl alcohol)/graphene oxide nanocomposites prepared by a simple eco-process, Polym. J. 44 (2012) 1056.

[81] Y.Y. Qi, Z.X. Tai, D.F. Sun, J.T. Chen, H.B. Ma, X.B. Yan, et al., Fabrication and characterization of poly(vinyl alcohol)/graphene oxide nanofibrous biocomposite scaffolds. J. Appl. Polym. Sci. 127 (2013) 1885-1894.

[82] Y. Ye, M. Cheng, X. Xie, J. Rick, Y. Huang, F. Chang, et al., Alkali doped polyvinyl alcohol/graphene electrolyte for direct methanol alkaline fuel cells, J. Power Sources. 239 (2013) 424-432.

[83] C. Li, J. Vongsvivut, X. She, Y. Li, F. She, L. Kong, New insight into non-isothermal crystallization of PVA–graphene composites, Physical Chemistry Chemical Physics. 16 (2014) 22145-22158.

[84] J. Li, L. Shao, L. Yuan, Y. Wang, A novel strategy for making poly(vinyl alcohol)/reduced graphite oxide nanocomposites by solvothermal reduction, Materials & Design (1980-2015). 54 (2014) 520-525.

[85] N. Wang, P.R. Chang, P. Zheng, X. Ma, Graphene–poly(vinyl alcohol) composites: Fabrication, adsorption and electrochemical properties, Appl. Surf. Sci. 314 (2014) 815-821.

[86] S. Kashyap, S.K. Pratihar, S.K. Behera, Strong and ductile graphene oxide reinforced PVA nanocomposites, J. Alloys Compounds. 684 (2016) 254-260.

[87] J. Ma, Y. Li, X. Yin, Y. Xu, J. Yue, J. Bao, et al., Poly(vinyl alcohol)/graphene oxide nanocomposites prepared by in situ polymerization with enhanced mechanical properties and water vapor barrier properties, RSC Advances. 6 (2016) 49448-49458.

[88] D. Liu, Q. Bian, Y. Li, Y. Wang, A. Xiang, H. Tian, Effect of oxidation degrees of graphene oxide on the structure and properties of poly(vinyl alcohol) composite films. Compos. Sci. Technol. 129 (2016) 146-152.

[89] J. Xiao, J. Zhang, W. Lv, Y. Song, Q. Zheng, Multifunctional graphene/poly(vinyl alcohol) aerogels: in situ hydrothermal preparation and applications in broad-spectrum adsorption for dyes and oils, Carbon. 123 (2017) 354-363.

[90] J. Zhang, Y. He, P. Zhu, S. Lin, S. Ju, D. Jiang, In situ reduction of graphene oxide in the poly(vinyl alcohol) matrix via microwave irradiation, Polymer Composites. 40 (2019) 170-178.

[91] S. Stankovich, D.A. Dikin, G.H. Dommett, K.M. Kohlhaas, E.J. Zimney, E.A. Stach, et al., Graphene-based composite materials, Nature. 442 (2006) 282.

[92] Z. Li, D. Wang, M. Zhang, L. Zhao, Enhancement of the thermal conductivity of polymer composites with Ag–graphene hybrids as fillers, physica status solidi (a). 211 (2014) 2142-2149.

[93] R. Surudžić, A. Janković, N. Bibić, M. Vukašinović-Sekulić, A. Perić-Grujić, V. Mišković-Stanković, et al., Physico–chemical and mechanical properties and antibacterial activity of silver/poly(vinyl alcohol)/graphene nanocomposites obtained by electrochemical method, Composites Part B: Engineering. 85 (2016) 102-112.

[94] K. Nešović, M.M. Abudabbus, K.Y. Rhee, V. Mišković-Stanković, Graphene Based Composite Hydrogel for Biomedical Applications, Croat. Chem. Acta. 90 (2017) 1-7.

[95] A. Usman, Z. Hussain, A. Riaz, A.N. Khan, Enhanced mechanical, thermal and antimicrobial properties of poly(vinyl alcohol)/graphene oxide/starch/silver nanocomposites films. Carbohydr. Polym. 153 (2016) 592-599.

[96] C.A. Finch, Polyvinyl Alcohol: Developments, Wiley 1992.

[97] F.J. Liou, Y.J. Wang, Preparation and characterization of crosslinked and heat-treated PVA-MA films. J. Appl. Polym. Sci. 59 (1996) 1395-1403.

[98] J.H. Choi, W.S. Lyoo, S. Ko, Effect of stereoregularity on the properties of syndiotactic-rich ultrahigh-molecular-weight poly(vinyl alcohol)/dimethyl sulfoxide/water gel. Macromol. Chem. Phys. 200 (1999) 1421-1427.

[99] C. Chen, F. Wang, C. Mao, C. Yang, Studies of chitosan. I. Preparation and characterization of chitosan/poly(vinyl alcohol) blend films. J. Appl. Polym. Sci. 105 (2007) 1086-1092.

[100] V.K. Thakur, M.K. Thakur, M.R. Kessler, Handbook of Composites from Renewable Materials, Nanocomposites: Advanced Applications, Wiley 2017.

[101] A. Takamura, F. Ishii, H. Hidaka, Drug release from poly(vinyl alcohol) gel prepared by freeze-thaw procedure, Journal of Controlled Release. 20 (1992) 21-27.

[102] N.A. Peppas, J.E. Scott, Controlled release from poly(vinyl alcohol) gels prepared by freezing-thawing processes, Journal of Controlled Release. 18 (1992) 95-100.

[103] Y. Qiu, K. Park, Environment-sensitive hydrogels for drug delivery, Advanced Drug Delivery Reviews. 53 (2001) 321-339.

[104] M. Mohsen-Nia, H. Modarress, Viscometric study of aqueous poly(vinyl alcohol) (PVA) solutions as a binder in adhesive formulations. J. Adhes. Sci. Technol. 20 (2006) 1273-1280.

[105] A. Suzuki, M. Fujiwara, M. Nishijima, High spin/low spin phase transitions of a spin-crossover complex in the emulsion polymerization of trifluoroethyl methacrylate (TFEMA) using PVA as a protective colloid. Colloid Polym. Sci. 286 (2008) 525-534.

[106] Z. Ajji, A.M. Ali, Adsorption of methyl violet and brilliant blue onto poly(vinyl alcohol) membranes grafted with N-vinyl imidazole/acrylic acid. Nucl. Instrum. Methods Phys. Res. , Sect. B. 265 (2007) 362-365.

[107] S.Y. Nam, H.J. Chun, Y.M. Lee, Pervaporation separation of water-isopropanol mixture using carboxymethylated poly(vinyl alcohol) composite membranes. J. Appl. Polym. Sci. 72 (1999) 241-249.

[108] M.I. Baker, S.P. Walsh, Z. Schwartz, B.D. Boyan, A review of polyvinyl alcohol and its uses in cartilage and orthopedic applications, Journal of Biomedical Materials Research Part B: Applied Biomaterials. 100 (2012) 1451-1457.

[109] M. Kobayashi, J. Toguchida, M. Oka, Preliminary study of polyvinyl alcohol-hydrogel (PVA-H) artificial meniscus. Biomaterials. 24 (2002) 639-647.

[110] M. Kobayashi, M. Oka, Characterization of a polyvinyl alcohol-hydrogel artificial articular cartilage prepared by injection molding, Journal of Biomaterials Science, Polymer Edition. 15 (2004) 741-751.

[111] M. Kobayashi, Y. Chang, M. Oka, A two year in vivo study of polyvinyl alcohol-hydrogel (PVA-H) artificial meniscus. Biomaterials. 26 (2005) 3243-3248.

[112] M. Oka, K. Ushio, P. Kumar, K. Ikeuchi, S.H. Hyon, T. Nakamura, et al., Development of artificial articular cartilage, Proc Inst Mech Eng H. 214 (2000) 59-68.

[113] T. Young, N. Yao, R. Chang, L. Chen, Evaluation of asymmetric poly(vinyl alcohol) membranes for use in artificial islets. Biomaterials. 17 (1996) 2139-2145.

[114] K. Burczak, E. Gamian, A. Kochman, Long-term in vivo performance and biocompatibility of poly(vinyl alcohol) hydrogel macrocapsules for hybrid-type artificial pancreas, Biomaterials. 17 (1996) 2351-2356.

[115] W. Paul, C.P. Sharma, Acetylsalicylic acid loaded poly(vinyl alcohol) hemodialysis membranes: effect of drug release on blood compatibility and permeability. J. Biomater. Sci. , Polym. Ed. 8 (1997) 755-764.

[116] M. Kita, Y. Ogura, Y. Honda, S.H. Hyon, W. Cha 2nd, Y. Ikada, Evaluation of polyvinyl alcohol hydrogel as a soft contact lens material, Graefes Arch Clin Exp Ophthalmol. 228 (1990) 533-537.

[117] J.A. Stammen, S. Williams, D.N. Ku, R.E. Guldberg, Mechanical properties of a novel PVA hydrogel in shear and unconfined compression, Biomaterials. 22 (2001) 799-806.

[118] J.L. Holloway, K.L. Spiller, A.M. Lowman, G.R. Palmese, Analysis of the in vitro swelling behavior of poly(vinyl alcohol) hydrogels in osmotic pressure solution for soft tissue replacement, Acta Biomaterialia. 7 (2011) 2477-2482.

[119] M. Kokabi, M. Sirousazar, Z.M. Hassan, PVA–clay nanocomposite hydrogels for wound dressing, European Polymer Journal. 43 (2007) 773-781.

[120] E. Kenawy, E.A. Kamoun, M.S. Mohy Eldin, M.A. El-Meligy, Physically crosslinked poly(vinyl alcohol)-hydroxyethyl starch blend hydrogel membranes: Synthesis and characterization for biomedical applications, Arabian Journal of Chemistry. 7 (2014) 372-380.

[121] S.K. Mallapragada, N.A. Peppas, P. Colombo, Modification of drug release profiles and swelling behavior in poly(vinyl alcohol) due to the presence of a crystalline phase. Polym. Mater. Sci. Eng. 74 (1996) 416-417.

[122] B. Gajra, S.S. Pandya, G. Vidyasagar, H. Rabari, R.R. Dedania, S. Rao, Poly vinyl alcohol hydrogel and its pharmaceutical and biomedical applications: A review, International Journal of Pharmaceutical Research. 4 (2012) 20-26.

[123] A. Takamura, F. Ishii, H. Hidaka, Drug release from poly(vinyl alcohol) gel prepared by freeze-thaw procedure, J. Controlled Release. 20 (1992) 21-27.

[124] N.A. Peppas, N.K. Mongia, Ultrapure poly(vinyl alcohol) hydrogels with mucoadhesive drug delivery characteristics, European journal of pharmaceutics and biopharmaceutics. 43 (1997) 51-58.

[125] T.K. Mandal, L.A. Bostanian, R.A. Graves, S.R. Chapman, Poly(D, L-lactide-co-glycolide) encapsulated poly(vinyl alcohol) hydrogel as a drug delivery system, Pharm. Res. 19 (2002) 1713-1719.

[126] M.J.D. Nugent, C.L. Higginbotham, Preparation of a novel freeze thawed poly(vinyl alcohol) composite hydrogel for drug delivery applications, European Journal of Pharmaceutics and Biopharmaceutics. 67 (2007) 377-386.

[127] B.E.B. Jensen, I. Dávila, A.N. Zelikin, Poly(vinyl alcohol) Physical Hydrogels: Matrix-Mediated Drug Delivery Using Spontaneously Eroding Substrate, J Phys Chem B. 120 (2016) 5916-5926.

[128] European Society of Clinical Microbiology and Infectious Diseases (EUCAST), Antimicrobial susceptibility testing, 2020.

[129] D.D. Evanoff Jr, G. Chumanov, Synthesis and optical properties of silver nanoparticles and arrays, ChemPhysChem. 6 (2005) 1221-1231.

[130] A. Gautam, S. Ram, Preparation and thermomechanical properties of Ag-PVA nanocomposite films, Mater. Chem. Phys. 119 (2010) 266-271.

[131] R. Brause, H. Moeltgen, K. Kleinermanns, Characterization of laser-ablated and chemically reduced silver colloids in aqueous solution by UV/VIS spectroscopy and STM/SEM microscopy, Applied Physics B. 75 (2002) 711-716.

[132] X. Qi, X. Yao, S. Deng, T. Zhou, Q. Fu, Water-induced shape memory effect of graphene oxide reinforced polyvinyl alcohol nanocomposites, Journal of Materials Chemistry A. 2 (2014) 2240-2249.

[133] T. Cooney, L. Wang, S. Sharma, R. Gauldie, A. Montana, Raman spectral study of solid and dissolved poly(vinyl alcohol) and ethylene-vinyl alcohol copolymer, Journal of Polymer Science Part B: Polymer Physics. 32 (1994) 1163-1174.

[134] J. Paredes, S. Villar-Rodil, P. Solís-Fernández, A. Martínez-Alonso, J. Tascon, Atomic force and scanning tunneling microscopy imaging of graphene nanosheets derived from graphite oxide, Langmuir. 25 (2009) 5957-5968.

[135] J. Li, C. Liu, Ag/graphene heterostructures: synthesis, characterization and optical properties, European Journal of Inorganic Chemistry. 2010 (2010) 1244-1248.

[136] H.E. Assender, A.H. Windle, Crystallinity in poly(vinyl alcohol). 1. An X-ray diffraction study of atactic PVOH, Polymer. 39 (1998) 4295-4302.

[137] D. Adame, G.W. Beall, Direct measurement of the constrained polymer region in polyamide/clay nanocomposites and the implications for gas diffusion, Appl. Clay. Sci. 42 (2009) 545-552.

[138] H. Huang, J. Xu, Y. Fan, L. Xu, Z. Li, Poly(L-lactic acid) crystallization in a confined space containing graphene oxide nanosheets, The Journal of Physical Chemistry B. 117 (2013) 10641-10651.

[139] Y. Yin, J. Liu, G. Jiang, Sunlight-induced reduction of ionic Ag and Au to metallic nanoparticles by dissolved organic matter, ACS nano. 6 (2012) 7910-7919.

[140] A. Fonseca de Faria, D.S.T. Martinez, S.M.M. Meira, A.C. Mazarin de Moraes, A. Brandelli, A.G. Souza Filho, et al., Anti-adhesion and antibacterial activity of silver nanoparticles supported on graphene oxide sheets. Colloids Surf. , B. 113 (2014) 115-124.

[141] Y. Tsuchiya, K. Sumi, Thermal decomposition products of poly(vinyl alcohol), Journal of Polymer Science Part A-1: Polymer Chemistry. 7 (1969) 3151-3158.

[142] P. Budrugeac, Kinetics of the complex process of thermo-oxidative degradation of poly(vinyl alcohol), Journal of thermal analysis and calorimetry. 92 (2008) 291-296.

[143] Y. Cao, J. Feng, P. Wu, Preparation of organically dispersible graphene nanosheet powders through a lyophilization method and their poly(lactic acid) composites, Carbon. 48 (2010) 3834-3839.

[144] T. Kelen, Polymer degradation, 1983.

[145] J. Jang, D.K. Lee, Plasticizer effect on the melting and crystallization behavior of polyvinyl alcohol, Polymer. 44 (2003) 8139-8146.

[146] K. Liao, S. Aoyama, A.A. Abdala, C. Macosko, Does graphene change T g of nanocomposites? Macromolecules. 47 (2014) 8311-8319.

[147] J.W. Suk, R.D. Piner, J. An, R.S. Ruoff, Mechanical properties of monolayer graphene oxide, ACS nano. 4 (2010) 6557-6564.

[148] D.A. Dikin, S. Stankovich, E.J. Zimney, R.D. Piner, G.H. Dommett, G. Evmenenko, et al., Preparation and characterization of graphene oxide paper, Nature. 448 (2007) 457-460.

[149] H. Kim, A.A. Abdala, C.W. Macosko, Graphene/polymer nanocomposites, Macromolecules. 43 (2010) 6515-6530.

[150] L. Jiang, X. Shen, J. Wu, K. Shen, Preparation and characterization of graphene/poly(vinyl alcohol) nanocomposites, J Appl Polym Sci. 118 (2010) 275-279.

[151] X. Yang, S. Shang, L. Li, Layer-structured poly(vinyl alcohol)/graphene oxide nanocomposites with improved thermal and mechanical properties, J Appl Polym Sci. 120 (2011) 1355-1360.

[152] C. Bao, Y. Guo, L. Song, Y. Hu, Poly(vinyl alcohol) nanocomposites based on graphene and graphite oxide: a comparative investigation of property and mechanism, Journal of Materials Chemistry. 21 (2011) 13942-13950.

[153] S. Manna, S.K. Batabyal, A.K. Nandi, Preparation and characterization of silver-poly(vinylidene fluoride) nanocomposites: formation of piezoelectric polymorph of poly(vinylidene fluoride). The Journal of Physical Chemistry B. 110 (2006) 12318-12326.

[154] C. Liu, J. Shen, K.W.K. Yeung, S.C. Tjong, Development and antibacterial performance of novel polylactic acid-graphene oxide-silver nanoparticle hybrid nanocomposite mats prepared by electrospinning, ACS Biomaterials Science & Engineering. 3 (2017) 471-486.

[155] Y. Xianda, W. Anlai, C. Suqin, Water-vapor permeability of polyvinyl alcohol films, Desalination. 62 (1987) 293-297.

[156] M. Klopffer, B. Flaconneche, Transport properties of gases in polymers: bibliographic review; Transport de molecules gazeuses dans les polymeres: revue bibliographique, (2001).

[157] Y. Rao, J.M. Pochan, Mechanics of polymer-clay nanocomposites, Macromolecules. 40 (2007) 290-296.

[158] Z. Zhu, M. Su, L. Ma, L. Ma, D. Liu, Z. Wang, Preparation of graphene oxide-silver nanoparticle nanohybrids with highly antibacterial capability. Talanta. 117 (2013) 449-455.

[159] V.H. Nguyen, B. Kim, Y. Jo, J. Shim, Preparation and antibacterial activity of silver nanoparticles-decorated graphene composites. J. Supercrit. Fluids. 72 (2012) 28-35.

[160] T. Galya, V. Sedlarik, I. Kuritka, R. Novotny, J. Sedlarikova, P. Sáha, Antibacterial poly(vinyl alcohol) film containing silver nanoparticles: preparation and characterization, J Appl Polym Sci. 110 (2008) 3178-3185.

[161] Y. Cao, W. Wei, J. Liu, Q. You, F. Liu, Q. Lan, et al., The preparation of graphene reinforced poly(vinyl alcohol) antibacterial nanocomposite thin film, International Journal of Polymer Science. 2015 (2015).

[162] J. Fan, C.D. Grande, D.F. Rodrigues, Biodegradation of graphene oxide-polymer nanocomposite films in wastewater, Environmental Science: Nano. 4 (2017) 1808-1816.

[163] J. Peña Bahamonde, V. San Miguel, J. Cabanelas, D. Rodrigues, Biological degradation and biostability of nanocomposites based on polysulfone with different concentrations of reduced graphene oxide, Macromolecular Materials and Engineering. 303 (2018) 1700359.

[164] I. De-la-Pinta, M. Cobos, J. Ibarretxe, E. Montoya, E. Eraso, T. Guraya, et al., Effect of biomaterials hydrophobicity and roughness on biofilm development, J. Mater. Sci. Mater. Med. 30 (2019) 77.

[165] S. Wu, F. Zuber, K. Maniura-Weber, J. Brugger, Q. Ren, Nanostructured surface topographies have an effect on bactericidal activity, Journal of nanobiotechnology. 16 (2018) 20.

[166] A.M. Pinto, S. Moreira, I.C. Gonçalves, F.M. Gama, A.M. Mendes, F.D. Magalhães, Biocompatibility of poly(lactic acid) with incorporated graphene-based materials, Colloids and Surfaces B: Biointerfaces. 104 (2013) 229-238.

[167] A.C.M. Moraes, P.F. Andrade, A.F. de Faria, M.B. Simões, Salomão, Francisco Carlos Carneiro Soares, E.B. Barros, et al., Fabrication of transparent and ultraviolet shielding composite films based on graphene oxide and cellulose acetate, Carbohydr. Polym. 123 (2015) 217-227.

[168] F. Zou, H. Zhou, D.Y. Jeong, J. Kwon, S.U. Eom, T.J. Park, et al., Wrinkled surface-mediated antibacterial activity of graphene oxide nanosheets, ACS applied materials & interfaces. 9 (2017) 1343-1351.

[169] V.T. Pham, V.K. Truong, M.D. Quinn, S.M. Notley, Y. Guo, V.A. Baulin, et al., Graphene induces formation of pores that kill spherical and rod-shaped bacteria, ACS nano. 9 (2015) 8458-8467.

[170] I.E.M. Carpio, C.M. Santos, X. Wei, D.F. Rodrigues, Toxicity of a polymer–graphene oxide composite against bacterial planktonic cells, biofilms, and mammalian cells, Nanoscale. 4 (2012) 4746-4756.

[171] Y. Ma, D. Bai, X. Hu, N. Ren, W. Gao, S. Chen, et al., Robust and antibacterial polymer/mechanically exfoliated graphene nanocomposite fibers for biomedical applications, ACS applied materials & interfaces. 10 (2018) 3002-3010.

[172] T.J. Silhavy, D. Kahne, S. Walker, The bacterial cell envelope, Cold Spring Harb Perspect. Biol. 2 (2010) a000414.

[173] J.R. Morones, J.L. Elechiguerra, A. Camacho, K. Holt, J.B. Kouri, J.T. Ramírez, et al., The bactericidal effect of silver nanoparticles, Nanotechnology. 16 (2005) 2346.

[174] S. Kim, J.E. Choi, J. Choi, K. Chung, K. Park, J. Yi, et al., Oxidative stress-dependent toxicity of silver nanoparticles in human hepatoma cells, Toxicology in vitro. 23 (2009) 1076-1084.

[175] Z. Xiu, Q. Zhang, H.L. Puppala, V.L. Colvin, P.J. Alvarez, Negligible particle-specific antibacterial activity of silver nanoparticles, Nano letters. 12 (2012) 4271-4275.

[176] E. Navarro, F. Piccapietra, B. Wagner, F. Marconi, R. Kaegi, N. Odzak, et al., Toxicity of silver nanoparticles to Chlamydomonas reinhardtii, Environ. Sci. Technol. 42 (2008) 8959-8964.

[177] K. Kawata, M. Osawa, S. Okabe, In vitro toxicity of silver nanoparticles at noncytotoxic doses to HepG2 human hepatoma cells, Environ. Sci. Technol. 43 (2009) 6046-6051.

[178] C. Gunawan, W.Y. Teoh, C.P. Marquis, J. Lifia, R. Amal, Reversible antimicrobial photoswitching in nanosilver, Small. 5 (2009) 341-344.

[179] N.S. Wigginton, A.d. Titta, F. Piccapietra, J. Dobias, V.J. Nesatyy, M.J. Suter, et al., Binding of silver nanoparticles to bacterial proteins depends on surface modifications and inhibits enzymatic activity, Environ. Sci. Technol. 44 (2010) 2163-2168.

[180] O. Bondarenko, A. Ivask, A. Kakinen, I. Kurvet, A. Kahru, Particle-cell contact enhances antibacterial activity of silver nanoparticles, PLoS One. 8 (2013) e64060.

[181] C. Beer, R. Foldbjerg, Y. Hayashi, D.S. Sutherland, H. Autrup, Toxicity of silver nanoparticles - nanoparticle or silver ion? Toxicol. Lett. 208 (2012) 286-292.

[182] M.E. Samberg, P.E. Orndorff, N.A. Monteiro-Riviere, Antibacterial efficacy of silver nanoparticles of different sizes, surface conditions and synthesis methods, Nanotoxicology. 5 (2011) 244-253.

[183] I. Sondi, B. Salopek-Sondi, Silver nanoparticles as antimicrobial agent: a case study on E. coli as a model for Gram-negative bacteria, J. Colloid Interface Sci. 275 (2004) 177-182.

[184] S. Agnihotri, S. Mukherji, S. Mukherji, Size-controlled silver nanoparticles synthesized over the range 5-100 nm using the same protocol and their antibacterial efficacy. RSC Adv. 4 (2014) 3974-3983.

[185] G.A. Sotiriou, S.E. Pratsinis, Antibacterial activity of nanosilver ions and particles, Environ. Sci. Technol. 44 (2010) 5649-5654.

[186] H. Zhao, R. Ding, X. Zhao, Y. Li, L. Qu, H. Pei, et al., Graphene-based nanomaterials for drug and/or gene delivery, bioimaging, and tissue engineering, Drug Discov. Today. 22 (2017) 1302-1317.

[187] T. Zhang, L. Wang, Q. Chen, C. Chen, Cytotoxic potential of silver nanoparticles, Yonsei Med. J. 55 (2014) 283-291.

[188] Y. Yang, A.M. Asiri, Z. Tang, D. Du, Y. Lin, Graphene based materials for biomedical applications, Materials today. 16 (2013) 365-373.

[189] L. Li, J. Sun, X. Li, Y. Zhang, Z. Wang, C. Wang, et al., Controllable synthesis of monodispersed silver nanoparticles as standards for quantitative assessment of their cytotoxicity, Biomaterials. 33 (2012) 1714-1721.

[190] M.V. Park, A.M. Neigh, J.P. Vermeulen, de la Fonteyne, Liset JJ, H.W. Verharen, J.J. Briedé, et al., The effect of particle size on the cytotoxicity, inflammation, developmental toxicity and genotoxicity of silver nanoparticles, Biomaterials. 32 (2011) 9810-9817.

[191] E.N. Sowa-Söhle, A. Schwenke, P. Wagener, A. Weiss, H. Wiegel, C.L. Sajti, et al., Antimicrobial efficacy, cytotoxicity, and ion release of mixed metal (Ag, Cu, Zn, Mg) nanoparticle polymer composite implant material, BioNanoMaterials. 14 (2013) 217-227.

[192] R. Oliveira, R. Rouzé, B. Quilty, G. Alves, G. Soares, R. Thiré, et al., Mechanical properties and in vitro characterization of polyvinyl alcohol-nano-silver hydrogel wound dressings, Interface focus. 4 (2014) 20130049.

[193] M. Bosetti, A. Massè, E. Tobin, M. Cannas, Silver coated materials for external fixation devices: in vitro biocompatibility and genotoxicity, Biomaterials. 23 (2002) 887-892.

[194] F. Paladini, M. Pollini, A. Sannino, L. Ambrosio, Metal-based antibacterial substrates for biomedical applications, Biomacromolecules. 16 (2015) 1873-1885.

[195] Y. Li, T. Yu, T. Yang, L. Zheng, K. Liao, Bio-inspired nacre-like composite films based on graphene with superior mechanical, electrical, and biocompatible properties, Adv Mater. 24 (2012) 3426-3431.

CHAPTER 5

POLY(VINYL ALCOHOL)/CHITOSAN BLENDS AND THEIR GRAPHENE-BASED NANOCOMPOSITES

The previous chapters covered the synthesis and characterization of different graphene-based nanocomposites, with a matrix built by a single polymer, chitosan or PVA, with and without a plasticizer. In this part of the thesis, GO and GS sheets have been intercalated or exfoliated in the PVA/CS blend by the solution casting method and in situ reduction approach. However, previous to the preparation of these nanocomposites, a morphological, thermal and mechanical analysis of the whole range of PVA/CS compositions has been performed in order to determine which composition is the most optimal for the development and the study of PVA/CS/graphene-based nanocomposites. The structural and morphological characterization of the different nanocomposites was performed by XRD, SEM and TEM. Thermal characterization by thermogravimetric analysis (TGA) and differential scanning calorimetry (DSC) allowed to detect thermal changes in the PVA/CS blend due to the presence of the filler. Tensile tests were used to examine the reinforcing effect of GO and GS and, in turn, to assess the interactions between polymers and fillers. Considering the possible application of this type of material in the biomedical field, the water vapor permeability (WVP) was also determined, as well as the degree of swelling and dissolution of the films.

Part of the work reported in this chapter was presented at the 3rd International Conference on Bioinspired and Biobased Chemistry and Materials in Nice (France).

INDEX

5.1. Introduction

The polymer industry is one of the most developed in the world being now very difficult to consider our daily life without the influence and impact of these polymer materials. However, the cost of new polymer (or copolymer) production and the constant need for new materials with some specific properties and good performance/cost ratio have led researchers to develop the polymer blending system [1], i.e., instead of trying to synthesize a new polymer with certain desired properties, the polymer blend is used to obtain those properties.

Polymer blends are physical mixtures of two or more polymers (or copolymers) with or without any chemical bonding between them. The main goal of polymer blending is to achieve cheap and commercially viable materials with unique properties. Polymer blending is a huge and increasingly interesting field that requires a great deal of attention both theoretically and experimentally. Compared to its component polymers, blended polymers have been found to have superior properties. Some of these advantages achieved by blending are [2]:

- Develop materials with a wide range of properties to meet specific needs.
- Reduce the cost of materials with little or no sacrifice in properties.
- Develop polymers much more quickly to meet emerging needs by avoiding the polymerization step.
- Form high performance blend from synergistically interacting polymers.
- Extended service temperature range.
- Enhanced modulus and hardness.
- Improved barrier and flame retardant properties.
- Increased resistance to environmental impact and stress cracking.
- Recycle industrial plastics scrap.

5.1.1. Classification and properties of polymer blends

Principally, the polymer blends can be characterized as miscible or immiscible. Miscibility is the capability of a mixture to form a single phase over certain ranges of temperature, pressure and composition. It can be affected by several factors such as morphology, crystalline phase, intermolecular interactions, and surface tension [1]. Hence, the polymer blending miscibility can be assessed

by chemical structure, molecular weight distribution, and molecular architecture of the components that can be confirmed by light scattering, X-ray scattering, and neutron scattering.

Nonetheless, it is well-known that the majority of the physical blends of high molecular weight polymers prove to be immiscible. As a consequence, when mixed, the components of the blend are likely to separate into phases containing predominantly their own type or characteristics. In addition, the physical attraction forces across the immiscible phase boundaries are often low, resulting in immiscible mixing systems that exhibit poorer mechanical properties compared to those achieved by the co-polymerization route [3].

The miscibility or immiscibility is governed at the molecular level as given by the laws of thermodynamics. Given enough time, the internal disorder of the polymer system will eventually result in phase separation on a macroscopic scale. The behavior of polymer blends is understood through the Gibbs free energy, ΔG_M. The free energy of mixing can be described in terms of enthalpy and entropic contributions as shown below:

$$\Delta G_{\mathrm{M}} = \Delta H_{\mathrm{M}} - T \cdot \Delta S_{\mathrm{M}} \qquad \text{(Eqn. 5.1)}$$

where ΔG is the change in free energy, ΔH the change in enthalpy, ΔS the change in entropy, T the absolute temperature, and M refers to mixing.

A homogeneous miscible blend must display a negative ΔG_M value. In the case of high molecular weight polymer blends, the gain in entropy (S) is insignificant since the combinatorial entropy of mixing of two polymers is dramatically less than that for two low molecular mass compounds. Therefore, ΔG_M can only be negative if ΔH_M is negative, which means that the mixture must be exothermic, and that is achieved if there are favorable "specific interactions" between them. These interactions may range from strongly ionic to nonbonding and/or weak bonding that includes hydrogen bonding, ion–dipole, dipole–dipole, and donor–acceptor interactions [4].

Mainly, considering the applicable conditions and the miscibility, three types of blends can be found: miscible, compatible or partially miscible and immiscible. The term "compatible" or "incompatible" is used to describe the blends according to their resulting properties. Compatible blends have a fine

phase morphology that means good physical properties. Generally, the probability of achieving synergistic properties is high in a compatible blend. Incompatible mixtures are totally immiscible and have poor mechanical properties. Table 5.1 details the properties and conditions of the above-mentioned mixtures.

Table 5.1. Properties for different types of polymer blends in relation to their miscibility [2].

Completely Miscible Blends	Partially Miscible Blends	Immiscible Blends
▪ Homogeneous system with chain segments of the different polymers miscible down to the molecular level (one phase). ▪ Mechanical properties of components averaged. ▪ $\Delta H < 0$ due to specific interactions. ▪ $\Delta G < 0$ ▪ Single glass transition temperature (between the glass transition temperatures of the blend components). ▪ *Example: Polystyrene /Poly(phenylene oxide), Poly(ethylene terephthalate) /Poly(butylene terephthalate), and Poly(methylmethacryl ate) /Poly(vinylidene fluoride).*	▪ Neither completely miscible nor immiscible. Therefore, two homogenous phases. Fine phase morphology. ▪ These blends show limited mutual interactions, but small amounts of one polymer is miscible in the other. ▪ The best properties of each polymer may be combined often without the need of developing a compatibilization mechanism. ▪ $\Delta G > 0$ ▪ Two glass transition temperatures. Both T_gs are shifted from the values for the pure blend components towards the T_g of the blend component. ▪ *Example: PC/ABS.*	▪ Complete phase separation. Coarse morphology, sharp interface and poor adhesion between the blend phases. ▪ Poor interface leading to poor mechanical properties. ▪ $\Delta G > 0$ ▪ Two glass transition temperatures of the component polymers. ▪ *Example: Polystyrene/Polybuta diene, Poly(ethylene terephthalate)/Poly(v inyl alcohol), and Polyvinylidene fluoride/Polylactic acid blends.* ▪ These blends have become commercially successful, after being efficiently compatibilized using suitable compatibilizers.

5.1.2. The equilibrium of binary blends

According to the laws of thermodynamics, for a blend of polymer A and polymer B to be completely miscible, the following conditions must be met [5]:

1. Thermodynamically Gibbs free energy of the blend must be negative:

$$\Delta G_{AB} < \Delta G_A + \Delta G_B$$

2. The enthalpy of the blend must also be negative:

$$\Delta H_M - T \cdot \Delta S_M < 0$$

3. The second derivative of Gibbs free energy of mixing (ΔG_M) with respect to volume fraction ($\emptyset$) must be greater than zero, i.e., positive.

$$[\Delta \partial^2 \Delta G_M / \Delta \emptyset^2] > 0$$

Gibbs energy graphs and phase diagrams, depicted in Figure 5.1 and Figure 5.2, respectively, can be used to understand the equilibria of binary systems.

5.1.2.1. Gibbs energy graphs

Figure 5.1 shows, for one mole of mixture, the relationship between Gibbs free energy of mixing (ΔG_M) and the composition of the components in terms of volume fraction ($\emptyset$) for binary blends at a given pressure and temperature. In this type of graphs, with only one extreme, two curves are represented, one for each phase. According to the conditions described above, a miscible blend must display a positive second derivative of Gibbs free energy with respect to their composition, which means that there is a composition that presents a minimum point of Gibbs free energy, in other words, a concave curve [1].
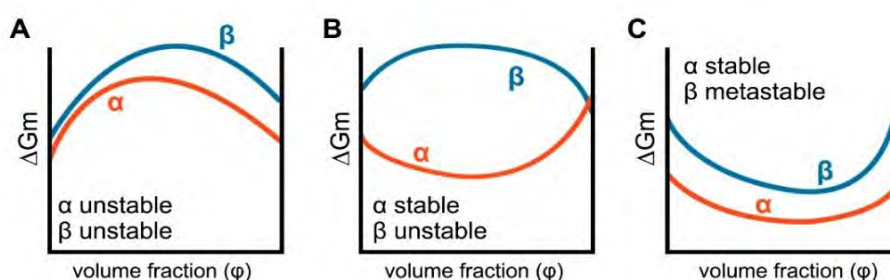
Figure 5.1. Relative arrangements of the Gibbs energy curves of two binary phases.

In Figure 5.1A, the two curves are convex (α and β phases), so the second derivative of Gibbs energy is negative in relation to composition, i.e. with any composition it is an immiscible mixture, both phases are unstable in relation to their two pure components. In Figure 5.1B, one curve is concave (phase α) and the other convex (phase β). Therefore, the phase α displays a second derivative positive for all compositions and is stable with respect to the pure components in any proportion. However, the phase β being convex is unstable with respect to the two pure components and also with respect to the phase α. As a result, it is a phase that will not take place as the system would only be stable in the form of a phase α. Additionally, it can also occur that both curves are concave (Figure 5.1C), which means that, for all compositions, the two phases are stable in relation to the two pure substances. However, it can be seen that the Gibbs energy is lower for the phase α, and therefore is stable with respect to β. The latter is stable relative to pure components but unstable relative to the phase α, so phase β is said to be metastable [6].

5.1.2.2. Phase diagrams

The phase diagram is the fundamental tool for using the thermodynamic data of a binary system. It shows the nature and composition of the phases in equilibrium in function of the temperature when pressure remains constant (isobaric diagrams). The graph is constructed with the same abscissa axis as before which indicates the general composition, and the temperature is used as the ordinate axis. It can be used to decide the phase behavior of the polymer blends. In Figure 5.2, the bimodal separates miscible and metastable regions from each other, while the spinodal curves separates unstable phase regions from metastable.

Spontaneous concentration fluctuations dictate phase separation from the spinodal line (spinodal phase separation). The system divides into two distinct phases, one phase contains more polymer A, the other more polymer B. However, from the metastable region, phase separation into pure substances take place by a nucleation and growth mechanism that is called binodal phase separation.

As shown in Figure 5.2, when two polymers are mixed at low temperatures and phase separation occurs upon heating, this mixture is said to exhibit a lower critical solution temperature (LCST). Whereas if two polymers remain phase

separated at ordinary temperatures and form a single phase at high temperatures, they show upper critical solution temperature (UCST) behavior.
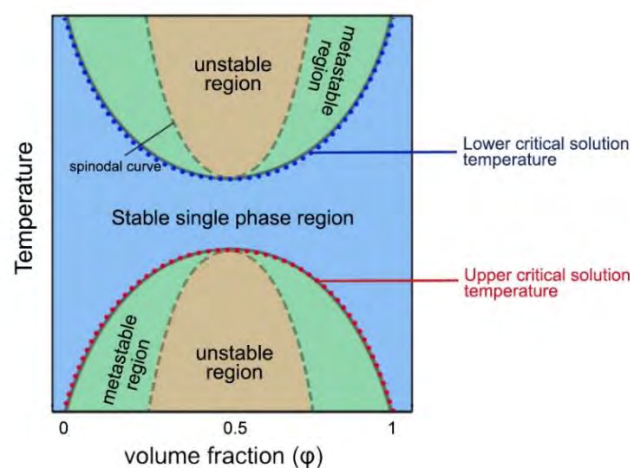
Figure 5.2. Temperature-Composition phase diagram for a binary polymer blend.

5.1.3. Compatibilization strategy for good properties

The miscibility of polymer mixtures is a complex phenomenon that is governed by the interactions between the two polymers, and therefore determines the properties of the blends. The interactions are regulated by several factors described below:

- Polarity: polymers that are similar in structure or generally similar in polarity are less likely to repel each other and more likely to form miscible blends.
- Specific group influence: The presence of special interactions in a blend favors the enthalpy of mixing, and allows the components to mix completely. Among all these interaction, hydrogen bonding is quite common and efficiently improves the miscibility.
- Molecular weight: The low molecular weight allows a higher randomness of the polymer chains when mixed, and consequently a higher increase of entropy, which favors miscibility. Most surprisingly, polymers with similar molecular weights are more miscible, while polymers with very different molecular weights can be immiscible even if they both have the same composition.

- <u>Composition</u>: in line with the previous section, two polymers can be immiscible in a fairly equal composition, but it is also very possible that a small amount of one polymer can be soluble in a large amount of the other polymer, resulting in moderate miscibility. Thus, by varying the composition of one of the constituent polymers, a blend may result in partial miscibility.

Regarding mechanical properties, when polymer A is mixed with polymer B, the blend is generally expected to have properties that are an average of that of pure A and pure B. However, some properties such as strength and toughness do not follow an additive relationship and they are often found to exhibit lesser values than pure components [7]. This situation is the result of a low degree of interfacial adhesion between the two polymers, and is the real problem that delimits the mixture of two polymers.

The compatibilization is the method by which the general mechanical properties of the polymer blend are enhanced by mean of reducing the interfacial tension and stabilizing morphology. The resulting mechanical properties of the immiscible compatible blend will have a balance of their parent polymers properties or show a synergistic improvement. There are several strategies to reduce interfacial tension in the melted state and enhance the adhesion between the immiscible phases [8]. It is important to choice the most suitable blending technique in order to achieve a continuous or interpenetrating phase morphology that can lead to load sharing. However, many commercial polymer blends are mostly compatibilized using a compatibilizer [9].

One type of **compatibilization is called** reactive or *in situ* compatibilization and is based on introducing a compatibilizer that can promote a chemical reaction or a specific interaction between the blend components. Several reactive compatibilizers have been identified in the literature [10-14].

Another approach is the addition of a third component such as homopolymers, block or graft copolymers, or low molecular weight reactive compounds, which are miscible in both phases (Figure 5.3). This is considered as non-reactive compatibilization. The use of block copolymers requires that the copolymer has a maximum solubility with components of the blend. This leads to an enhanced interfacial adhesion while reducing interfacial tension between the components. The concentration and molecular weight of the block copolymer

must be slightly higher than that of critical micelle concentration and critical entanglement, respectively [15]. There are many common polymer blends compatibilized with a block copolymer. For example, styrene acrylonitrile (SAN) and styrene butadiene styrene (SBS) blends, have been compatibilized by the addition of a diblock copolymer [8].
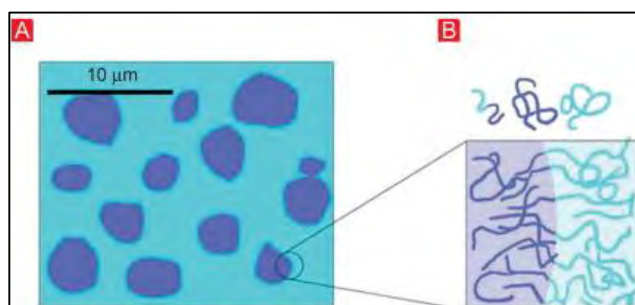
Figure 5.3. Polymer blend with a diblock copolymer. (A) Compatibilized blend with dispersed phase morphology, represented by a minority dark blue phase and a majority turquoise phase. (B) Molecular schematic showing how the diblock copolymers are segregated at the interface between the two phases [8].

The addition of plasticizers is another example of non-reactive compatibility. As mentioned in Chapter 3, plasticizers are relatively low molecular weight liquids that are miscible with the polymer in question and their main function is to improve the flexibility and processability of the polymer by reducing the glass transition temperature (T_g) [3]. The small size of the plasticizers allows them to occupy the intermolecular spaces between the polymer chains, reducing the interactions between them. In addition, these molecules change the three-dimensional molecular organization of the polymers by reducing both the energy required for molecular movement and the formation of intramolecular hydrogen bonds. As a result, an increase in free volume and, therefore, in molecular mobility is observed [16]. Commercially, the most common plasticized polymers are PVC, poly(vinyl butyral) (PVB), poly(vinyl acetate) (PVAc), acrylics, cellulose molding compounds, nylon, polyamides and certain copolyamides. Particularly, 80% of the PVC production uses plasticizers and phthalic acid esters constitute more than 85% of the total plasticizer consumption [17,18].

5.1.4. Blending techniques

Several methods are currently available to synthesizing and/or preparing polymer blends. The following is a brief summary of some viable techniques:

1. Melt Blending: This technique involves high temperatures and strong shear forces during the melting process, which gives the polymer chains the ability to move and diffuse in the other component. Typically, the raw materials are fed into a chamber and extruded to obtain a uniform mixture of the components. This method is used for a blends in which thermal degradation does not occur at the processing temperature. It is often considered a good mixing method because of its simplicity and low environmental impact, but the necessary machinery makes it an expensive technique and the polymer mixture may not be uniform [19].

2. Mill and fine powder mixing technique: A simple and direct method in which the components of the mixture are mixed through grinding and crushing. The raw materials are ground to a very fine powder and mixed to produce a uniform product at the micrometric level. The Bunbury mixer, also known as the Master Mixer, is widely used for mechanical mixing in which two interrupted spiral rotors move in opposite directions (at 30 or 40 rpm). The product is then subjected to additional operations to obtain the desired polymer mixtures. In some cases, the mixture can be integrated into the extrusion or molding stage, such as in twin-screw extruders [1].

3. Solution Casting Method: The simplest and common method in which the blend is casted from a common solvent. The choice of solvent is crucial to obtain a miscible blend. Frequently, the solution mixture is kept stirring for a certain period of time to get the homogenous solution. Binders and compatibilizers may be added. However, this method presents a limit, the possible incompatibility of the component polymer and the removal of the solvent from the product, since residual solvent can distress the properties of the blend [1].

4. Interpenetrating Polymer Networks (IPN): The conventional method of synthesizing an IPN involves swelling a cross-linked primary polymer network with a similar long chain monomeric sequences and cross-linking agent, followed by *in situ* polymerization of the second network, which ideally results in an

extended primary network intermingled that shows a single glass transition temperature. This method is also called mechanochemical blending [3].

5. Lyophilization (freeze-drying): A process commonly used to remove the solvent from the mixture by sublimation, keeping the temperature low enough to prevent any remixing or phase-separated polymer solution. The material is first dissolved in the solvent and frozen in a dry ice bath. Then, the solvent is sublimated and removed by vacuum, leaving a dry powder. This method has been used in studies related to tissue regeneration to develop scaffolds based on polymers such as PLA, chitosan, gelatin, carboxymethyl cellulose, etc [20].

6. Latex Blending: This method is referring to a stable dispersion of small polymer particles mixed in an aqueous medium. To achieve such blends, the contributing polymers should be in the latex or in the emulsion form, which is followed by mixing. Examples of latex blending may include natural rubber or synthetic rubbers such as acrylonitrile-butadiene rubber (NBR) [21].

5.1.5. The reason for PVA/CS blends

As described in the previous chapters, in the biomedical field biodegradable, biocompatible and water-soluble polymers, such as chitosan, are of considerable interest. However, chitosan has fragile properties (Chapter 3), more specifically, unplasticized chitosan films are very brittle when stored at low relative humidity [22]. Consequently, the use of plasticizer can be a suitable strategy to increase the flexibility of the films, but it may also involve the decrease of barrier properties as a result of increased free volume. Additionally, the plasticizer decreases the chitosan mechanical strength and thermal stability. So, in order to maintain the stiffness, blending CS with another polymer with high mechanical properties seems to be a good alternative. In this sense, polyvinyl alcohol (PVA) is one of the best candidates since it is also a biodegradable, biocompatible and soluble polymer with good mechanical properties (Chapter 4). Since there are lots of hydroxyl groups in CS and PVA backbone, both polymers can be potentially miscible due to the formation of hydrogen bonds.

Several studies reported in the literature describe PVA/CS blends, but none includes a deep morphological, chemical and mechanical analysis covering the whole range of compositions, as well as their behavior in the presence of

plasticizer. Wu *et al.* [23] prepared films of PVA and chitosan blends and established that these polymers interacted *via* physics and cross-linked through the formation of intermolecular hydrogen bonds. Jiang *et al.* [24] used an aqueous solution of $AlCl_3.6H_2O$ to dissolve chitosan and prepared the blends with PVA and glycerol as plasticizer. In their work the combined use of glycerol and the aluminum chloride compound proved to have a synergistic effect on different film properties. Fan *et al.* [25] prepared chitosan, PVA and gelatin hydrogels for wound dressing, using gamma irradiation and demonstrated that the presence of chitosan can increase the tension and strength of PVA/Gelatin mixtures. Chen *et al.* [26] examined different properties of PVA/chitosan mixtures in various proportions and concluded that chitosan can decrease the crystallinity of PVA. Moreover, in order to enhance the properties of PVA/chitosan blends for different applications such as food packaging, some studies have examined the effect of the addition of different nanofillers such as montmorillonite and halloysite nanotubes into the blend [27-29].

5.2. Experimental section

5.2.1. Materials

Poly(vinyl alcohol) (M_w= 61,000 Da; degree of hydrolysis 98.0–98.8 mol%), Glycerol, L-ascorbic acid (L-AA) and chitosan powder (M_w=190,000–310,000 Da; deacetylation degree of 82%) were supplied by Sigma-Aldrich. All chemicals were used as received without further purification.

5.2.2. Preparation of PVA/CS blends

The binary polymer blends were prepared by solution casting method. Chitosan was dissolved in 2% (v/v) acetic acid aqueous solution upon stirring overnight at room temperature. Then, CS dissolution was filtered with a G4 porous plate filter funnel, in order to remove the remaining chitin that does not dissolve in acetic acid. Separately, an aqueous solution of PVA was prepared in deionized water at 100 °C upon stirring for 1 h, and subsequently cooled to room temperature. After that, the PVA solution was added into the CS solution while stirring and the final solution was left for 2 h in vigorous agitation. The different compositions were prepared by mixing different PVA and CS mass ratios, where part of the PVA was gradually replaced by CS, until the pure polymers, i.e. in each composition the CS content is increased by 10%, the PVA is decreased in the same proportion. Finally, PVA/CS blend films were obtained after evaporation the water and acetic acid of the solution in a petri dish at room temperature. The films were dried under vacuum at 60 °C for a week. The plasticized PVA/CS blend films were prepared in the same manner, except for the incorporation of glycerol (20% weight) in the PVA solution. The formulations were named indicating the mass ratio of the two polymers, being the first number referred to PVA.

5.2.3. Preparation of PVA/CS/GO nanocomposite films

The composition of PVA/CS 60/40 was chosen for the preparation and study of graphene-based nanocomposites. The PVA/CS/GO nanocomposites were prepared with different GO amounts (0.25, 0.5, 0.75, 1.0, 1.5, 2.0 and 2.5 wt%) and also its plasticized counterparts. First, graphite oxide was exfoliated into GO sheets by sonicating in water for 15 min using a tip sonicator. The GO suspension

was added to an aqueous solution of PVA, and the mixture was stirred for at least 1 h at room temperature. The resulting PVA/GO suspension was added to a stirred acetic acid aqueous solution 2% (v/v) of CS, and stirring was continued for 15 h at room temperature. After, the homogeneous suspension was transferred onto a plastic plate and then dried at room temperature. The resulted films were dried under vacuum at 60 °C for a week and then stored in desiccators. Plasticized films were prepared following the same procedure. The nanocomposites were denoted as PVA/CS/GO-x. where x indicates the weight percentage of GS.

5.2.4. Preparation of PVA/CS/GS nanocomposite films

Similar to the previous procedure, PVA/CS/GS nanocomposites were prepared with different GS amounts (0.25, 0.5, 0.75, 1.0, 1.5, 2.0 and 2.5 wt%) and also its plasticized counterparts. The GO dispersion was added to an aqueous PVA solution, and the mixture was stirred for 1 hour at room temperature. The resulting suspension was added to an aqueous CS solution, and continued to be shaken for 15 h at room temperature. After that, PVA/CS/GO mixture was heated to 60 °C using an oil bath, followed by the addition of the desired amount of an aqueous solution of L-AA (L-AA:GO = 3.5) with vigorous agitation. This mixture was kept at 60 °C for 6 hours in the absence of light to obtain graphene sheets (GS). The homogeneous suspension was then transferred to a plastic plate and dried at room temperature. Finally, the films were peeled and vacuum dried at 60 °C for one week and then stored in desiccators. The plasticized films were prepared using the same route. The nanocomposite films were called PVA/CS/GS-x, where x indicates the weight percentage of GS.

5.2.5. Characterization

The structure and the morphology of the PVA/CS blends and synthetized nanocomposite films were examined by X-ray diffraction (XRD), scanning electron microscopy (SEM) and transmission electron microscopy (TEM). Thermal characterization was realized by thermogravimetric analysis (TGA) and differential scanning calorimetry (DSC). Tensile tests (MTS) were carried out to study the mechanical properties of all prepared films in order to examine the effect of fillers and plasticizer. Water vapor permeability (WVP) was determined

according to the ASTM E96 standard, using the upright cup method (UCM). Nanocomposite film water swelling (SD) and dissolution degree (fDD) were calculated by applying some specific equations. Details of the equipment and protocols are shown in Appendix I. The following Table 5.2 details the section of each technique or method performed.

Table 5.2. Characterization methods used for the analysis of different compositions of the PVA/CS blend as well as, PVA/CS/GO and PVA/CS/GS nanocomposites.

Analysis	Technique or Method	Appendix Section
Crystalline structure	XRD	I.1.6
Nanostructure and morphology	SEM	I.1.8
	TEM	I.1.9
Thermal behavior	TGA	I.2.1
	DSC	I.2.2
Mechanical Properties	MTS	I.3
Permeability	UCM	I.5
Swelling and Dissolution degree	SD and fDD	I.7

5.3. Results and discussion

5.3.1. PVA/CS blends

5.3.1.1. Structural and morphological characterization

X-ray diffraction (XRD)

The XRD patterns of unplasticized and plasticized pure CS, pure PVA and different compositions of PVA/CS blends measured in the range of $2\theta = 5°\text{-}80°$ are displayed in Figure 5.4. Briefly, according to Chapter 3, the diffractogram of CS film (Figure 5.4A) shows three main peaks around 11.8°, 18.6°, and 23.5°. The peak at $2\theta = 11.8°$ is associated with a hydrated crystalline structure. The broad peak at 23.5° indicates an amorphous structure, predominantly the CS structure, while the 18.6° peak is attributed to the regular chitosan crystal lattice [30,31]. The addition of glycerol does not generate any change in the position and shape of the CS diffraction peaks (Figure 5.4B). For unplasticized and glycerol-plasticized PVA films, XRD patterns show a main diffraction peak at $2\theta = 19.9°$, and another at $2\theta = 40.8°$ corresponding to planes (101) and (111), respectively [32].
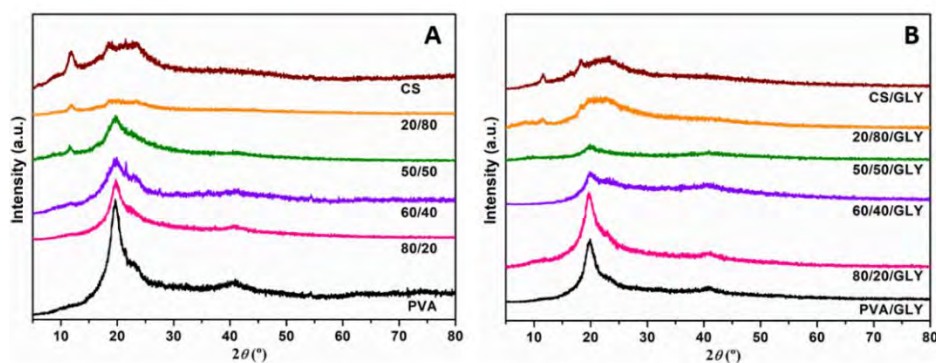
Figure 5.4. XRD patterns of: (A) unplasticized and (B) plasticized pure CS, pure PVA and PVA/CS blends.

XRD diffraction scans of polymer blends can be used as criteria for examining their overlap and homogeneity. The lack of interaction between two polymers would result in an immiscible blend in which each polymer would have its own crystalline region, and therefore the XRD patterns would be expressed as simple mixed patterns of the different components of the blend [33].

XRD patterns of unplasticized and plasticized PVA/CS blends show changes in the diffraction peak intensities in relation to the composition (Figure 5.4). Taking as a reference the intensity of PVA diffraction peak at 19.9°, it can be seen that as the amount of CS increases in the blend the intensity of this peak becomes lower and wider. Likewise, the diffraction peak at 18.6° related to the CS is not detected even with low PVA content and the intensity of the peak at 11.8° decreases as the PVA content increases, even disappearing from the PVA/CS 60/40 composition for unplasticized blends and from the 50/50 composition for plasticized ones. These results suggest that the presence of CS decreases the crystallinity of PVA, meanwhile the two diffraction peaks resulting from the hydrated crystalline structure of CS disappear. This phenomenon is because of the hydrogen bonding interaction between PVA and CS, which eliminates the hydrated crystalline structure of CS.

Nanostructure and morphology

SEM micrographs of the fractured cross sections of unplasticized and plasticized PVA/CS blend in both formulations are shown in Figure 5.5, where a continuous and homogeneous phase can be observed, without any evidence of phase separation. In addition, no irregularities, such as air bubbles, pores, cracks or droplets are detected.
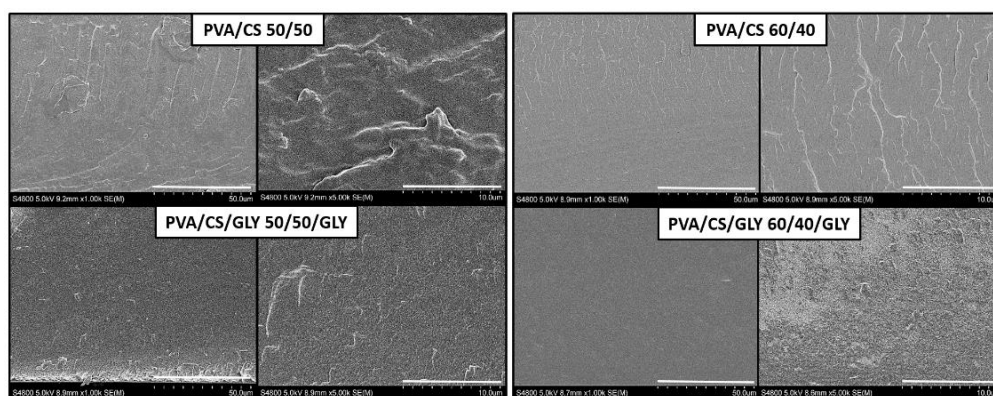
Figure 5.5. SEM images of the fractured surface of unplasticized and plasticized PVA/CS blends in 50/50 and 60/40 weight ratios.

The roughness of the fractured surface shown in the images is attributed to interfacial adhesion and compatibility between the polymer matrices. In this

sense, in the analyzed PVA/CS compositions, the roughness surface increases when the plasticizer is present, which confirms an improvement in the compatibility between the two polymeric matrices with the plasticizer. Moreover, comparing both compositions, the roughness becomes more noticeable with increasing PVA content, therefore, it can be deduced that PVA and CS are partially more compatible (fine phase morphology) with a richer PVA composition. These results are similar to those reported by Wu *et al.* [34] in their study about the inhibition of biofilm formation in PVA/CS blends.

5.3.1.2. Thermal characterization of PVA/CS blends

Thermogravimetric analysis (TGA)

TGA analysis was conducted for studying the thermal stability of the blends. The weight loss (TG) and derivate (DTG) curves of PVA/CS blends films with different weight compositions are reported in Figure 5.6, while Table 5.3 and Table 5.4 show the results of the thermograms in thermal parameters for unplasticized and plasticized blends, respectively.

Considering the TGA results shown in previous chapters, TG curves may have a small weight loss as the temperature increases from 50 to 120 °C, which commonly corresponds to the loss of adsorbed and bound water, and also to the acetic acid residue. However, in the thermograms shown in Figure 5.6, this loss is not appreciated because these films were kept in the oven at 60 °C until the time of TGA analysis, and therefore moisture absorption has been prevented [35]. The first stage, which can be distinguished in the TG curves of unplasticized blends (Figure 5.6A), takes place between 150 °C and 240 °C with a 5 - 7% weight loss. This change in weight corresponds to a loss of methane and ammonia generated through the elimination reaction between the -NH$_2$ and -H groups [36]. In plasticized blends, in the same temperature range, the weight loss is higher compared to unplasticized blends (a weight loss of 15 - 20% in all compositions), because apart from methane and ammonia, there is also glycerol evaporation (Figure 5.6C). The next weight loss step at 240 - 420 °C is the largest weight loss of the blends (more than 45% weight loss), and is associated with the rapid decomposition of polymer segments of PVA and CS due to the thermal scission of the polymer backbone [37,38]. The third weight loss occurs at 420 - 500 °C and is

due to the degradation of by-products generated by PVA during its thermal degradation, and consequently this loss is not distinguished in CS rich blends. Finally, a carbonaceous residue of the remaining degraded structures is found at 600 °C and remains constant up to 800 °C. In both unplasticized and plasticized PVA/CS blends the amount of residue obtained increases with increasing CS content (Table 5.3 and Table 5.4).

Table 5.3. TGA data for unplasticized PVA/CS nanocomposites in inert atmosphere.

Glycerol-Free Samples (in N_2)	$T_{5\%}$ (°C)	$T_{50\%}$ (°C)	T_{max} (°C)				Residue (%)
			(a)	(b)	(c)	(d)	
PVA	271	339	-	302	350	425	2.9
PVA/CS 90/10	232	365	212	314	365	468	6.3
PVA/CS 80/20	223	367	220	294	363	465	9.7
PVA/CS 70/30	214	371	224	299	354	460	13.6
PVA/CS 60/40	206	372	226	298	347	466	17.9
PVA/CS 50/50	191	365	219	306	335	460	20.0
PVA/CS 40/60	188	368	228	313	-	461	25.6
PVA/CS 30/70	199	375	220	307	-	460	30.3
PVA/CS 20/80	190	366	-	301	-	457	32.0
PVA/CS 10/90	198	370	-	294	-	-	34.7
CS	171	365	-	293	-	-	35.6

(a) 1st stage; (b) 2nd stage; (c) 3rd stage; (d) 4th stage

From the DTG curve of unplasticized and plasticized PVA/CS blends (Figures 5.6B,D), two superimposed processes can be observed during the largest decomposition phase (second stage). For unplasticized PVA in this temperature range, there are two peaks with similar intensity at 302 and 350 °C, but with the addition of CS the intensity of these peaks changes. The first peak becomes more intense than the second as the CS content increases. Concretely, for compositions with CS content higher than 50 wt%, the second peak disappears and the first one becomes more intense reaching its maximum temperature between 313-293 °C.

For plasticized blends, the changes in intensity and shape of the DTG curves are similar to those of unplasticized samples.
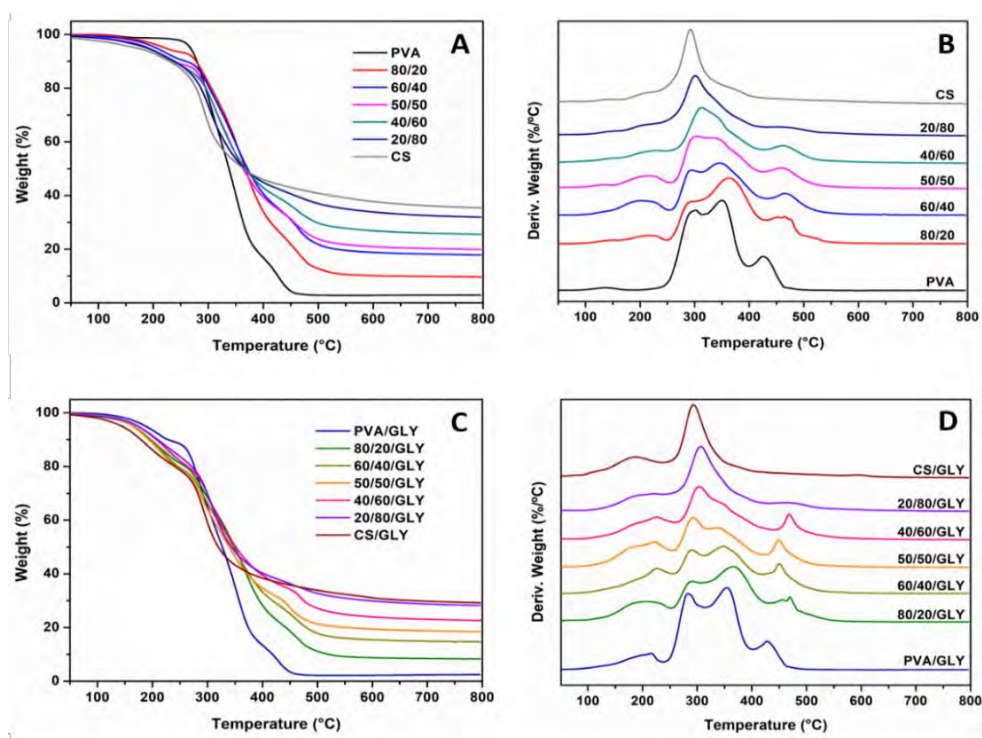
Figure 5.6. TG (A,C) and DTG (B,D) curves of unplasticized and plasticized PVA/CS nanocomposites in nitrogen atmosphere.

The thermal decomposition temperature for 5% weight loss ($T_{5\%}$) of CS increases with the addition of PVA, but this temperature for unplasticized blends in any composition does not exceed that of PVA (Table 5.3). Therefore, it can be understood that the addition of PVA to CS delays the onset of thermal degradation, or in other words increases the thermal stability of CS. For plasticized blends, $T_{5\%}$ also increases with the CS content, but in this cases the temperature values are lower than that of unplasticized blends due to glycerol evaporation temperature range. However, temperatures of 5% weight loss of the plasticized blends are much closer to PVA/GLY than to CS/GLY with low PVA content (Table 5.4). This can be attributed to an improvement in compatibility between CS and PVA due to the effect of the plasticizer. Additionally, the 50% weight loss temperature of unplasticized and plasticized PVA/CS blends is higher

than that of pure polymers. Hence, taking into account the values of $T_{5\%}$ and $T_{50\%}$ it could be assumed that the blends are slightly more stable than the pure polymers.

Table 5.4. TGA data for plasticized PVA/CS nanocomposites in inert atmosphere.

Glycerol Plasticized Samples (in N_2)	$T_{5\%}$ (°C)	$T_{50\%}$ (°C)	T_{max} (°C)				Residue (%)
			(a)	(b)	(c)	(d)	
PVA	188	327	216	283	355	430	2.5
PVA/CS 90/10	175	348	227	304	369	469	5.7
PVA/CS 80/20	166	349	218	290	366	466	7.6
PVA/CS 70/30	162	348	226	291	357	464	12.1
PVA/CS 60/40	165	347	225	291	350	452	14.7
PVA/CS 50/50	165	340	224	293	338	449	18.5
PVA/CS 40/60	174	352	225	305	-	468	22.6
PVA/CS 30/70	180	348	224	306	-	468	25.2
PVA/CS 20/80	175	344	221	306	-	472	28.2
PVA/CS 10/90	180	345	211	307	-	-	30.5
CS	145	320	189	294	-	-	30.1

(a) 1st stage; (b) 2nd stage; (c) 3rd stage; (d) 4th stage

Generally, assuming no interaction between the polymers that conform the blend, thermal parameters such as the initial degradation temperature or $T_{5\%}$ should not change significantly with the composition. This would mean that in the thermograms of the blends, the starting degradation temperature would be similar to that of the less stable polymer [39]. However, the obtained TGA results indicate that the $T_{5\%}$, $T_{50\%}$, and T_{max} of the blends change with the different weight composition, even giving values of $T_{50\%}$ higher than those of pure CS and PVA. Therefore, this leads to the conclusion that there are certain hydrogen bonding interactions between PVA and CS in each blend, as well as a good mixture of the polymers together.

Differential scanning calorimetry (DSC)

Thermal transition behavior of PVA/CS blends was investigated by DSC. First cooling and second heating scans for unplasticized and plasticized PVA and PVA/CS blends are shown in Figure 5.7. The DSC data for unplasticized samples are summarized in Table 5.5, while for plasticized ones in Table 5.6. The parameters shown in the tables are obtained in the same way as in Chapter 4.

The thermal behavior of chitosan, and especially its glass transition temperature (T_g), has been the subject of controversy. Some studies reported in the literature have described the T_g of chitosan at 203 °C [40], while others find no evidence of T_g, suggesting that the T_g of chitosan may be at a higher temperature, where degradation prevents its determination [41]. Moreover, according to Neto *et al.* [42] the source or extraction method of CS strongly influences the T_g values. Tripathi *et al.* [43] describes in the chitosan DSC thermogram a sharp exothermic peak of 290 °C, associated to the chitosan decomposition. In this thesis work, the chitosan did not show any significant transition in the temperature range of the DSC scans.

Table 5.5. DSC data for unplasticized PVA/CS blends.

PVA/CS samples	T_g (°C)	T_m (°C)	ΔH_m (J/g)	T_c (°C)	ΔH_c (J/g)	X_c (%)
PVA	76.1	221.7	76.2	197.7	66.5	53.7
90/10	78.4	217.9	53.9	188.8	50.5	42.2
80/20	82.9	211.8	40.4	180.3	32.8	35.6
70/30	86.8	206.5	28.9	171.7	28.6	29.1
60/40	87.7	203.2	21.9	167.5	20.2	25.7
50/50	85.1	196.5	13.1	153.0	13.0	23.1
40/60	85.5	191.5	10.4	146.3	9.4	14.7
30/70	85.0	185.4	5.3	134.7	4.9	9.3
20/80	85.6	178.0	1.7	128.3	1.2	4.0
10/90	86.6	-	-	-	-	-
CS	-	-	-	-	-	-

The glass transition temperature values of unplasticized blends are higher for all compositions compared to pure PVA, achieving the maximum increase of 11.6 °C for the PVA/CS 60/40 composition (Table 5.5). This behavior is explained by the interactions of the polymers through hydrogen bonds, which results in an effective increase of the average molecular weight and therefore of the T_g values. With regard to this transition, it is important to point out that the combination of compatible or partially compatible polymers implies that the T_g values are intermediate between the respective values of the pure polymers. In this sense, and according to those values reported for chitosan in the literature, the increase achieved in T_g values in the blends points to the good miscibility of both polymers.
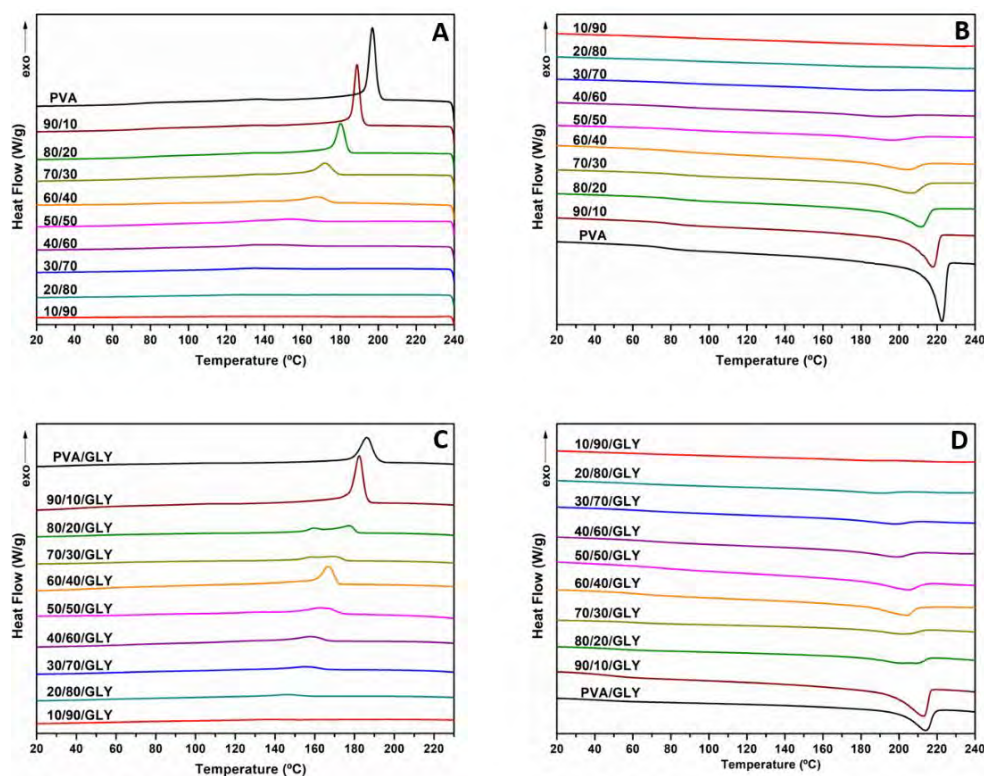
Figure 5.7. DSC thermograms. (A,C) First cooling and (B,D) second heating for unplasticized (A,B) and plasticized (C,D) PVA/CS blends.

The addition of plasticizer to the different PVA/CS compositions means that the T_g values are lower than their unplasticized counterparts because glycerol improves the mobility of the segments of the polymer chain. Despite this

behavior, on this point it should be noted that the effect of adding CS to PVA is more prominent in the presence of glycerol, since the glass transition temperature increases to a greater extent, obtaining an increase of 29 °C for the PVA/CS/GLY 40/60 composition. Therefore, this improvement is attributed to a better compatibility between the polymers with glycerol.

On the other hand, the melting temperature (T_m) values of both unplasticized and plasticized blends are reduced as the CS content increases. This behavior also suggests a certain miscibility between PVA and CS, which in turn leads to a reduction in the crystallization process of PVA. The degree of crystallinity (X_c), shown in the Table 5.5 and Table 5.6 and calculated by the second DSC heating scan using the equation that relates the melt enthalpy values of the blends (ΔH_m) and of the 100% crystalline PVA (ΔH^0_m) with the PVA fraction in the blend (Appendix I, equation I.2.2), confirms the decrease of the PVA crystallinity when the CS ratio increases in the blend.

Table 5.6. DSC data for plasticized PVA/CS blends.

PVA/CS/GLY samples	T_g (°C)	T_m (°C)	ΔH_m (J/g)	T_c (°C)	ΔH_c (J/g)	X_c (%)
PVA/GLY	42.5	216.0	49.8	188.7	47.7	35.1
90/10/GLY	47.4	212.7	47.8	182.4	47.1	37.4
80/20/GLY	52.9	204.8	17.9	177.2	14.5	15.8
70/30/GLY	58.8	202.6	11.6	169.0	9.9	11.7
60/40/GLY	63.5	204.3	21.8	166.9	21.2	25.6
50/50/GLY	69.9	203.9	16.3	162.6	11.6	28.7
40/60/GLY	71.5	198.9	12.8	157.3	9.3	18.0
30/70/GLY	68.1	198.8	7.9	155.3	5.3	13.9
20/80/GLY	58.7	189.5	5.3	146.4	3.5	12.4
10/90/GLY	62.9	184.5	1.0	137.0	0.8	3.5
CS/GLY	-	-	-	-	-	-

The crystallization temperature (T_c) of PVA is also affected by the addition of CS. In both plasticized and unplasticized blends, the T_c value decreases as the CS content increases, and even in the unplasticized 10/90 composition it is not detected. For unplasticized blends, the T_c is delayed by 69.4 °C at 20/80 composition, while in plasticized blends it is reduced by 52 °C at 10/90.

In short, increased CS content results into more amorphous blends (lower crystallization degree) with a lower melting and crystallization temperatures. Moreover, the addition of glycerol plasticizer to the blends improves the compatibility between PVA and CS which, through the analysis of their T_g values, are confirmed to be partially miscible polymers.

5.3.1.3. Mechanical characterization

Tensile tests were used to determine the mechanical properties of the PVA/CS blends and also to analyze which composition is suitable to improve the stiffness and brittleness of the chitosan films shown in Chapter 3. Typical stress-strain curves of unplasticized and plasticized PVA/CS compositions are presented in Figure 5.8. Unplasticized blends (Figure 5.8A) show a ductile behavior, as the deformations are moderate and present yield stress. However, within the different compositions studied, CS-rich films have proved to be less stretchable. Likewise, this can be explained by the fact that the blends show a plastic deformation that increases enormously as the PVA proportion increases. On the contrary, plasticized blends (Figure 5.8B) show higher deformations and moderate maximum-stress, as well as relatively low elastic module values. Additionally, yield stress can only be distinguished in those compositions with high CS content.

The tensile properties as Young's modulus, break stress and percentage of elongation at fracture for unplasticized and plasticized pure polymers and PVA/CS blends are given in Table 5.7 and Table 5.8, respectively, and their graphical representation is shown in Figure 5.9. The mechanical properties of pure CS are considerably altered with the addition of PVA and the differences are more noticeable in the presence of glycerol-plasticizer (Figure 5.9).
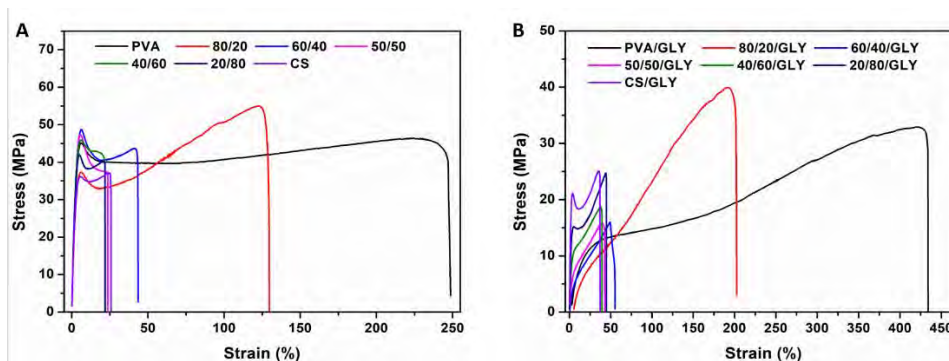
Figure 5.8. Stress–strain curves of (A) unplasticized and (B) glycerol plasticized CS, PVA and PVA/CS blends.

Table 5.7. Mechanical properties data of unplasticized PVA/CS blends.

Sample	Young's modulus (MPa)	Break Stress (MPa)	Elongation at break (%)
PVA	1337±156	45.4±6.3	211.5±38.7
90/10	964±63	55.3±2.8	208.2±27.4
80/20	1170±147	56.2±3.3	132.2±19.5
70/30	1585±153	51.6±4.2	69.3±7.1
60/40	1807±140	41.8±3.5	38.1±7.7
50/50	1840±209	40.3±3.2	26.1±5.1
40/60	1751±104	38.4±2.6	26.3±5.3
30/70	1759±196	41.0±3.2	22.1±3.7
20/80	1778±110	40.0±2.1	21.9±3.1
10/90	1616±170	38.2±3.1	24.4±4.0
CS	1679±141	31.2±6.1	27.3±6.4

Young's modulus and break stress of the CS film increase slightly with the addition of PVA, while elongation at break also increases, and does significantly with the composition (Figure 5.9). Specifically, for unplasticized blends, as the PVA ratio increased up to 50-60%, the elastic modulus shows a slight increase (9.6%), but above of this amount of PVA, the modulus worsens with respect to pure polymers. The break stress of pure CS is also improved with the addition of

PVA, achieving an increment of 22.6% only with the addition of 10% PVA. The maximum increment is observed in PVA/CS 80/20 composition. Moreover, the break stress values of 90/10, 80/20 and 70/30 composition blends exceed those of pure polymers (Table 5.7). This behavior suggests the establishment of bonds between the chains of both polymers in the blends, which reinforce the network structure, thus improving the mechanical strength of the films. With respect to the elongation at break, it is not until an addition of 60 wt% PVA that it is improved in 39.5% compared to pure CS. Below this PVA content the elongation at break remains almost constant, and above increases with the composition, but in any case it does exceed the value obtained for pure PVA.
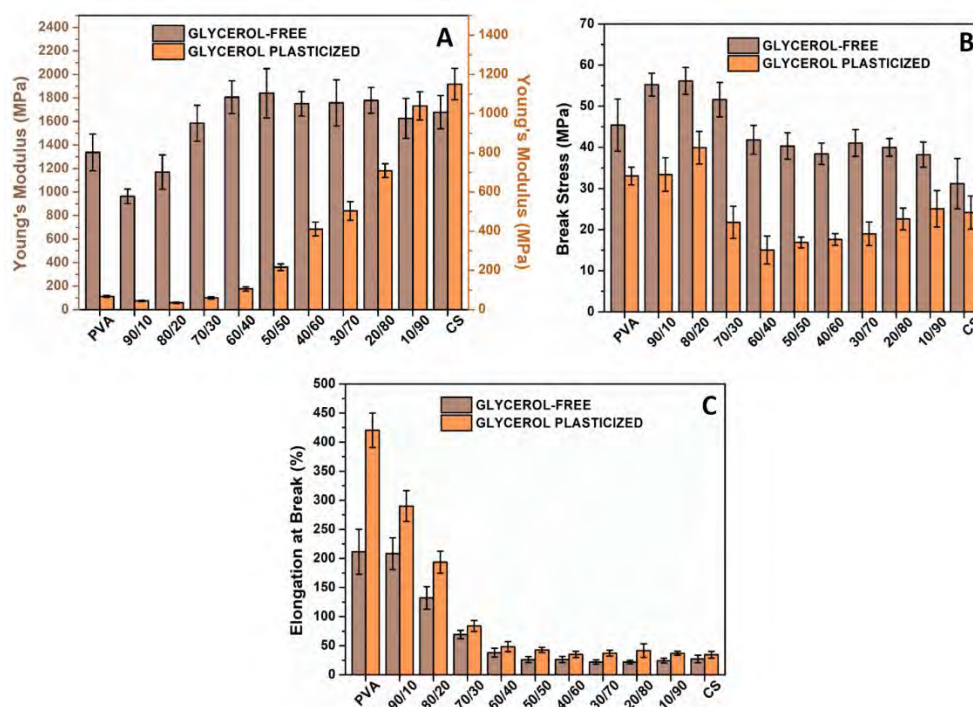
Figure 5.9. Mechanical properties of PVA/CS blends: (A) Young's modulus, (B) break stress and (C) elongation at break.

According to what has been observed in the previous chapters, the addition of the plasticizer in PVA/CS blends leads to lower Young's modulus and break stress values and higher elongation at break compared to its unplasticized counterparts because glycerol destroys the inter- and intramolecular hydrogen

bonds in the polymer chains which facilitates molecular movements and thus makes the films more flexible.

For plasticized blends, a gradual decrease in the elastic modulus can be observed with the increase in the PVA content (Figure 5.9), whereas break stress for some compositions it gets worse and for others with a PVA composition higher than 70%, it improves (Table 5.8). The increase in elongation at break is more prominent in PVA-rich compositions.

Table 5.8. Mechanical properties data of glycerol-plasticized PVA/CS blends.

Sample	Young's modulus (MPa)	Break Stress (MPa)	Elongation at break (%)
PVA/GLY	68±5	33.0±2.2	420.4±29.5
90/10/GLY	45±3	22.4±4.1	290.0±26.5
80/20/GLY	35±4	39.9±4.0	193.6±18.8
70/30/GLY	60±6	21.8±3.9	83.9±9.3
60/40/GLY	106±11	15.0±3.4	48.5±9.7
50/50/GLY	217±17	16.9±1.3	42.8±4.4
40/60/GLY	411±36	17.6±1.4	35.1±5.4
30/70/GLY	504±47	19.0±2.8	37.2±4.9
20/80/GLY	709±35	22.6±2.6	41.6±11.6
10/90/GLY	1039±72	25.1±4.4	37.0±3.4
CS/GLY	1150±80	24.2±4.0	34.5±5.8

In short, this mechanical properties analysis allows us to conclude that PVA/CS blends, especially those with a CS-rich composition (above 50 wt%), can be considered strong and more resistant to fracture than pure polymer films, although their extensibility is considerably reduced compared to PVA films. This behavior is in line with the formation of bonds between chains that reinforce compatibility between PVA and CS, but limits the sliding of the polymer chains during the tensile test, thus reducing the extensibility of the film. In general, the addition of PVA to CS leads to a decrease in material stiffness and brittleness.

5.3.1.4. Water vapour permeability of PVA/CS blends

Water permeability is an important property that can determine the application of a polymer in food packaging. In this area for high barrier packaging, vacuum packaging and packaging of dehydrated products, a high water vapor barrier is generally required. CS is commonly described as a material with great potential for food packaging due to its antimicrobial activity. However, the high sensitivity of CS films to water makes their long-term application difficult. Therefore, it is necessary to improve this property to make feasible the use of this material as a packaging component. Water vapor permeability (WVP) results of different compositions of unplasticized and plasticized PVA/CS blends are shown in are shown in Figure 5.10. This analysis was performed at a vapor pressure difference of 100/58% RH (i.e. at a RH gradient of 100/58) across the film.
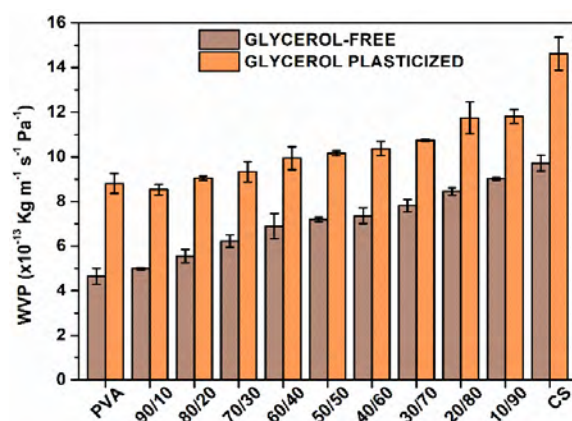
Figure 5.10. Water vapor permeability (WVP) for unplasticized and glycerol plasticized PVA/CS blends.

In line with the behavior of pure CS and PVA observed in Chapters 3 and 4, respectively, the unplasticized PVA/CS blends show significant differences ($p < 0.05$) with respect to the plasticized ones. The increased permeability of plasticized blends is due to the hydrophilic nature of glycerol. The hydroxyl groups of the glycerol interact with the hydroxyl groups present in the PVA and CS structures, so the intramolecular attractions along the PVA or CS chains are reduced and, consequently, the mobility of the chains increases, facilitating the diffusivity of water vapor through the film and accelerating the transmission of water vapor [44].

WVP values of all unplasticized PVA/CS formulations are higher than those of pure PVA ($p < 0.05$) and the results represented in Figure 5.10 reveal that WVP values increase gradually as the CS ratio increases. In the same way, the addition of PVA to CS decreases permeability properties. This can be explained through the hydrophilic nature of CS which is higher than that of PVA [45,46]. The hydrophilicity of CS is due to the existence of -NH and -OH groups in its structure, while that of PVA to its -OH groups. This assertion can be proved through the water absorption results shown in Chapter 3 for CS and in Chapter 4 for PVA, where, under the same conditions, CS absorbed more water than PVA. Consequently, the higher hydrophilicity of CS favors the transport of water molecules through the film [47]. However, there would be another factor to consider, the effect of crystallinity. Thermal characterization of PVA/CS films through DSC has shown that the crystallinity of the blends decreases as the CS content increases, and consequently the free amorphous regions increase which means that there is more open matrix in the blends and these regions show less resistance to water vapor permeability than the crystalline ones, leading to an increase in permeability. In other words, the polymer chains are less densely packed due to the wider hydration layers of CS [38].

WVP values of plasticized PVA/CS formulations are also higher than that of PVA/GLY ($p < 0.05$). However, in this case the increment by increasing the CS content is less pronounced than in unplasticized ones, because glycerol plasticizer already enhances the WVP at great extent by increasing the intermolecular interactions between CS and PVA, and preventing the intramolecular interactions that decrease the diffusion of water.

Taking into account the results of unplasticized PVA/CS blends discussed in this section, and in particular, the DSC and mechanical properties results, 60/40 composition has been chosen as the most optimal for the preparation and study of PVA/CS/graphene-based nanocomposites. This composition showed the highest glass transition temperature, indicating good partial miscibility between PVA and CS (Table 5.5). Likewise, in the tensile tests, the composition with 60% PVA and 40% CS showed one of the highest values of elastic modulus, as well as a remarkable value in elongation (Table 5.7). In the rest of the compositions, if the elongation at break was high, the modulus values did not exceed those of pure polymers or were even worse.

5.3.2. Graphene-based PVA/CS nanocomposites

5.3.2.1. Structural and morphological characterization

X-ray diffraction (XRD)

X-ray diffractograms of unplasticized and plasticized PVA/CS (60:40 v/v ratio) blend, and its nanocomposite films with 0.5, 1 and 2.5 wt% of GO, measured in the range of $2\theta = 2°-60°$, are presented in Figure 5.11. The XRD pattern of the PVA/CS 60/40 blend shows four diffraction peaks of which the small one at 11.8° and the other at 23.5° are related to CS, while the more intense one at 19.9° and the width at 40.8° are associated with PVA. The plasticized blend shows a similar diffraction pattern, but with a decrease in peak intensity at 19.9° that could be ascribed to a decrease in PVA crystallinity.
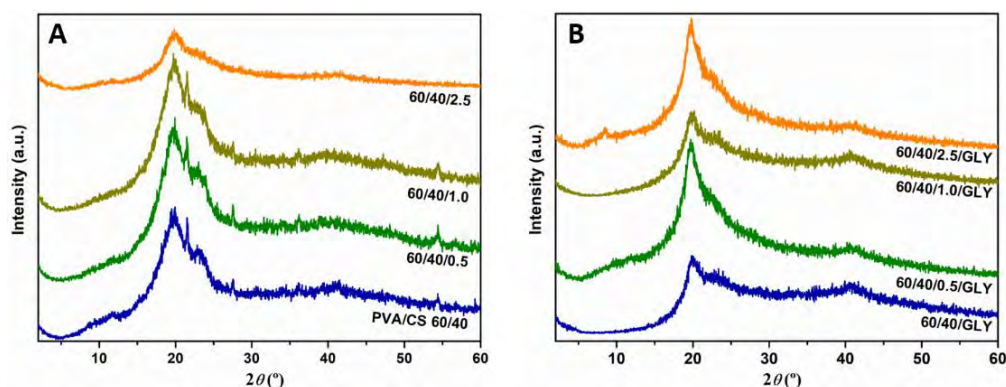
Figure 5.11. XRD patterns of: (A) unplasticized PVA/CS/GO nanocomposites and (B) plasticized PVA/CS/GO nanocomposites.

XRD results of unplasticized and glycerol-plasticized PVA/CS/GO nanocomposite films reveal that the addition of GO does not change the peak positions described for the blend. However, in the case of unplasticized nanocomposites only the addition of 2.5 wt% GO leads to a decrease in the intensity of the 19.9° peak related to PVA crystallinity (Figure 5.11A). In the case of plasticized nanocomposites, the intensity variation is detected with a 1 wt% of GO content, but the peak positions are maintained as in the uncharged blend (Figure 5.11B).

The absence of the characteristic peak of GO (Chapter 2, Figure 2.22) is indicating that most GO sheets are well dispersed within the blend, or the peak is weak (just low content of GO aggregates are formed) and overlapped by the peak of CS at 11.8°.
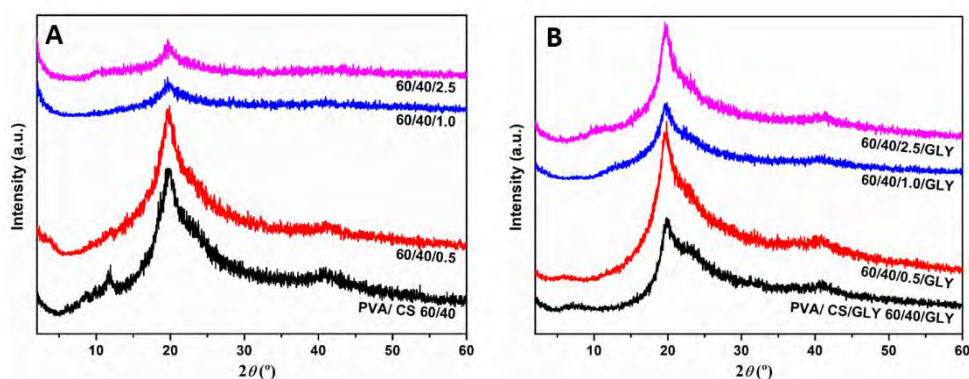
Figure 5.12. XRD patterns of: (A) unplasticized PVA/CS/GS nanocomposites and (B) plasticized PVA/CS/GS nanocomposites.

The X-ray diffraction spectra of the unplasticized and plasticized PVA/CS/GS nanocomposites synthesized through the *in situ* method are shown in Figure 5.12. Compared to PVA/CS blend, the nanocomposite samples show peaks at $2\theta = 19.9°$ and $40.8°$, while the broad GS peak at $2\theta = 24.3°$ disappears (Chapter 2, Figure 2.22) suggesting that the GS sheets are homogeneously dispersed in the matrix. For unplasticized nanocomposites, the diffraction peak intensity at $2\theta = 19.9°$ decreases with the addition of 1 wt% GS or higher content, indicating a decrease in PVA crystallinity. However, this behavior is not equally apparent for glycerol-plasticized nanocomposites. Therefore, XDR results suggest that the crystallinity of the PVA/CS blend decreases with increasing GS content, but this effect is less pronounced in the presence of plasticizer. However, this statement has to be confirmed by the DSC analysis in which crystallinity values can be calculated.

Nanostructure and morphology

The morphological analysis of the different graphene-based PVA/CS nanocomposites was performed by SEM and TEM. Figure 5.13 displays SEM micrographs of the fractured cross sections of unplasticized and plasticized nanocomposites films containing 1 wt% of GO and 1 wt% GS. Unlike the PVA/CS blend (Figure 5.5), which structure is smooth, the morphology of the nanocomposite changes, becomes rough and exhibits little wrinkles assigned to the GO or GS sheets presence.

SEM micrographs of unplasticized and plasticized PVA/CS/GO show a uniform distribution of GO sheets through single-phase PVA/CS blend. The homogeneous distribution of the filler leads to the uniform load transfer within the blend matrix which suggests the strong hydrogen bonding interactions of nanofiller and polymers.
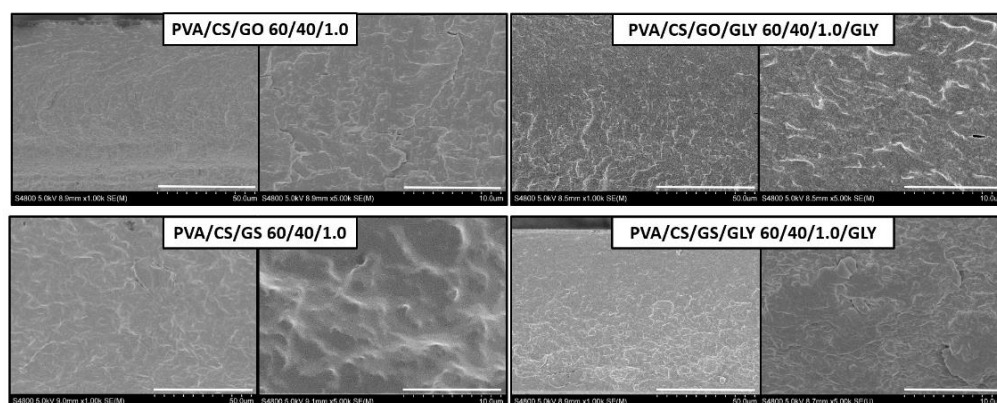
Figure 5.13. SEM images of the fractured surface of unplasticized and plasticized PVA/CS/GO and PVA/CS/GS nanocomposites with 1 wt% of filler.

Likewise, the images of unplasticized and plasticized PVA/CS/GS, prepared by *in situ* reduction exhibit a rougher fractured surface with no aggregates of GS, and a wave-like morphology.

Furthermore, analyzing the glycerol effect, the roughness of the fracture surface slightly increases when the plasticizer is present, which suggests an improvement in the dispersion of the filler in the PVA/CS blend.

TEM images of unplasticized and plasticized PVA/CS/GO and PVA/CS/GS nanocomposites with 1 and 2 wt% of filler presented in Figure 5.14 confirm the good dispersion of GO or chemically reduced graphene oxide sheets (GS) throughout the blend, but a slight improvement in dispersion could be noted in the plasticized nanocomposites.
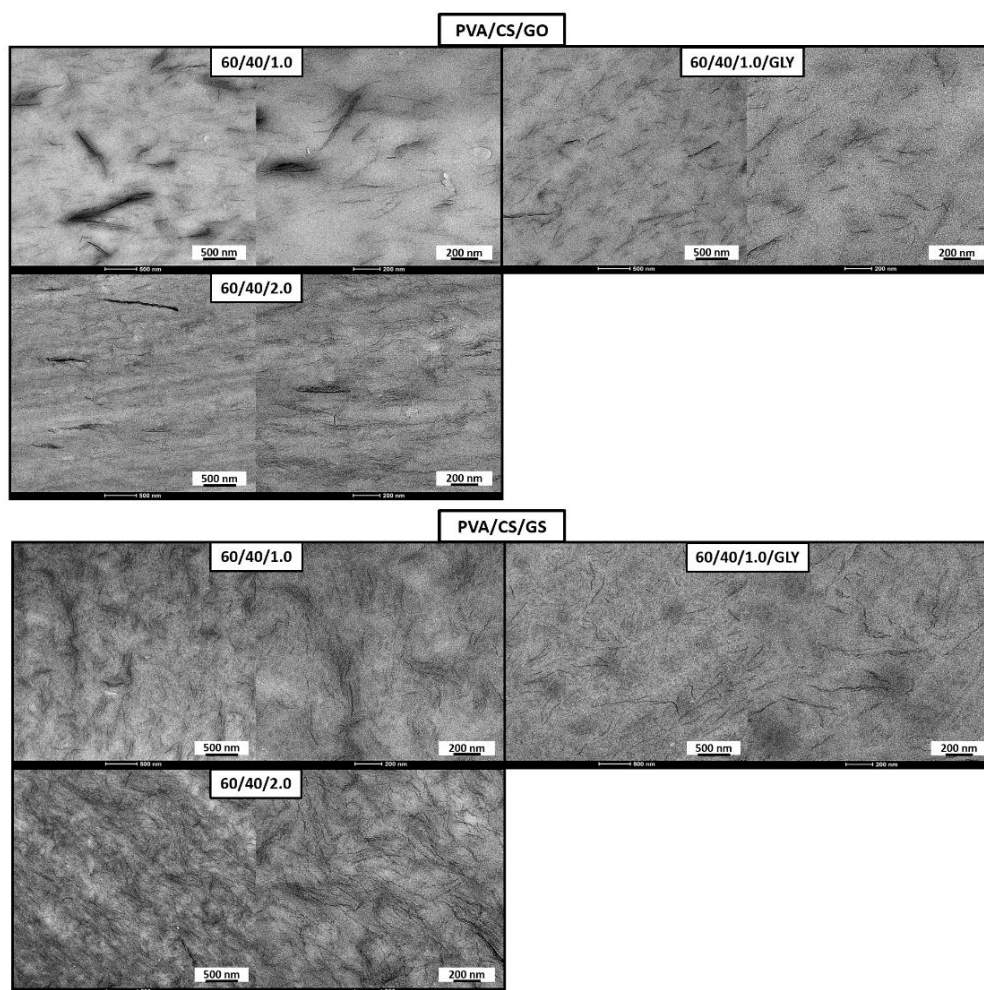
Figure 5.14. TEM images of: plasticized and unplasticized PVA/CS/GO and PVA/CS/GS nanocomposites filled with 1 and 2 wt% of GO or GS at different magnifications.

5.3.2.2. <u>Thermal characterization</u>

<u>*Thermogravimetric analysis (TGA)*</u>

The influence of GO and GS on the thermal stability of PVA/CS 60/40 blend was evaluated by TGA. Thermogravimetric (TG) and derivative thermogravimetric (DTG) curves of plasticized and unplasticized GO-based nanocomposites in inert atmosphere are displayed in Figure 5.15, and Table 5.9 summarizes the data collected from these curves.

In line with the results described above for blends, the first stage, which can be distinguished in the TG curves of unplasticized PVA/CS/GO nanocomposites takes place in a temperature range of 150 - 250 °C and results in a weight loss of ≈10% in all samples (Figure 5.15A). At this stage there is a loss of methane and ammonia due to the removal reaction that takes place in the chitosan [36]. Likewise, plasticized nanocomposites in this temperature range also show this stage, but with a different peak shape in the DTG curve and with a higher weight loss (≈15%) due to glycerol evaporation (Figures 5.15C,D). The second weight loss step, between 250 and 430 °C, for both unplasticized and plasticized nanocomposites, is the largest weight loss, with over 55% weight loss and is related to the rapid decomposition of polymers segments. The third weight loss at 420 - 500 °C, is associated to the degradation of by-products generated by PVA during its thermal degradation. Finally, from 600 °C to 800 °C, the weight is kept constant and allows the calculation of the percentage of carbonaceous residue of the degraded structures.

The addition of GO alters the degradation temperatures and DTG profile of PVA/CS 60/40 blend. The second stage of decomposition of unplasticized and plasticized PVA/CS blends exhibits two peaks in the DTG curve which are ascribed to the elimination of the side groups (-OH) and the polymers chain scission reactions. In the presence of GO, as the content grows the first peak becomes less intense and even shifts giving higher T_{max} values, i.e. closer to the temperatures where the second peak appears. However, the intensity of the other peak increases and also shifts with the content. Specifically, in the case of unplasticized nanocomposites, the first peak shifts notably with a GO content above 1.5%, but in the plasticized ones the increase is more gradual (Figures 5.15B,D). In both unplasticized and plasticized nanocomposites the greatest

difference in T_{max} of the two peaks is found in the maximum GO content studied. Therefore, the removal of the side groups occurs at higher temperatures in the presence of GO.

The $T_{5\%}$ and $T_{50\%}$ of the unplasticized 60/40 blend are hardly altered by the presence of GO (Table 5.9). The addition of 2.5 wt% causes a decrease of 5 °C in the temperatures corresponding to 5% weight loss, while the $T_{50\%}$ increases by 9 °C. However, for plasticized nanocomposites in all GO compositions, $T_{5\%}$ and $T_{50\%}$ increase. Among the different compositions of GO analyzed, no remarkable differences are detected, but with respect to the unfilled blend, for example, the higher GO content causes an increase of 32 °C in $T_{5\%}$ and 22 °C in $T_{50\%}$.
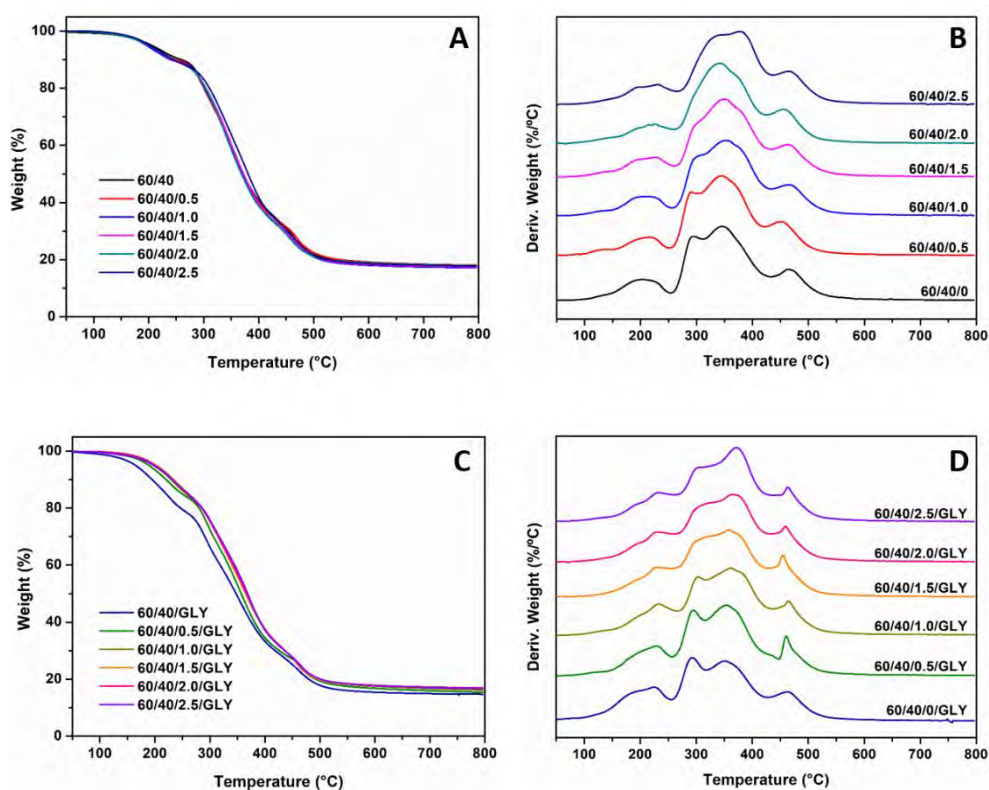
Figure 5.15. TG (A,C) and DTG (B,D) curves of unplasticized and plasticized PVA/CS/GO nanocomposites in nitrogen atmosphere.

The residue percentage obtained for both plasticized and unplasticized nanocomposites hardly changes with the addition of GO. The variations recorded

are attributed to the experimental error, since the percentages of filler analyzed are very low (the higher the content, the higher is the carbonaceous residue) in comparison with the amount of polymer in the nanocomposites.

Table 5.9. TGA data for unplasticized and plasticized PVA/CS/GO nanocomposites.

Glycerol-Free PVA/CS/GO	$T_{5\%}$ (°C)	$T_{50\%}$ (°C)	T_{max} (°C) (a)	(b)	(c)	(d)	Residue (%)
PVA/CS 60/40	206	372	226	298	347	466	17.9
60/40/0.25	202	369	214	301	347	467	18.1
60/40/0.5	201	372	216	300	347	469	18.2
60/40/0.75	191	371	213	299	349	468	16.9
60/40/1.0	197	372	215	300	354	465	17.3
60/40/1.5	200	373	223	302	350	466	17.5
60/40/2.0	201	369	226	339	372	456	18.0
60/40/2.5	201	381	229	340	377	465	17.8
Glycerol Plasticized PVA/CS/GO	$T_{5\%}$ (°C)	$T_{50\%}$ (°C)	T_{max} (°C) (a)	(b)	(c)	(d)	Residue (%)
PVA/CS 60/40	165	347	225	291	350	452	14.7
60/40/0.25	197	362	231	297	353	457	16.2
60/40/0.5	189	357	228	295	354	461	15.6
60/40/0.75	190	366	231	300	366	466	15.2
60/40/1.0	197	367	233	303	362	464	16.2
60/40/1.5	202	365	228	315	358	456	16.8
60/40/2.0	200	367	229	316	366	459	17.0
60/40/2.5	197	369	230	314	373	464	16.7

(a) 1st stage; (b) 2nd stage; (c) 3rd stage; (d) 4th stage

Considering the whole degradation process, the thermal stability of the unplasticized PVA/CS 60/40 blend is slightly improved by the addition of GO. However, in the presence of glycerol the effect of GO is more pronounced, obtaining higher stability with all filler contents, since maximum stabilization is observed at the temperature at which the highest rate of weight loss occurs.

On the other hand, the effect of GS (*in situ* reduced GO) on the thermal stability of PVA/CS 60/40 blend was also evaluated. TG and DTG curves for GS nanocomposites are shown in Figure 5.16. The thermal degradation characteristics $T_{5\%}$, $T_{50\%}$, T_{max} and the solid residue fraction at 800 °C are recorded in Table 5.10. The degradation stages observed for PVA/CS/GS nanocomposites are similar as with their GO counterparts.
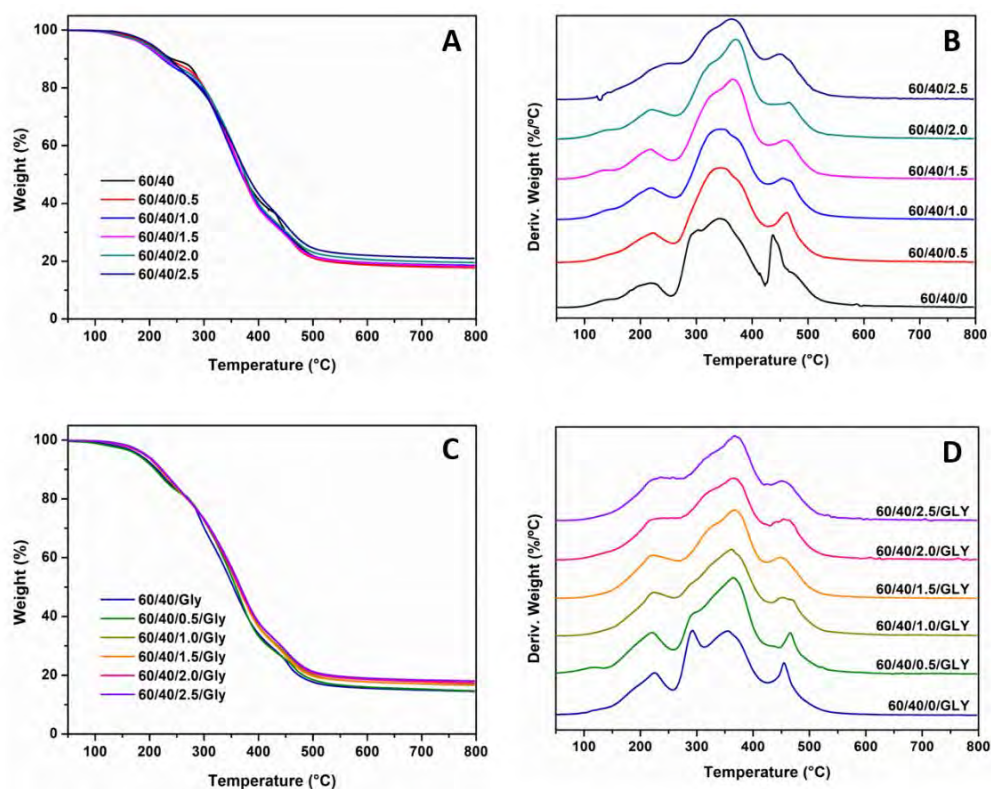
Figure 5.16. TG (A,C) and DTG (B,D) curves of unplasticized and plasticized PVA/CS/GS nanocomposites in nitrogen atmosphere.

Table 5.10. TGA data for unplasticized and plasticized PVA/CS/GS nanocomposites.

Glycerol-Free PVA/CS/GS	$T_{5\%}$ (°C)	$T_{50\%}$ (°C)	T_{max} (°C)				Residue (%)
			(a)	(b)	(c)	(d)	
PVA/CS 60/40 (6 h at 60 °C)	197	371	220	303	342	437	17.8
60/40/0.25	200	369	223	343	375	462	17.0
60/40/0.5	198	370	220	344	374	463	17.8
60/40/0.75	198	372	221	338	365	462	17.1
60/40/1.0	188	369	219	344	372	459	18.6
60/40/1.5	190	371	217	331	365	459	18.3
60/40/2.0	194	375	218	330	371	464	19.5
60/40/2.5	204	379	241	328	363	450	21.1
Glycerol Plasticized PVA/CS/GS	$T_{5\%}$ (°C)	$T_{50\%}$ (°C)	T_{max} (°C)				Residue (%)
			(a)	(b)	(c)	(d)	
PVA/CS 60/40 (6 h at 60 °C)	182	354	224	292	356	455	14.6
60/40/0.25	193	359	223	293	360	462	15.3
60/40/0.5	180	359	220	295	366	466	14.8
60/40/0.75	195	364	221	293	359	465	16.6
60/40/1.0	194	363	221	-	362	468	16.8
60/40/1.5	192	364	218	-	367	453	17.0
60/40/2.0	191	365	219	-	366	464	17.5
60/40/2.5	194	367	222	-	369	454	18.1

(a) 1st stage; (b) 2nd stage; (c) 3rd stage; (d) 4th stage

The presence of GS has effect on unplasticized and plasticized PVA/CS 60/40 blend degradation, there is a significant change in the shape of the DTG curves (Figures 5.16B,D). In the DTG curve, the second stage contains two peaks, but after adding 0.5 wt% GS to the unplasticized PVA/CS blend, the first peak is

less pronounced and the intensity of the second peak increases. However, for plasticized nanocomposites, the first peak of this stage is not clearly detected above 0.75% GS and the second peak gives higher T_{max} values.

Similar to what happened with GO, the $T_{5\%}$ and $T_{50\%}$ of the unplasticized blend is slightly altered by the addition of GS (Table 5.10). The nanocomposite with 2.5 wt% of GS exhibits the highest thermal stability, due to $T_{5\%}$ and $T_{50\%}$ increases 7 and 4 °C, respectively. However, this improvement is more remarkable in the case of PVA/CS/GS plasticized nanocomposites. $T_{5\%}$ increases with the addition of GS (Table 5.10), as well as $T_{50\%}$, achieving an increment of 12 and 13 °C, respectively, for a 2.5 wt% GS content. Considering all these results, the thermal stability of PVA/CS 60/40 or plasticized PVA/CS blend is improved with the addition of GS, but this filler provides greater stability in the presence of glycerol.

In accordance with the description in Chapter 4, the increased thermal stability of the PVA/CS blend loaded with graphene-based fillers can be attributed to the high thermal stability of these nanofillers, specifically to the mass transport barrier effect of the uniformly dispersed graphene sheets to the volatile degradation products, and also to char formation [48]. The diffusion of the evolved volatile gas during thermal decomposition is delayed, the diffusion of oxygen in the polymer matrix is prevented.

Differential scanning calorimetry (DSC)

The effect of different graphene-based fillers on the thermal transition behavior of the PVA/CS 60/40 blend was also investigated by DSC. First cooling and second heating scans for unplasticized and plasticized PVA/CS/GO nanocomposites are shown in Figure 5.17 and the DSC data for these samples are summarized in Table 5.11.

The unplasticized 60/40 blend was the composition that showed the highest glass transition temperature value among all the PVA/CS compositions studied (Table 5.5), suggesting a good and higher interaction between the two polymers through the hydrogen bonds. The T_g of this blend increase slightly with GO content, obtaining the highest temperature with the addition of 2.5 wt% GO, an increase of 6.2 °C. The use of plasticizers results in lower T_g values than their

unplasticized counterparts. However, the addition of GO to plasticized blend also changes the T_g values. The 0.25 wt% and 2.5 wt% of GO leads to a remarkable increase in the T_g, exactly 13.3 and 9.4 °C respectively, while the rest of GO contents change only between 0.1 - 3.6 °C. The increase in T_g is explained by reduced mobility of the polymer chains due to interfacial interactions between the hybrid and the polymer blend.

Table 5.11. DSC data for unplasticized and plasticized PVA/CS/GO nanocomposites.

Glycerol-Free PVA/CS/GO	T_g (°C)	T_m (°C)	ΔH_m (J/g)	T_c (°C)	ΔH_c (J/g)	X_c (%)
PVA/CS 60/40	86.4	203.2	21.9	167.5	20.2	25.7
60/40/0.25	88.0	197.4	19.6	154.9	17.2	23.1
60/40/0.5	85.3	199.7	18.7	156.6	16.7	22.1
60/40/0.75	88.0	196.3	17.4	155.1	15.9	20.6
60/40/1.0	88.4	199.7	16.7	158.9	14.9	19.8
60/40/1.5	89.0	196.0	14.7	151.2	13.9	17.5
60/40/2.0	85.2	194.1	13.9	148.2	12.7	16.6
60/40/2.5	92.6	195.2	14.6	154.4	11.7	17.6
Glycerol Plasticized PVA/CS/GO	T_g (°C)	T_m (°C)	ΔH_m (J/g)	T_c (°C)	ΔH_c (J/g)	X_c (%)
PVA/CS 60/40/GLY	63.5	204.3	21.8	166.9	21.2	25.6
60/40/0.25/GLY	76.7	208.9	20.2	170.1	20.0	23.8
60/40/0.5/GLY	64.5	205.1	20.5	168.8	20.2	24.2
60/40/0.75/GLY	67.1	204.0	18.8	167.0	17.6	22.2
60/40/1.0/GLY	65.3	199.6	19.9	161.1	19.0	23.6
60/40/1.5/GLY	63.6	198.8	18.5	160.5	18.5	22.0
60/40/2.0/GLY	65.5	202.2	19.9	161.1	19.8	23.8
60/40/2.5/GLY	72.9	204.7	17.7	165.3	17.2	21.3
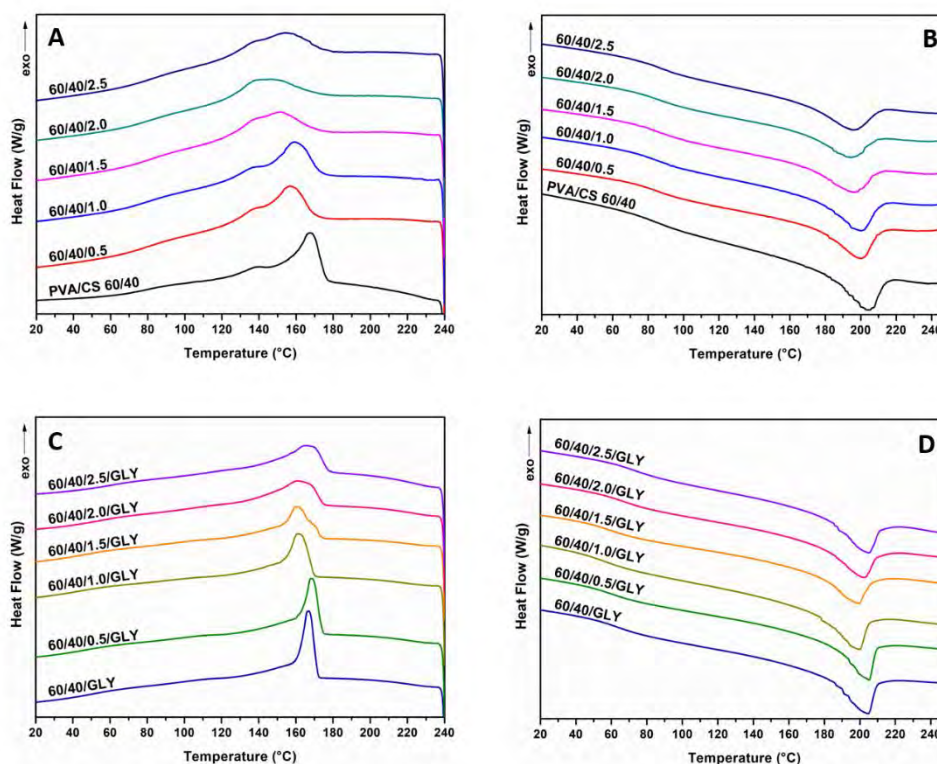
Figure 5.17. DSC thermograms. (A,C) First cooling and (B,D) second heating for unplasticized (A,B) and plasticized (C,D) PVA/CS/GO nanocomposites.

Regarding the melting temperature (T_m), in unplasticized nanocomposites the incorporation of GO causes a slight temperature decrement and not gradually with increasing content. The highest load contents (2 wt% and 2.5 wt%) undergo the greatest decrease, which means that the graphene oxide sheets cause the fusion to take place a little earlie (Table 5.11). For the plasticized nanocomposites the T_m is hardly altered, in low contents it increases slightly, but from 0.75 wt% of GO it decreases a few degrees.

The addition of GO also causes a decrease in the degree of crystallinity (X_c) of both plasticized and unplasticized PVA/CS blends. The reduction is gradual for unplasticized nanocomposites, while for plasticized ones the variance between the different GO contents is very low. A content of 2.5 wt% GO reduces the degree of crystallinity of the unplasticized blend from 25.7% to 17.6%, but with glycerol it changes from 25.6% to 21.3%. Additionally, the crystallization

temperature (T_c) is also affected by the GO (Figures 5.17A,B). For unplasticized nanocomposites, the T_c value is lower in all contents compared to the unfilled blend. However, in plasticized the contents below 0.75 wt% the T_c increases by a maximum of 3.2 °C, while at higher contents it decreases slightly.

Table 5.12. DSC data for unplasticized and plasticized PVA/CS/GS nanocomposites.

Glycerol-Free PVA/CS/GS	T_g (°C)	T_m (°C)	ΔH_m (J/g)	T_c (°C)	ΔH_c (J/g)	X_c (%)
PVA/CS 60/40 (6 h at 60 °C)	82.5	200.6	20.7	159.4	18.2	24.3
60/40/0.25	91.5	192.7	15.1	141.1	14.3	17.8
60/40/0.5	91.9	191.1	12.3	138.1	7.2	14.5
60/40/0.75	92.7	190.2	10.8	140.5	5.7	12.8
60/40/1.0	91.0	184.7	10.1	135.5	3.1	12.0
60/40/1.5	90.4	187.5	11.5	154.4	2.9	13.7
60/40/2.0	91.2	180.2	9.9	150.0	2.4	11.9
60/40/2.5	91.5	161.7	6.8	122.0	2.2	8.2
Glycerol Plasticized PVA/CS/GS	T_g (°C)	T_m (°C)	ΔH_m (J/g)	T_c (°C)	ΔH_c (J/g)	X_c (%)
PVA/CS 60/40/GLY (6 h at 60 °C)	54.2	199.9	26.3	164.8	24.9	30.9
60/40/0.25/GLY	57.4	195.9	20.9	159.7	17.9	24.6
60/40/0.5/GLY	69.9	197.0	19.1	158.8	13.7	22.5
60/40/0.75/GLY	62.5	190.9	18.0	160.8	11.9	21.3
60/40/1.0/GLY	76.9	192.2	14.8	169.8	7.6	17.6
60/40/1.5/GLY	75.3	183.6	12.2	157.5	5.3	14.5
60/40/2.0/GLY	72.3	183.0	10.9	156.0	6.7	13.1
60/40/2.5/GLY	70.4	176.7	9.9	149.8	5.9	11.9

The effect of chemically reduced GS on the thermal transitions of the PVA/CS 60/40 blend (heated sample according to PVA/CS/GS nanocomposite synthesis conditions) can be evaluated with the data displayed in Table 5.12 and with the DSC thermograms shown in Figure 5.18. The glass transition temperature is increased by at least 9 °C for unplasticized nanocomposites with the GS addition. The 0.75% GS content results in the maximum T_g value observed among all the nanocomposites studied, 92.7 °C. In plasticized films, the T_g also increased and the highest temperature is recorded adding 1.0 wt% of GS. As before, the enhanced T_g can be explained by the reduced polymer chain mobility due to the interfacial interactions between the hybrid and the blend.
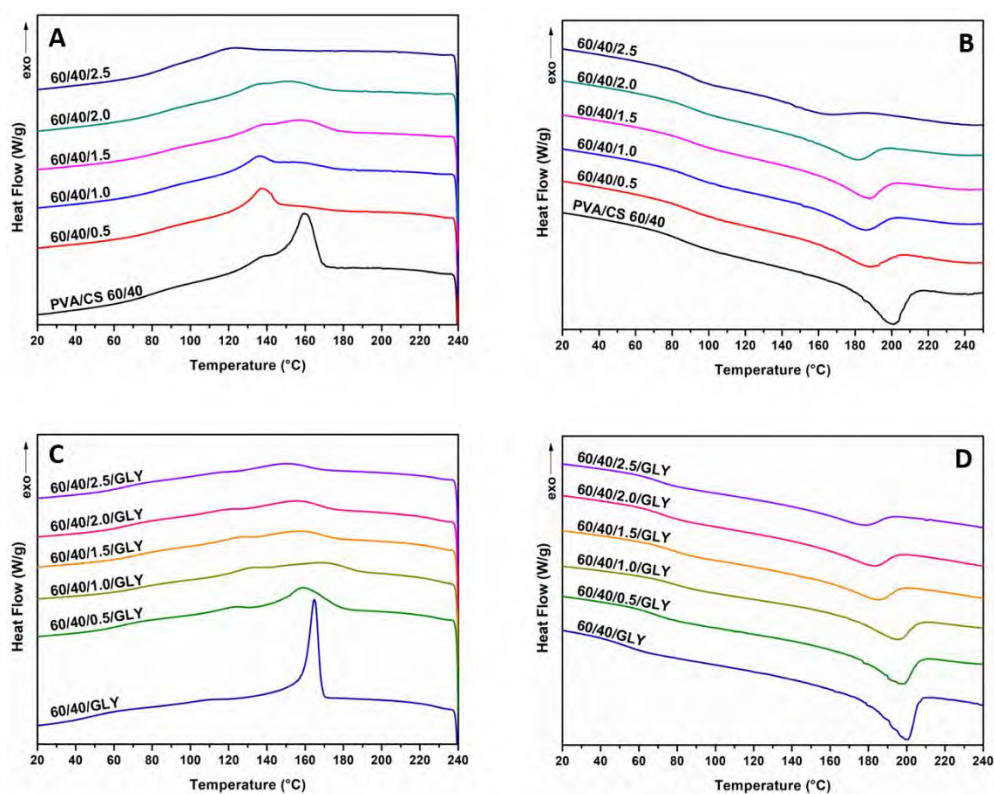
Figure 5.18. DSC thermograms. (A,C) First cooling and (B,D) second heating for unplasticized (A,B) and plasticized (C,D) PVA/CS/GS nanocomposites.

In the second heating (Figures 5.18B,D), the incorporation of different amounts of GS, in both unplasticized and glycerol plasticized blend, leads to

important changes in the T_m values compared to PVA/CS blend (Table 5.12). Melting temperature decreases gradually as the GS content increases, and the same pattern can be seen in the case of melting enthalpy. The greatest decrease in T_m is registered in the absence of plasticizer, where with 2.5 wt% of GS it changes from 200.6 °C to 161.7 °C.

The incorporation of GS also causes a remarkable decrease in crystallization temperature and the degree of crystallinity as the filler content rises. For unplasticized samples, with the highest GS content the T_c drops to 37.4 °C, while in the presence of plasticizer it decreases by 15 °C. These results suggest that GS in the absence of glycerol greatly delays crystallization. However, with regard to the degree of crystallinity, the reduction is greater in the presence of plasticizer.

Considering all the results discussed, it can be concluded that, among the graphene-based nanofillers used, the addition of GS results in a more amorphous blend with a lower melting and crystallization temperature. In addition, compatibility between the PVA and CS is enhanced by the integration of any of the two graphene-based fillers.

5.3.2.3. Mechanical characterization

The good dispersion of GO and GS within the PVA/CS blend confirmed by SEM, TEM and XRD, combined with the hydrogen bond interaction between the PVA/CS polymer chains and fillers has resulted in improved thermal stability of the films and enhanced miscibility, so this can anticipate improved mechanical properties. To this effect, the mechanical characterization of PVA/CS based nanocomposites with different filler contents was performed through tensile tests.

The representative stress-strain curves of unplasticized and plasticized PVA/CS/GO nanocomposites are shown in Figure 5.19 and the mechanical data are listed in Table 5.13, as well as their representation in Figure 5.20. The unplasticized nanocomposites (Figure 5.19A) show a ductile behavior with yield stress points, while plasticized nanocomposites (Figure 5.19B) have an elastomeric behavior with low elastic modulus values, without the presence of yield stress. In general, an improvement of the mechanical performance of the nanocomposites can be distinguished in comparison to the pure PVA/CS blend (Figure 5.20).
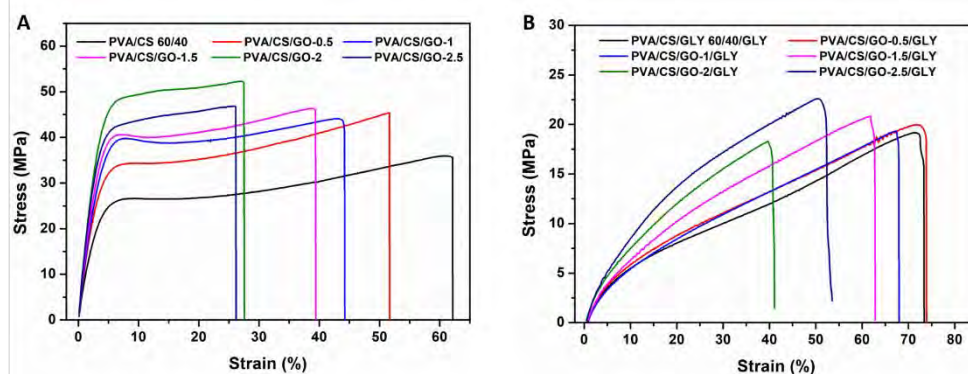
Figure 5.19. Stress–strain curves of (A) unplasticized and (B) glycerol plasticized PVA/CS/GO nanocomposites.

The GO presence in unplasticized and plasticized PVA/CS matrix leads to an increase in the elastic modulus, which in turn, is affected by the filler content (Figure 5.20A). In the case of unplasticized nanocomposites, the addition of a small amount of GO within the matrix has only a marginal effect, with 0.25 wt% Young's modulus increasing from 946 MPa to 1071 MPa. However, by adding 2.5 wt% the modulus increment is very significant, increasing by ≈50%. With glycerol, the addition of 0.25 wt% results in a low decrease in elastic modulus, but the rest of the compositions show higher values than the unloaded plasticized blend. The incorporation of 2.0 and 2.5 wt% has an important increase in modulus, 71 and 82%, respectively (Table 5.13). This trend is common and is attributed to the above-mentioned interaction between the PVA/CS matrix and GO, as well as to the good dispersion of GO, which leads to a more uniform distribution of stress and minimizes the presence of stress concentration centers [49]. Another important factor that can alter the tensile properties of a polymer is the change of crystallinity, but in this case the low reduction of the degree of crystallinity with the GO content (Table 5.11), has not affected the mechanical behavior.

For unplasticized PVA/CS/GO nanocomposites, the break stress also increases with GO content, but in glycerol plasticizers it remains constant, the variation is almost within the experimental error (Figure 5.20B). The addition of 2.0 wt% GO to unplasticized PVA/CS leads to the greatest increase in break stress, an increase of about 72%. The yield stress points of unplasticized nanocomposites

increase with GO content (Table 5.13), but with glycerol they could not be identified because the limits of the elastic behavior and the start of the plastic behavior could not be precisely differentiated by the MTS TestWorks 4 software.
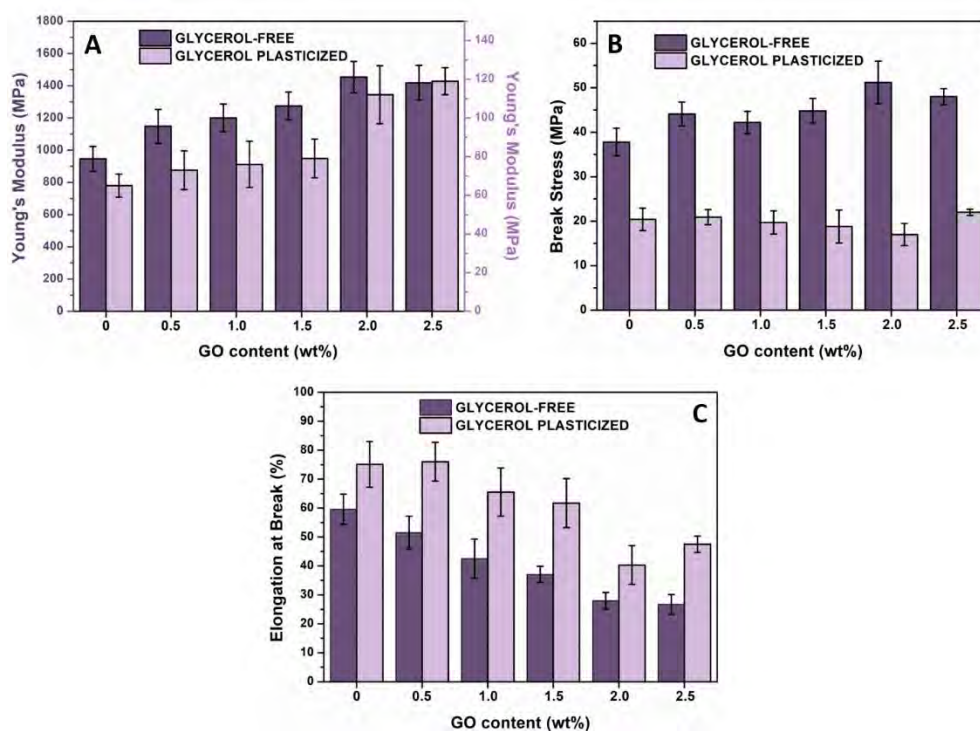
Figure 5.20. Mechanical properties of PVA/CS/GO nanocomposites: (A) Young's modulus, (B) break stress and (C) elongation at break.

The elongation at break of unplasticized and plasticized PVA decreases with the addition of GO (Figure 5.20D). From a content higher than 0.75 wt% the decrease in elongation is significant (Table 5.13). The lowest elongation at break is obtained for unplasticized films with 2.5 wt% of GO in comparison with unloaded PVA/CS blend, the reduction is about 55%. With glycerol the addition of GO affects to a lesser extent, giving the maximum decrease with 2.0 wt% GO ($\approx$46%). These results indicate that the addition of GO results in more brittle materials compared to the blend.

Table 5.13. Mechanical properties data of unplasticized and glycerol-plasticized PVA/CS/GO nanocomposites.

Sample	Young's modulus (MPa)	Yield stress (MPa)	Break Stress (MPa)	Elongation at break (%)
PVA/CS 60/40	946±78	28.6±1.9	37.8±3.1	59.6±5.2
PVA/CS/GO-0.25	1071±88	33.0±2.9	40.8±4.2	54.8±7.4
PVA/CS/GO-0.5	1148±105	35.9±3.0	44.1±2.7	51.5±5.7
PVA/CS/GO-0.75	1191±71	36.9±2.8	41.6±4.3	45.1±8.4
PVA/CS/GO-1	1200±86	37.4±2.8	42.2±2.5	42.5±6.8
PVA/CS/GO-1.5	1275±86	40.2±2.6	44.8±2.8	37.1±2.8
PVA/CS/GO-2	1454±97	49.2±5.3	51.2±4.9	28.0±2.8
PVA/CS/GO-2.5	1418±108	47.5±2.4	48.0±1.8	26.7±3.4
PVA/CS/GLY 60/40/GLY	65±6	-	20.4±2.5	75.1±7.9
PVA/CS/GO-0.25/GLY	52±6	-	17.3±0.9	72.9±2.9
PVA/CS/GO-0.5/GLY	73±10	-	20.9±1.7	76.9±6.7
PVA/CS/GO-0.75/GLY	77±8	-	18.7±1.6	62.5±4.8
PVA/CS/GO-1/GLY	76±12	-	19.7±2.6	65.5±8.3
PVA/CS/GO-1.5/GLY	79±10	-	18.8±3.7	61.7±8.5
PVA/CS/GO-2/GLY	112±15	-	17.0±2.5	40.3±6.7
PVA/CS/GO-2.5/GLY	119±7	-	22.0±0.7	47.5±2.8

Regarding PVA/CS/GS nanocomposites, the stress-strain curves of unplasticized and plasticized nanocomposites are shown in Figure 5.21, the mechanical properties data in Table 5.14 and their graphics in Figure 5.22. Based on stress-strain curves, unplasticized PVA/CS/GS films can be considered ductile materials, while plasticized nanocomposites, having no yield point and low Young's modulus as elastomeric type materials.

According to Chapter 4, the difference in mechanical properties data of the unplasticized and plasticized PVA/CS blend shown in Table 5.13 and Table 5.14 is attributed to the heat treatment (6 h at 60 °C) carried out to subject the blend to the same conditions as for the *in situ* GO reduction synthesis.
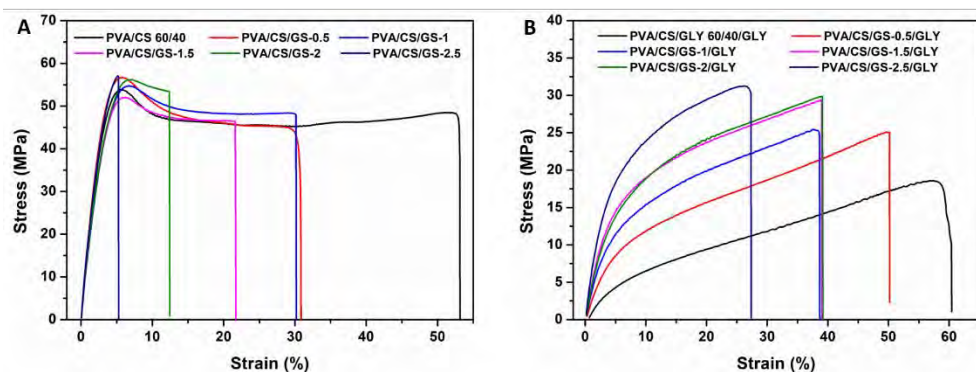
Figure 5.21. Stress–strain curves of (A) unplasticized and (B) glycerol plasticized PVA/CS/GS nanocomposites.
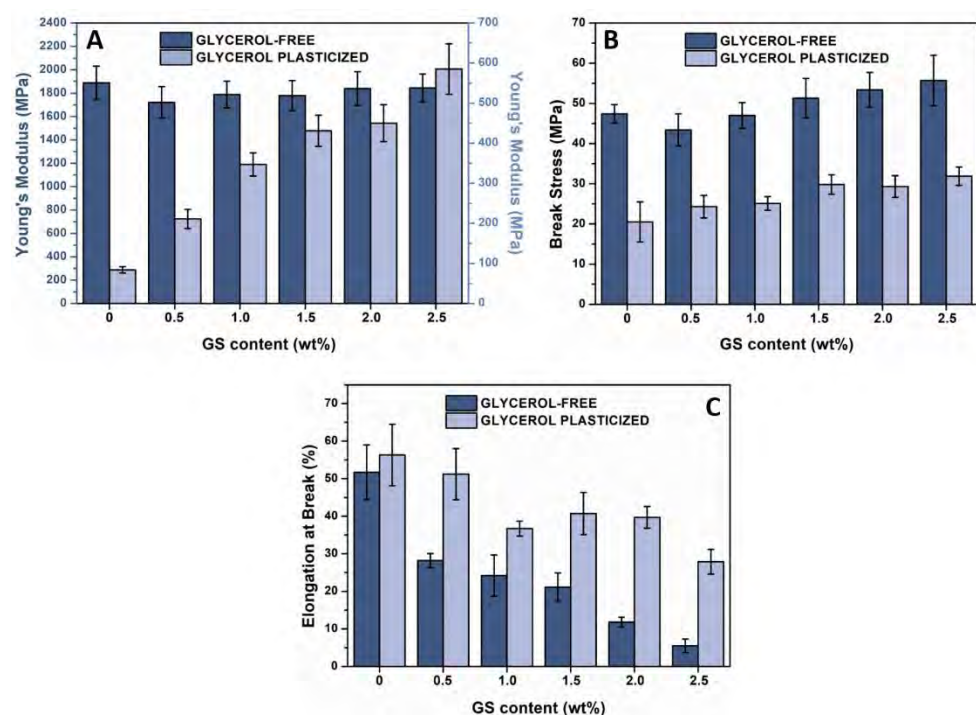
Figure 5.22. Mechanical properties of PVA/CS/GS nanocomposites: (A) Young's modulus, (B) break stress and (C) elongation at break.

The addition of GS in the PVA/CS 60/40 blend only has a significant improvement effect in the presence of plasticizer (Figure 5.22A). A 0.25 wt% GS content causes a notable reduction in the Young's modulus of unplasticized

nanocomposites (17%). The rest of the contents show a constant elastic modulus, but lower values than unloaded blend. In contrast, in the plasticized nanocomposites the modulus increases as the GS content increases, the maximum increase reached is ≈595% with a load of 2.5 wt% GS. Therefore, the reinforcing action of GS is stronger in the presence of glycerol due to the better interfacial contact of the filler with the PVA/CS matrix, which is in good agreement with the SEM and TEM results.

Table 5.14. Mechanical properties data of unplasticized and glycerol-plasticized PVA/CS/GS nanocomposites.

Sample	Young's modulus (MPa)	Yield stress (MPa)	Break Stress (MPa)	Elongation at break (%)
PVA/CS 60/40	1888±143	55.1±3.0	47.4±2.3	51.7±7.4
PVA/CS/GS-0.25	1574±144	49.7±5.7	45.6±2.8	44.9±8.5
PVA/CS/GS-0.5	1721±135	52.3±4.3	43.4±4.0	28.2±1.9
PVA/CS/GS-0.75	1717±158	48.3±3.1	43.1±3.3	30.2±5.8
PVA/CS/GS-1	1788±115	53.6±4.0	47.0±3.2	24.2±5.5
PVA/CS/GS-1.5	1779±129	55.7±4.7	51.3±4.9	21.2±3.8
PVA/CS/GS-2	1839±144	55.6±4.6	53.4±4.3	11.8±1.3
PVA/CS/GS-2.5	1845±119	57.5±6.8	55.7±6.3	5.5±1.8
PVA/CS/GLY 60/40/GLY	84±8	-	20.5±5.9	56.3±8.2
PVA/CS/GS-0.25/GLY	123±15	-	23.0±2.3	62.2±8.0
PVA/CS/GS-0.5/GLY	211±24	-	24.3±2.8	51.2±6.8
PVA/CS/GS-0.75/GLY	322±31	-	25.6±2.3	50.5±3.9
PVA/CS/GS-1/GLY	347±29	-	25.1±1.8	36.7±2.0
PVA/CS/GS-1.5/GLY	431±39	-	29.8±2.4	40.7±4.8
PVA/CS/GS-2/GLY	450±46	-	29.3±2.7	39.7±2.9
PVA/CS/GS-2.5/GLY	585±63	-	31.9±2.3	27.9±2.6

In unplasticized PVA/CS/GS nanocomposite films the yield stress is not altered by the presence of GS and the break stress is not significantly increased up to a content of 2.0 wt% (Table 5.14). However, in films with glycerol, apart from the fact that the yield point is not observed, the stress at break increases with the

GS content. A GS content higher than 1 wt% results in an increase of the break stress by at least 39%. The elongation at break of both unplasticized and plasticized PVA/CS/GS nanocomposite films decreases as the GS content increases (Figure 5.22D), achieving the highest reduction in the case of the unplasticized nanocomposites. Specifically, the elongation of the PVA/CS/GS-2.5 film is reduced by ≈89% and that of its glycerol-plasticized counterpart by ≈50%. This behavior indicates that the graphene increases the brittleness of the blend.

In order to observe the difference in the effect of the two graphene-based fillers examined, Figure 5.23 displays the rate change of mechanical properties for unplasticized and plasticized PVA/CS/GO and PVA/CS/GS nanocomposites (with a 60/40 PVA/CS ratio).
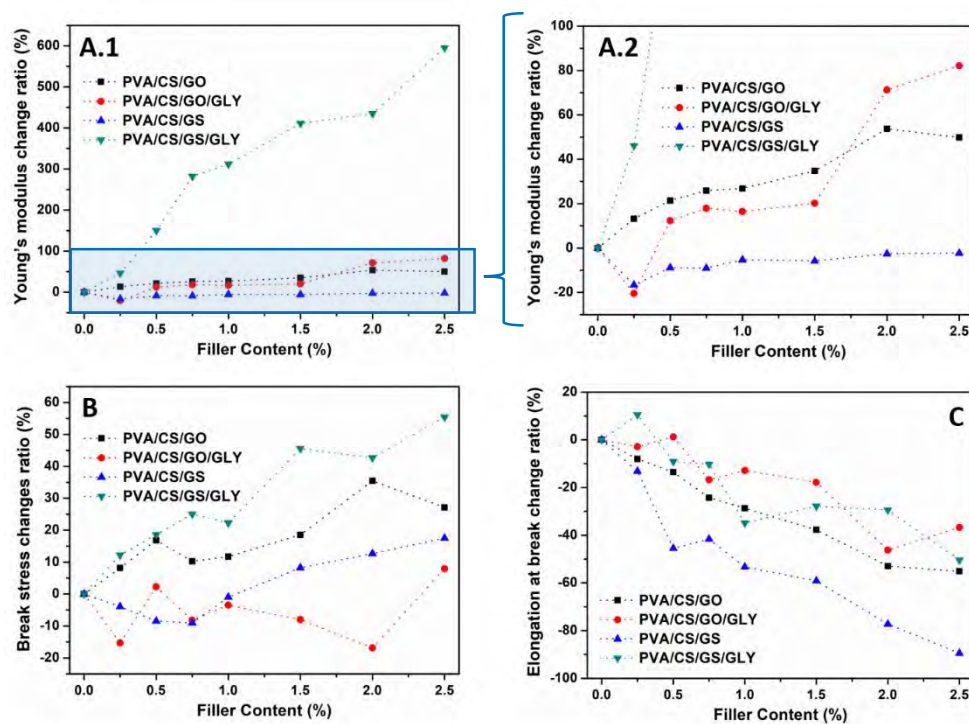
Figure 5.23. Change ratio of: (A.1 and A.2) Young's modulus, (B) break stress and (D) elongation at break for unplasticized and plasticized PVA/CS/GO and PVA/CS/GS nanocomposites.

From the above results, it can be concluded that the synergistic reinforcing effect is mainly observed in nanocomposites containing GS and glycerol. GO also improves the mechanical properties of the PVA/CS blend, but in a lesser extent. This difference can be attributed to a better dispersion of the filler in the polymer matrix due to the heat treatment needed for *in situ* GO reduction, which seems to ease and increase the interface interactions between filler, PVA and CS.

5.3.2.4. Water vapour permeability

The water vapor permeability (WVP) results of unplasticized and plasticized PVA/CS/GO nanocomposites with different filler contents are shown in Figure 5.24A, and their counterparts with GS as a nanofiller in the Figure 5.24B.

According to the permeability results of PVA/CS blends described above (Figure 5.10), the unplasticized nanocomposites show significant differences ($p < 0.05$) in permeability with respect to the plasticized ones. WVP values are higher because the hydroxyl groups of the glycerol interact with the polar groups present in the polymer structures, resulting in a higher diffusion of the water molecules.
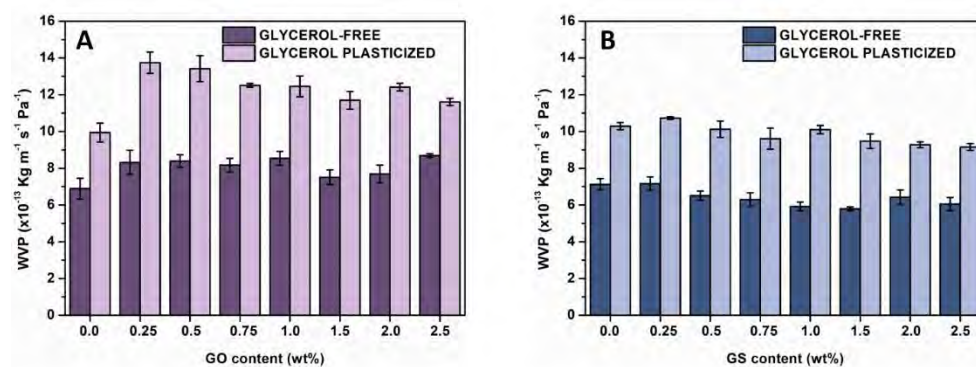
Figure 5.24. Water vapor permeability (WVP) for unplasticized and glycerol plasticized (A) PVA/CS/GO and (B) PVA/CS/GS nanocomposites.

The permeability of unplasticized PVA/CS 60/40 blend is increased by the addition of different GO contents, ranging from 0.5 wt% to 2.5 wt% (Figure 5.24A). However, the apparent increase is not linear with the increment in filler content. Furthermore, compared to the blend, the change observed is not

statistically significant ($p > 0.05$) with the addition of 1.5 and 2% GO, but with the rest of the contents there are statistically significant differences ($p < 0.05$). For the plasticized PVA/CS/GO nanocomposites, the addition of GO increases considerably the permeability (Figure 5.24B), obtaining statistically significant differences for all the studied compositions ($p < 0.05$). Specifically, the addition of 0.5 wt% GO to the plasticized PVA/CS blend increases the permeability value by 38.2%, but this modification is lower with increasing filler content.

According to the results of the DSC (Table 5.11) the increased permeability achieved by the addition of GO to the unplasticized and plasticized PVA/CS blends can be explained though the reduction of crystallinity. However, there is another effect to be considered that could explain the observed decrease as the GO content increases (contents higher than 0.25 wt%) in the case of plasticized nanocomposites. The presence of the sheets leads to a more tortuous path that water molecules require to permeate through film, leading to lower diffusion process and consequently, lower WVP.

In the case of unplasticized and plasticized PVA/CS/GS nanocomposites, compared to heated-PVA/CS 60/40 blends, in general the permeability seems to be less affected by the addition of GS (Figure 5.24B). In more detail, for unplasticized nanocomposites, the addition of 1, 1.5 or 2.5 wt% of GS results in a statistically significant decrease ($p < 0.05$) in permeability, whereas for plasticized ones only the addition of 2.5 wt% of GS shows a significant decrease. The rest of the GS compositions do not show any noticeable effect on the WVP values.

Comparing water vapor permeability values for GO and GS nanocomposites, it can be emphasized that the WVP is higher for PVA/CS/GO nanocomposites (Figure 5.24). This difference can be attributed to the fact that the functional oxygen groups of GO make it a hydrophilic filler that interacts with the hydroxyl and –NH groups of the blends, but also with water, facilitating the diffusion, and therefore permeability.

5.3.2.5. <u>Swelling and dissolution degree</u>

The water absorption capacity is an important factor to consider in hydrophilic polymers because the mechanical properties of the materials will be altered as a function of water retention. In addition, water absorption plays an important role for biomedical applications, especially for tissue engineering.

In this chapter, instead of providing the water absorption degree, swelling degree of the nanocomposites will be discussed, since the films, after being immersed in water for a while, were falling apart when trying to remove the excess of water or water surface. This behavior is ascribed to the fact that the two polymers that compose the nanocomposite matrix are not cross-linked (physical bonding). Therefore, keeping the films submerged for 24 h at room temperature, the water molecules penetrate the three-dimensional network formed by the PVA and the CS, breaking the interactions between the two polymers and weakening the structure, which makes it difficult to manipulate. For the swelling degree, the underwater nanocomposite pieces have been weighed without vigorously drying the film surfaces. Thus, in this analysis we are measuring the water strongly associated with the polymer matrix (through hydrogen bonds) and water with a high degree of mobility that is not affected by the polymer environment known as free water or non-integrated water [50].

Figure 5.25 displays the swelling ratio for unplasticized and plasticized pure PVA, pure CS, PVA/CS blend (with a 60/40 ratio) and PVA/CS/GO nanocomposites films, as well as the degree of dissolution of these films as a result of being immersed in water for a day at room temperature, calculated from equation I.7.2 described in Section I.7. of the Appendix I. According to Figure 5.25A, the use of glycerol prevents swelling of the films as a result of hydrogen interactions between polymers and plasticizer, leaving no hydroxyl or -NH free groups to interact and catch water molecules. Similarly, these interactions prevent to some extent the dissolution of the short polymer chains in most of the analyzed specimens (Figure 5.25B).

Unplasticized PVA/CS blend exhibits a higher swelling degree than the two pure polymers because PVA and CS are partially miscible and together result in an amorphous polymer structure. The 60/40 blend shows a decrease in crystallinity compared to pure PVA (Table 5.5), which makes the polymer chains

more available to interact with the water. However, the dissolution degree of the blend is between the values of the two pure polymers.
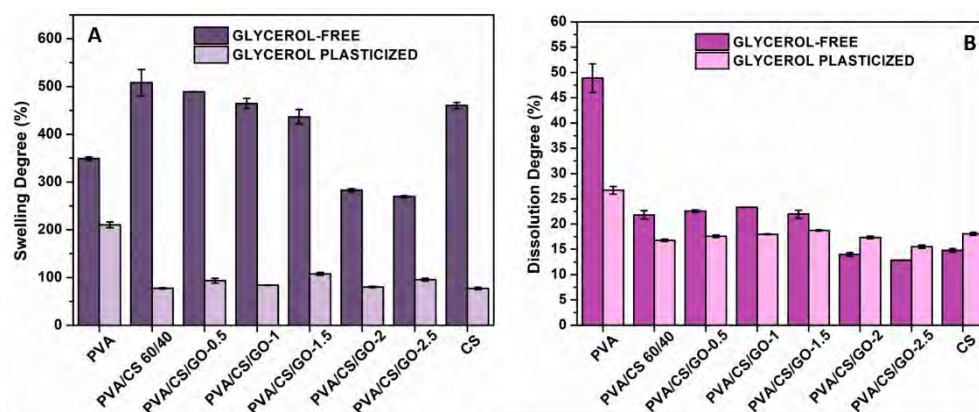
Figure 5.25. (A) Swelling ratio and (B) dissolution degree for PVA, CS, PVA/CS 60/40 blend and PVA/CS/GO nanocomposites films.

The presence of GO in the unplasticized blend affects the structure of the polymers network decreasing the swelling degree as the GO content increases. The addition of 2 and 2.5 wt% of GO leads to a lower swelling rate than pure polymers, and with respect to the unfilled blend, these contents decreases swelling degree by 44% and 47%, respectively. Therefore, the interactions of the filler with the polymers prevent them from catching water. In contrast, in plasticized films there are no noticeable differences between the samples with different GO contents. The addition of 20% glycerol (relative to the total weight of the polymer) hides the effect of the filler because the GO contents tested are at least ten times lower. Regarding the dissolution degree, as it was expected, PVA being a polymer that dissolves in water, is the film with the highest dissolution degree, since CS requires a slightly acid medium. The GO content does not have a remarkable effect, only in the unplasticized nanocomposites with 2.0 and 2.5 wt% it can be pointed out a decrease of 36 and 41%, respectively. For plasticized nanocomposites the dissolution degree is almost constant.

Following the same discussion, the effect of GS and plasticizer on swelling and dissolution degree of pure PVA, pure CS, PVA/CS blend and PVA/CS/GS nanocomposite films is presented in Figure 5.26. It should be noted that all

unfilled samples have been heat treated for 6 h at 60 °C according to the *in situ* GO reduction conditions.

In the case of the unplasticized blend, GS also alters the swelling and dissolution degrees, since only with a content of 0.5 wt% the swelling degree decreases by 74% and the dissolution degree by 61%. Consequently, the presence of the graphene sheets in the PVA/CS blend decreases the inclusion of water in the polymer network. However, no differences are observed between the different filler contents. When glycerol is present, GS does not seem to have any noticeable effect.
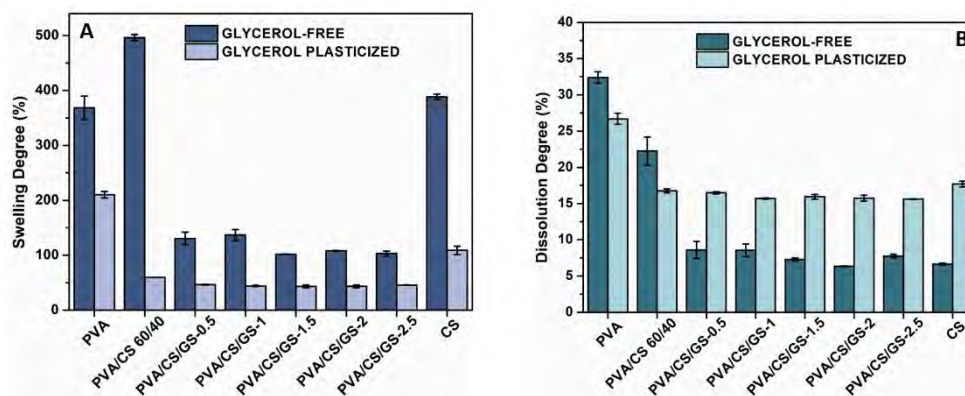
Figure 5.26. (A) Swelling ratio and (B) dissolution degree for PVA, CS, PVA/CS 60/40 blend and PVA/CS/GO nanocomposites films. *All samples have been 6 h at 60 °C.*

Comparing GO and GS results, it is worth noting that in the presence of GS, the PVA/CS blend absorbs somewhat less water and dissolves less polymer quantity. This difference could be explained by the large number of hydrophilic groups grafted onto the surface of the GO that promote water absorption and hence film swelling. These hydrophilic groups in the GS are less as a result of chemical reduction undertaken.

5.4. <u>Conclusions</u>

The blending of chitosan and PVA resulted in homogeneous films, which means a good interfacial adhesion and compatibility between the polymer matrices. The addition of contents above 20% PVA to CS caused an increase in the degree of crystallinity, as well as an improvement in the thermal stability of CS. Compared to pure PVA, the glass transition temperatures of unplasticized and glycerol-plasticized blends were higher for all compositions, due to the interactions of the polymers through hydrogen bonds. With regard to the mechanical properties, the addition of PVA to CS produced a decrease in the stiffness and brittleness of the material. Likewise, CS-rich compositions proved to be stronger and more resistant to fracture than the pure polymers as a result of the interactions and good compatibility of the polymer matrix. Despite the remarkable hydrophilic nature of CS, the presence of PVA resulted in a gradual decrease in WVP values. The blend with 60% PVA and 40% CS proved to be the most suitable composition for the incorporation of graphene-based fillers, due to the good mechanical and thermal properties shown.

In accordance with the previous chapters, GO was properly introduced into unplasticized and glycerol-plasticized PVA/CS 60/40 blend *via* solution casting method, while GS was incorporated by *in situ* reduction of GO with L-AA as the reducing agent. It was observed by SEM, TEM and X-ray diffraction that GO and GS were largely dispersed at the nanoscale in the PVA/CS matrix. Thermogravimetric measurements showed that the thermal stability of the PVA/CS blend was improved by the addition of both graphene-based fillers, due to high thermal stability of these nanofillers. However, this behavior was more prominent in the presence of plasticizer. Likewise, the content of fillers and the use of glycerol affected the thermal transitions (T_g, T_m and T_c) and the degree of crystallinity of the blend, achieving higher variations with GS. The mechanical properties of the blend were also altered with the addition of GO and GS, but to a different extent depending on the type of filler. In the case of GO, both with and without plasticizer, the elastic modulus was increased with the content, but with GS only the presence of plasticizer causes an improvement. However, GS with glycerol was shown to have a greater reinforcing effect than GO. In general, the addition of PVA to CS results in a decrease in the stiffness and brittleness of

chitosan and the incorporation of different GO and GS contents allows further adjustment of the final material properties. The water vapor permeability of the nanocomposites increased with the presence of glycerol and decreased slightly with the filler content. Also, due to the fact that GO is a hydrophilic filler, the WVP values for PVA/CS/GO nanocomposites were higher than for PVA/CS/GS. The values of swelling and dissolution degree measurements showed changes in PVA/CS 60/40 blend as a result of the addition of fillers. However, it was found that PVA/CS/GS nanocomposites absorbed slightly less water than GO-based ones due to the lower hydrophilic nature of GS.

5.5. <u>References</u>

[1] I. Khan, M. Mansha, M.A.J. Mazumder, Polymer blends, Polymers and Polymeric Composites: A Reference Series. (2018) 1-38.

[2] S. Thomas, R. Shanks, S. Chandran, Nanostructured polymer blends, William Andrew 2013.

[3] D. Paul, J. Barlow, A brief review of polymer blend technology, ACS Publications, 1979,.

[4] D.R. Paul, Polymer Blends Volume 1, Elsevier 2012.

[5] E. Manias, L.A. Utracki, Thermodynamics of polymer blends, Polymer blends handbook. (2014) 171-289.

[6] G. Kostorz, Phase transformations in materials, Wiley-vch Weinheim 2001.

[7] D. Paul, C. Vinson, C. Locke, The potential for reuse of plastics recovered from solid wastes, Polymer Engineering & Science. 12 (1972) 157-166.

[8] R. Muthuraj, M. Misra, A. Mohanty, Studies on mechanical, thermal, and morphological characteristics of biocomposites from biodegradable polymer blends and natural fibers, Biocomposites, Elsevier, 2015, pp. 93-140.

[9] B. Imre, B. Pukánszky, Compatibilization in bio-based and biodegradable polymer blends, European Polymer Journal. 49 (2013) 1215-1233.

[10] N. Zhang, Q. Wang, J. Ren, L. Wang, Preparation and properties of biodegradable poly (lactic acid)/poly (butylene adipate-co-terephthalate) blend with glycidyl methacrylate as reactive processing agent, J. Mater. Sci. 44 (2009) 250-256.

[11] M. Kumar, S. Mohanty, S. Nayak, M.R. Parvaiz, Effect of glycidyl methacrylate (GMA) on the thermal, mechanical and morphological property of biodegradable PLA/PBAT blend and its nanocomposites, Bioresour. Technol. 101 (2010) 8406-8415.

[12] K. Sirisinha, W. Somboon, Melt characteristics, mechanical, and thermal properties of blown film from modified blends of poly (butylene adipate-co-terephthalate) and poly (lactide), J Appl Polym Sci. 124 (2012) 4986-4992.

[13] S. Lin, W. Guo, C. Chen, J. Ma, B. Wang, Mechanical properties and morphology of biodegradable poly (lactic acid)/poly (butylene adipate-co-terephthalate) blends compatibilized by transesterification, Materials & Design (1980-2015). 36 (2012) 604-608.

[14] B.Y. Shin, Compatibilization of immiscible poly (lactic acid)/poly (ε-caprolactone) blend through electron-beam irradiation with the addition of a compatibilizing agent, Radiat. Phys. Chem. 83 (2013) 98-104.

[15] N. Liu, W. Baker, Reactive polymers for blend compatibilization, Advances in Polymer Technology: Journal of the Polymer Processing Institute. 11 (1992) 249-262.

[16] M.G.A. Vieira, M.A. da Silva, L.O. dos Santos, M.M. Beppu, Natural-based plasticizers and biopolymer films: A review, European Polymer Journal. 47 (2011) 254-263.

[17] E. Białecka-Florjańczyk, Z. Florjańczyk, Solubility of plasticizers, polymers and environmental pollution, Thermodynamics, Solubility and Environmental Issues, Elsevier, 2007, pp. 397-408.

[18] M. Rahman, C.S. Brazel, The plasticizer market: an assessment of traditional plasticizers and research trends to meet new challenges, Progress in polymer science. 29 (2004) 1223-1248.

[19] B. Shen, W. Zhai, C. Chen, D. Lu, J. Wang, W. Zheng, Melt blending in situ enhances the interaction between polystyrene and graphene through π–π stacking, ACS applied materials & interfaces. 3 (2011) 3103-3109.

[20] M.A. Ghalia, Y. Dahman, Advanced nanobiomaterials in tissue engineering: synthesis, properties, and applications, Nanobiomaterials in Soft Tissue Engineering, Elsevier, 2016, pp. 141-172.

[21] G.L. Rempel, H. Wang, Nitrile Rubber Latex Blends: Preparation, Characterization and Applications, Rubber Nano Blends, Springer, 2017, pp. 67-88.

[22] V. Epure, M. Griffon, E. Pollet, L. Avérous, Structure and properties of glycerol-plasticized chitosan obtained by mechanical kneading, Carbohydr. Polym. 83 (2011) 947-952.

[23] Z. Yu, B. Li, J. Chu, P. Zhang, Silica in situ enhanced PVA/chitosan biodegradable films for food packages, Carbohydr. Polym. 184 (2018) 214-220.

[24] X. Jiang, Y. Zhao, L. Hou, The effect of glycerol on properties of chitosan/poly (vinyl alcohol) films with $AlCl_3 \cdot 6H_2O$ aqueous solution as the solvent for chitosan, Carbohydr. Polym. 135 (2016) 191-198.

[25] L. Fan, H. Yang, J. Yang, M. Peng, J. Hu, Preparation and characterization of chitosan/gelatin/PVA hydrogel for wound dressings, Carbohydr. Polym. 146 (2016) 427-434.

[26] S. Chen, C. Tsao, C. Chang, Y. Lai, M. Wu, Z. Liu, et al., Synthesis and characterization of reinforced poly (ethylene glycol)/chitosan hydrogel as wound dressing materials, Macromolecular Materials and Engineering. 298 (2013) 429-438.

[27] H. Li, S. Chen, Y. Wang, Preparation and characterization of nanocomposites of polyvinyl alcohol/cellulose nanowhiskers/chitosan. Compos. Sci. Technol. 115 (2015) 60-65.

[28] E. Butnaru, C.N. Cheaburu, O. Yilmaz, G.M. Pricope, C. Vasile, Poly(vinyl alcohol)/chitosan/montmorillonite nanocomposites for food packaging applications: influence of montmorillonite content. High Perform. Polym. 28 (2016) 1124-1138.

[29] W.S. Khoo, H. Ismail, A. Ariffin, Tensile, swelling, and oxidative degradation properties of crosslinked polyvinyl alcohol/chitosan/halloysite nanotube composites. Int. J. Polym. Mater. Polym. Biomater. 62 (2013) 390-396.

[30] S. Wang, L. Shen, W. Zhang, Y. Tong, Preparation and mechanical properties of chitosan/carbon nanotubes composites, Biomacromolecules. 6 (2005) 3067-3072.

[31] R.E. Abou-Zeid, E.A. Hassan, F. Bettaieb, R. Khiari, M.L. Hassan, Use of cellulose and oxidized cellulose nanocrystals from olive stones in chitosan bionanocomposites, Journal of Nanomaterials. 2015 (2015).

[32] H.E. Assender, A.H. Windle, Crystallinity in poly(vinyl alcohol). 1. An X-ray diffraction study of atactic PVOH, Polymer. 39 (1998) 4295-4302.

[33] C. Chen, F. Wang, C. Mao, C. Yang, Studies of chitosan. I. Preparation and characterization of chitosan/poly(vinyl alcohol) blend films. J. Appl. Polym. Sci. 105 (2007) 1086-1092.

[34] Y. Wu, Y. Ying, Y. Liu, H. Zhang, J. Huang, Preparation of chitosan/poly vinyl alcohol films and their inhibition of biofilm formation against Pseudomonas aeruginosa PAO1, Int. J. Biol. Macromol. 118 (2018) 2131-2137.

[35] K. Lewandowska, Miscibility and thermal stability of poly (vinyl alcohol)/chitosan mixtures, Thermochimica Acta. 493 (2009) 42-48.

[36] I. Quijada-Garrido, V. Iglesias-González, J. Mazón-Arechederra, J. Barrales-Rienda, The role played by the interactions of small molecules with chitosan and their transition temperatures. Glass-forming liquids: 1, 2, 3-Propantriol (glycerol), Carbohydr. Polym. 68 (2007) 173-186.

[37] C. Chen, F. Wang, C. Mao, W. Liao, C. Hsieh, Studies of chitosan: II. Preparation and characterization of chitosan/poly (vinyl alcohol)/gelatin ternary blend films, Int. J. Biol. Macromol. 43 (2008) 37-42.

[38] J. Bonilla, E. Fortunati, L. Atares, A. Chiralt, J.M. Kenny, Physical, structural and antimicrobial properties of poly vinyl alcohol-chitosan biodegradable films, Food Hydrocoll. 35 (2014) 463-470.

[39] H. Wu, Y. Wan, X. Cao, Q. Wu, Interlocked chitosan/poly (dl-lactide) blends, Mater Lett. 62 (2008) 330-334.

[40] K. Sakurai, T. Maegawa, T. Takahashi, Glass transition temperature of chitosan and miscibility of chitosan/poly (N-vinyl pyrrolidone) blends, Polymer. 41 (2000) 7051-7056.

[41] F. Kittur, K.H. Prashanth, K.U. Sankar, R. Tharanathan, Characterization of chitin, chitosan and their carboxymethyl derivatives by differential scanning calorimetry, Carbohydr. Polym. 49 (2002) 185-193.

[42] C.d.T. Neto, J.A. Giacometti, A.E. Job, F.C. Ferreira, J.L.C. Fonseca, M.R. Pereira, Thermal analysis of chitosan based networks, Carbohydr. Polym. 62 (2005) 97-103.

[43] S. Tripathi, G. Mehrotra, P. Dutta, Physicochemical and bioactivity of cross-linked chitosan–PVA film for food packaging applications, Int. J. Biol. Macromol. 45 (2009) 372-376.

[44] H. Jafari, M. Pirouzifard, M.A. Khaledabad, H. Almasi, Effect of chitin nanofiber on the morphological and physical properties of chitosan/silver nanoparticle bionanocomposite films, Int. J. Biol. Macromol. 92 (2016) 461-466.

[45] J. Ren, S. Wang, C. Gao, X. Chen, W. Li, F. Peng, TiO 2-containing PVA/xylan composite films with enhanced mechanical properties, high hydrophobicity and UV shielding performance, Cellulose. 22 (2015) 593-602.

[46] P. Campa-Siqueiros, T.J. Madera-Santana, J.F. Ayala-Zavala, J. López-Cervantes, M.M. Castillo-Ortega, P.J. Herrera-Franco, Nanofibers of gelatin and polivinyl-alcohol-chitosan for wound dressing application: fabrication and characterization, Polímeros. 30 (2020).

[47] P. Fernandez-Saiz, M. Ocio, J. Lagaron, Antibacterial chitosan-based blends with ethylene-vinyl alcohol copolymer, Carbohydr. Polym. 80 (2010) 874-884.

[48] Y. Cao, J. Feng, P. Wu, Preparation of organically dispersible graphene nanosheet powders through a lyophilization method and their poly (lactic acid) composites, Carbon. 48 (2010) 3834-3839.

[49] X. Yang, Y. Tu, L. Li, S. Shang, X. Tao, Well-dispersed chitosan/graphene oxide nanocomposites, ACS applied materials & interfaces. 2 (2010) 1707-1713.

[50] P. Allen, D. Bennett, D. Williams, Water in methacrylates—I. Sorption and desorption properties of poly (2-hydroxyethyl methacrylate-co-glycol dimethacrylate) networks, European polymer journal. 28 (1992) 347-352.

CHAPTER 6

GENERAL CONCLUSIONS

6.1. <u>General Conclusions</u>

The main objective of this thesis was the development of new bionanocomposites with good thermal, mechanical and permeability properties, as well as antimicrobial capabilities for their potential application in the biomedical field and the food packaging industry. For this purpose, different derivatives based on graphene were synthesized and used as a dispersed phase in the nanocomposites. The effect of the addition of the fillers on the properties of biodegradable polymers such as PVA and chitosan and their blend was investigated. In addition, different strategies were developed to produce the nanocomposites. The two methods of synthesis made it possible to evaluate the differences in the dispersion of the fillers in the polymer matrix, which in turn is closely related to the final properties of the nanocomposite films. A summary of the most relevant conclusions obtained throughout this thesis is presented below:

i. The chemical reduction of the graphene oxide, previously synthesized by the modified Hummers' method, was achieved successfully employing L-ascorbic acid as the green reducer. Likewise, this agent in combination with $AgNO_3$ was suitable to synthesize GO-AgNPs nanohybrids through a one-step approach. The results showed a uniform distribution of AgNPs anchored in the partially reduced GO surface and also that, under the tested synthesis conditions, the lower the concentration of the silver precursor and the lower temperature, the smaller the size of the silver nanoparticles.

ii. GO and GS dispersions showed lack of antimicrobial activity against *E. coli, P. aeruginosa, S. aureus* and *C. albicans,* while GO-AgNPs nanohybrids displayed dose- and time-dependent antimicrobial effect against all four microorganisms. The highest antimicrobial activity was achieved against *C. albicans* and *S. aureus.*

iii. The solution casting method resulted to be an effective procedure to obtain a homogeneous dispersion of GO in the different PVA- and CS-based nanocomposites, as well as in the blends. However, GS nanocomposites with a homogeneous dispersion were successfully synthesized through *in situ* reduction of the graphene oxide sheets in

the presence of the polymer matrix. Regarding PVA nanocomposites containing GO-AgNPs, two different strategies were developed, *in situ* and *ex situ* methods, which regarded good results.

iv. The good dispersion and strong interfacial adhesion of the GO and GS with the chitosan matrix significantly improved the thermal and mechanical properties of the CS, achieving a more outstanding effect with glycerol. In addition, changes in the water vapor permeability of CS nanocomposites were detected in the presence of the plasticizer, but not with the GO and GS content.

v. The antibacterial activity of CS against *E. coli* decreased with the storage period.

vi. The results of the structural and morphological characterization revealed a good dispersion for GO, GS and GO-AgNPs in PVA, with the exception of the *ex situ* PVA/GS1 nanocomposite due to the lack of bonding between GS and PVA. Overall, the exfoliated structure of the PVA nanocomposites resulted in increased thermal stability, mechanical properties and water resistance.

vii. The incorporation of GO into PVA did not prevent bacterial growth. In contrast, PVA films filled with GO-AgNPs showed antibacterial effect against *E. coli* and *S. aureus*, being more effective (at the same content, 2 wt%) in the case of the *in situ* method. Moreover, the higher the silver salt concentration the greater the long-term antibacterial efficiency. The direct contact of the bacteria with the composite films led to a greater bactericidal effect than the contact with the leachates from those films. The bacterial inactivation was higher for *S. aureus*.

viii. The good interfacial adhesion and compatibility between PVA and CS resulted in a partially miscible blends. The addition of PVA to CS resulted in a decrease in the stiffness and brittleness of chitosan, being the composition of PVA/CS 60/40 the most suitable for the incorporation of the different reinforcements.

ix. The different contents of GO and GS improved the thermal stability of the blend, but the nanofillers effect was more notorious in the presence of glycerol. As far as mechanical properties are concerned, these were affected depending on the type and content of nanofillers. The hydrophilic character of GO led to a higher WVP for PVA/CS/GO nanocomposites than for those containing GS, as well as a slightly higher water absorption.

x. All synthesized nanofillers had an effective reinforcing effect on the polymeric matrices studied, but GO also proved to be an excellent platform to support and stabilize the silver nanoparticles, and act as a synergistic agent in the antibacterial activity of AgNPs.

6.2. <u>Publications from this thesis</u>

i. Cobos, M., González, B., Fernández, M. J., & Fernández, M. D. Chitosan–graphene oxide nanocomposites: Effect of graphene oxide nanosheets and glycerol plasticizer on thermal and mechanical properties. *Journal of Applied Polymer Science*, **2017,** *134*(30), 45092.

ii. Cobos, M., González, B., Fernández, M. J., & Fernández, M. D. Study on the effect of graphene and glycerol plasticizer on the properties of chitosan-graphene nanocomposites via in situ green chemical reduction of graphene oxide. *International journal of biological macromolecules*, **2018**, *114*, 599-613.

iii. Cobos, M., Fernández, M. J., & Fernández, M. D. Graphene based poly(vinyl alcohol) nanocomposites prepared by *in situ* green reduction of graphene oxide by ascorbic acid: Influence of graphene content and glycerol plasticizer on properties. *Nanomaterials*, **2018**, *8*(12), 1013.

iv. Cobos, M., De-La-Pinta, I., Quindós, G., Fernández, M. J., & Fernández, M. D. One-step eco-friendly synthesized silver-graphene oxide/poly(vinyl alcohol) antibacterial nanocomposites. *Carbon*, **2019**, *150*, 101-116.

v. Cobos, M., De-La-Pinta, I., Quindós, G., Fernández, M. J., & Fernández, M. D. Graphene oxide–silver nanoparticle nanohybrids: Synthesis, characterization, and antimicrobial properties. *Nanomaterials*, **2020**, *10*(2), 376.

vi. Cobos, M., De-La-Pinta, I., Quindós, G., Fernández, M. J., & Fernández, M. D. Synthesis, Physical, Mechanical and Antibacterial Properties of Nanocomposites Based on Poly(vinyl alcohol)/Graphene Oxide–Silver Nanoparticles. *Polymers*, **2020**, *12*(3), 723.

6.3. Other publications

i. Fernández, M. J., Fernández, M. D., & Cobos, M. Synthesis, characterization and properties of telechelic hybrid biodegradable polymers containing polyhedral oligomeric silsesquioxane (POSS). *RSC Advances*, **2014**, *4*(41), 21435-21449.

ii. Fernández, M. D., Fernández, M. J., & Cobos, M. Effect of polyhedral oligomeric silsesquioxane (POSS) derivative on the morphology, thermal, mechanical and surface properties of poly(lactic acid)-based nanocomposites. *Journal of materials science*, **2016**, *51*(7), 3628-3642.

iii. Mun, S. C., Park, J. J., Park, Y. T., Lee, S. W., Cobos, M., Ye, S. J., Macosko, C. W & Park, O. O. High electrical conductivity and oxygen barrier property of polymer-stabilized graphene thin films. *Carbon*, **2017**, *125*, 492-499.

iv. Llamas-Arriba, M. G., Puertas, A. I., Prieto, A., López, P., Cobos, M., Miranda, J. I., ... & Dueñas, M. T. Characterization of dextrans produced by *Lactobacillus mali* CUPV271 and *Leuconostoc carnosum* CUPV411. *Food Hydrocolloids*, **2019**, *89*, 613-622.

v. Cobos, M., Ramos, J. R., Guzmán, D. J., Fernández, M. D., & Fernández, M. J. PCL/POSS nanocomposites: Effect of POSS derivative and preparation method on morphology and properties. *Polymers*, **2019**, *11*(1), 33.

vi. Mun, S. C., Kim, M. J., Cobos, M., Gu, L., & Macosko, C. W. Strategies for interfacial localization of graphene/polyethylene-based cocontinuous blends for electrical percolation. *AIChE Journal*, **2019**, *65*(6), e16579.

vii. De-la-Pinta, I., Cobos, M., Ibarretxe, J., Montoya, E., Eraso, E., Guraya, T., & Quindós, G. Effect of biomaterials hydrophobicity and roughness on biofilm development. *Journal of Materials Science: Materials in Medicine*, **2019**, *30*(7), 77.

ANNEX A

SELECTIVE LOCALIZATION OF GRAPHENE IN POLYETHYLENE/POLYPROPYLENE BLENDS

This section details the scientific and technical activities realized during the three-month stay at the University of Minnesota, USA. The research was held in the Department of Chemical Engineering and Materials Science under the supervision and guidance of Professor Christopher W. Macosko, and help and support of Dr. Sung Cik Mun. The principal aim of the study conducted was to improve electrical properties of polyethylene (PE)/graphene nanocomposites. Polypropylene (PP) was used as a secondary matrix to induce co-continuous morphology with PE. Selective localization of graphene in the blend was intended in order to increase electrical conductivity, thereby lowering percolation threshold. It was also considered the functionalization of graphene oxide (GO) with polyethylene-block-polyethylene oxide (PE-b-PEO) diblock copolymer followed by thermal reduction to attempt a better dispersion in PE matrix.

The results shown in this section are part of the publication entitled "Strategies for interfacial localization of graphene/polyethylene-based cocontinuous blends for electrical percolation" in the AlChE Journal in 2019.

INDEX

A.1. <u>Introduction</u>

The field of nanoscience has grown up over the last twenty years, and the importance for nanotechnology will increase as miniaturization becomes more important in areas such as computing, sensors, biomedical and many other applications. Advancements in these disciplines depend largely on the ability to synthesize nanoparticles of various materials, sizes and shapes, as well as to assemble them efficiently into complex architectures to achieve new properties.

According to the chapters developed above, research on polymer nanocomposites has made it possible to improve the properties of polymers. The discovery of graphene, with its combination of outstanding physical properties and its ability to disperse into various polymer matrices, has created a new class of polymer nanocomposites with many possible applications. For instance, in electronic applications, conductive polymer nanocomposites have been widely developed for protection against electrostatic discharges (ESD) and shielding against electromagnetic interference. However, a high concentration of conventional conductive carbon fillers is required to achieve electrical percolation, indicating the formation of an interconnected network of fillers for electrical conduction through the polymer matrix. For example, carbon black percolation thresholds are around 5 and 10 vol% in HDPE and PMMA, respectively [1]. These high charges are often accompanied by high material costs, poor processability, optical opacity, and detachment of fillers from the surface of the products. Based on the results found in the literature, the percolation thresholds of polymer/graphene nanocomposites are below 3 wt%, lower than those of carbon black nanocomposites [2-12]. In addition to the high aspect ratio of graphene, the threshold of percolation can be further reduced by modifying the surface of the graphene or the polymer matrix which minimizes the interfacial energy between them and, at the same time, it prevents the agglomeration of the graphene improving the dispersion in a polymer matrix.

The dissolution of the polymer in the solvent and later the addition of graphene, often using sonication, or the polymerization of monomers in the presence of graphene, has made it possible to reach the lowest thresholds of electrical percolation. The fusion blend generally leads to higher percolation values, however, it is much more economical. Attempts have been made to

localize graphene in one phase [13,14] or at the interface [15,16] of polymer blends to increase the effective concentration of the conductive fillers, thus improving the electrical conductivity and reducing the percolation threshold. The improvement by localization in one phase has been explained by the concept of so-called double percolation [13,14].

A.2. Objectives

The aim of the research performed with Dr. Sung Cik Mun and under the supervision of Prof. Macosko was focused on the manufacture of electrically conductive Polyethylene (PE) -based co-continuous polymer blends by localizing graphene at the blend interface.

PE is one of the most common plastics, but electrically conductive PE has not been attained at very low filler concentrations by melt compounding which is preferred in regard of mass production. Co-continuous low density polyethylene/ polypropylene (LDPE/PP) blends were chosen as matrices in our first attempt. The use of functionalized graphene oxide (GO) with polyethylene-*block*-polyethylene oxide (PE-*b*-PEO) diblock copolymer and thermal reduction were also suggested as a strategy to obtain a better dispersion in the PE matrix.

A.3. Experimental section
A.3.1. Materials

LLDPE (EngageTM 8200), PP (two isotactic PPs: PP6262 and HD915CF) and HDPE (HD KF 251A) were provided by Dow Chemical, ExxonMobil, Borealis and JREX, respectively. Few-layer graphene (N002-PDR, lateral dimension < 10 μm, thickness ~ 1 nm) powder was purchased from Angstron Materials. Dimethyl formamide (DMF, Sigma-Aldrich) and other solvents were reagent grade.

A.3.2. Complex viscosity

Complex viscosity of several PEs and PPs were measured with a rotational rheometer (ARES, Rheometric Scientific) under small amplitude oscillatory shear within a linear viscoelastic regime. A dynamic frequency sweep test was performed at 180, 200, and 220 °C in the range of 0.1 ~ 100 rad/s in parallel plate geometry with a diameter of 25 mm and a gap of ~1 mm.

A.3.3. Preparation of Polymer/graphene Nanocomposites

All nanocomposites were prepared by melt compounding in DSM Xplore Microcompounder at 180 °C with a rotational speed of 200 rpm for 10 min after feeding materials at 50 rpm for 15 min. A PE/PP blend of 50/50 weight ratio or PE resin only was used as a matrix, and nearly pure graphene (N002-PDR, oxygen content < 2.5%, Angstron Materials), GO and functionalized GO (FGO, functionalized with PE-b-PEG diblock copolymer, M_n: 2275 g/mol, ethylene oxide content 80%) were used as conductive nanofillers. An illustration of immiscible PE/PP blends and graphene derivatives is shown in Figure A.1.
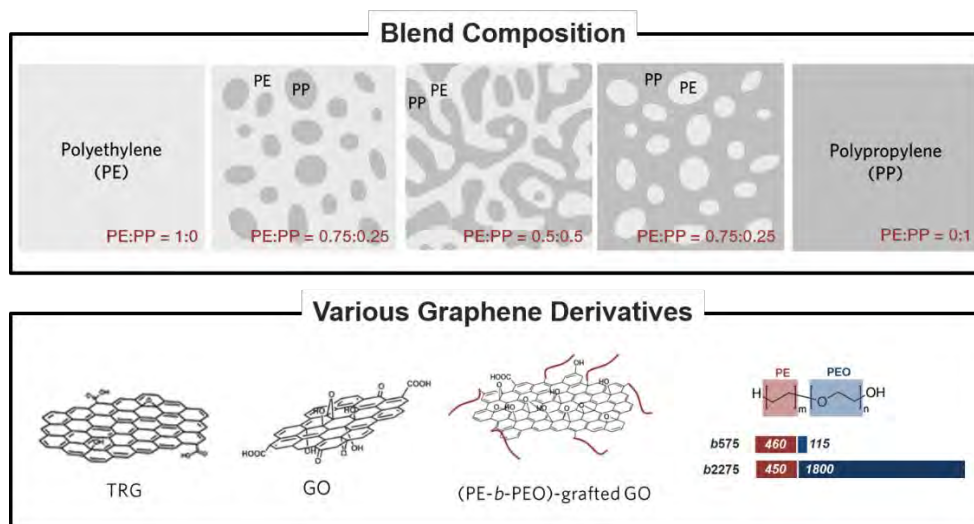
Figure A.1. Scheme of the blend morphology on the preferential location of graphene in immiscible PE/PP blends (*illustration created by Dr. Sung Cik Mun*).

A.3.4. Compression molding and thermal annealing

The nanocomposites were compression molded between two glass substrates with a polyimide spacer at 230 °C for 5 min in a vacuum oven. The typical thickness of compression-molded films is 200 - 500 μm. Some films were thermally annealed at 230 °C for 2 h in an oven without pressure.

A.3.5. Electrical properties: Two Probe Method

Copper foil tape (3M™ 1181) was attached on either side of compression-molded specimens as an electrode. The current-voltage (I-V) curve was measured by using the two-probe method with a manual probe station along with a source measure unit (2400 SourceMeter, Keithely) in voltage-sweep mode from -20 to 20 V with intervals of 1 V. The resistance (R) was obtained from the average slope of I-V curve and then converted to the electrical conductivity (σ) using the following equation (Eqn. A.1).

$$\sigma = \rho^{-1} = \left(R \frac{A}{t} \right)^{-1} = \left\{ \left(\frac{V}{I} \right) \left(\frac{A}{t} \right) \right\}^{-1} = \left(\frac{I}{V} \right) \left(\frac{t}{A} \right) \qquad \text{(Eqn. A.1)}$$

where ρ is the electrical resistivity, A and t are the cross-sectional area and the length of specimen, respectively.

A.4. Results and discussion

A.4.1. Complex viscosity and morphology of PE/PP blends

The complex viscosity is an important parameter to characterize the rheological properties of a material. The real part of the complex viscosity is an energy dissipation term similar to the imaginary part of the complex modulus. The complex viscosity of linear low density PE (Engage 8200, Dow Chemical), high density PE (BB2588, Borouge) and two isotactic PPs (PP6262, ExxonMobil and HD915CF, Borealis) at 180, 200 and 220 °C are shown in Figure A.2. The shear rate during processing at melt compounder was estimated at 79.1 1/s. It is assumed that Cox-Merz rule works for these polymer melts. Taking this into account, Engage 8200 and PP6262 (PE and PP) were selected to induce co-continuous morphology at 180 °C because of their similar viscosity at those conditions.
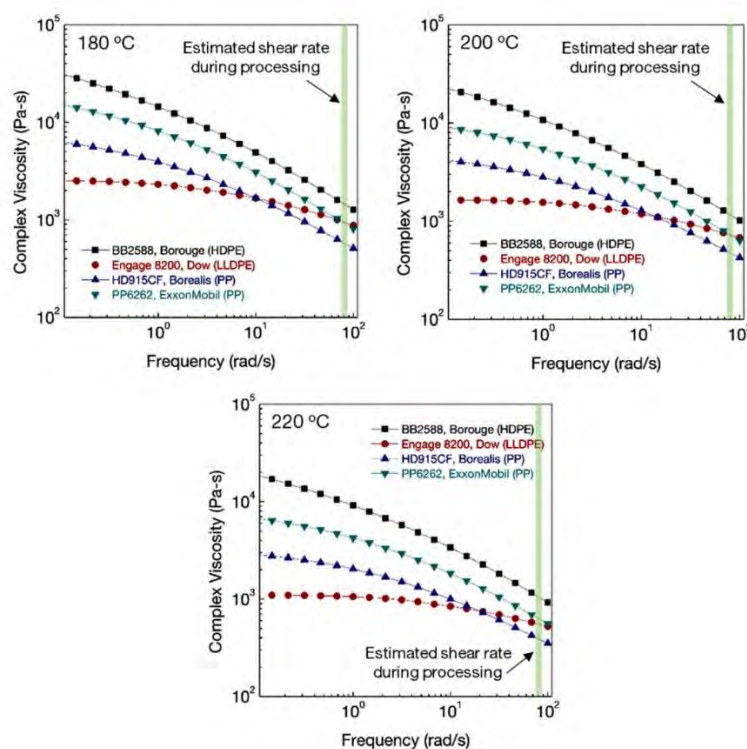
Figure A.2. Complex viscosity of PEs and PPs at 180, 200 and 220 °C.

Figure A.3 clearly shows that PE/PP blend (50/50, by weight) has co-continuous morphology, whereas PE/PP blend (25/75) presents sea-island morphology. Therefore, the blend ratio of 50/50 was fixed for this study.
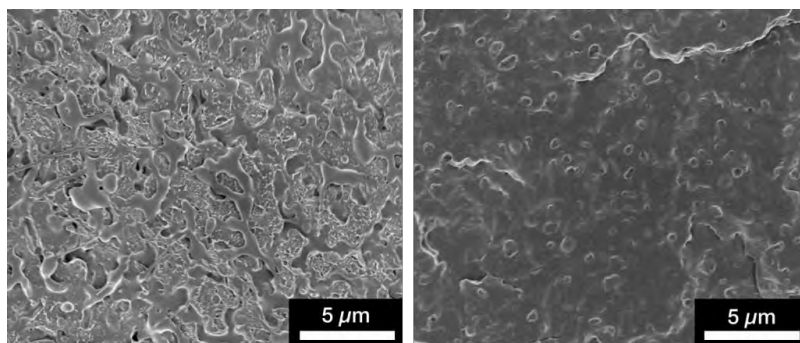
Figure A.3. SEM images of PE/PP blends: (a) PE/PP (50/50) and (b) (25/75) blends.

A.4.2. Selective localization of nanofillers

When conductive fillers are selectively located in one polymer component or at the interface of a co-continuous structure, it could result in a much lower electrical percolation threshold than that of the corresponding single polymer-based nanocomposites. According to a work done by Macoskos' group, reduced graphene oxide (rGO) was preferentially localized at the interface of co-continuous PLA/PS blends, which reduced the percolation threshold from ⁻0.5 wt% (PLA/rGO) to ⁻0.05 wt% (PLA/PS/rGO) [15,16]. This localization of nanofillers at the interface is regarded as the ideal scenario to reach the lowest possible electrical percolation threshold.
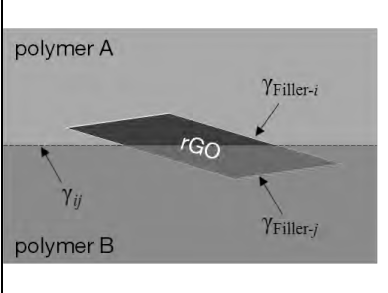
The selective localization of the conductive fillers is determined by thermodynamic and/or kinetic factors. The former involves the systems' tendency to minimize its free energy which can be evaluated by the generally valid principle of wetting coefficient, the latter concerning the transport/migration of fillers has been proposed by a combination of particle diffusion in one polymer component and shear-induced collisions of the fillers with interface, which relates to the mixing sequence, viscosity ratio, and interplay between polymer and fillers etc.

A wetting coefficient gives an estimation of nanofillers' distribution in polymer blends at thermodynamic equilibrium. Here, graphene used in this study was assumed to have the same surface tension as rGO. Wu's harmonic mean average equation (Eqn. A.3) was used to calculate interfacial tension (γ_{ij}) between two components (i and j) from surface tensions of each component (Table A.1).

$$\gamma_{ij} = \gamma_i + \gamma_j - F \qquad \text{(Eqn. A.2)}$$

$$F = 4\left\{ \frac{\gamma_i^d \gamma_j^d}{\gamma_i^d + \gamma_j^d} + \frac{\gamma_i^p \gamma_j^p}{\gamma_i^p + \gamma_j^p} \right\} \qquad \text{(Eqn. A.3)}$$

Table A.1. Surface tension of polymers and nanofillers at 180 °C. (unit: mN/m).

Material	γ	γ^d	γ^p
PE[†]	26.5	26.5	0
PP[†]	20.8	20.4	0.4
GO[‡]	122.0	70.8	51.2
rGO[‡]	100.9	93.8	7.1

Polarities (γ^p/γ) are independent of temperature; $-d\gamma/dT$ was assumed to be 0.1 mN/m-K for GO and rGO [17,18].

From Young's equation (Eqn. A.4), wetting coefficient (ω_a) was obtained from interfacial tensions (γ_{ij}) between two components (i and j). When $\omega_a > 1$ or $\omega_a < -1$, nanofillers are distributed within the PE or PP phase, respectively. When $-1 < \omega_a < 1$, they are localized at the interface.

$$\omega_a = \frac{\gamma_{\text{Filler-PP}} - \gamma_{\text{Filler-PE}}}{\gamma_{\text{PE-PP}}} \qquad \text{(Eqn. A.4)}$$

ω_a of PE/PP/GO and PE/PP/graphene nanocomposites is 5.34 and 6.93, respectively (Table A.2). Graphene is predicted to be distributed in the PE phase only, which is presumably consistent with electrical conductivity results in the following section. In these cases, where conductive fillers are located in one component, the concept of double percolation is applicable to explain the decreased electrical percolation threshold in polymer blends.

Table A.2. Interfacial tension between polymers and nanofillers at 180 °C. (unit: mN/m).

γ_{ij}	GO	rGO
$\gamma_{Filler-PE}$	71.4	44.75
$\gamma_{Filler-PP}$	77.9	53.16
γ_{PE-PP}	1.19	
ω_a	5.34	6.93
prediction	PE phase	PE phase

A.4.3. Electrical conductivity

Figure A.4a shows that electrical conductivity of PE/PP/graphene was slightly better than that of PE/graphene. Accordingly, electrical percolation threshold was reduced from 2 – 3 wt% (PE/graphene) to 1 – 2 wt% (PE/PP/graphene). This result implies that graphene was preferentially located in the PE phase. We conducted thermal annealing at 230 °C for PE/graphene and PE/PP/graphene nanocomposites. Thermal annealing of nanocomposites does not reduced graphene further, but rather it makes nanofillers rearranged and lead to thermodynamic equilibrium. Electrical conductivity of both nanocomposites was improved after 2 h annealing at 230 °C (Figure A.4b). It should be noted that PE/PP/graphene nanocomposite shows much enhanced electrical conductivity and lower percolation threshold (< 0.5 wt%) after thermal annealing. It is probably due to that kinetically trapped graphene which is still in the PP phase migrated into the PE phase, which increases the effective filler concentration with respect to the PE phase, accordingly.
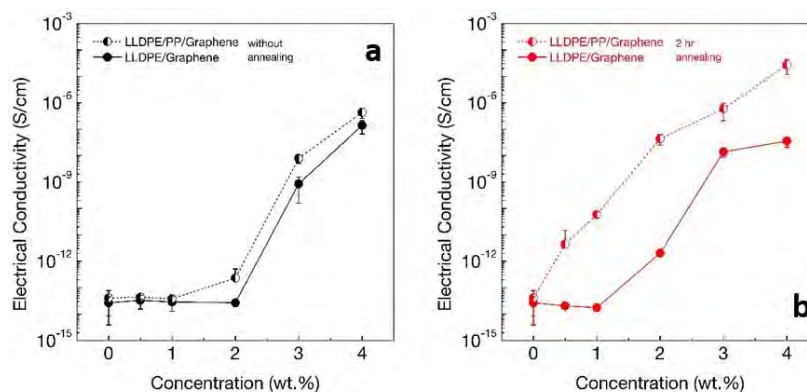
Figure A.4. Electrical conductivity of PE/graphene and PE/PP/graphene nanocomposites (a) before and (b) after 2 h thermal annealing at 230 ℃.

The effect of functionalization of graphene oxide on electrical properties was also analyzed. It was previously reported that GO could be reduced by thermal annealing of polymer/GO nanocomposites. However, it was observed no improvement in electrical conductivity of PE/PP/GO and PE/PP/FGO nanocomposites after 2 h annealing at 230 ℃ (Figure A.5a and b). GO and FGO were not fully reduced enough to recover its graphitic sp^2-hybridized carbons as much as graphene used in this study. It was suggested another strategy that included modifying graphene instead of GO. However, because of limited time, this part was not conducted during this term.
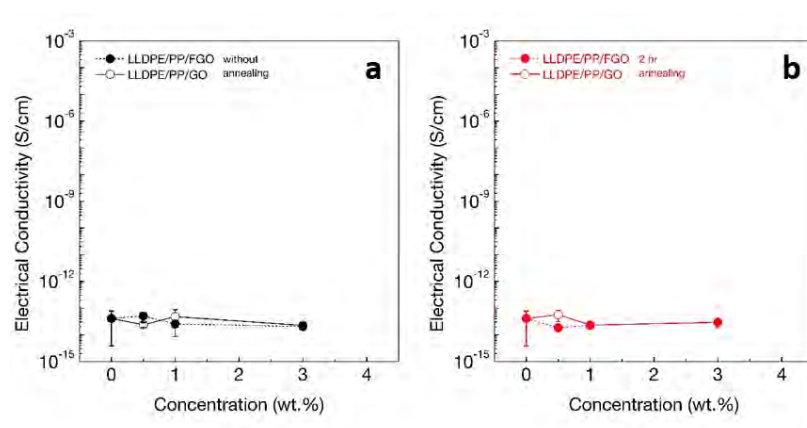
Figure A.5. Electrical conductivity of PE/PP/GO and PE/PP/FGO nanocomposites (a) before and (b) after 2 h thermal annealing at 230 ℃.

A.5. <u>Conclusions</u>

In this study, the effect of the preferential location of graphene in one phase of polymer blend (double percolation) on the electrical properties of the nanocomposites was investigated. It is worth noting that thermal annealing under static condition (no external mechanical force) after processing could lead closer to the ideal thermodynamic equilibrium. We postulate that graphene kinetically trapped in the PP phase migrated to the thermodynamically favorable PE phase, but this should be verified by observation of the morphology. Future work, for which we continued in a remote collaboration, included SEM or TEM imaging of the nanocomposites, improvement of graphene dispersion through functionalization and the corresponding characterizations.

A.6. <u>References</u>

[1] M. Sumita, K. Sakata, S. Asai, K. Miyasaka, H. Nakagawa, Dispersion of fillers and the electrical conductivity of polymer blends filled with carbon black, Polymer bulletin. 25 (1991) 265-271.

[2] K. Liao, Y. Qian, C.W. Macosko, Ultralow percolation graphene/polyurethane acrylate nanocomposites, Polymer. 53 (2012) 3756-3761.

[3] S. Stankovich, D.A. Dikin, G.H. Dommett, K.M. Kohlhaas, E.J. Zimney, E.A. Stach, et al., Graphene-based composite materials, Nature. 442 (2006) 282.

[4] J. Thomassin, M. Trifkovic, W. Alkarmo, C. Detrembleur, C. Jérôme, C. Macosko, Poly(methyl methacrylate)/graphene oxide nanocomposites by a precipitation polymerization process and their dielectric and rheological characterization, Macromolecules. 47 (2014) 2149-2155.

[5] M.Z. Iqbal, A.A. Abdala, V. Mittal, S. Seifert, A.M. Herring, M.W. Liberatore, Processable conductive graphene/polyethylene nanocomposites: Effects of graphene dispersion and polyethylene blending with oxidized polyethylene on rheology and microstructure, Polymer. 98 (2016) 143-155.

[6] H. Kim, Y. Miura, C.W. Macosko, Graphene/polyurethane nanocomposites for improved gas barrier and electrical conductivity, Chemistry of Materials. 22 (2010) 3441-3450.

[7] S. Ansari, E.P. Giannelis, Functionalized graphene sheet—Poly(vinylidene fluoride) conductive nanocomposites, Journal of Polymer Science Part B: Polymer Physics. 47 (2009) 888-897.

[8] H. Zhang, W. Zheng, Q. Yan, Y. Yang, J. Wang, Z. Lu, et al., Electrically conductive polyethylene terephthalate/graphene nanocomposites prepared by melt compounding, Polymer. 51 (2010) 1191-1196.

[9] S.H. Ryu, A. Shanmugharaj, Influence of long-chain alkylamine-modified graphene oxide on the crystallization, mechanical and electrical properties of isotactic polypropylene nanocomposites, Chem. Eng. J. 244 (2014) 552-560.

[10] H. Kim, C.W. Macosko, Morphology and properties of polyester/exfoliated graphite nanocomposites, (2008).

[11] H. Kim, C.W. Macosko, Processing-property relationships of polycarbonate/graphene composites, Polymer. 50 (2009) 3797-3809.

[12] D. Hofmann, M. Keinath, R. Thomann, R. Mülhaupt, Thermoplastic carbon/polyamide 12 composites containing functionalized graphene, expanded graphite, and carbon nanofillers, Macromolecular Materials and Engineering. 299 (2014) 1329-1342.

[13] C. Mao, Y. Zhu, W. Jiang, Design of electrical conductive composites: tuning the morphology to improve the electrical properties of graphene filled immiscible polymer blends, ACS applied materials & interfaces. 4 (2012) 5281-5286.

[14] R. Tchoudakov, O. Breuer, M. Narkis, A. Siegmann, Conductive polymer blends with low carbon black loading: polypropylene/polyamide, Polymer Engineering & Science. 36 (1996) 1336-1346.

[15] L. Bai, S. He, J.W. Fruehwirth, A. Stein, C.W. Macosko, X. Cheng, Localizing graphene at the interface of cocontinuous polymer blends: Morphology, rheology, and conductivity of cocontinuous conductive polymer composites, J. Rheol. 61 (2017) 575-587.

[16] L. Bai, R. Sharma, X. Cheng, C.W. Macosko, Kinetic control of graphene localization in co-continuous polymer blends via melt compounding, Langmuir. 34 (2018) 1073-1083.

[17] S. Wu, Polar and nonpolar interactions in adhesion, The Journal of Adhesion. 5 (1973) 39-55.

[18] J. Dai, G. Wang, L. Ma, C. Wu, Surface properties of graphene: relationship to graphene-polymer composites, Rev.Adv.Mater.Sci. 40 (2015) 60-71.

APPENDIX I

Structural, Morphological, Thermal, Mechanical and Electrical Characterization Techniques and Procedures

I.1. Structural and morphological characterization

I.1.1. NMR spectroscopy

Chitosan structural analysis was carried out by ^{13}C NMR with CP/MAS technique using a Bruker Avance III instrument equipped with a cylindrical zirconium rotor of 7 mm of external diameter. NMR spectrum was recorded at a ^{13}C and ^{1}H frequencies of 100.6 MHz (field of 9.40 T) and 400.0 MHz, respectively. The ^{13}C {^{1}H} cross-polarization magicangle spinning (CPMAS) spectrum was measured at a spin rate of 4 kHz and 5400 scans were collected. The measurement was carried out at ambient temperature. The acetylation degree (DA) of chitosan was determined by dividing the intensity of the resonance of the methyl group carbon by the average intensity of the resonances of the glycosyl ring carbon atoms. The DA was calculated using the following relationship:

$$\%DA = \frac{I\,[CH_3]}{\left(I[C_1] + I[C_2] + I[C_3] + I[C_4] + I[C_5] + I[C_6]\right)/6}\; x\; 100 \qquad \text{(Eqn. I.1.1)}$$

I is the intensity of the particular resonance peak.

I.1.2. UV-vis spectroscopy

A Perkin Elmer Lambda 25 spectrometer was used to collect the UV–vis absorption spectra between 200 and 800 nm of graphene materials.

I.1.3. _Fourier-transform infrared (FTIR) spectroscopy_

The structure of GO, GS, GO-AgNPs hybrids and polymer nanocomposites were examined by FTIR spectroscopy using a Thermo Nicolet iS10 spectrometer equipped with an attenuated total reflectance accessory (ATR). The first step was to collect a background spectrum to subtract from the sample spectrum. Then few milligrams of sample were analyzed using the module for ten scans in a range from 400 to 4000 cm^{-1} at a resolution 4 cm^{-1}. After scanning, the baseline was corrected and the bands of the FTIR profile were used to obtain the qualitative information regarding functional groups present on each sample. All spectra were smoothed and fitted to an automatic base line correction using OMNIC 9.0 software.

I.1.4. _X-ray photoelectron spectroscopy (XPS)_

For the surface chemistry analysis, a SPECS system was used with a monochromatic Al Kα X-ray source (1486.6 eV) and a Phoibos 150 1D-DLD analyzer. The core level spectra were obtained at a photoelectron take-off angle of 90°, measured with respect to the sample surface. Both wide survey and high resolution spectra for C1s were collected. The XPS survey-scan spectra were recorded at a pass energy of 80 eV with 1 eV energy step, and 0.1 s dwell time. The individual high-resolution spectra were taken at a pass energy of 30 eV with 0.1 eV energy step, and 0.1 s dwell time.

I.1.5. _Raman Spectroscopy_

Raman spectra analysis was carried out by using a Renishaw Invia microscope with laser frequency of 514 nm as an excitation source. The spectra were measured from 500 to 3500 cm^{-1}. An average of three different locations within the sample was measured.

I.1.6. *X-ray diffraction (XRD)*

The XRD spectra of graphene materials were recorded using a Malvern Panalytical X'PERT PRO automatic diffractometer operating at 40 kV and 40 mA in theta–theta configuration, a secondary monochromator with Cu-Kα radiation (λ = 1.5418 Å), and a PIXcel solid state detector (active length in 2θ = 3.347°).

Data were collected from 1 to 50° 2θ for graphite, GO and GS, and from 1 to 90° 2θ for GO–AgNPs (step size = 0.026° and time per step = 80 s, total time 20 min) at room temperature. The nanohybrids measurements were performed on the same samples analyzed by Raman spectroscopy. Polymer nanocomposite film samples were scanned in the range of 1 to 50° with a step size of 0.02°, and a counting time of 10 s per step. A variable divergence slit giving a constant 5 mm area of sample illumination was used. The interlayer separation in the graphene material was calculated by Bragg's law:

$$n\lambda = 2d \cdot \text{sen}\theta \qquad \text{(Eqn. I.1.6)}$$

where n is the order of reflection (equal to 1), λ the wavelength of the copper irradiation (0.154 nm), d the distance between the graphenic sheets, and θ the angle of diffraction.

I.1.7. *Atomic force microscopy (AFM)*

Graphene oxide sheets were characterized by a Bruker (ICON) atomic force microscope (AFM) using tapping mode operated in air. The samples for AFM measurement were prepared using a spin-coating method. Exfoliated GO in an aqueous suspension was pipetted onto mica support. AFM image analysis was performed with Nano-Scope Analysis software. Size and thickness distributions were carried out after counting the lateral dimension and height respectively of approximately 100 individual graphene sheets, from several AFM images.

I.1.8. *Scanning electron microscopy (SEM)*

SEM images of GO and GS were obtained on a Hitachi S-4800 scanning electron microscope at an accelerating voltage of 5 kV. Likewise, images of the fractured surface of CS- and PVA-based nanocomposite films were obtained after being fractured the films in liquid nitrogen and sputtered with gold.

I.1.9. *Transmission electron microscopy (TEM)*

TEM micrographs of the graphene-based derivatives (GO, GS and GO-AgNPs) and polymer nanocomposites were obtained using a Philips Tecnai G2 20 TWIN TEM at 200 kV accelerated voltage. Graphene derivative samples were prepared by drop-coating dilute suspensions onto carbon coated copper grids and dried at room temperature. PVA-based nanocomposite films were sectioned with a Leica EM UC6 ultramicrotome apparatus and placed in coated cooper grids. In the case of GO-AgNPs hybrids, the average diameter of silver nanoparticles was obtained by analyzing the TEM photos using the software named Image Pro Plus.

I.2. Thermal characterization

I.2.1. *Thermogravimetric analysis (TGA)*

TGA test were performed on a TA instruments TG-Q-500 at a heating rate of 10 °C/min under nitrogen or air-flow rate of 75 mL/min, within the temperature range of 40–800 °C.

I.2.2. *Differential scanning calorimetry (DSC)*

Differential scanning calorimetry analyses (DSC) were performed on a Mettler Toledo DSC 3+ unit, at a heating rate of 10 °C /min under nitrogen atmosphere (flow rate of 20 mL/min), in order to evaluate the thermal transitions of the composites. The samples were heated from -30 °C to 240 °C, maintained at this temperature for 5 min to erase the thermal history, then cooled to -30 °C and

heated again to 250 °C. Values were obtained from the first cooling and second heating scans.

For PVA-based nanocomposites, the degree of crystallinity (X_c) of PVA was calculated from the second heating scan by using the following equation I.3:

$$X_c(\%) = \left[\frac{\Delta H_m}{\Delta H_m^0(1-\emptyset)}\right] \text{x}100 \qquad \text{(Eqn. I.2.2)}$$

where ΔH_m is the enthalpy of fusion of the nanocomposite samples, ΔH^0_m is the enthalpy of fusion of the 100% crystalline PVA (141.932 J/g), and ϕ is the weight fraction of filler in the composite.

I.3. Mechanical characterization

Nanocomposite films mechanical properties were measured using an electromechanical testing machine (MTS Insight 10). The gauge length was set at 10 mm and the cross head speed of testing at 5 mm/min at room temperature with a 250 N load cell. Before testing, the films were cut into a dog-bone shape and kept at room temperature at a relative humidity of 58% for more than 1 week to ensure equilibration of the moisture uptake in the films. Ten identical specimens of each composite film were tested and the average values were reported.

The properties evaluated were modulus of elasticity (Young's modulus), yield stress, break stress and elongation at break. The rate of change of the properties was calculated from the following equation I.3:

$$\eta = \frac{\chi_{CP} - \chi_P}{\chi_P}\text{x}100 \qquad \text{(Eqn. I.3)}$$

where χ_{CP} and χ_P are the value of one of the evaluated mechanical properties of the composite and polymer without filler, respectively.

I.4. Electrical conductivity

The electrical conductivity of the film samples with 80 μm thickness was measured at five different points by using a four-point probe resistivity meter (Loresta GP, Model MCP-T610, Mitsubishi Chemical Co.) at room temperature.

I.5. <u>Barrier properties</u>

Water vapor permeability (WVP) of nanocomposite films was determined according to the ASTM E96 standard, using the upright cup method. All dried film samples were conditioned for 1 week at 58% relative humidity (RH) and 25 °C before being analyzed. The films were sealed on cups containing deionized water and then the test cups were placed in an environmental chamber at 25 °C and 58 % RH. Each cup was weighed to the nearest 0.00001 g on an electronic scale. The weight of each cup and the time were recorded. The weight of the cups was measured every 12 h up to 168 h after placement in the environmental chamber. Each sample was tested in triplicate.

The water vapor transmission rate (WVTR) was calculated from the slope of the curve weight change as a function of time using linear regression analysis, according to equation I.5:

$$WVTR = \frac{slope \cdot d}{A\,(R_1 - R_2)} \qquad \text{(Eqn. I.5.1)}$$

where d is the average thickness of the film, A the test area, $R1$ the relative vapor pressure in the permeation cell, and $R2$ the relative vapor pressure in the environmental chamber.

The water vapor permeability (WVP) was calculated as:

$$WVP = \frac{WVTR}{S} \qquad \text{(Eqn. I.5.2)}$$

where S is the saturation vapor pressure (Pa) of water at test temperature.

SPSS 24 (IBM SPSS statistic, USA) was used to analyze the data by variance (ANOVA) analysis with Tukey's post-Hoc test, and significant differences were determined between pure polymers and the different nanocomposites studied. A p-value less than 0.05 was considered statistically significant.

I.6. <u>Water absorption</u>

For the evaluation of water absorption, the samples (three replicates per sample) were dried at 60 °C for three days to a constant weight, then cooled in a desiccator, and weighted (W_0). The films were then immersed in deionized water at room temperature for 24 hours. Specimens were removed, and weighted (W_w) after wiping the excess water on their surfaces with a filter paper. Finally, the samples were weighted (W_d) again after vacuum drying for three days at 60 °C. The total water content (W_t) for each sample was calculated from the following equation I.6:

$$W_t(\%) = \frac{W_w - W_d}{W_0} \times 100 \qquad \text{(Eqn. I.6)}$$

I.7. <u>Swelling and dissolution degree</u>

The protocol consists in weighting the dry films (dry_{mass}), exactly dried at 60 °C for three days and immersed them in deionized water at room temperature for 24 hours. Then, the swollen samples were carefully removed from the medium and placed on filter paper for a few seconds (without hardly touching them) and weighed again (wet_{mass}). The swelling degree (SD) was determined using equation I.7.1. The data points were calculated as the average of 3 different values.

$$SD\ (\%) = \frac{wet_{mass} - dry_{mass}}{dry_{mass}} \times 100 \qquad \text{(Eqn. I.7.1)}$$

Once the swelling degree was adquired, the tested specimens were dried again during three days at 60 °C with vacuum. After, the samples were left to cool in a desiccator and weighed again ($mass_{after}$). The polymer dissolution degree (pDD %) for each sample was calculated from the following equation I.7.2:

$$pDD\ (\%) = \frac{dry_{mass} - mass_{after}}{mass_{after}} \times 100 \qquad \text{(Eqn. I.7.2)}$$

-

APPENDIX II

List of Abbreviations

^{1}H NMR	Proton Nuclear Magnetic Resonance
^{13}C NMR	Carbon-13 Nuclear Magnetic Resonance
A	Cross-sectional area
AFM	Atomic force microscopy
Ag^+	Silver ions
Ag^0	Silver atoms
$AgNO_3$	Silver Nitrate
AgNPs	Silver nanoparticles
BAL	Bioartificial liver
BHI	Brain heart infusion
CCG	Chemically converted graphene
CFU	Colony-forming units
CNTs	Carbon nanotubes
COS	Chitooligosaccharides
CP/MAS-NMR	Cross Polarization/Magic Angle NMR Spectroscopy
CS	Chitosan
CT	Chitin
CVD	Chemical vapor deposition
DA	Degree of acetylation
DD	Degree of deacetylation
DH	Degree of hydrolysis

DMF	N,N-dimethylformamide
DMSO	Dimethyl sulfoxide
DP	Degree of polymerization
DTG	Derivative thermogravimetric
E	Elongation
ESD	Electrostatic discharge
EUCAST	European Committee on Antimicrobial Susceptibility Testing
FCC	Face-centered cubic
fDD	Film dissolution degree
FET	Field-effect transistor
FPR	Four-point resistivity meter
FTIR	Fourier Transform Infrared Spectroscopy
FWHM	Full width at half maximum
G	Graphene
GC	Growth Control
GLY	Glycerol
GO	Graphene oxide
GO-AgNPs	GO decorated with silver nanoparticles
GrO	Graphite oxide
GS	Chemically reduced graphite sheets
HDPE	High density Polyethylene
HES	Hydroxyethyl starch
ILs	Ionic liquids
IPN	Interpenetrating Polymer Networks
ITO	Indium Tin Oxide
L-AA	L-ascorbic acid
LCD	Liquid Crystal Displays

LCST	Lower critical solution temperature
LD_{50}	Lethal dose (50% of the group)
LLDPE	Low density Polyethylene
LPS	Lipopolysaccharide
MHB	Mueller-Hinton Broth
MIC	Minimum Inhibitory Concentration
M_n	Number average molecular weight
MTS	Measure Test Simulate
M_w	Weight average molecular weight
NBR	Acrylonitrile-butadiene rubber
NMP	N-methyl-pyrrolidone
NPs	Nanoparticles
OLEF	Organic Light-Emitting Diodes
P(VAc-co-VA)	Copolymer of vinyl acetate and vinyl alcohol
PBS	Phosphate-buffered saline
PCA	Plate count agar
PCL	Poly(ε-caprolactone)
pDA	Polydopamine
PE	Polyethylene
PE-b-PEO	Polyethylene-block-polyethylene oxide
PEG	Polyethylene Glycol
PEO	Poly(ethylene oxide)
PLA	Poly(lactic acid)
PMMA	Poly(methyl methacrylate)
POSS	Polyhedral silsesquioxanes
PP	Polypropylene
PS	Polystyrene

PVA	Poly(vinyl alcohol)
PVAc	Poly(vinyl acetate)
PVB	Poly(vinyl butyral)
PVC	Poly(vinyl chloride)
PVP	Poly(vinylpyrrolidone)
R	Resistance
rGO	Reduced graphene oxide
RH	Relative humidity
ROS	Reactive Oxygen Species
RPMI	Roswell Park Memorial Institute (Buffer)
RT	Room temperature
SAED	Selected area electron diffraction
SAN	Styrene acrylonitrile
SBS	Styrene-butadiene-styrene
SC	Sterility Control
SD	Swelling degree
SDBS	Dodecylbenzenesulphate
SEM	Scanning electron microscopy
SERS	Surface Enhanced Raman scattering
SiC	Silicon Carbide
SPR	Surface Plasmon Resonance
$T_{5\%}$	Temperatures for 5% weight loss
$T_{50\%}$	Temperatures for 50% weight loss
T_c	Crystallization temperature
TEM	Transmission Electron Microscopy
TG	Thermogravimetric
T_g	Grass transition temperature

TGA	Thermogravimetric analysis
THF	Tetrahydrofuran
T_m	Melting temperature
T_{max}	Temperature of the maximum loss rate
TRGO	Thermally reduced graphene oxide,
UCM	Upright cup method
UCST	Upper critical solution temperature
UV-Vis	Ultraviolet–visible Spectroscopy
VASA	Vacuum-assisted self-assembly
WAC	Water absorption capacity
WVP	Water vapor permeability (WVP)
X_c	Degree of crystallinity
XPS	X-ray Photoelectron Spectroscopy
XRD	X-ray diffraction Spectroscopy
γ_{ij}	Interfacial tensions
ΔH_c	Crystallization enthalpy
ΔH_m	Melting enthalpy
ε_f	Fermi energy
ρ	Electrical resistivity
σ	Electrical conductivity
ω_a	Wetting coefficient

APPENDIX III

List of Figures

Appendix III

APPENDIX IV

List of Tables

Polymer nanocomposites have emerged as an effective strategy to improve the structural and functional properties of polymers expanding their applications in different sectors such as construction, automobile or medical field. This approach can only be achieving in the presence of well-dispersed nanofillers and strong interfacial adhesion. Likewise, the design of biomaterials with antimicrobial properties is also of vital importance due to the increase in medical implants-associated infections. Therefore, the main objective of this PhD thesis has been to develop bionanocomposites that have a combination of good thermal, mechanical and permeability properties, as well as antimicrobial capacity. For this purpose, different nanostructures based on graphene have been synthesized and characterized to be used later as reinforcements in chitosan (CS) and poly(vinyl alcohol) (PVA) polymers through different routes.

Throughout the reading of the different chapters, the synthesis methods used in the manufacture of these bionanocomposites are described and the results of the structural and morphological characterization are analyzed, as well as the mechanical, thermal, permeability and antimicrobial properties. The designed materials can serve as a basis for the development of potentially interesting components for transdermal drug administration and as wound dressings.